Simulation and Robust Optimization for Electric Devices with Uncertainties

Simulation und Robuste Optimierung von Elektrischen Geräten mit Unsicherheiten
Zur Erlangung des akademischen Grades Doktor-Ingenieur (Dr.-Ing.)
genehmigte Dissertation von Zeger J.A.K.E. Bontinck aus Brügge, Belgien
Tag der Einreichung: 26. Juni 2018, Tag der Prüfung: 2. November 2018
Darmstadt — D 18

1. Gutachten: Prof. Dr. Sebastian Schöps
2. Gutachten: Prof. Dr. Herbert De Gersem

TECHNISCHE
UNIVERSITÄT
DARMSTADT

Fachbereich Elektrotechnik
und Informationstechnik
Institut für
Theorie Elektromagnetischer Felder
Graduate School of
Computational Engineering

Simulation and Robust Optimization for Electric Devices with Uncertainties
Simulation und Robuste Optimierung von Elektrischen Geräten mit Unsicherheiten

Genehmigte Dissertation von Zeger J.A.K.E. Bontinck aus Brügge, Belgien

1. Gutachten: Prof. Dr. Sebastian Schöps
2. Gutachten: Prof. Dr. Herbert De Gersem

Tag der Einreichung: 26. Juni 2018
Tag der Prüfung: 2. November 2018

Darmstadt — D 18

Bitte zitieren Sie dieses Dokument als:
URN: urn:nbn:de:tuda-tuprints-83302
URL: http://tuprints.ulb.tu-darmstadt.de/id/eprint/83302

Erklärung zur Dissertation

Ich versichere hiermit, dass die elektronische Version meiner Dissertation mit der schriftlichen Version übereinstimmt. Ich versichere hiermit, dass zu einem vorherigen Zeitpunkt noch keine Promotion versucht wurde. Die vorliegende Dissertation wurde selbstständig und nur unter Verwendung der angegebenen Quellen verfasst. Die Arbeit hat bisher noch nicht zu Prüfungszwecken gedient.

Darmstadt, den 26. Juni 2018

(Zeger J.A.K.E. Bontinck)

Abstract

This dissertation deals with modeling, simulation and optimization of low-frequency electromagnetic devices and quantification of the impact of uncertainties on these devices. The emphasis of these methods is on their application for electric machines.

A Permanent Magnet Synchronous Machine (PMSM) is simulated using Iso-Geometric Analysis (IGA). An efficient modeling procedure has been established by incorporating a harmonic stator-rotor coupling. The procedure is found to be stable. Furthermore, it is found that there is strong reduction in computational time with respect to a classical monolithic finite element method. The properties of the ingredients of IGA, i.e. B-splines and Non-Uniform B-Splines, are exploited to conduct a shape optimization for the example of a Stern-Gerlach magnet. It is shown that the IGA framework is a reliable and promising tool for simulating and optimizing electric devices.

Different formulations for robust optimization are recalled. The formulations are tested for the optimization of the size of the permanent magnet in a PMSM. It is shown that under the application of linearization the deterministic and the stochastic formulation are equivalent. An efficient deterministic optimization algorithm is constructed by the implementation of an affine decomposition. It is shown that the deterministic algorithm outperforms the widely used stochastic algorithms for this application.

Finally, different models to incorporate uncertainties in the simulation of PMSMs are developed. They incorporate different types of rotor eccentricity, uncertainties in the permanent magnets (geometric and material related) and uncertainties that are introduced by the welding processes during the manufacturing. Their influences are studied using stochastic collocation and using the classical Monte Carlo method. Furthermore, the Multilevel Monte Carlo approach is combined with error estimation and applied to determine high dimensional uncertainties in a PMSM.

Zusammenfassung

Diese Dissertation befasst sich mit der Modellierung, Simulation und Optimierung niederfrequenter elektromagnetischer Geräte, unter Berücksichtigung von Unsicherheiten. Der Schwerpunkt liegt in die Anwendung auf elektrische Maschinen.

Eine Permanentmagnetsynchronmaschine (PMSM) wird mit isogeometrischer Analyse (IGA) simuliert. Ein numerisch effizientes Verfahren erhält man mit einer harmonischen Stator-Rotor-Kopplung. Das Verfahren ist stabil und die Rechenzeit lässt sich im Vergleich mit der klassischen Finite-Elemente-Methode weitgehend reduzieren. Die inhärenten Strukturen der B-Splines in der IGA ermöglichen die Entwicklung eines effizienten Optimierungsverfahrens für die Optimierung der Geometrie elektrischer Geräte.

Verschiedene etablierte Optimierungsverfahren werden vorgestellt und zur Optimierung einer PMSM angewendet. Es wird gezeigt, dass die deterministische und stochastische Formulierung mit einander äquivalent sind. Ein effizientes Optimierungsverfahren wird durch eine affine Dekomposition bewirkt.

Abschließend werden Unsicherheiten während der Simulation elektrischer Maschinen berücksichtigt. Diese Unsicherheiten treten durch Rotor-Exzentrizitäten und Materialeigenschaften auf. Sie werden mit stochastischer Kollokation und mit einem Monte Carlo Verfahren untersucht. Zur Reduktion der numerischen Kosten wird die Anwendbarkeit des Multilevel Monte Carlo Verfahrens untersucht. Dieses Verfahren wird mit einem Fehlerschätzer kombiniert.

> “It would be possible to describe everything scientifically, but it would make no sense. It would be a description without meaning, as if you described a Beethoven symphony as a variation of wave pressure.”
>
> A. Einstein cited in
> *Physik im Wandel meiner Zeit* – M. Born

Contents

List of Figures

List of Tables

List of Abbreviations

B-spline	Basis spline
BFGS	Broyden-Fletcher-Goldfarb-Shanno
CAD	Computer Aided Design
CFS	Closed Form Solution
D-N	Dirichlet-to-Neumann
DFP	Davidon-Fletcher-Powell
DoF	Degrees of Freedom
EMF	Electromotive Force
FEM	Finite Element Method
GA	Genetic Algorithm
gPC	generalized Polynomial Chaos
HS-RC	Harmonic Stator-Rotor Coupling
IBVP	Initial-Boundary Value Problem
IGA	Iso-Geometric Analysis
MC	Monte Carlo
MLMC	Multilevel Monte Carlo
MOR	Model Order Reduction
MSE	Mean Square Error
MVP	Magnetic Vector Potential
N-D	Neumann-to-Dirichlet
NLP	Non-linear Optimization Problem
NURBS	Non-Uniform Rational B-splines
PDE	Partial Differential Equation
PDF	Probability Density Function
PM	Permanent Magnet
PMSM	Permanent Magnet Synchronous Machine
POD	Proper Orthogonal Decomposition
PSO	Particle Swarm Optimization
qMC	quasi Monte Carlo
QP	Quadratic Programming
QoI	Quantity of Interest
RB	Reduced Basis
RSM	Response Surface Model
SC	Stochastic Collocation
sPDE	stochastic PDE
SQP	Sequential Quadratic Programming
std	Standard Deviation
THD	Total Harmonic Distortion
UQ	Uncertainty Quantification

Movement I

Allegro: Prologue

1 Introduction

> "Zu Hilfe! Zu Hilfe! Sonst bin ich verloren!"
>
> Tamino in *Die Zauberflöte*
> – W. A. Mozart

In this introductory chapter the reader is acquainted with the bigger framework of this dissertation. In the first section the current state of the research fields is addressed. The second section writes down the research goals of this thesis.

1.1 Background of This Work

The use of electric machines in society has taken a high rise in the recent years. This is caused by the increased automation in industry and by the growing awareness of climate change, which encouraged the market of e-mobility. Where some automobile manufacturers, such as Tesla, use induction machines as drive units, others like Toyota rely on Permanent Magnet Synchronous Machines (PMSMs). The advantage of the former is that they are cheaper to construct, however, the latter have a higher volume to torque ratio and overall efficiency, see for example [57, 163]. Hence, PMSMs are also often used in e-bikes, e.g. Figure 1.1. In industry electric machines are developed approaching their technical limit. In former times, during the development of new devices, different prototypes were constructed, measured and tested. Nowadays, a large number of these physical prototypes have been replaced by numerical models [127], often called virtual prototypes. The governing differential equations, in the case of electrical machines, stem from (an approximation of) the Maxwell equations and are discretized into a system of equations. The advantages using virtual prototypes are numerous. There is the reduction in development time and costs and the reduction of material waste, just to name two of them. However, the virtual models have to be reliable and they have to be good representatives of the produced machine. The gain in computational power has enabled the construction of very accurate virtual prototypes, so that uncertainties introduced in the machines during the manufacturing process have become more relevant due to their influence on the machine's performance, e.g. [36, 93]. These uncertainties are commonly not considered until very late in the design process of the machine (if at all). Including these imprecisions in early design stages of development will lead to more robust designs.

In literature different sources of uncertainties in electric devices are identified. They might originate from uncertain material properties, e.g. [89, 126], caused by welding of the machine [36, 93], geometri-

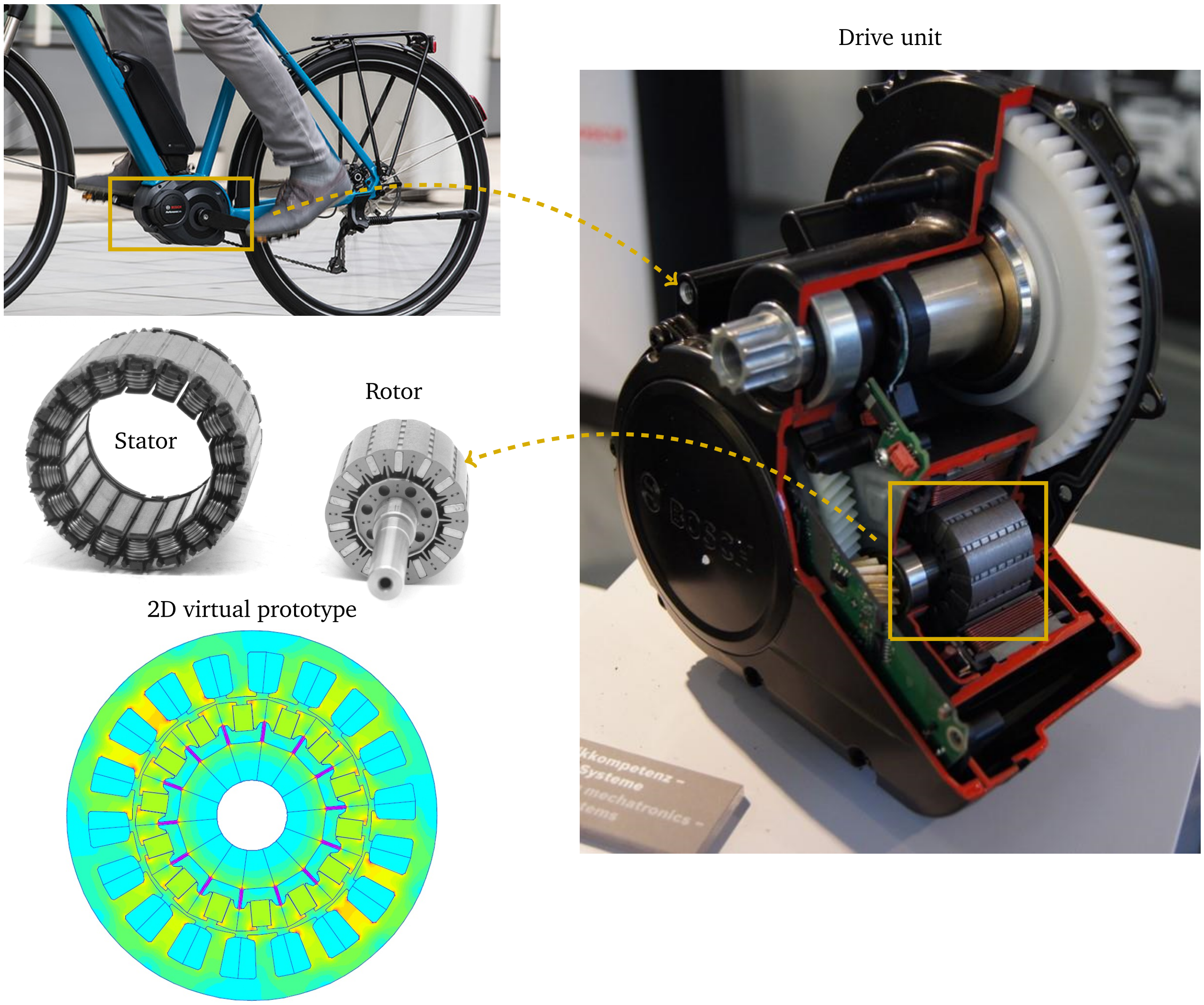

Figure 1.1: The drive unit and permanent magnet synchronous machine as developed for an e-bike at Robert Bosch GmbH (Source: Robert Bosch GmbH). The 2D virtual prototype shows the magnetic field, obtained using FEMM [103].

cal uncertainties, such as rotor eccentricity [149], the length of stator teeth [113], or uncertainties in the sources, such as the permanent magnets [90, 99]. Relying on virtual prototypes enables the engineer to study the influence of these kind of uncertainties on a Quantity of Interest (QoI) by adding them to the numerical model that constitutes the virtual prototype. This research area is called Uncertainty Quantification (UQ). To determine the statistical quantities, such as the expectation values and higher moments, different numerical methods have been proposed in the literature. The most well known procedure is the Monte Carlo (MC) method. It uses random samples to determine the stochastic quantities and every sample corresponds to a different configuration of the machine. For every configuration the system of equations has to be assembled and solved. When high accuracies are demanded these systems have high dimensions and are computationally heavy to solve. This implies long simulation times. Depending on the total number of random variables under consideration, other methods need less samples than MC and are thus more efficient in determining the stochastic quantities. An example addressed in this work is Stochastic Collocation (SC) [159] which is an appropriate alternative when the number of random samples is low and the QoI is smooth with respect to the uncertain parameters. For high-dimensional uncertainties, one has to come around with MC and needs a large number of samples. Another way to circumvent the high cost of MC, is by relying on a lot of computationally cheap evaluations for the majority of the samples and the high accurate, computationally costly simulations only for a few number of samples. This is the underlying idea of Multilevel Monte Carlo (MLMC) [69]. In this dissertation this method is benchmarked on a simple electric device and then applied to determine uncertainties in a Permanent Magnet Synchronous Machine (PMSM).

Traditionally, the classical Finite Element Method (FEM) is utilized to obtain the discrete system of equations, e.g. [132]. Many implementations make only use of first order hat functions, while higher order approaches are mathematically well understood [161]. A drawback of the method is that the maps used for the elements of the mesh are unable to exactly represent simple geometries such as conic sections (i.e. circles). Refinement can reduce the geometrical approximation error, but it can never fully eliminate it. This becomes particularly troublesome if small geometry variations should be analyzed, e.g. in UQ. Mesh sensitivities may be larger than the uncertainty in the geometry. Another shortcoming is that the common basis functions in FEM are only C^0 continuous across elements. This may influence the computational accuracy for some of the QoIs. For example, forces and torques in electrical machines are often calculated via the Maxwell stress tensor evaluated in the airgap. It is known that the results are very sensitive to the discretization of the airgap and to the location in the airgap where the quantities are evaluated [84, 105, 145]. The application of the FEM for simulating rotating machines often involves mesh deformations, e.g. moving band strategies [45]. However, these mesh deformations introduce spurious effects on the ripple of the acting forces [154]. A sliding surface method such as a time stepping method e.g. [24], or harmonic stator-rotor coupling [42], introduces less spurious effects [154].

Iso-Geometric Analysis (IGA) [40, 87] overcomes many of the drawbacks of classical FEM. Basically, IGA exploits the basis functions used in Computer Aided Design (CAD) for the parametrization of the geometry to also approximate the solutions during the analysis. These basis functions are B-Splines and Non-Uniform Rational B-Splines (NURBS). Conic sections in the CAD framework are represented exactly. Furthermore, the wider support of the basis functions leads to a higher regularity of the solution, which is solely limited by the chosen approximation order. Using a basis of degree p leads to a regularity of $p-1$. IGA also features a better accuracy with respect to the number of degrees of freedom compared to FEM [40, 88]. The ingredients used to construct the CAD geometry allow easily to introduce deviations in the geometry and enable an elegant way to optimize the shape of devices, e.g. [97]. IGA has already been applied in different fields such as, e.g., mechanical engineering [147], fluid dynamics [71]. Even though IGA might appear as a holy grail with respect to FEM, it also has its drawbacks. Firstly, the construction of the geometries often requires manual intervention. Secondly, the wider support of the basis functions leads to denser matrices, albeit smaller matrices compared to FEM when considering a similar accuracy. Finally, also local refinement is harder to achieve due to the tensor product construction. In this work the applicability of IGA for the simulation of electric devices is studied. Furthermore, the easy handling of geometric changes is exploited to apply shape optimization to a Stern-Gerlach magnet.

In the final stages of developing electrical machines, the virtual prototypes are submitted to numerical optimization in order to, e.g. minimize the material costs [104] by for example optimizing the rotor shape [65], or the size [99] and shape of the Permanent Magnet (PM) [100]. These PMs are often constructed from rare earth elements, e.g. NdFeB magnets and the separation of these rare earth elements is known to be environmentally polluting [21]. An overview of different optimization algorithms applied to electrical machines can be found in [54]. Optimization algorithms are generally divided into two groups: deterministic optimization and stochastic/population-based optimization. In the literature there is a strong tendency for the stochastic optimization algorithms and the most popular under these methods are Genetic Algorithm (GA) e.g. [158] and nature inspired optimization algorithms, e.g. [11, 48, 137, 160]. The advantages of these methods are the straightforwardness of their parallelization, the fact that one can use the finite element solvers as a black-box and that one is able to find a global optimum. A complication is that at every iteration many machine configurations are considered and many finite element solves are needed. In the literature different approaches can be found to reduce the computational burden of optimization, e.g. surrogate models [47], kriging [96]. Another approach

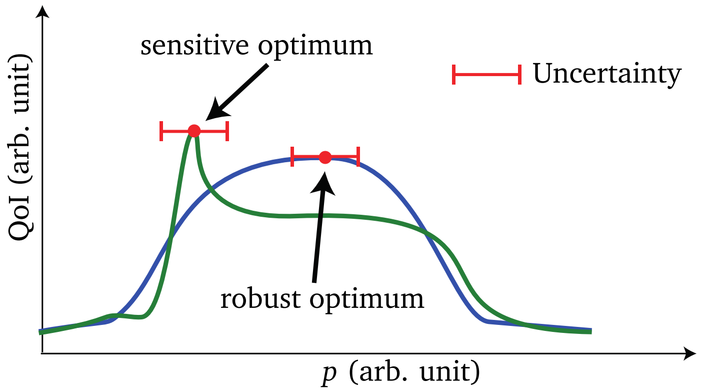

Figure 1.2: Visualization of a sensitive and robust optimum. The green and blue lines represent two different virtual prototypes.

for reducing the computational costs is Model Order Reduction (MOR). One of those methods is called Proper Orthogonal Decomposition (POD) [34] and has been used to reduce the discretization matrices for calculating electric machines [1, 81]. The use of MOR during optimization has shown remarkable improvements in efficiency, e.g. [73, 162]. Another, close related technique is the Reduced Basis (RB) method [131]. In, for example-[109], this method has been applied in combination with optimization.

The deterministic optimization algorithms are known to converge faster, and are more efficient than the stochastic algorithms [54]. The drawback is however, that they may only find local minima and make use of gradients. This can be cumbersome when geometric parameters are considered during optimization. Yet, applying an affine decomposition [131] alleviates this issue and the combination with RB has been shown to result in very efficient optimization algorithms, e.g. [52, 109].

Also in the optimization parameters uncertainties might occur. The found optimum might be very sensitive to these changes and might become sub-optimal, which will lead to under-performances of the manufactured machines. Therefore one is interested in finding robust optima, which are barely influenced by the deviations (Figure 1.2). Different formulations to conduct robust optimization exist. In this work, the focus is on worst-case optimization, see e.g. [50, 94] and a mean-variance formulation [41, 86]. The probability density functions are only considered in the latter formulation, whereas in the former formulation the uncertainties are restricted to a bounded uncertainty set [17]. However, the former might lead to over-engineering, since the worst-case scenario might be very unlikely to occur. This work combines the two formulation with the optimization algorithms mentioned in the previous paragraphs and tries to find equivalences between the different formulations.

More efficient models and algorithms for machine simulation, optimization and quantification of uncertainties reduce the CPU-runtimes and thus less energy is needed to obtain more robust machine models. The construction of reliable robust models that can be used as virtual prototypes will prevent over-engineering and will lead to a reduction in development costs and material waste. The main application of the thesis is a PMSM, which have become more and more present in e-mobility, e.g. Figure 1.1.

1.2 Research Goals

This thesis aims to develop and to test the applicability of efficient numerical models and algorithms for the simulation and the robust optimization of electrical machines under the consideration of uncertainties. Therefore,

- it is examined if IGA is a worthy alternative for the classical FEM for simulating and optimizing electric devices;

- different models and evaluation methods that numerically cheaply handle uncertainties in electric machines, such as eccentric rotor positions, welding influences and magnet uncertainties, are constructed and analyzed;
- the analysis of the applicability of MLMC for modeling high-dimensional uncertainties in electric machines is performed;
- different optimization algorithms are implemented to study their efficiency and equivalences between the different robust optimization formulations are discussed.

1.3 Résumé

In this chapter the thesis has been embedded in the current state of scientific research. More precisely in the field of electric machine simulation, robust optimization and uncertainty quantification. This works aims to construct and apply new and problem-specific numerical methods in order to have efficient algorithms at hand for the simulation of electric machines. The algorithms deal with the simulation and robust optimization of electric devices while considering uncertain parameters in the model.

2 Maxwell’s Equations

> “Physics is really nothing more than a search for ultimate simplicity, but so far all we have is a kind of elegant messiness.”
>
> *A Short History of Nearly Everything*
> – B. Bryson

In physics four fundamental forces (or interactions) are identified, the strong force, the electromagnetic force, the weak force and gravitation. Physicist strive to combine those interactions into the *theory of everything*, which should fully explain all physical phenomena happening in the universe. However, there is still a long way to go and it requires the unification of gravity with the grand unified theory, which incorporates the weak and strong forces with electromagnetism. Electromagnetism is the only force that is completely understood and, which itself, is the combination of electricity and magnetism. Their phenomena were already discovered by the ancient Greeks, who wondered how a lodestone (in Greek “μαγνητις λίϑος”, which translates to “Magnesian stone”) was able to attract pieces of metal. Moreover, also amber (in Greek “ἤλεκτρον”) seems to have an astonishing property, namely, when rubbed, it attracs very light objects [91]. These two peculiarities, on first sight, not linked to each other, where combined more than two millennia later into a set of four equations describing, what it is now called, electromagnetism. This unification was achieved by James Clerk Maxwell in 1873. He ended up with a set of twenty equations [102] which were later more elegantly written down in four equations by Oliver Heaviside [80]. He was able to omit the use of potentials and wrote everything down in vector notation. These equations, called Maxwell’s equations, are the governing equations describing physical phenomena in electric devices and are, therefore, introduced in more detail in this chapter. However, for devices with a complex topology, solving Maxwell’s equations analytically is unfeasible. One has thus to rely on numerical methods such as the Finite Element Method (FEM) and Iso-Geometric Analysis (IGA) introduced in Section 3.2.

As a guidance, I address here some comments on notation. Algebraic vectors are distinguished from scalars, by using bold typeface, e.g. the algebraic vector $\mathbf{p}$ consists of N scalars $[p_1, \dots, p_N]$. On the other hand, physical quantities that are vectors are indicated by vector arrows, e.g. $\vec{A}$. Capital bold face symbols in general represent matrices, e.g. $\mathbf{K}$ and it has as entries the scalars k_{ij}. One exception is made. Distributions related to the scalars p_1 are depicted by the capital letters P_1 and they are gathered in a vector $\mathbf{P}$.

2.1 General Set of Maxwell's Equations

The origin of the first equation of the Maxwell's equations lies in discovery of Hans Christian Ørsted (some source acknowledge Romagnosi [143]), that a wire carrying a current generates a magnetic field. André-Marie Ampère wrote down the phenomenon mathematically, hence the equation is known as *Ampère's law*. While unifying electricity and magnetism, Maxwell introduced an extra-term on the right hand side of the equation, resulting in

$$\nabla \times \vec{H} = \vec{J}_{\mathrm{f}} + \frac{\partial \vec{D}}{\partial t}, \tag{2.1a}$$

where $\vec{H} = \vec{H}(\vec{x}, t)$ is the magnetic field strength, $\vec{J}_{\mathrm{f}} = \vec{J}_{\mathrm{f}}(\vec{x}, t)$ the free current density, which are currents that might flow through wires embedded in the magnetized substance, $\vec{D} = \vec{D}(\vec{x}, t)$ is the displacement field, $\vec{x} = (x, y, z)$ is a position vector and t depicts time. In words this equation states that a current or a time-varying displacement field generate a magnetic field.

The second law was first published by Michael Faraday[1] and is known as *Faraday-Lenz' law*. It states that a changing magnetic field $\vec{B} = \vec{B}(\vec{x}, t)$ induces an electric field $\vec{E} = \vec{E}(\vec{x}, t)$, i.e.,

$$\nabla \times \vec{E} = -\frac{\partial \vec{B}}{\partial t}. \tag{2.1b}$$

The contribution of Emil Lenz seems minor, namely adding the minus sign on the right hand side, but nevertheless important, since the induced electric field will always oppose the change by which it was induced.

The last two laws are named after Friedrich Gauß. The first one is related to the displacement field,

$$\nabla \cdot \vec{D} = \rho_{\mathrm{f}}, \tag{2.1c}$$

with $\rho_{\mathrm{f}} = \rho_{\mathrm{f}}(\vec{x})$ the density of free electric charges. The second one states that there are no magnetic monopoles

$$\nabla \cdot \vec{B} = 0. \tag{2.1d}$$

Maxwell's equations are accompanied with a set of material laws:

$$\vec{D} = \varepsilon \vec{E}, \tag{2.2a}$$

with $\varepsilon = \varepsilon(\vec{x})$ the permittivity,

$$\vec{H} = \nu \vec{B} + \vec{H}_{\mathrm{pm}}, \tag{2.2b}$$

with the reluctivity $\nu = \nu(\vec{x})$, which is related to $\mu = \mu(\vec{x})$ the permeability by $\mu = \nu^{-1}$ and $\vec{H}_{\mathrm{pm}} = \vec{H}_{\mathrm{pm}}(\vec{x})$ the magnetic field strength caused by permanent magnets. For completeness, one has to mention that this material law does not have to be linear, i.e. $\nu(|\vec{B}|)$. However, non-linearity is not addressed in this thesis. Furthermore it is assumed that ν is isotropic. The last material law is *Ohm's law*,

$$\vec{J}_{\mathrm{f}} = \sigma \vec{E}, \tag{2.2c}$$

where $\sigma = \sigma(\vec{x})$ is the conductivity.

From (2.1d) a Magnetic Vector Potential (MVP) $\vec{A} = \vec{A}(\vec{x}, t)$ can be introduced

$$\vec{B} = \nabla \times \vec{A}. \tag{2.3}$$

Rewriting (2.1b) in $\vec{A}$ and integrating both sides of over space, one retrieves

$$\vec{E} = -\frac{\partial \vec{A}}{\partial t} - \nabla \varphi, \tag{2.4}$$

where $\varphi = \varphi(\vec{x})$ is the electric scalar potential.

---

[1] It should be mentioned that Michael Faraday and Joseph Henry almost simultaneously made the same discovery.

2.2 Magnetoquasistatics and Magnetostatics

In the applications discussed in this thesis, the electrical energy is low compared to the time dependent power losses and the magnetic energy, therefore the displacement currents can be neglected, i.e. the *magnetoquasistatic approximation* of Maxwell's equations [141]. Meaning that combining (2.1a), (2.2c), (2.3) and (2.4) results in the parabolic Partial Differential Equation (PDE)

$$\sigma\frac{\partial\vec{A}}{\partial t}+\nabla\times\left(\nu\nabla\times\vec{A}\right)=\underbrace{-\sigma\nabla\varphi}_{\vec{J}_{\mathrm{s}}}\underbrace{-\nabla\times\vec{H}_{\mathrm{pm}}}_{\vec{J}_{\mathrm{pm}}},\tag{2.5}$$

where $\vec{J}_{\mathrm{s}}=\vec{J}_{\mathrm{s}}(\vec{x})$ is the source current density and $\vec{J}_{\mathrm{pm}}$ the current induced by the permanent magnets. From now on, one depicts the terms in the right hand side by $\vec{J}_{\mathrm{tot}}=\vec{J}_{\mathrm{s}}+\vec{J}_{\mathrm{pm}}$. In frequency domain this equation translates to

$$\imath\sigma\omega\vec{A}+\nabla\times\left(\nu\nabla\times\vec{A}\right)=\vec{J}_{\mathrm{tot}},\tag{2.6}$$

where $\imath$ is the imaginary number and ω the applied frequency.

Sometimes, as in the case of electric machines constructed with laminated steel, such that the current flow is aligned with the stacking direction of the laminations, also the eddy currents can be neglected, meaning that the first term in (2.6) can be omitted and the following semi-elliptic PDE is retrieved,

$$\nabla\times\left(\nu\nabla\times\vec{A}\right)=\vec{J}_{\mathrm{tot}}.\tag{2.7}$$

In the literature this is often addressed as the *curl-curl equation* and represents the *magnetostatic approximation* of Maxwell's equations.

For cylindrical machines with lengths comparable to or larger than their diameters, a sufficient accuracy for the parameters of the devices is obtained by relying on 2D models [108]. In these cases it is assumed that $\vec{B}=(B_x(x,y),B_y(x,y),0)$ and thus that $\vec{J}_{\mathrm{tot}}=(0,0,J_{\mathrm{tot},z}(x,y))$ and $\vec{A}=(0,0,A_z(x,y))$. Equation (2.6) transforms into

$$\imath\omega\sigma A_z(x,y)-\nabla\cdot\left(\nu\nabla A_z(x,y)\right)=J_{\mathrm{tot},z}(x,y).\tag{2.8a}$$

The curl-curl equation in 2D becomes

$$-\nabla\cdot\left(\nu\nabla A_z(x,y)\right)=J_{\mathrm{tot},z}(x,y),\tag{2.8b}$$

which is Poisson's equation. To uniquely solve the PDEs on a computational domain Ω (Figure 2.1), boundary conditions and if applicable initial conditions and gauge conditions have to be applied. In this work only three types of boundary conditions are used. They read in the 2D case:

- *Dirichlet boundary conditions* often called "essential boundary conditions" or "electric conditions"

  $$A_z(x,y)=g(x,y)\quad\text{on}\quad\Gamma_{\mathrm{D}}\tag{2.9a}$$

  where $\Gamma_{\mathrm{D}}\subset\partial\Omega$. When $g(\vec{x})=0$ one speaks of homogeneous Dirichlet conditions.

- *Neumann boundary conditions*, often called "natural boundary conditions" or "magnetic conditions", when $h(x,y)\not\equiv 0$

  $$\nu\nabla A_z(x,y)\cdot\vec{n}=h(x,y)\quad\text{on}\quad\Gamma_{\mathrm{N}}\tag{2.9b}$$

  with $\vec{n}$ the outward unit vector perpendicular on $\partial\Omega$, $\Gamma_{\mathrm{N}}\subset\partial\Omega\setminus\Gamma_{\mathrm{D}}$ and $h:\mathbb{R}^2\to\mathbb{R}$.

- *Anti-periodic boundary conditions*, so that on Γ_{l} and Γ_{r} it holds that

  $$A_z|_{\Gamma_{\mathrm{l}}}(x,y)=-A_z|_{\Gamma_{\mathrm{r}}}(x,y),\tag{2.9c}$$

  $$\nu\nabla A_z|_{\Gamma_{\mathrm{l}}}(x,y)\cdot\vec{n}=\nu\nabla A_z|_{\Gamma_{\mathrm{r}}}(x,y)\cdot\vec{n},\tag{2.9d}$$

  with $\Gamma_{\mathrm{D}}\cup\Gamma_{\mathrm{N}}\cup\Gamma_{\mathrm{l}}\cup\Gamma_{\mathrm{r}}=\partial\Omega$ and that $\Gamma_{\mathrm{l,r}}\subset\partial\Omega\setminus\Gamma_{\mathrm{D}}\setminus\Gamma_{\mathrm{N}}\setminus\Gamma_{\mathrm{r,l}}$.

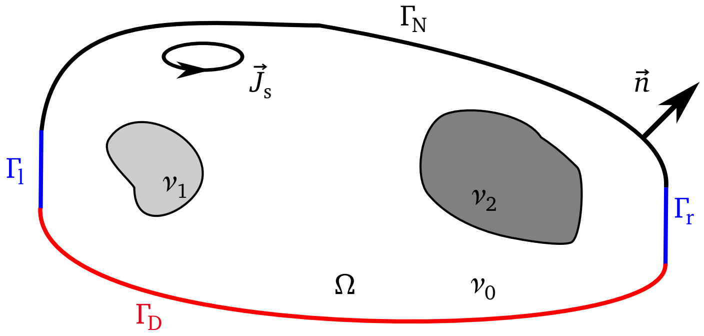

Figure 2.1: General representation of the computational domain for the magnetostatic problem.

2.3 Résumé

In this chapter Maxwell's equations were introduced. The magnetostatic approximation of these equations has been derived and two different boundary conditions, needed to solve the obtained partial differential equations were formulated. In the next part of this dissertation, it is discussed how the partial differential equations are solved numerically and how the discretized versions of the equations can be solved efficiently.

Movement II
Adagio: Numerical Methods

3 Mathematical Foundations for Solving Partial Differential Equations

> “Mathematics is the music of reason.”
>
> Attributed to J.J. Sylvester

The solution of a physical problem can often be found by solving a differential equation. If the solution is only dependent on one variable, e.g. time, one has to solve an ordinary differential equation. A well-known example is Newton’s second law of motion, which describes the position of an object as a function of time under the presence of acting forces. However, it might be that the solution one seeks, depends on more than one variable, e.g. position in space which is the case for the magnetostatic approximation of Maxwell’s equations, i.e. (2.7). In that case the system has to be described by a Partial Differential Equation (PDE), which includes the different dependencies of the Quantity of Interest (QoI) on those variables. A well-known example is the wave equation, which expresses the propagation of a disturbance over time in all spatial directions, or the parabolic equation in (2.5). Generally, for a scalar space and time dependent function $u = u(x, y, z, t)$, a PDE can be written in the form

$$G\left(x, \ldots, z, u, \frac{\partial u}{\partial x}, \ldots, \frac{\partial u}{\partial t}, \frac{\partial^2 u}{\partial x \partial x}, \ldots, \frac{\partial^2 u}{\partial x \partial y \partial t}, \ldots\right) = 0,$$

where G is a functional. In this work only second order linear PDEs are considered meaning that G is linear in u and in its derivatives. These kind of PDEs are categorized in three types: hyperbolic PDEs, parabolic PDEs and elliptic PDEs . In Chapter 2 it was shown under which assumptions Maxwell’s equations reduce to the last two types of PDEs, see (2.5) and (2.7).

However, a differential equation in itself is not sufficient to specify a physical solution. For that, further conditions are needed. If one is only interested in the solution on an enclosed space, there is the need for *boundary conditions*, which specify how the system behaves at the boundary. In (2.9) the three types of boundary conditions addressed in this work have been introduced, namely Dirichlet and Neumann boundary conditions and anti-periodic boundary conditions. For time dependent problems, one also needs to know how the system behaves at a certain point in time. Often, one opts for *initial conditions*, which describes the needed quantities at the initial point in time of the problem.

Since it is not always possible to find a closed form solution to the problem, one needs a numerical formulation in order to solve the PDE. In this chapter the mathematical foundations for solving PDEs numerically are discussed. In the first section the mathematical background, needed for transforming the PDE into its weak formulation (Section 3.2), is introduced. These parts are based on Chapter 1, Chapter 6 and Chapter 11 of [124]. Afterwards the weak formulation is discretized using the Ritz-Galerkin approach (based on [106]) and two possible ways to define the test-functions are addressed. The first method is the classical finite element method, where the test-functions are actually hat-functions. The main idea is to approximate the solution field with hat-functions defined on the triangles in 2D or tetrahedrons in 3D and then use the edges of the triangles to approximate the geometry of the problem. The discussion is based on [60, 132]. The second method is Iso-Geometric Analysis (IGA), where first the geometry is represented by Non-Uniform Rational B-splines (NURBS) and then these NURBS are used as a basis for the approximation space for the solution. Its discussion relies on [40].

3.1 Introduction to Sobolev Spaces

Let Ω be an open, simply connected bounded domain in $\mathbb{R}^d$, with $d = 2$ and with a Lipschitz continuous boundary $\partial\Omega$. The vector $\vec{x}$ is a position vector in Ω. Let us introduce the Hilbert space $L^2(\Omega)$, which contains all square integrable functions and which is endowed with the scalar product $(\cdot,\cdot)_{L^2(\Omega)} : L^2(\Omega) \times L^2(\Omega) \to \mathbb{R}$,

$$(v,w)_{L^2(\Omega)} := \int_\Omega v(\vec{x})w(\vec{x})\,\mathrm{d}\Omega, \tag{3.1}$$

and the associated norm

$$\|v(\vec{x})\|_{L^2} := \left(\int_\Omega |v(\vec{x})|^2\,\mathrm{d}\Omega\right)^{1/2}.$$

From now on the scalar product will be depicted by $(\cdot,\cdot)$ and $v = v(\vec{x})$.

Defining a differential operator $D^{\boldsymbol{\alpha}}$, where $\boldsymbol{\alpha} = (\alpha_1 \ldots, \alpha_d)$, with $\alpha_i \in \mathbb{N} \wedge a_i \neq 0$ and $i = 1, \ldots, d$, one can write for $v \in C_0^\infty(\Omega)$, which is the space of infinitely differentiable functions with closed support, that

$$D^{\boldsymbol{\alpha}} v(\vec{x}) := \frac{\partial^{|\boldsymbol{\alpha}|} v}{\partial x^{\alpha_1} \partial y^{\alpha_2}}, \tag{3.2}$$

where $|\boldsymbol{\alpha}| := \sum_{i=1}^d \alpha_i$. The *Sobolev spaces* H^k are then defined by

$$H^k(\Omega) := \left\{ v \in L^2(\Omega) \mid D^{\boldsymbol{\alpha}} v \in L^2(\Omega), \forall \alpha_i \neq 0 \wedge |\boldsymbol{\alpha}| \leq k \right\}. \tag{3.3}$$

If v is restricted to be zero on $\Gamma_\mathrm{D} \subset \partial\Omega$, which is written as $v|_{\partial\Gamma_\mathrm{D}} = 0$, it is needed to construct a subspace of these Sobolev spaces, i.e.

$$H^k_{\Gamma_\mathrm{D}}(\Omega) := \left\{ v \in H^k(\Omega) \mid v|_{\Gamma_\mathrm{D}} = 0 \right\}. \tag{3.4}$$

If $\Gamma_\mathrm{D} = \partial\Omega$, the notation $H^k_0(\Omega)$ is used, implying $H^k_0(\Omega) = H^k_{\Gamma_\mathrm{D}}(\Omega) = H^k_{\partial\Omega}(\Omega)$.

Consider the magnetostatic elliptic PDE introduced in (2.8b) and let us write that $A_z(x,y) = u$, and for the source term $J_{\text{tot},z}(x,y) = f$. Let first be noted that one actually deals with a non-standard right-hand-side due to the presence of the permanent magnets a singular excitation is introduced. However, this type of problem is well understood e.g. [6, 38]. The elliptic PDE with Dirichlet and Neumann boundary conditions is then written as

$$\begin{aligned} -\nabla \cdot \nu \nabla u &= f \quad \text{in} \quad \Omega, && (3.5a)\\ u &= g \quad \text{on} \quad \Gamma_{\mathrm{D}}, && (3.5b)\\ \nabla u \cdot \vec{n} &= h \quad \text{on} \quad \Gamma_{\mathrm{N}}. && (3.5c) \end{aligned}$$

with $f : \mathbb{R}^d \to \mathbb{R}^d$, $g : \mathbb{R}^d \to \mathbb{R}^d$ and $h : \mathbb{R}^d \to \mathbb{R}^d$. Let us choose the linear differential operator, $\mathscr{L}(v)$ to be the Laplace operator

$$\mathscr{L}(v) = -\nabla \cdot \nu \nabla (v), \tag{3.6}$$

then (3.5) translates into

$$\begin{aligned} \mathscr{L}(u) &= f \quad \text{in} \quad \Omega, && (3.7a)\\ u &= g \quad \text{on} \quad \Gamma_{\mathrm{D}}, && (3.7b)\\ \nabla u \cdot \vec{n} &= h \quad \text{on} \quad \Gamma_{\mathrm{N}}. && (3.7c) \end{aligned}$$

The parabolic PDE in (2.8a) can be written, respectively, as

$$\begin{aligned} \imath\omega\sigma u + \mathscr{L}(u) &= f \quad \text{in} \quad \Omega, && (3.8a)\\ u &= g \quad \text{on} \quad \Gamma_{\mathrm{D}}, && (3.8b)\\ \nabla u \cdot \vec{n} &= h \quad \text{on} \quad \Gamma_{\mathrm{N}}. && (3.8c) \end{aligned}$$

Let us now consider different boundary conditions.

Homogeneous Dirichlet Boundary Conditions

First it is assumed that only homogeneous Dirichlet boundary conditions are applied, meaning $g \equiv 0$. Introducing test-functions $v \in V = H_0^1(\Omega)$, so that they fulfill the conditions on $\partial\Omega$, multiplying left and right-hand-side of (3.7) with v, applying partial integration, Gauß's integral theorem and the information on u on the boundary [60], one finally retrieves

$$\int_\Omega \nu \nabla u \cdot \nabla v \, \mathrm{d}\Omega = \int_\Omega f \, v \, \mathrm{d}\Omega. \tag{3.9}$$

Notice that the second order derivatives have been reduced to first order derivatives. The PDE is said to be written in it is *variational* or *weak* form. Let us now introduce a certain, for the moment undefined Sobolev space W from which the solutions stem. Defining the bilinear form $b(\cdot,\cdot) : W \times V \to \mathbb{R}$ as

$$b(u,v) := \int_\Omega \nabla u \cdot \nu \nabla v \, \mathrm{d}\Omega, \tag{3.10}$$

and using (3.1), then solving (3.7) can be rewritten as

$$\text{find} \quad u \in W \quad \text{so that} \quad b(u,v) = (f,v) \quad \forall v \in V.$$

The same reasoning can be applied for solving (3.8). Testing with $v \in V$, one retrieves the weak form,

$$\imath\omega\sigma(u,v) + b(u,v) = (f,v) \quad \forall v \in V. \tag{3.11}$$

Non-homogeneous Dirichlet Boundary Conditions

In the case of inhomogeneous Dirichlet boundary conditions, the function g is extended into the interior and called $\tilde{g}$, which is called *lifting* [124]. One then looks for the solution $\tilde{u} = u - \tilde{g}$ of

$$\mathscr{L}(\tilde{u}) = f - \mathscr{L}(\tilde{g}) \quad \text{in} \quad \Omega, \tag{3.12a}$$

$$\tilde{u} = 0 \quad \text{on} \quad \Gamma_\mathrm{D} = \partial\Omega, \tag{3.12b}$$

where $\tilde{g} \in H^1(\Omega)$ and $g \in H^{1/2}(\partial\Omega)$ [124]. $H^{1/2}$ is a more general functional space for the restriction of the boundary. A profound discussion can be found in [28].

Using test-functions $v \in V = H_0^1(\Omega)$, solving the PDE in its weak form means: find $\tilde{u} \in W$ so that

$$b(\tilde{u}, v) = (f, v) - b(\tilde{g}, v), \quad \forall v \in V.$$

For the parabolic problem in the frequency domain the weak formulation is formulated as

$$\text{find} \quad \tilde{u} \in W \quad \text{so that} \quad \imath\omega(\tilde{u}, v) + b(\tilde{u}, v) = (f, v) - b(\tilde{g}, v) - \imath\omega(\tilde{g}, v) \quad \forall v \in V.$$

Neumann Boundary Conditions

Assume that $\Gamma_\mathrm{N} = \partial\Omega$ and $\Gamma_\mathrm{D} = \emptyset$. Then the elliptic PDE is solved by using test-functions $v \in V = H^1(\Omega)$ so one has to find $u \in W$, so that

$$b(u, v) = (f, v) + (h, v)_{\partial\Omega} \quad \forall v \in V,$$

where $(\cdot, \cdot)_{\partial\Omega}$ is the scalar product in $L^2(\partial\Omega)$. Analogously one finds as weak from for the parabolic PDE

$$\imath\omega(u, v) + b(u, v) = (f, v) + (h, v)_{\partial\Omega} \quad \forall v \in V.$$

Neumann and Homogeneous Dirichlet Boundary Conditions

In this case the subsets Γ_D and Γ_N of $\partial\Omega$ are open and disjoint, and $\overline{\Gamma}_\mathrm{D} \cup \overline{\Gamma}_\mathrm{N} = \partial\Omega$. It is assumed that $f \in L^2(\Omega)$ and $h \in L^2(\Gamma_\mathrm{N})$ [124]. Using test-functions $v \in V = H^1_{\Gamma_\mathrm{D}}(\Omega)$ the weak formulation of the elliptic and parabolic PDE are given, respectively, by: find $u \in W$ so that

$$b(u, v) = (f, v) + (h, v)_{\Gamma_\mathrm{N}} \quad \forall v \in V,$$

or

$$\imath\omega\,(u, v) + b(u, v) = (f, v) + (h, v)_{\Gamma_\mathrm{N}} \quad \forall v \in V.$$

Neumann and Non-Homogeneous Dirichlet Boundary Conditions

The last case, is the most general case. There are Neumann boundary conditions on Γ_N and non-homogeneous Dirichlet conditions on Γ_D. The same reasoning as for purely non-homogeneous Dirichlet boundary conditions can be applied, i.e. introducing $\tilde{u} = u - \tilde{g}$ so that the Dirichlet condition becomes again homogeneous. Due to the presence of the Neumann conditions, the space of the test-functions v is restricted to $V = H^1_{\Gamma_\mathrm{D}}(\Omega)$. The weak formulation for the elliptic problem reads as

$$b\,(\tilde{u}, v) = (f, v) + (h, v)_{\Gamma_\mathrm{N}} - b\,(\tilde{g}, v) \quad \forall v \in V. \tag{3.14a}$$

and for the parabolic problem reads as

$$\imath\omega\,(\tilde{u}, v) + b\,(\tilde{u}, v) = (f, v) + (h, v)_{\Gamma_\mathrm{N}} - b\,(\tilde{g}, v) - \imath\omega\,(\tilde{g}, v) \quad \forall v \in V. \tag{3.14b}$$

For the weak formulations it has been shown that there exists an unique solution to the problems [59]. When only purely Neumann boundary conditions are applied the weak formulation is not anymore uniquely solvable [59].

3.3 Discretization of the Weak Formulation by the Ritz-Galerkin Approach

For now it has remained unclear how the space W is defined. In the *Ritz-Galerkin* approach the solution space W is chosen to be same space of the test-functions used to construct the weak-form, i.e. the space V. To solve the weak formulations of the PDEs numerically, one has to find an approximation to its solution. This means approximating the space V by a finite dimensional space $V_\ell = V_{h_\ell}$, where $V_\ell \subset V$. It is assumed that $h_\ell > 0$, where ℓ depicts a certain refinement level of the mesh, and that

$$\forall v \in V, \inf_{v_\ell \in V_\ell} \|v - v_\ell\| \to 0, \text{ if } h_\ell \to 0.$$

Let $\left\{v_j \mid j = 1, \ldots, N_{\mathrm{DoF}}\right\}$ be the basis of V_ℓ, then one can approximate u by a linear combination of basis functions v_j,

$$u(\vec{x}) \approx u_\ell(\vec{x}) = \sum_{j=1}^{N_{\mathrm{DoF}}} u_j v_j(\vec{x}), \tag{3.15a}$$

and, similarly the lifting

$$\tilde{g}(\vec{x}) \approx \tilde{g}_\ell(\vec{x}) = \sum_{j=1}^{N_{\mathrm{DoF}}} g_j v_j(\vec{x}). \tag{3.15b}$$

Choosing the test-function to be v_i and introducing the approximations of the solutions in (3.15), one obtains

$$\begin{aligned} \imath\omega \sum_{j=1}^{N_{\mathrm{DoF}}} u_j \underbrace{\int_\Omega \sigma v_j v_i \,\mathrm{d}\Omega}_{m_{ij}} + \sum_{j=1}^{N_{\mathrm{DoF}}} u_j \underbrace{\int_\Omega \nu \nabla v_j \cdot \nabla v_i \,\mathrm{d}\Omega}_{k_{ij}} = \underbrace{\int_\Omega f\, v_i \,\mathrm{d}\Omega}_{f_i} + \underbrace{\int_{\Gamma_\mathrm{N}} h v_i \,\mathrm{d}\Gamma_\mathrm{N}}_{h_i} \\ - \sum_{j=1}^{N_{\mathrm{DoF}}} g_j \underbrace{\int_\Omega \nu \nabla v_j \cdot \nabla v_i \,\mathrm{d}\Omega}_{k_{ij}} - \imath\omega \sum_{j=1}^{N_{\mathrm{DoF}}} g_j \underbrace{\int_\Omega \sigma v_j v_i \,\mathrm{d}\Omega}_{m_{ij}}. \end{aligned} \tag{3.16}$$

This results in the system of equations

$$\imath\omega \mathbf{M}\mathbf{u} + \mathbf{K}\mathbf{u} = \mathbf{f} + \mathbf{h} - \mathbf{K}\mathbf{g} - \imath\omega\mathbf{M}\mathbf{g}, \tag{3.17a}$$

where matrix $\mathbf{K}$ is called the *stiffness matrix*, matrix $\mathbf{M}$ the *mass matrix*, $\mathbf{u}$ depicts the unknowns and $\mathbf{f}$, $\mathbf{h}$ and $\mathbf{g}$ are respectively the discretized versions of f, h and $\tilde{g}$.

When only homogeneous Dirichlet conditions are applied, one obtains

$$\imath\omega \mathbf{M}\mathbf{u} + \mathbf{K}\mathbf{u} = \mathbf{f}, \tag{3.17b}$$

and in the Poisson case $\omega = 0$ the system of equations further reduces to

$$\mathbf{K}\mathbf{u} = \mathbf{f}. \tag{3.17c}$$

Let us now define the spaces V_ℓ and W_ℓ.

3.3.1 Classical Finite Element Method

In the classical FEM the basis functions are element-wise defined polynomials with C^0-continuity among elements and associated with the mesh nodes. In this work primarily 2D linear finite elements are used. They are defined on a reference domain as

$$\hat{v}_i(\hat{x},\hat{y}) = \frac{\hat{N}_i(\hat{x},\hat{y})}{\ell_{\hat{z}}}, \tag{3.18}$$

with $\hat{N}_i$ the shape functions, $\ell_{\hat{z}}$ the length of the device in $\hat{z}$-direction. One can write that $\vec{v}_i = \hat{v}_i\vec{e}_{\hat{z}}$, with $\vec{e}_{\hat{z}}$ the unit vector.

Let us consider the triangular reference element $\hat{E}$ as depicted in Figure 3.1 constructed from the nodes $\hat{1}$, $\hat{2}$ and $\hat{3}$, with respectively the coordinates $(\hat{x}_1,\hat{y}_1)=(0,0)$, $(\hat{x}_2,\hat{y}_2)=(1,0)$ and $(\hat{x}_3,\hat{y}_3)=(0,1)$. The hat-function $\hat{N}_i$ at node i is defined to be 1 at the node and 0 at all other nodes (Figure 3.2),

$$\hat{N}_i(\hat{x},\hat{y}) = \frac{a_i + b_i\hat{x} + c_i\hat{y}}{2\Delta_{\hat{E}}}, \tag{3.19}$$

with $\Delta_{\hat{E}}$ the area of the element and

$$\begin{cases} a_i = & \hat{x}_j\hat{y}_k - \hat{x}_k\hat{y}_j, \\ b_i = & \hat{y}_j - \hat{y}_k, \\ c_i = & \hat{x}_k - \hat{x}_j. \end{cases}, \tag{3.20}$$

with $\{\{i\},\{j\},\{k\}\}$ a partition of $\{\hat{1},\hat{2},\hat{3}\}$ [132]. Due to the definition, the sum of all shape functions at any point in the triangle is 1.

The mesh used to solve the PDE on Ω is constructed from a total number of N_{el} elements. Every element m can be interpreted as the result of an affine mapping T_{el} from the reference triangle $\hat{E}$ onto an element E_m in the computational domain (Figure 3.1), i.e.

$$T_{\text{el}} : \hat{E} \to E_m \ : \ (\hat{x},\hat{y}) \mapsto \mathbf{T}_{\text{m}} \begin{pmatrix} \hat{x} \\ \hat{y} \end{pmatrix} + \mathbf{t}_{\text{m}}$$

The entries of matrix $\mathbf{T}_{\text{m}}$ are given by $T_{11} = x_j - x_i$, $T_{21} = y_j - y_i$, $T_{12} = x_k - x_i$ and $T_{22} = y_k - y_i$. For the second term it holds that $t_1 = x_i$ and $t_2 = y_i$ [60]. The size of the triangles is defined by the parameter h_ℓ, which is the radius of the incircle of the triangle in Ω.

Let N_i be the linear basis function in Ω, then it holds that [60],

$$\hat{N}_i = \hat{N}_i(\hat{x},\hat{y}) = N_i\left(T(\hat{x},\hat{y})\right), \tag{3.21}$$

and for the entries of the stiffness matrix it can be explicitly computed

$$k_{ij} = \int_\Omega \nu \nabla v_j \cdot \nabla v_i \, \mathrm{d}\Omega = \sum_{m=1}^{N_{\text{el}}} \underbrace{\nu^{(m)} \int_{\hat{\Omega}} \nabla v_j \cdot \nabla v_i \, \mathrm{d}\hat{\Omega},}_{k_{ij}^{(m)}}$$

where it is assumed that $\nu^{(m)}$ is constant over every element and $k_{ij}^{(m)}$ is defined as the contribution of the m^{th} triangle to the matrix. The entries of the stiffness matrix can be expressed with respect to the hat-functions on the reference element by

$$k_{ij}^{(m)} = \frac{\nu^{(m)}}{\ell_{\hat{z}}} \int_{\hat{E}} \mathbf{J}_{\text{m}} \nabla \hat{N}_j \cdot \nabla \hat{N}_i |\det(\mathbf{T}_{\text{m}})| \, \mathrm{d}\hat{E}, \tag{3.22}$$

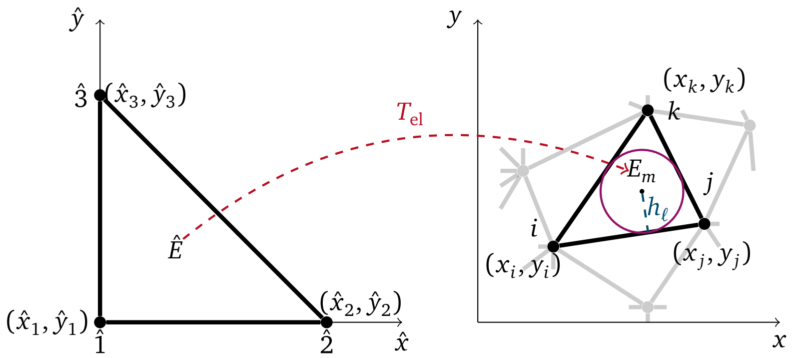

Figure 3.1: Transformation of a reference element to an element in the mesh and visualization of h_ℓ.

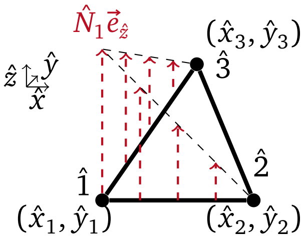

Figure 3.2: Visualization of the hat-function for the triangular reference element.

where $\mathbf{J}_{\text{m}} = \mathbf{T}_{\text{m}}^{-1}\mathbf{T}_{\text{m}}^{-\top}$ and $|\det(\mathbf{T}_{\text{m}})|$ corresponds to the Jacobian of the matrix $\mathbf{T}_{\text{m}}$ [60]. A similar reasoning will express the entries of $\mathbf{M}$, $\mathbf{f}$, $\mathbf{h}$ and $\mathbf{g}$ as a function of the hat-functions on the reference element. Since the mappings T_{el} are piecewise bijective and collectively continuous, they induce a global affine transformation from a reference domain to the computational, i.e. physical domain, Ω, $T : \hat{\Omega} \to \Omega$.

To increase the quality of the approximation of the solution, one could rely on

(i) h-refinement, which means that one considers smaller elements. This leads to larger system matrices.

(ii) p-refinement, where p stands for the order of the basis functions used for the approximation. This results in smaller but denser system matrices, when compared with h-refinement of the same quality.

3.3.2 Iso-Geometric Analysis

In IGA the geometry of the device is modeled by using tools from CAD. In CAD curves and surfaces are generated by using Basis spline (B-spline)s and NURBS. Using NURBS in the IGA framework has some advantages, such as the exact representation of conic intersections [87]. The idea of IGA is to use these NURBS also as basis functions in (3.15).

Construction of B-splines

To construct a B-spline one introduces a knot vector,

$$\xi = \left[\xi_1, \xi_2, \ldots, \xi_{n+p+1}\right], \quad \text{with } \xi_i \leq \xi_{i+1} \land \xi_i \in [0,1] \tag{3.23}$$

which partitions the unit interval. ξ_i is called a i^{th} knot and i is the knot index. The number of basis functions used to construct the B-spline curve is denoted by n and p is the degree of the B-spline basis.

When the knots are equally spaced the vector is called uniform, in the other case it is called non-uniform. The values of the knots may be repeated. This multiplicity has implications for the basis. Open knot vectors, i.e. the first and last knot in the vector appear $p+1$ times, cause the basis functions to be interpolatory at the ends of the interval.

From the knot vector one constructs the B-spline basis function recursively. Let us define the piecewise constant functions ($p=0$)

$$B_i^0(\xi) = \begin{cases} 1 & \text{if } \xi_i \leq \xi \leq \xi_{i+1}, \\ 0 & \text{otherwise.} \end{cases} \tag{3.24a}$$

For higher orders the basis functions are defined by the Cox-de Boor recursion formula [26],

$$B_i^p(\xi) = \frac{\xi - \xi_i}{\xi_{i+p} - \xi_i} B_i^{p-1}(\xi) + \frac{\xi_{i+p+1} - \xi}{\xi_{i+p+1} - \xi_{i+1}} B_{i+1}^{p-1}(\xi). \tag{3.24b}$$

Since the nominator and the denominator can be zero, it is defined that $0/0 \doteq 0$. The resulting basis functions are presented in Figure 3.3. For $p=1$ one obtains the same hat-functions used for the linear FEM (Figure 3.3b). One can identify several important features of the B-spline functions [40]. Firstly, the basis functions constitutes a partition of unity, i.e. $\sum_{i=1}^{n} B_i^p(\xi) = 1, \forall \xi$. Secondly, each basis function is point-wise non-negative over the full domain. Thirdly, $B_i^0(\xi)$ is a step function. Its image is zero everywhere except on the half-open interval $\xi \in [\xi_i, \xi_{i+1}[$, which is the i^{th} knot-span. Furthermore it holds that for $p > 0$, $B_i^p(\xi)$ is a linear combination of two basis functions of degree $(p-1)$. Moreover, each p^{th} order function has $p-1$ continuous derivatives across the knots. Finally, the B-spline functions of order p has always $p+1$ knot spans, this implies that higher order functions have support over much larger portions of the domain. This will lead to more dense stiffness and mass matrices.

The second last feature can be addressed more generally by considering knots with different multiplicity. Let m_i depict the multiplicity of the value ξ_i in the knot vector. Then, in general the basis functions have C^{p-m_i} continuity across ξ_i. In the particular case of a knot repeated exactly $m_i = p+1$ times, the basis becomes interpolatory at the knot ξ_i. Below, it is always assumed, that we are dealing with open knot vectors since this requirement is needed to deal with the boundary conditions.

By applying a tensor product between two unit intervals, one can define a basis over a unit square. These squares are called *patches* in the IGA-framework. One can then define knot vectors $\boldsymbol{\xi}_d$, the degrees p_d and the number of basis functions n_d with $d = 1,2$. The B-spline basis functions are then defined as

$$B_{\mathbf{i}}^{\mathbf{p}}(\xi) = B_{i_1}^{p_1}(\xi) B_{i_2}^{p_2}(\xi),$$

with $\mathbf{p} = (p_1, p_2)$ and $\mathbf{i} = (i_1, i_2)$ with $1 < i_d < n_d$.

Constructing Geometries

Using the B-spline basis functions, one is able to construct piecewise-polynomial curves by

$$\mathbf{F}(\xi) = \sum_{i=1}^{n} N_i^p(\xi) \mathbf{C}_i, \tag{3.25}$$

where n is the number of control points $\mathbf{C}_i$ and where the notion of rational basis functions has been introduced by relying on B-splines, i.e.,

$$N_i^p(\xi) = \frac{w_i B_i^p(\xi)}{\sum_{j=1}^{n} w_j B_j^p(\xi)}, \tag{3.26}$$

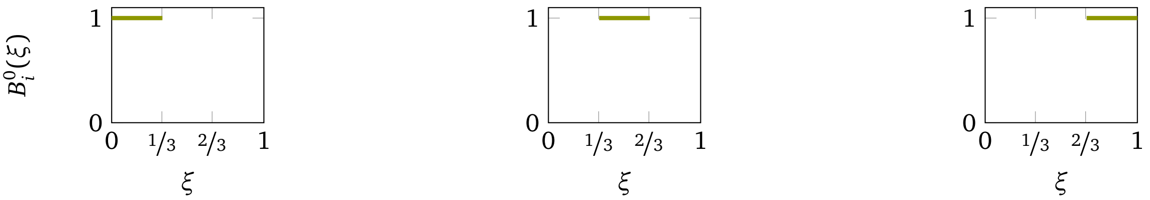

(a) B-Spline basis of degree 0, with knot vector $\xi = [0, 1/3, 2/3, 1]$

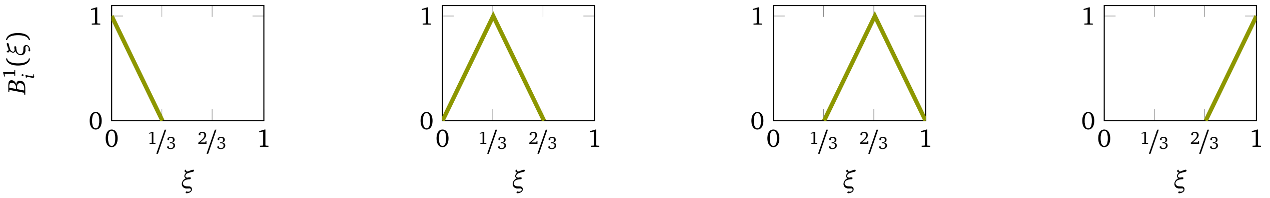

(b) B-Spline basis of degree 1 with knot vector $\xi = [0, 0, 1/3, 2/3, 1, 1]$

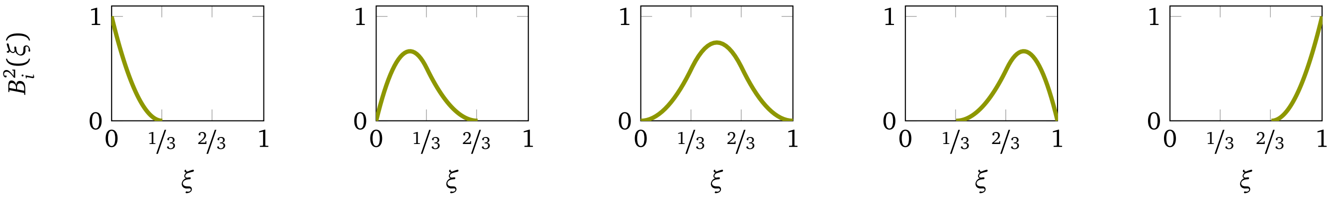

(c) B-Spline basis of degree 2 with knot vector $\xi = [0, 0, 0, 1/3, 2/3, 1, 1, 1]$

Figure 3.3: B-spline basis functions of order 0, 1 and 2 on an open, uniform knot vector.

with weights $w_i > 0$. One can interpret these NURBS as a more general setting of B-splines, since for the latter the weights are all equal. The control polygon is defined as the piecewise linear interpolation of the control points (see the dotted line in Figure 3.4c and 3.4d).

A first benefit of the properties in CAD is the easy handling of sharp corners and changes in the regularity of the curve. This is obtained by changing the repetition of a knot as depicted in Figure 3.4. Combining (3.24) and (3.25) shows that changing the multiplicity of a knot changes the continuity of the curve associated with that knot.

A second benefit is the precision one can obtain. To change the shape of a curve one only has to change the control points, which are acting as weights in (3.25). The continuity of the curve remains the same (see Figure 3.5). Thanks to the local support of the basis functions, changing the control points only influences the geometry in no more than $p+1$ partitions of the curve. Here it also becomes clear, where the advantage of using NURBS instead of using B-splines in (3.25) lies. Namely, changing the weight w_i will pull the curve closer or further away from the control C_i.

Again relying on tensor products, the idea applied to construct curves can be extended to construct surfaces. Let $\mathbf{C}_{i,j}$ depict a control net with $i = 1, \ldots, n$ and $j = 1, \ldots, m$. Let p and q depict the polynomial orders and given the knot vectors $\boldsymbol{\xi} = [\xi_1, \ldots, \xi_{n+p+1}]$ and $\boldsymbol{\eta} = [\eta_1, \ldots, \eta_{m+q+1}]$, then a tensor product B-spline surface is defined by

$$\mathbf{S}(\xi, \eta) = \sum_{i=1}^{n} \sum_{j=1}^{m} N_{i,j}(\xi, \eta) \mathbf{C}_{i,j}, \tag{3.27}$$

where $\mathbf{C}_{i,j}$ is called the control net and with

$$N_{i,j}(\xi, \eta) = \frac{w_{i,j} B_i^p(\xi) B_j^q(\eta)}{\sum_{k=1}^{n} \sum_{\ell=1}^{m} w_{j,\ell} B_k^p(\xi) B_\ell^q(\eta)}. \tag{3.28}$$

$\mathbf{S}$ can be understood as a map from a parameter domain, often called the reference domain, $\hat{\Omega} = [0,1] \times [0,1]$ to a physical domain $\Omega \in \mathbb{R}^d$. The implications for the hat-functions in the physical domain is as

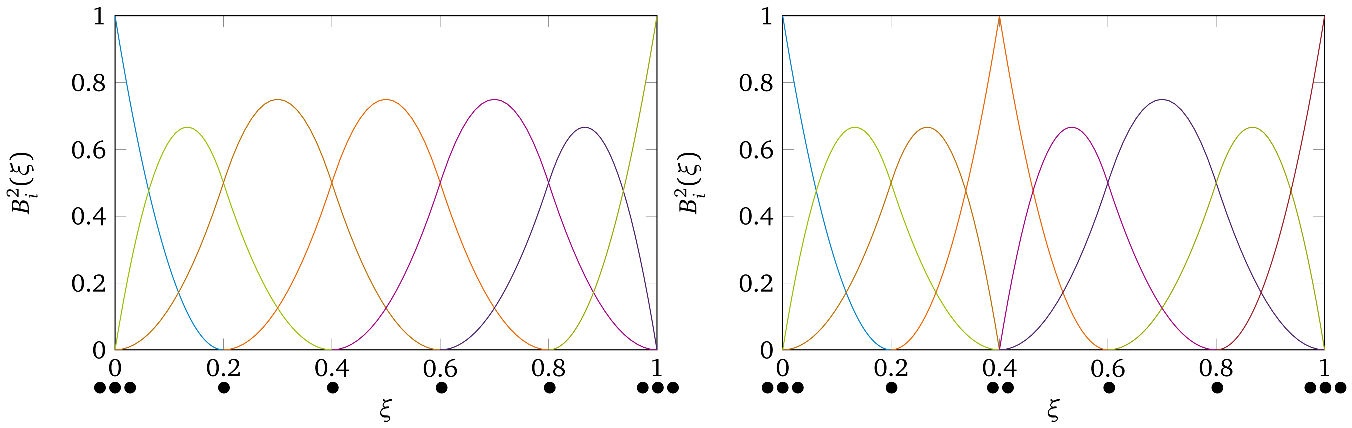

(a) No repetition at knot 0.4 constructs a basis with C^1 continuity.

(b) A repetition at knot 0.4 constructs a basis with C^0 continuity.

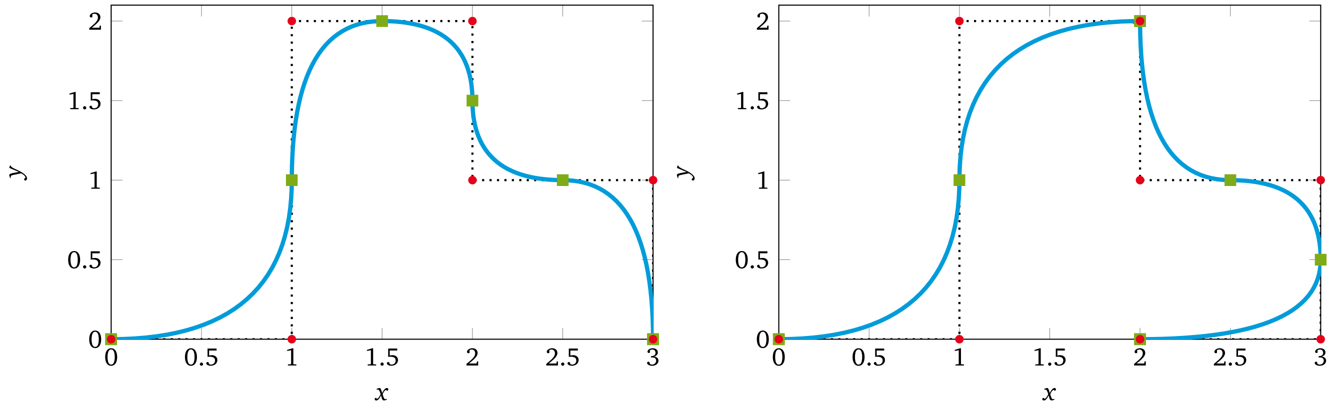

(c) Curve with C^1 continuity with control points as red dots and the knots as green squares.

(d) Curve with C^0 continuity, with control points as red dots and the knots as green squares.

Figure 3.4: Influence of the knot repitition (black dots) on the B-spline basis functions and the continuity of the curve.

mentioned in (3.21), where T should be replaced by $\mathbf{S}$. The construction of the stiffness matrix is similar as described in (3.22).

Iso-parametric Concept

The spline basis introduced in the previous subsections for representing the geometry, can be used as the basis for the solution of the numerical method. This is the principle idea behind IGA and is often called the *iso-parametric* concept. Whereas in FEM the basis is commonly firstly introduced to approximate the unknown field and then reused to approximate the known geometry, IGA works the other way around. A basis is constructed to represent the geometry (exactly in case of conic sections) and then it is reused to calculated the fields. In FEM every triangle in the physical domain is constructed by mapping a reference triangle to it. Mesh-refinement is carried out in the physical domain, i.e., introducing new mappings for every newly introduced triangle. In IGA a single reference domain (patch) is mapped to the full physical domain and the mesh-refinement is also conducted in the reference space.

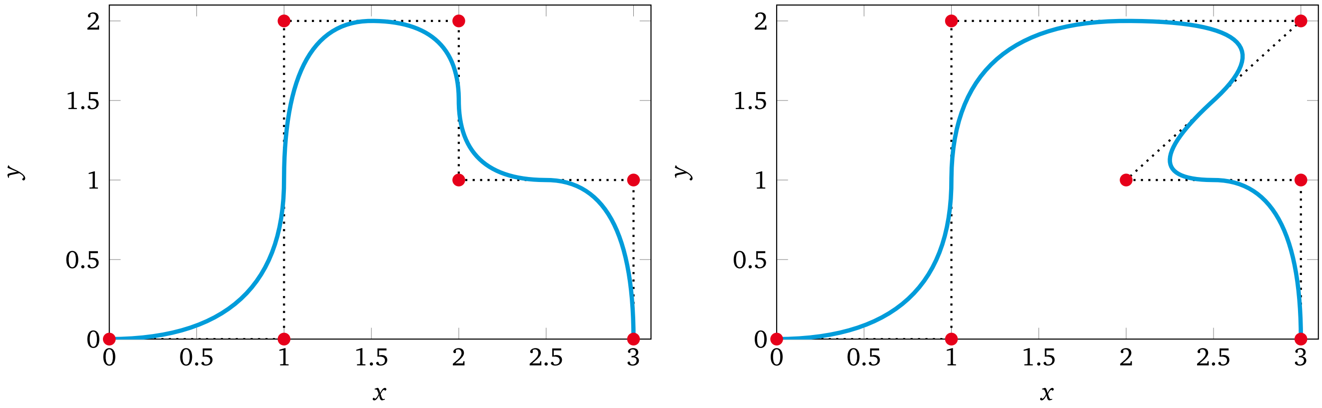

Figure 3.5: Influence of the control point $\mathbf{C}_4$ on the shape of the curve. The basis functions for the curves are depicted in Figure 3.4a.

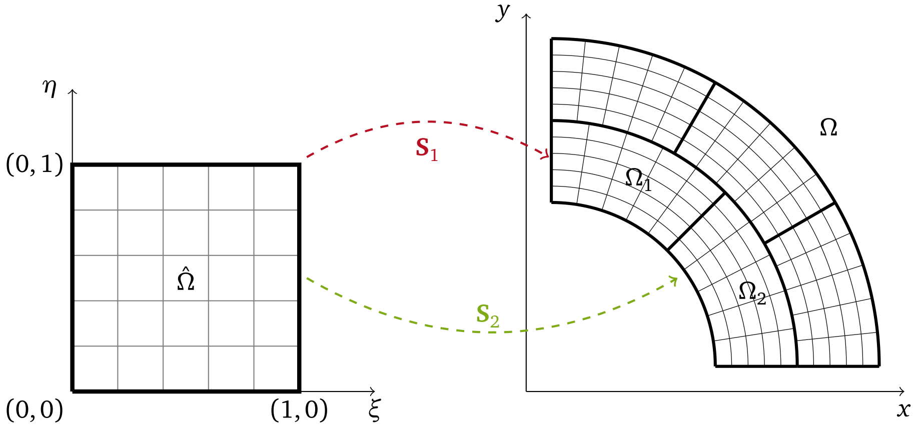

Figure 3.6: Mapping of the reference domain $\hat{\Omega}$ to two patches in the physical domain.

Multipatch

To construct complicated geometries or geometries with different material properties it may not be possible to find one single map from the reference domain to the physical domain. The multipatch approach circumvents this issue [40]. The geometry is subdivided in N_{sub} subdomains so that

$$\Omega = \cup_{i=1}^{N_{\text{sub}}} \Omega_i \quad \text{and} \quad \Omega_i \cap \Omega_j = \emptyset, \forall i \neq j.$$

Every subdomain is constructed by a different map $\mathbf{S}_i$ so that $\mathbf{S}_i : \hat{\Omega} \rightarrow \Omega_i$ (Figure 3.6). The different patches are then glued together to form the full domain in such a way that two neighbouring patches only share one full face $\Gamma_{i,j} = \overline{\Omega}_i \cap \overline{\Omega}_j$ or none at all and such that the discretization of the patches matches.

Two drawbacks of the multipatch approach have to be mentioned. Consider two knot vectors as depicted in Figure 3.7. Across the two patches there is only C^0-continuity (as in classical FEM), however within every patch the C^{p-1}-continuity is maintained. Also local refinement is cumbersome. Since the discretization of the patches should match, h-refinement would quickly propagate over many patches. A way to solve this issue is by applying a hierarchical approach for adaptive local refinement [31, 157]. However, this area is still a trendy topic of research. In the case of p-refinement the basis-functions on the interface would not match anymore.

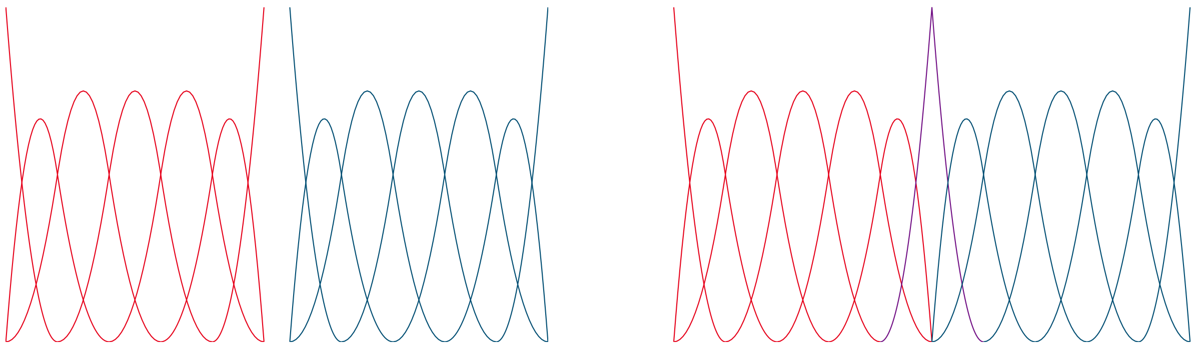

Figure 3.7: Combination of two open knot vectors introducing C^0 continuity at the interface (Figure adapted from [40]).

3.4 Richardson Extrapolator

Let $F = F(u)$ be a QoI which depends on the solution of the PDE. By numerically solving the PDE one obtains an approximation of the solution, and thus $F_\ell = F(\mathbf{u}_\ell)$, where ℓ is related to the parameter h_ℓ defining the mesh size. The exact value of the QoI can be written as [129],

$$F = F_\ell + c h_\ell^{k_0} + \mathcal{O}(h_\ell^{k_1}), \tag{3.29}$$

where c is an unknown constant and k_0, k_1 are method depending constants, for which it holds that $k_0 < k_1$. Introducing a refinement parameter $\lambda \in \,]0,1[\,$, so that the meshes of different refinement can be calculated from the original coarsest mesh with parameter h_0 by

$$h_\ell = h_0 \lambda^\ell .$$

The finite element error for $\ell + 1$ can then be expressed as

$$\begin{aligned} F &= F_{\ell+1} + C h_{\ell+1}^{k_0} + \mathcal{O}(h_{\ell+1}^{k_1}), \\ &= F_{\ell+1} + C h_\ell^{k_0} \lambda^{k_0} + \mathcal{O}(h_\ell^{k_1} \lambda^{k_1}), \\ &= F_{\ell+1} + C h_\ell^{k_0} \lambda^{k_0} + \mathcal{O}(h_\ell^{k_1}). \end{aligned} \tag{3.30}$$

Multiplying both sides with λ^{-k_0} and subtracting (3.29) leads to

$$\begin{aligned} F &= \frac{\lambda^{-k_0} F_{\ell+1} - F_\ell}{\lambda^{-k_0} - 1} + \mathcal{O}(h_\ell^{k_1}) \\ &= \hat{F} + \mathcal{O}(h_\ell^{k_1}), \end{aligned} \tag{3.31}$$

where $\hat{F}$ is called the *Richardson extrapolator* and is the new approximation for F. Please note that the convergence order has improved from k_0 to k_1.

To study the suitability of the Richardson extrapolator as an estimate for the exact solution, one can introduce

$$\epsilon_{\text{FEM}} = \frac{|F_\ell - F|}{|F|} \quad \text{and} \quad \epsilon_{\text{Rich}} = \frac{\left|\hat{F}_\ell - F\right|}{|F|}. \tag{3.32}$$

The first error is the relative discretization error caused by FEM, the second error is the relative error caused by using the estimator for the FEM solution. Both errors are with respect to the closed form solution of the QoI. In Figure 3.8 it can be seen, that, like predicted by the theoretic considerations, a gain of one order in convergence rate is obtained, when using this extrapolator.

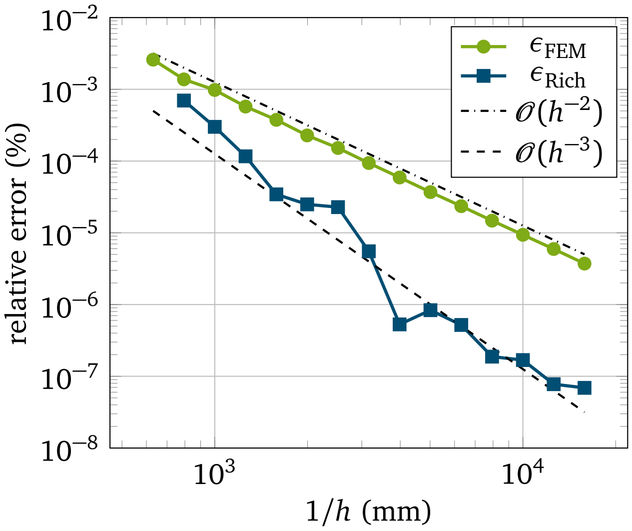

Figure 3.8: Convergence of the relative error for the magnetic energy in a coaxial cable (see Section 7.1) calculated by conventional FEM and the Richardson extrapolator.

3.5 Résumé

In this chapter the mathematical framework for discretizing Partial Differential Equations (PDE) has been introduced. The PDEs have been transformed to their weak form by introducing the appropriate Sobolev spaces. Afterwards the equations have been discretized using the Ritz-Galerkin approach. This procedure results in a system of linear equations.

In more detail the choice of basis functions has been discussed. Two approaches have been addressed: classical Finite Element Method (FEM) and Iso-Geometric Analysis (IGA). The former makes use of a triangulation of the computational domain and considers polynomial (in this work only linear) basis functions, which are related to this triangulation. The latter makes use of B-splines and NURBS. They are not only used to represent the geometry exactly, but also as basis functions for the approximation spaces.

In the next chapter, parametric dependencies are introduced into the PDE. It is discussed how a numerically efficient procedure can be constructed even though one is using a finite element approach.

4 Parametric Models

> "The parameters of music: melody, harmony, timbre, etc., are more or less independent variables."
>
> *Style and Music: Theory, History, and Ideology*
> – L. B. Meyer

Real word problems often depend on several parameters, depicted by a vector $\mathbf{p} \in \mathcal{P} \subset \mathbb{R}^{N_p}$, where $\mathbb{R}^{N_p}$ represents a parameter space. These parameters can describe the geometry, material properties or they can be control parameters. Some of the parameters could describe deformations of the computational domain Ω. It thus inherits the parametric dependency and one writes $\Omega(\mathbf{p})$. For a parametric elliptic Partial Differential Equation (PDE) in its weak form, one will write

$$b(u(\mathbf{p}), v; \mathbf{p}) = (f(\mathbf{p}), v), \quad v \in V(\Omega(\mathbf{p})). \tag{4.1}$$

As mentioned in [131] it is known that this type of parametric PDE has a unique solution, under the assumptions that the bilinear form is continuous and coercive and the assumption that the right hand side is bounded. Starting from the reference domain Ω_0, one does not want to reconstruct the geometry or construct the discretization anew for different values of the parameters, since it costs time and may introduce mesh noise in the results. In the case of Iso-Geometric Analysis (IGA) the control points of the geometry mapping can be used. In the classical Finite Element Method (FEM), a way to elegantly handle parameter dependent geometries is by introducing an affine decomposition. The discussion on the affine decomposition is based on [131] and is the topic of Section 4.1.

A Quantity of Interest (QoI) F, which is calculated from the solution of the parametric PDE, inherits, as a consequence, the parametric dependence. One might be interested in how strongly the different parameters influence the QoI. This influence is expressed by sensitivities which are introduced in Section 4.2.

To obtain high accuracy for the solution of the PDE the applied discretization is often chosen to be very fine. This leads to very large systems of equations and thus to a huge computational load. In the literature different methods are proposed to reduce the computational cost. They all have the same main principle, namely, instead of using the high dimensional problems, one constructs low dimensional substitutes. This can be obtained by relying on e.g. Kriging surrogates models [96], Proper Orthogonal

Decomposition (POD) [34]. In [1] POD has been applied for a multiobjective optimization of a moving nonlinear electromagnetic device while considering design parameters. A more popular method for reducing the complexity when dealing with a parametrized PDE is the Reduced Basis (RB) method [43, 117]. This method is addressed in Section 4.3. The advantage of the method is that thanks to the use of a posteriori error estimators, a certain accuracy can be guaranteed and the total cost of the procedure can be split into an offline and online computational cost. When dealing with parameter affine problems, one can reliably decouple the generation of the basis from the projection stage of the approximation, which results in a computational cost-friendly methodology [121]. In the offline phase the PDE is solved for selected values of the parameter set, whose results are called snapshots. These snapshots are then used to reduce the complexity such that less complex problems are solved during the online phase for any new value of the parameters. So in general the method consists of three components, namely,

- construction of a space spanned by the solution of the original problem by the snapshots,
- a posteriori error estimation which provides bounds for the error between the approximated reduced basis solution and the solution obtained if one would solve the full system of equations,
- an offline/online computational procedure, where the offline phase is time-consuming and parameter independent, whereas during the online phase inexpensive calculations for each new input/output evaluation are performed.

4.1 Affine Decomposition

For this section it is assumed that all parameters are related to the description of the computational domain. In the first part of this section the reader is introduced to the affine geometry preconditioning. The second part focuses on the affine formulation of the bilinear form, where finally the discretized PDE is written relying on the affine decomposition. The content is obtained from [131].

A parameter-dependent bilinear form $b(u, v; \mathbf{p})$ is affine in the parameter $\mathbf{p}$ when it can be decomposed into parameter-independent bilinear forms $b^\ell(u, v)$ and coefficients that are parameter dependent $\vartheta^\ell(\mathbf{p})$,

$$b(u, v; \mathbf{p}) = \sum_{\ell=1}^{N_L} \vartheta^\ell(\mathbf{p}) b^\ell(u, v). \tag{4.2}$$

4.1.1 Affine Geometry Preconditioning

Let $\Omega(\mathbf{p}) \subset \mathbb{R}^d$ be a parameter-dependent domain that can be constructed from N_L non-overlapping domains, so that

$$\overline{\Omega}(\mathbf{p}) = \cup_{\ell=1}^{N_L} \overline{\Omega}^\ell(\mathbf{p}), \quad \text{and} \quad \Omega^\ell(\mathbf{p}) \cap \Omega^{\ell'}(\mathbf{p}) = \emptyset, \quad 1 \leq \ell < \ell' \leq N_L. \tag{4.3}$$

Let $\mathbf{p}_{\text{ref}}$ depict the reference for the parameters, then one can define a reference domain Ω_o as $\Omega_\text{o} = \Omega(\mathbf{p}_{\text{ref}})$. In this domain it holds that

$$\overline{\Omega}_\text{o} = \cup_{\ell=1}^{N_L} \overline{\Omega}_\text{o}^\ell, \quad \text{and} \quad \Omega_\text{o}^\ell \cap \Omega_\text{o}^{\ell'} = \emptyset \quad 1 \leq \ell < \ell' \leq N_L, \tag{4.4}$$

By these constructions, one can define an affine mapping $T^\ell(\cdot, \mathbf{p}) : \Omega_\text{o}^\ell \to \Omega^\ell(\mathbf{p}) : \vec{x}_0 \mapsto \vec{x}$ which is bijective and continuous such that

$$\vec{x} = T_\ell(\vec{x}_0; \mathbf{p}), \quad \text{for} \quad \vec{x} \in \Omega^\ell \text{ and } \vec{x}_0 \in \Omega_\text{o}^\ell. \tag{4.5}$$

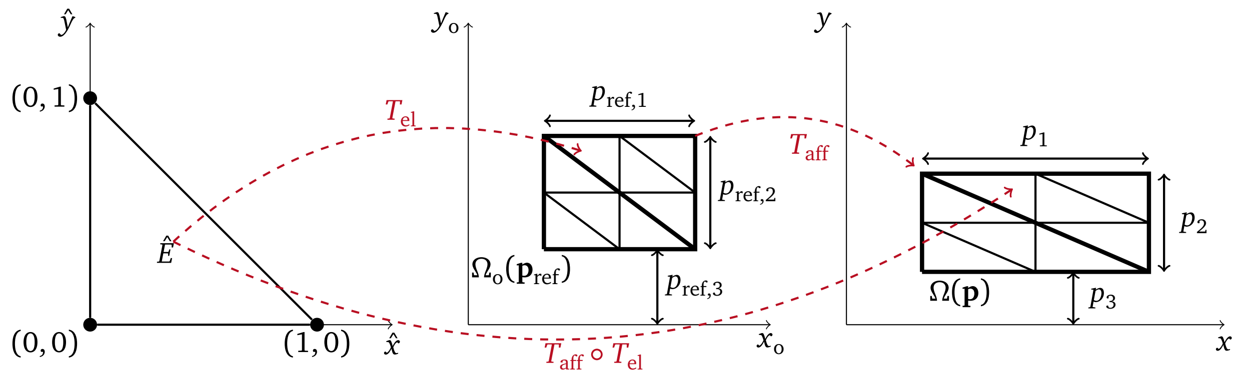

Figure 4.1: Transformation by T_{el} of a reference element to an element in $\Omega_{\mathrm{o}}(\mathbf{p}_{\mathrm{ref}})$, which is subdivided in two subdomains, and the affine mapping T_{aff} for the subdomains to $\Omega(\mathbf{p})$.

The mappings are given for any $\vec{x}_o \in \Omega^{\ell}_{\mathrm{o}}$, with $1 \le \ell \le N_L$, by

$$T^{\ell}_i(\vec{x}_o;\mathbf{p}) = C^{\ell}_i(\mathbf{p}) + \sum_{j=1}^{d} G^{\ell}_{i,j}(\mathbf{p}) x_{\mathrm{o},j},$$

with $1 \le i \le d$ and where $C^{\ell} : \mathbb{R}^{N_p} \to \mathbb{R}^d$ and $G^{\ell} : \mathbb{R}^{N_p} \to \mathbb{R}^{d\times d}$. The associated Jacobian is defined as

$$J^{\ell}(\mathbf{p}) = \left|\det(G^{\ell}(\mathbf{p}))\right| \tag{4.6}$$

and it is constant over each subdomain [131]. Let us note here that there exists a strong analogy with the IGA setting (Section 3.3.2). In IGA patches were constructed on a unit square, the reference domain, and then mapped to the phyiscal domain. Here subdomains in the reference domain are mapped to subdomains on the computational domain. These subdomains can thus also be interpreted as patches.

Parametrized geometries which fulfill (4.3) and where the Jacobian is constant in space over each subdomain are said to fulfill the affine geometry preconditioning and allow for the construction of the decomposition of the bilinear form, i.e. (4.2) [131].

Since the local mappings T^{ℓ} are piecewise bijective and collectively continuous, they induce a global affine transformation $T_{\mathrm{aff}}(\,\cdot\,,\mathbf{p}) : \Omega_{\mathrm{o}} \to \Omega(\mathbf{p})$ [82]. In two dimensions, an affine transformation maps straight lines to straight lines, parallel lines to parallel lines and parallel lines of equal length to parallel lines of equal length. This implies that triangles are mapped to triangles [131], therefore the subdomains are chosen to be triangular, e.g. Figure 4.1. The finite element triangulation (depicted by the thin lines in 4.1) is then a subtriangulation of the coarse triangles for the decomposition (depicted by the thick lines in 4.1) and is as a consequence also mapped to $\Omega(\mathbf{p})$ by T_{aff}.

4.1.2 Affine Formulation of the Bilinear Form

The goal is now to perform the computations on the reference domain Ω_{o}, similar to the discussion in Section 3.3.1. For the integrals in the bilinear form, one obtains now, e.g. [94],

$$\begin{aligned} b(u,v;\mathbf{p}) &= \int_{\Omega(\mathbf{p})} \nabla u \cdot \nu \nabla v \, \mathrm{d}\Omega \\ &= \sum_{\ell=1}^{N_L} \sum_{i,j=1}^{d} \underbrace{\left[G^{\ell}(\mathbf{p})^{-1} \nu^{\ell} G^{\ell}(\mathbf{p})^{-\top}\right]_{ij} J^{\ell}(\mathbf{p})}_{\vartheta^{\ell}_{ij}(\mathbf{p})} \underbrace{\int_{\Omega^{\ell}_{\mathrm{o}}} \frac{\partial u_{\mathrm{o}}}{\partial x_{\mathrm{o},i}} \frac{\partial v_{\mathrm{o}}}{\partial x_{\mathrm{o},j}} \, \mathrm{d}\Omega_{\mathrm{o}}}_{b^{\ell}_{ij}(u_{\mathrm{o}},v_{\mathrm{o}})} \\ &= \sum_{\ell=1}^{N_L} \sum_{i,j=1}^{d} \vartheta^{\ell}_{ij}(\mathbf{p}) b^{\ell}_{ij}(u_{\mathrm{o}}, v_{\mathrm{o}}), \end{aligned} \tag{4.7}$$

where it is assumed that subdomains are constructed such that each of them has a homogeneous material. For the right hand side ones finds

$$f(v;\mathbf{p}) = \sum_{\ell=1}^{N_L} \underbrace{J^\ell(\mathbf{p})}_{\vartheta_f^\ell(\mathbf{p})} \underbrace{\int_{\Omega_o^\ell} f\, v_o \,\mathrm{d}\Omega_o}_{f_o^\ell}. \tag{4.8}$$

Applying the discretization to obtain the system of equations and assuming that only a part of the geometry is treated by the affine decomposition we will write for the stiffness matrix

$$\mathbf{K}(\mathbf{p}) = \mathbf{K}^{\text{out}} + \sum_{\ell=1}^{N_L} \vartheta_K^\ell(\mathbf{p})\mathbf{K}^\ell, \tag{4.9}$$

where $\mathbf{K}^{\text{out}}$ is the stiffness matrix for the elements outside the domain decomposed region and where $\vartheta_K^\ell(\mathbf{p})\mathbf{K}^\ell := \vartheta_{11}^\ell(\mathbf{p})\mathbf{K}_{11}^\ell + \vartheta_{22}^\ell(\mathbf{p})\mathbf{K}_{22}^\ell + \vartheta_{12}^\ell(\mathbf{p})\mathbf{K}_{12}^\ell + \vartheta_{21}^\ell(\mathbf{p})\mathbf{K}_{21}^\ell$.

The same reasoning can be applied for the right hand side. Furthermore, if one considers the time harmonic description of the parabolic PDE one can introduce in an analogous way the matrices $\mathbf{M}^\ell$. One finally writes

$$\imath\omega\left(\mathbf{M}^{\text{out}} + \sum_{\ell=1}^{N_L} \vartheta_M^\ell(\mathbf{p})\mathbf{M}^\ell\right)\mathbf{u} + \left(\mathbf{K}^{\text{out}} + \sum_{\ell=1}^{N_L} \vartheta_K^\ell(\mathbf{p})\mathbf{K}^\ell\right)\mathbf{u} = \mathbf{f}^{\text{out}} + \sum_{\ell=1}^{N_L} \vartheta_f^\ell(\mathbf{p})\mathbf{f}^\ell. \tag{4.10}$$

During numerical realizations, the mesh does not have to be deformed and all components can be precomputed. The introduction of the parametrized PDE eases the optimization procedures as will be shown in the next section.

4.2 Local Sensitivities

Sensitivities of the QoI with respect to the parameters are important since they measure how strongly a parameter influences the QoI. Let us therefore introduce, analogously to [38], a set of sequences of non-negative integers

$$\mathcal{A} := \{\boldsymbol{\alpha} = (\alpha_1, \alpha_2, \ldots) : \alpha_i \in \mathbb{N} \wedge \alpha_i \neq 0 \quad \text{for a finite number of } i\},$$

so that $|\boldsymbol{\alpha}| = \sum_{i\geq 1} |\alpha_i|$ is finite if and only if $\boldsymbol{\alpha} \in \mathcal{A}$, then a partial derivative operator $\partial^{\boldsymbol{\alpha}}$ is defined as

$$\partial^{\boldsymbol{\alpha}} = \frac{\partial^{|\boldsymbol{\alpha}|}}{\partial^{\alpha_1} p_1 \ldots \partial^{\alpha_{N_p}} p_{N_p}}.$$

A first tool for sensitivity analysis is relying on sensitivity equations which require the calculation of the derivatives of the QoI, i.e.,

$$\partial^{\boldsymbol{\alpha}} F(u(\mathbf{p})) = F(\mathbf{s}_{\boldsymbol{\alpha}}), \tag{4.11}$$

where $\mathbf{s}_{\boldsymbol{\alpha}} := \partial^{\boldsymbol{\alpha}} u(\mathbf{p})$ and linearity of the functional F with respect to $u(\mathbf{p})$ is assumed. With a slight abuse of notation, we denote the first order sensitivities $\mathbf{s} = [s_1, s_2, \ldots, s_{N_p}]$ with $s_i := \partial u(\mathbf{p})/\partial p_i$. Deriving (4.1) and applying the chain rule one finds, that the sensitivities satisfy

$$b(\mathbf{s}_{\boldsymbol{\alpha}}, v; \mathbf{p}) = \partial^{\boldsymbol{\alpha}}(f(\mathbf{p}), v) - \partial^{\boldsymbol{\alpha}} b(u(\mathbf{p}), v; \mathbf{p}), \quad \forall v \in V, \tag{4.12}$$

with

$$\partial^{\boldsymbol{\alpha}} b(u, v; \mathbf{p}) = \partial^{\boldsymbol{\alpha}} \sum_{\ell=1}^{N_L} \sum_{i,j=1}^{2} \vartheta_{ij}^\ell(\mathbf{p}) b_{ij}^\ell(u, v), \tag{4.13}$$

see e.g. [98]. Additionally, the derivatives of the source term are determined by a similar reasoning. The sensitivities are easy to compute, due to the affine decomposition, by which the dependencies on the parameters are only expressed by the coefficients $\vartheta^\ell(\mathbf{p})$ and since the mappings T_{aff} can be computed exactly, their derivatives with respect to $\mathbf{p}$ are also known exactly [52].

Algorithm 1 Pseudo-code for the greedy algorithm

```
procedure GREEDY
    Define $tol$
    Initiate $j, error, \Phi_0$
    while $error > tol$ do
        $\mathbf{p}_j \leftarrow$ Find $\mathbf{p}$ with $\mathbf{u}(\mathbf{p})$ max $error$
        $\mathbf{u}_j \leftarrow$ Solve PDE for $\mathbf{p}_j$
        $\Phi_j \leftarrow$ orthonormalized $\mathbf{u}_j$ w.r.t $\Phi_{j-1} := [\mathbf{u}_1, \dots, \mathbf{u}_{j-1}]$
        $error \leftarrow$ calculate residual using $\Phi_j$
        $j \leftarrow j + 1$
    end while
end procedure
```

4.3 Model Order Reduction with Reduced Basis

Until now, the solution of the PDE $u(\mathbf{p}) \in V$, where V is the adequate Sobolev space for meeting the applied boundary conditions, has been approximated by the discrete solution $\mathbf{u}_\ell$ which stems from $V^\ell \subset V$. This implies that for calculating the QoI $F(\mathbf{u}(\mathbf{p}))$ one has to rely on the high dimensional solutions calculated on a mesh with N_{DoF} nodes. This can become cumbersome, especially when a lot of evaluations are needed, for example while doing optimization or applying uncertainty quantification. As a consequence one is interested in using a reduced solution space $V^n \subset V^\ell$, which approximates the solution under parameter changes. These reduced solutions are indicated by $\mathbf{u}_n$. In the case of parametrized PDEs the RB methods are an elegant way to construct V^n.

The method consists of two phases. In the first phase, called *offline* phase, the basis is constructed and in the second phase, the *online* phase, the matrices and vectors are projected onto the lower dimensional space. The offline phase stops when the approximation error introduced by relying on the obtained RB is sufficient low. This error is estimated by residuals.

4.3.1 Offline Phase

The algorithm needs a training set $M_{\mathrm{tr}} \subset \mathcal{P}$. Only the $\{\mathbf{p}_i\}_{i=1}^{N_{\mathrm{tr}}}$ in this set can be selected to be used for the construction of the basis. To construct the basis the *greedy algorithm* is employed [148] (see Algorithm 1). The algorithm accumulatively constructs the basis until a prescribed accuracy is guaranteed. Using the already constructed basis Φ_j, the approximation error is estimated (see below) in order to find the worst approximated solution of the PDE $\mathbf{u}(\mathbf{p}_{j+1})$ for $\mathbf{p} \in M_{\mathrm{tr}}$. It calculates $\mathbf{u}(\mathbf{p}_{j+1})$ using the high dimensional matrices and takes this result to extend the basis. The extension of the basis is done by using the Gram-Schmidt method for orthonormalization, which gives a vector ϕ_{j+1}. This vector is then appended to the old basis so that the resulting basis is given by $\Phi_{j+1} = \Phi_j \cup \{\phi_{j+1}\}$. The $\mathbf{u}(\mathbf{p}_{j+1})$ selected for the basis are called *snapshots*. This procedure is repeated until the error for the remaining $\mathbf{p}_i$ is below a certain tolerance and one finally retrieves the reduced basis $\Phi = \{\phi_1, \dots, \phi_n\}$, with $n \ll N_{\mathrm{DoF}}$ the rank. This basis is able to capture the dynamics of the parameter space.

4.3.2 Online Phase

A Ritz-Galerkin-type approach, i.e. using the ansatz from Section 3.3, one can write

$$\mathbf{u}_n(\mathbf{p}) := \sum_{i=1}^{n} \tilde{\mathbf{u}}_i(\mathbf{p}) \phi_i = \Phi \tilde{\mathbf{u}}(\mathbf{p}). \tag{4.14}$$

Multiplying the left and the right hand side of (3.17b) and inserting $\mathbf{u}_n(\mathbf{p})$ gives

$$\Phi^H \mathbf{K}(\mathbf{p})\Phi\tilde{\mathbf{u}}(\mathbf{p}) + \imath\omega\Phi^H \mathbf{M}(\mathbf{p})\Phi\tilde{\mathbf{u}}(\mathbf{p}) = \Phi^H \mathbf{f}(\mathbf{p}), \tag{4.15a}$$

where "H" depicts the Hermitian transpose. In combination with the affine decomposition introduced in the previous section one finds

$$\Phi^H \left(\mathbf{K}^{\mathrm{out}} + \sum_{\ell=1}^{N_L} \vartheta_K^\ell(\mathbf{p})\mathbf{K}^\ell \right) \Phi\tilde{\mathbf{u}}(\mathbf{p}) + \imath\omega\Phi^H \left(\mathbf{M}^{\mathrm{out}} + \sum_{\ell=1}^{N_L} \vartheta_M^\ell(\mathbf{p})\mathbf{M}^\ell \right) \Phi\tilde{\mathbf{u}}(\mathbf{p}) = \Phi^H \left(\mathbf{f}^{\mathrm{out}} + \sum_{\ell=1}^{N_L} \vartheta_f^\ell(\mathbf{p})\mathbf{f}^\ell \right). \tag{4.15b}$$

In the case of linear problems this results in

$$\left(\underbrace{\Phi^H \mathbf{K}^{\mathrm{out}}\Phi}_{\tilde{\mathbf{K}}^{\mathrm{out}}} + \sum_{\ell=1}^{N_L} \vartheta_K^\ell(\mathbf{p}) \underbrace{\Phi^H \mathbf{K}^\ell \Phi}_{\tilde{\mathbf{K}}^\ell} \right) \tilde{\mathbf{u}}(\mathbf{p}) + \imath\omega \left(\underbrace{\Phi^H \mathbf{M}^{\mathrm{out}}\Phi}_{\tilde{\mathbf{M}}^{\mathrm{out}}} + \sum_{\ell=1}^{N_L} \vartheta_M^\ell(\mathbf{p}) \underbrace{\Phi^H \mathbf{M}^\ell \Phi}_{\tilde{\mathbf{M}}^\ell} \right) \tilde{\mathbf{u}}(\mathbf{p}) = \left(\underbrace{\Phi^H \mathbf{f}^{\mathrm{out}}}_{\tilde{\mathbf{f}}^{\mathrm{out}}} + \sum_{\ell=1}^{N_L} \vartheta_f^\ell(\mathbf{p}) \underbrace{\Phi^H \mathbf{f}^\ell}_{\tilde{\mathbf{f}}^\ell} \right), \tag{4.15c}$$

where all quantities with a tilde are of dimension n. Thanks to the affine decomposition, these quantities do not depend on $\mathbf{p}$ and can thus be precomputed, except for $\tilde{\mathbf{u}}(\mathbf{p})$. This reduced system of equations is solved during the online phase.

4.3.3 Error Estimator

Let us now elaborate on how the greedy algorithm is capable of finding the next snapshot. Since the solution of the discretized PDE $\mathbf{u}(\mathbf{p})$ is approximated by the reduced solution $\mathbf{u}_n(\mathbf{p})$, it holds that

$$\mathbf{u}(\mathbf{p}) = \mathbf{u}_n(\mathbf{p}) + \epsilon(\mathbf{p}).$$

Normally, calculating the true error $\epsilon(\mathbf{p})$ would imply a calculation in the online phase of the high dimensional problem. However, for elliptic problems there exists an *a-posteriori* error estimator $\Delta_{\mathbf{u}}(\mathbf{p})$, which bounds $||\epsilon(\mathbf{p})|| \leq \Delta_{\mathbf{u}}(\mathbf{p})$ [52, 76]. Let $||\mathbf{v}||^2_{\mathbf{p}_{\mathrm{ref}}} = \mathbf{v}^H\mathbf{K}(\mathbf{p})\mathbf{v}$ depict a norm on a reference geometry then the estimator is given by

$$||\epsilon(\mathbf{p})||_{\mathbf{p}_{\mathrm{ref}}} \leq \Delta_{\mathbf{u}}(\mathbf{p}) := \frac{||\mathbf{r}(\mathbf{p})||_{\mathbf{p}_{\mathrm{ref}*}}}{c(\mathbf{p})}, \tag{4.16}$$

in which the dual norm $||\mathbf{r}(\mathbf{p})||^2_{\mathbf{p}_{\mathrm{ref}*}} = \mathbf{v}^H\mathbf{K}^{-1}(\mathbf{p})\mathbf{v}$ and the residual $\mathbf{r}$ defined as $\mathbf{r} = \mathbf{K}(\mathbf{p})\mathbf{u}_n - \mathbf{f}$ are introduced. In combination with the affine decomposition, the coercivity constant $c(\mathbf{p})$ can be calculated by the "$\min\Theta$"- approach [77], namely,

$$c(\mathbf{p}) = \min_{\ell=1,\dots N_L} \frac{\vartheta^\ell(\mathbf{p})}{\vartheta^\ell(\mathbf{p}_{\mathrm{ref}})}. \tag{4.17}$$

Since the error estimator is also decomposed according to the offline/online procedure, one only relies on low dimensional evaluations of the error estimator.

When $\mathcal{P}$ is high dimensional or extensive, the obtained reduced basis might also be large, which results in a lower computational gain. Therefore one opts to partition the parameter space into several subdomains. An example is sketched in Figure 4.2. One each subdomain i a reduced basis is constructed and on each subdomain the desired accuracy is fulfilled. In this way a *dictionary* of reduced bases is constructed [55, 75]. However, if the problem is dependent on many parameters, many partitions need to be considered and the construction of the dictionary will become inefficient. This phenomenon is addressed as the curse of dimensionality.

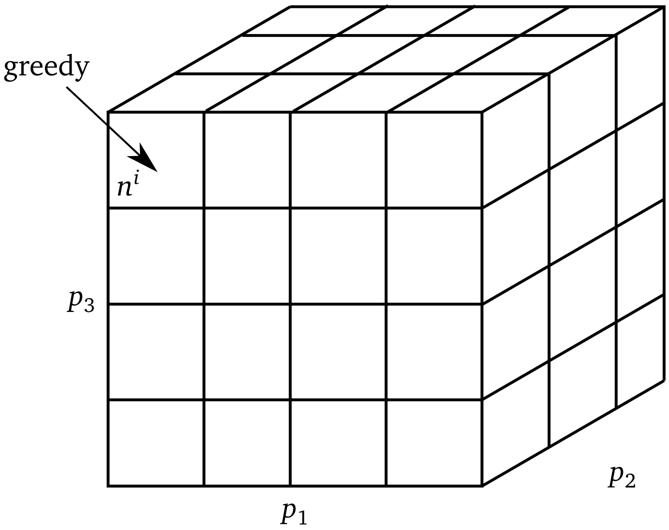

Figure 4.2: Schematic view of the dictionary principle used for the MOR, where the parameter space $\mathcal{P} \subset \mathbb{R}^3$ is divided in 48 partitions.

4.4 Résumé

In this chapter the parametric Partial Differential Equation (PDE) was introduced. It has been explained how parameter dependent geometric changes are easily handled by the introduction of an affine decomposition. Furthermore the parameter dependence has been exploited to construct a reduced order model by applying the reduced basis method.

Finally it has to be noted that the parameters might be not known exactly and small deviations might occur on the parameters under consideration. This will make the parametric PDE become a stochastic PDE and deviations on the solution will be introduced due to the input uncertainties. As a consequence the Quantity of Interest (QoI) will inherit the stochastic nature. Nevertheless, one still wants to make predictions of the QoI and thus one has to rely on stochastic measures. This is done in the field of uncertainty quantification, which is the topic of the next chapter.

5 Uncertainty Quantification

> “Io dubito ... eh cospetto! Che dubitar?”
>
> Bartolo in *Il Barbiere di Siviglia*
> – G. Rossini

The increase in computational power has enabled the use of very accurate numerical models of electromagnetic devices. These models serve as virtual prototypes for the devices, e.g. machines that are actually manufactured. However, during production small imperfections, i.e. mathematically speaking deviations, with respect to the input parameters in the numerical model are unavoidable. When those deviations strongly influence the important quantities of the device, increasing the precision of the numerical reference is futile. More interesting is to find on beforehand the most influential parameters which might indicate which production steps must be carried out with a higher precision. Moreover, taking these deviations into account during the numerical modeling phase helps to construct more robust reference models and might help to improve the prediction of the behavior of the produced machines. The field in which these uncertainties are tackled is called Uncertainty Quantification (UQ).

Generally uncertainties are categorized in two groups [46]. Firstly, there are the *epistemic* uncertainties. These uncertainties are systematic and might be introduced, for example by neglecting certain effects in the model or by the calibration for the measurements. An increased understanding of the model, a better comprehension of the underlying physics, will help to reduce this type of uncertainty. The second group is labeled by the term *aleatoric* uncertainties. They can be understood as statistical uncertainties. The quantification can be obtained by standard techniques, such as Monte Carlo (MC) methods or polynomial expansions and this group of uncertainties will be the focus of this work.

As discussed in Chapter 4 a Quantity of Interest (QoI), for which one has to solve a Partial Differential Equation (PDE), might be dependent on a set of N_p parameters. These parameters, or a subset of N_D parameters can be uncertain. However, for simplicity it is assumed that $N_D = N_p$. The stochastic nature of a parameter will be depicted by the Cyrillic letter ш so that $\mathbf{P}(ш)$. The uncertainties can be found in the material properties, in the source term or in the geometry. The PDE introduced in Section 3.2 becomes a stochastic PDE (sPDE),

$$\imath\omega\sigma(ш)u(\mathbf{P}(ш)) + \mathscr{L}(u(\mathbf{P}(ш))) = f(\mathbf{P}(ш)) \quad \text{on} \quad \Omega \times Ш, \tag{5.1}$$

where Ш is the outcome space of the events, see e.g. [4]. It is shown that with adequate boundary conditions this type of PDEs yields a unique solution [5]. For completeness, it has to be noted that also uncertainties on the boundary conditions can be considered [155], however, this is beyond the scope of this thesis. A QoI F, depending on the solution of the sPDE, will inherit the stochastic nature, $F(ш) = F(u(\mathbf{P}(ш)))$. In order to evaluate the influences of the deviations on the QoI one needs to define stochastic quantities, such as the expectation value and the Standard Deviation (std). In the next section these quantities are introduced together with other basic concepts of probability theory. As a reference [159] is used. Afterwards, different techniques to approximate the stochastic integrals are discussed, i.e. MC and Multilevel Monte Carlo (MLMC) (based on [69]) and Stochastic Collocation (SC) (based on [159]) To find the most influential parameters, a sensibility analysis can be applied. The definitions of global sensitivities are introduced in the last section of this chapter.

5.1 Basic Concepts of Probability Theory

As mentioned before, $Ш$ depicts the outcome space, which contains all possible outcomes $ш$. Let us also define relevant subsets of $Ш$ as events in a class Σ, which is called the σ-algebra. It contains all the $ш$ in the event space and also the union, difference and intersection of any event in Σ, the set $Ш$, its complement and $\emptyset$ [159]. The likelihood of the occurrence of an event is depicted by P, so that $\mathrm{P}(Ш) = 1$ and $0 \leq \mathrm{P}(B) \leq 1, \forall B \in \Sigma$. One can now introduce the probabilistic setting by means of a probability space $(Ш, \Sigma, \mathrm{P})$. The vector $\mathbf{P} = \mathbf{P}(ш) = [P_1(ш), \ldots, P_{N_D}(ш)]$ is called a vector of $N_D (\leq N_p)$ random input variables, such that $\mathbf{P} : Ш^{N_D} \rightarrow \Gamma_ш \subset \mathbb{R}^{N_D}$ and $\mathbf{p}^{(k)} = [p_1^{(k)}, \ldots, p_{N_D}^{(k)}]$ is a realization, with $p_i^{(k)} = P_i(ш^{(k)})$, for $i = 1, \ldots, N_D$. In this work it is assumed that all P_i are independently distributed. Furthermore let $\varrho_\mathbf{P}$ depict the joint probability density function of $\mathbf{P}$.

To study how the uncertainties influence the QoI one has to rely on stochastic measures, such as, the expectation value,

$$\mathbb{E}[F(\mathbf{P})] = \int_{\Gamma_ш} F(\mathbf{p}) \varrho_\mathbf{P}(\mathbf{p}) \, \mathrm{d}\mathbf{p}, \tag{5.2a}$$

and the k^{th} moment

$$\mathbb{M}^k[F(\mathbf{P})] = \int_{\Gamma_ш} F^k(\mathbf{p}) \varrho_\mathbf{P}(\mathbf{p}) \, \mathrm{d}\mathbf{p}. \tag{5.2b}$$

Centering the second moment gives the variance

$$\mathbb{V}[F(\mathbf{P})] = \int_{\Gamma_ш} \big(F(\mathbf{p}) - \mathbb{E}[F(\mathbf{P})]\big)^2 \varrho_\mathbf{P}(\mathbf{p}) \, \mathrm{d}\mathbf{p}, \tag{5.3}$$

from which the std can be determined, i.e., $\mathrm{std}[F(\mathbf{P})] = \sqrt{\mathbb{V}[F(\mathbf{P})]}$.

It is often possible to interpret the deviations on the parameter, as deviations around a central value, which is the expectation value. Introducing $\bar{\mathbf{P}} = \mathbb{E}[\mathbf{P}]$, where $\bar{\mathbf{P}} \in \overline{\mathcal{P}} \subset \mathcal{P}$, and assuming that $\mathbb{E}[\boldsymbol{\Delta}] = \mathbf{0}$, one can write $\mathbf{P} = \bar{\mathbf{P}} + \boldsymbol{\Delta}$, with the vector of independent random input variables $\boldsymbol{\Delta} = \boldsymbol{\Delta}(ш) = [\Delta_1(ш), \ldots, \Delta_{N_D}(ш)]$. Applying a Taylor expansion around $\bar{\mathbf{P}}$ for the expectation value gives

$$\mathbb{E}\big[F(\bar{\mathbf{P}} + \boldsymbol{\Delta})\big] = F(\bar{\mathbf{P}}) + \mathcal{O}(\boldsymbol{\delta}^2), \tag{5.4}$$

where $\boldsymbol{\delta} = [\delta_1, \ldots, \delta_{N_D}]$ with $\delta_i = \mathrm{supp}(\Delta_i)$. Applying the same reasoning for the variance and standard deviations gives,

$$\mathbb{V}\big[F(\bar{\mathbf{P}} + \boldsymbol{\Delta})\big] = \mathbb{V}[F(\mathbf{s}) \cdot \boldsymbol{\Delta}] + \mathcal{O}(\boldsymbol{\delta}^3) \tag{5.5}$$

$$= \sum_{i=1}^{N_D} F^2(s_i) \mathbb{V}[\Delta_i] + \mathcal{O}(\boldsymbol{\delta}^3), \tag{5.6}$$

where the notion of local sensitivities introduced in Section 4.2 is used. Neglecting the higher order terms, one finds for the standard deviation

$$\operatorname{std}\left[F(\bar{\mathbf{P}}+\mathbf{\Delta})\right] \approx \sqrt{\sum_{i=1}^{N_D} F^2(s_i)\mathbb{V}\left[\Delta_i\right]} \tag{5.7}$$

$$= \|\operatorname{std}\left[\mathbf{\Delta}\right] \circ F(\mathbf{s})\|_2, \tag{5.8}$$

where $\circ$ depicts here the element-wise product. Generally the integrals in (5.2) are seldom solved exactly, but rather different numerical integration techniques are used.

5.2 Monte Carlo

One of the most spread methods to approximate the integrals is the MC method. By independently generating realizations of random inputs $\left\{\mathbf{p}^{(1)},\dots,\mathbf{p}^{(N_{\mathrm{MC}})}\right\}$ based on their probability distribution, one can extract statistical information such as the expectation value by

$$\mathbb{E}\left[F(\mathbf{P})\right] \approx \mathbb{E}_{\mathrm{MC}}\left[F(\mathbf{P})\right] = \frac{1}{N_{\mathrm{MC}}}\sum_{j=1}^{N_{\mathrm{MC}}} F(\mathbf{p}^{(j)}), \tag{5.9a}$$

and the variance by

$$\mathbb{V}\left[F(\mathbf{P})\right] \approx \frac{1}{N_{\mathrm{MC}}}\sum_{j=1}^{N_{\mathrm{MC}}} \left(F(\mathbf{p}^{(j)}) - \mathbb{E}_{\mathrm{MC}}\left[F(\mathbf{P})\right]\right)^2. \tag{5.9b}$$

A drawback of this method is that the procedure converges slowly. The error can be measured by looking at the variance of $\mathbb{E}\left[F(\mathbf{P})\right]$. Since the estimator is unbiased it holds that,

$$\mathbb{V}\left[\mathbb{E}_{\mathrm{MC}}\left[F(\mathbf{P})\right]\right] = \frac{\mathbb{V}\left[F(\mathbf{P})\right]}{N_{\mathrm{MC}}}. \tag{5.10}$$

The error estimator is then given by,

$$\varepsilon_{\mathrm{MC}} = \frac{\sqrt{\mathbb{V}\left[F(\mathbf{P})\right]}}{N_{\mathrm{MC}}^{1/2}} = \mathcal{O}(N_{\mathrm{MC}}^{-1/2}), \tag{5.11}$$

this implies that for halving the error, one needs to take four times more samples. This can be very costly. If assumed that for every sample one has to solve one of the systems of equations mentioned in (3.17) and that there is only a linear cost for solving the linear system, the total cost for the MC procedure can be written as

$$C_{\mathrm{MC}} = N_{\mathrm{MC}} N_{\mathrm{DoF}}. \tag{5.12}$$

Since MC is straightforward to apply it is one of the most favored methods to approximate the integrals, despite the high costs when a high accuracy is wanted. Moreover, MC has another major advantage, namely that the convergence rate is not depending on the number of random variables N_D that are considered and thus it does not suffer from the *curse of dimensionality*. There are more sophisticated MC methods that try to make MC sampling cheaper. There is quasi Monte Carlo (qMC) in which the samples are not chosen randomly, but according to deterministic sequences [49]. This method, however, does again suffer from the curse since the errors are at best of $\mathcal{O}\left((\log N_{\mathrm{MC}})^{r(N_D)}/N_{\mathrm{MC}}\right)$, with $r(N_D) > 0$ [74]. Another possible way to reduce the error in (5.11) is by decreasing its numerator. This is the main idea behind MLMC.

5.2.1 Multilevel Monte Carlo

Following [69] and [64], let us consider $\mathbb{E}[F(\mathbf{P}_L)]$. Using MLMC one uses samples $\mathbf{P}_\ell$ which are approximating $\mathbf{P}_L$ in different refinement steps, i.e., $\ell = 0, \ldots, L-1$, where 0 corresponds to the coarsest level and L the finest. Meaning that the approximation is better with increasing fineness. One can then write the telescope series

$$\begin{aligned}\mathbb{E}[F(\mathbf{P}_L)] &= \underbrace{\mathbb{E}[F(\mathbf{P}_0)] - \mathbb{E}[F(\mathbf{P}_0)] + \cdots + \mathbb{E}[F(\mathbf{P}_{L-1})] - \mathbb{E}[F(\mathbf{P}_{L-1})]}_{=0} + \mathbb{E}[F(\mathbf{P}_L)], \\ &= \mathbb{E}[F(\mathbf{P}_0)] + \sum_{\ell=1}^{L} \mathbb{E}[F(\mathbf{P}_\ell) - F(\mathbf{P}_{\ell-1})], \end{aligned} \tag{5.13}$$

in which only zeros were added. Using the MC estimator, i.e. (5.9a), for the expectation value, one finds

$$\begin{aligned}\mathbb{E}[F(\mathbf{P}_L)] \approx \mathbb{E}_{\mathrm{ML}}[F(\mathbf{P}_L)] &= \mathbb{E}_{\mathrm{MC}}[F(\mathbf{P}_0] + \sum_{\ell=1}^{L} \mathbb{E}_{\mathrm{MC}}[F(\mathbf{P}_\ell) - F(\mathbf{p}_{\ell-1})], \\ &= \frac{1}{N_{\mathrm{MC},0}} \sum_{i=1}^{N_{\mathrm{MC},0}} F(\mathbf{p}_0^{(i,0)}) + \sum_{\ell=1}^{L} \left(\frac{1}{N_{\mathrm{MC},\ell}} \sum_{i=1}^{N_{\mathrm{MC},\ell}} \left(F(\mathbf{p}_\ell^{(i,\ell)}) - F(\mathbf{p}_{\ell-1}^{(i,\ell)}) \right) \right). \end{aligned} \tag{5.14}$$

The appearance of ℓ in the superscripts indicates that for each level, the samples are chosen independently. For the variance one obtains

$$\begin{aligned}\mathbb{V}[\mathbb{E}_{\mathrm{ML}}[F(\mathbf{P}_L)]] &= \mathbb{V}\left[\mathbb{E}_{\mathrm{MC}}[F(\mathbf{P}_0)] + \sum_{\ell=1}^{L} \mathbb{E}_{\mathrm{MC}}[F(\mathbf{P}_\ell) - F(\mathbf{P}_{\ell-1})] \right], \\ &= \mathbb{V}[\mathbb{E}_{\mathrm{MC}}[F(\mathbf{P}_0)]] + \mathbb{V}\left[\sum_{\ell=1}^{L} \mathbb{E}_{\mathrm{MC}}[F(\mathbf{P}_\ell) - F(\mathbf{P}_{\ell-1})] \right], \\ &= \frac{1}{N_{\mathrm{MC},0}} \underbrace{\mathbb{V}[F(\mathbf{P}_0)]}_{V_0} + \sum_{\ell=1}^{L} \frac{1}{N_{\mathrm{MC},\ell}} \underbrace{\mathbb{V}[F(\mathbf{P}_\ell) - F(\mathbf{P}_{\ell-1})],}_{V_\ell} \end{aligned} \tag{5.15}$$

in which it has been exploited that the variables are independently distributed, which implies that the covariances are zero. Since $\mathbf{p}_\ell^{(i,\ell)}$ and $\mathbf{p}_{\ell-1}^{(i,\ell)}$ approximate $\mathbf{p}_L^{(i,L)}$ and both use the same samples i on level ℓ their difference is small and hence is their variance. Furthermore, since $V_\ell \to 0$ as $\ell \to \infty$ fewer and fewer samples are needed on the finer levels to estimate $\mathbb{E}[F(\mathbf{P}_L)]$ [37].

Let C_0 be the cost for one sample on the coarsest level and let C_ℓ be the cost for a single sample of $(F(\mathbf{P}_\ell) - F(\mathbf{P}_{\ell-1}))$ then the overall costs are determined by

$$C = \sum_{\ell=0}^{L} N_{\mathrm{MC},\ell} C_\ell. \tag{5.16}$$

Minimizing the variance for a fixed computational budget and introducing a user specified accuracy ε, one can write the overall costs as

$$C = \varepsilon^{-2} \left(\sum_{\ell=0}^{L} \sqrt{V_\ell C_\ell} \right)^2 \tag{5.17}$$

and the number of samples per level as

$$N_{\mathrm{MC},\ell} = \varepsilon^{-2} \sqrt{V_\ell / C_\ell} \sum_{\ell=0}^{L} \sqrt{V_\ell C_\ell}. \tag{5.18}$$

If the costs increase per level, then the overall costs are dominated by the finest level and one finds $C \approx \varepsilon^{-2} V_L C_L$. When they decrease per level the overall costs are dominated by the coarsest level, i.e., $C \approx \varepsilon^{-2} V_0 C_0$. In both cases using MLMC instead of MC gives rise to lower costs [37]. The convergence rate of MLMC can even be improved by using a different estimator, e.g. qMC [70].

So far it has remained vague on what the different levels actually are. The only prerequisite that was mentioned is that the approximation of the solution and the cost to obtain the solution should increase per level. These levels could be a finer time stepping scheme, e.g. [68], or a model order reduction scheme where the higher levels correspond to bigger approximation spaces. In many applications, e.g. [7], and in the applications used in this dissertation, the different levels correspond to higher mesh refinements used for solving the governing PDE.

Geometric Multilevel Monte Carlo

In many applications the outputs $F_\ell(\mathbf{P}) := F(u_\ell(\mathbf{P}))$ are, even on the finest level L, an approximation of $F(\mathbf{P})$, which often cannot be simulated exactly. Choosing the MLMC method to approximate $\mathbb{E}[F(\mathbf{P})]$, one can define the Mean Square Error (MSE) as

$$\mathrm{MSE} := \mathbb{E}\left[\left(\mathbb{E}_{\mathrm{ML}}[F_L(\mathbf{P})] - \mathbb{E}[F(\mathbf{P})]\right)^2\right].$$

This can be reformulated as

$$\mathrm{MSE} = \mathbb{V}[\mathbb{E}_{\mathrm{ML}}[F_L(\mathbf{P})]] + \left(\mathbb{E}[F_L(\mathbf{P}) - F(\mathbf{P})]\right)^2, \tag{5.19}$$

where the first term is given by (5.15). The MSE consists of two parts: The first term depicts the error of the variance, which is caused by using the MC method. The second term is a so-called *weak error*, which is related to the approximation of the model. Since, in this work, the levels correspond to different mesh refinements (see Figure 5.1), the error originates from the FEM approximation of the solution of the PDE. To have a MSE below ε^2 it is sufficient to ensure that the variance and the weak error are below $\varepsilon^2/2$. The different levels of refinement are constructed according to a geometric sequence: $h_\ell = h_0 \lambda^\ell$, where h_0 is a parameter describing the mesh size on the coarsest level and $0 < \lambda < 1$ (see Figure 3.2). It is ensured that MSE is below ε^2, when the conditions in the following theorem are fulfilled [69];

Theorem 1 *Let $F(\mathbf{P})$ be the QoI depending on a vector of random variables and let $F_\ell(\mathbf{P})$ denote the corresponding level ℓ numerical approximation. When there exist independent estimators based on $N_{MC,\ell}$ MC samples, with expected costs C_ℓ and variances V_ℓ, and constants $\alpha, \beta, \gamma, c_1, c_2, c_3 \in \mathbb{R}^+$, such that $\alpha \geq \frac{1}{2}\min(\beta, \gamma)$ and*

(i) $\mathbb{E}[F_\ell(\mathbf{P}) - F(\mathbf{P})] \leq c_1 h_\ell^\alpha$,

(ii) $V_\ell \leq c_2 h_\ell^\beta$,

(iii) $C_\ell \leq c_3 h_\ell^{-\gamma}$,

then there exists a constant $c_4 \in \mathbb{R}^+$ so that for any $\varepsilon < \mathrm{e}^1$ there are values L and $N_{MC,\ell}$ for which the multilevel estimator

$$\mathbb{E}_{\mathrm{ML}}[F_L(\mathbf{P})] = \mathbb{E}_{\mathrm{MC}}[F_0(\mathbf{P})] + \sum_{\ell=0}^{L} \mathbb{E}_{\mathrm{MC}}[F_\ell(\mathbf{P}) - F_{\ell-1}(\mathbf{P})]$$

has a MSE, bounded by

$$\mathrm{MSE} = \mathbb{E}\left[\left(\mathbb{E}_{\mathrm{ML}}[F_L(\mathbf{P})] - \mathbb{E}[F(\mathbf{P})]\right)^2\right] < \varepsilon^2$$

with a computational complexity C with bound

$$C_{\mathrm{MLMC}} \leq \begin{cases} c_4\varepsilon^{-2}, & \beta > \gamma, \\ c_4\varepsilon^{-2}(\log\varepsilon)^2, & \beta = \gamma, \\ c_4\varepsilon^{-2-(\gamma-\beta)/\alpha}, & \beta < \gamma. \end{cases}$$

The parameters α and β measure, respectively, how the weak error and the variance decay. For certain problem classes, e.g. elliptic model problems [146], the parameters can be determined a priori. However, if the underlying problem is too complex, they can be determined numerically in a pre-processing step [69]. The growth of the costs is denoted by γ. In the case of $\beta > \gamma$ the dominant costs are on the coarsest level, meaning $\mathcal{O}(C_0)$. In the case $\beta < \gamma$ the dominant costs are on the finest level leading to $\mathcal{O}(C_L)$. When $\beta = \gamma$ the costs are equally spread over the different levels. The costs are mainly determined by solving the system of equations (3.17) governing the physics of the problem. Since a 2D FEM is used, $N_{\mathrm{DoF},\ell} \approx h_\ell^{-2}$ and under the assumption that one uses an optimized code and a solver with linear complexity one can obtain $\gamma \approx 2$, the total costs C are given by

$$C_{\mathrm{MLMC}} = \sum_{\ell=0}^{L} C_\ell = \sum_{\ell=0}^{L} N_{\mathrm{MC},\ell} N_{\mathrm{DoF},\ell}, \tag{5.20}$$

with C_ℓ the costs on the ℓ^{th} level. For completeness one has to remark that for the standard MC method, it holds $C_{\mathrm{MC}} = \mathcal{O}\left(\varepsilon^{-3}\right)$.

Three major remarks have to be made. Firstly, it is not always true that a geometric sequence of levels is the best choice. Under some conditions there is a minor advantage in using non-geometric sequences [78]. Secondly, splitting the error equally between the discretization and the variance error is clearly not optimal. When the dominant computational error is on the coarsest level, adding more levels has a negligible cost, meaning that it makes more sense to allocate the major contribution of the error to the variance term [69]. Finally, if one cannot calculate $F(\mathbf{P})$ exactly, since there is no closed form solution at hand, one has to find another way to determine or estimate the weak error in (5.19). A way to replace the exact solution is by using the Richardson-extrapolator introduced in Section 3.4.

Richardson-extrapolation-based error indicator

The Richardson-extrapolation-based error indicator relies on $\hat{F}_\ell$ to determine the weak error introduced by the discretization. However, the computation of $\mathbb{E}\left[F_\ell - \hat{F}_\ell\right]^2$ is computationally more expensive than calculating $\mathbb{E}\left[F_\ell\right]$. As a consequence an approximation based on the first-order second-moment method is introduced. For a sample $\mathbf{p}^{(k)}$ one can write that

$$F(\mathbf{p}^{(k)}) = F(\bar{\mathbf{P}}) + \sum_{i=1}^{N_D} \frac{\partial F(\bar{\mathbf{P}})}{\partial p_i^{(k)}} \left(p_i^{(k)} - \bar{P}_i\right) + \mathcal{O}(\bar{\mathbf{P}}^2). \tag{5.21}$$

The expectation value in (5.2a) can thus be approximated by

$$\mathbb{E}\left[F(\mathbf{P})\right] \approx \int_{\Gamma_{\text{Ш}}} F(\bar{\mathbf{P}}) \varrho_{\mathbf{P}}(\mathbf{p})\,\mathrm{d}\mathbf{p} + \int_{\Gamma_{\text{Ш}}} \sum_{i=1}^{N_D} \frac{\partial F(\bar{\mathbf{P}})}{\partial p_i} \left(p_i - \bar{P}_i\right) \varrho_{\mathbf{P}}(\mathbf{p})\,\mathrm{d}\mathbf{p} = F(\bar{\mathbf{P}}). \tag{5.22}$$

So at level ℓ, the restriction on the weak error can be rewritten as

$$\mathbb{E}\left[F_\ell - \hat{F}_\ell\right]^2 \approx \left|F_\ell(\bar{\mathbf{P}}) - \hat{F}_\ell(\bar{\mathbf{P}})\right|^2,$$

and its evaluation comes with a lower computational cost.

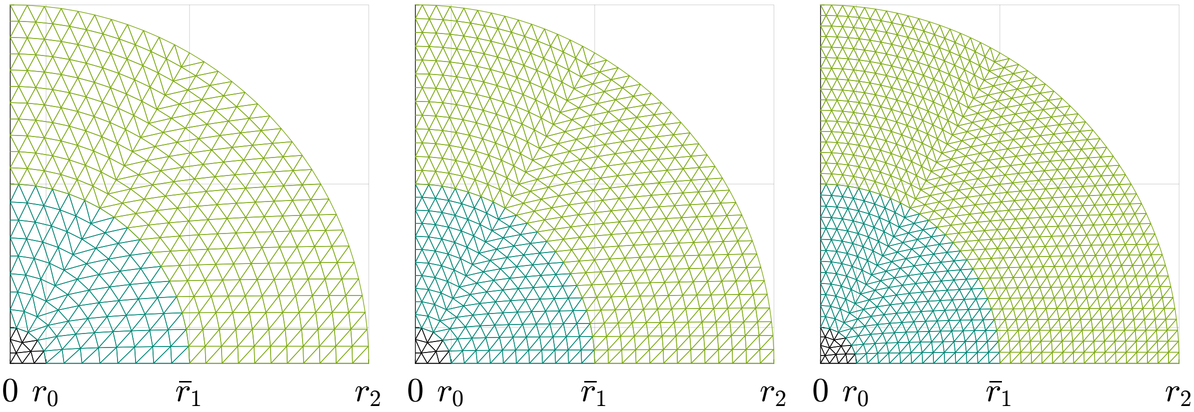

(a) Level 0 with $h_0 = 10^{-3}$ **(b)** Level 1 with $h_1 = 10^{-3.1}$ **(c)** Level 2 with $h_2 = 10^{-3.2}$

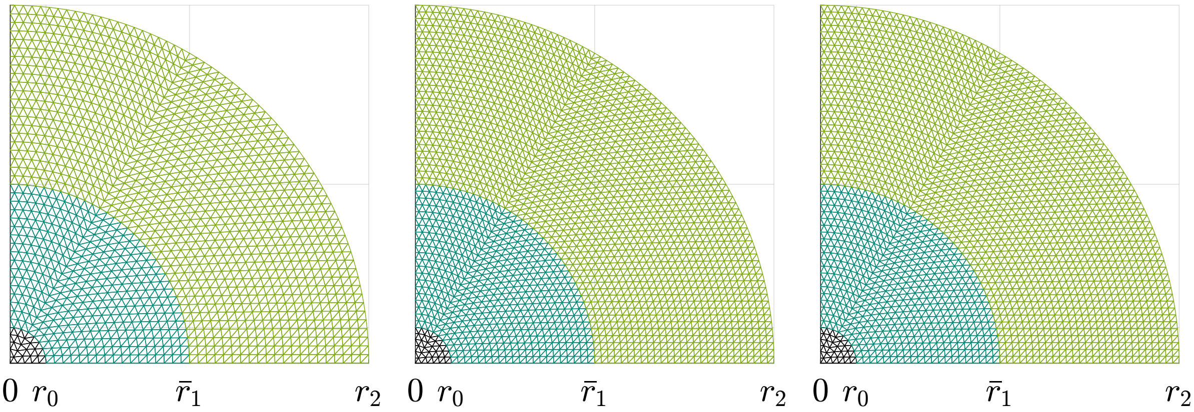

(d) Level 3 with $h_3 = 10^{-3.3}$ **(e)** Level 4 with $h_4 = 10^{-3.4}$ **(f)** Level 5 with $h_5 = 10^{-3.5}$

Figure 5.1: Example of different mesh refinements that are used as different levels for the MLMC method.

5.3 Stochastic Collocation

Contrary to the MC approaches, there also exist deterministic sampling methods. One of them is the SC method. It can be defined as follows: Let $\Theta_{N_{\mathrm{SC}}} = \left\{\mathbf{p}^{(j)}\right\}_{j=1}^{N_{\mathrm{SC}}}$ be a set of prescribed nodes, with $N_{\mathrm{SC}} > 1$ the number of nodes, also called collocation points. Let $\left\{F\left(\mathbf{p}^{(j)}\right)\right\}_{j=1}^{N_{\mathrm{SC}}}$ be the QoI depending on the solution of the governing PDE. Then the goal is to find a polynomial $w(\mathbf{P})$ in an appropriate polynomial space $\Pi(\mathbf{P})$, so that $w(\mathbf{P})$ is a good approximation to the true solution $F(\mathbf{P})$. For convergence it is required that $||w(\mathbf{P}) - F(\mathbf{p})|| \rightarrow 0$, when $N_{\mathrm{SC}} \rightarrow \infty$.

For the choice of the polynomials one relies on the framework of generalized Polynomial Chaos (gPC). For different random distributions, different polynomial bases are considered (see Table 5.1). Let us consider the polynomial bases $\{\Phi_k(\mathbf{P})\}_0^p$ which allows the construction of the gPC approximation of $F(\mathbf{P})$ by

$$F(\mathbf{P}) \approx \sum_{k=0}^{p} F(\mathbf{p}^{(k)})\Phi_k(\mathbf{P}) \tag{5.23}$$

where it holds that $\mathbb{E}[\Phi_m(\mathbf{P})\Phi_n(\mathbf{P})] = \mathbb{E}\left[\Phi_n^2(\mathbf{P})\right]\delta_{mn}$, with δ_{mn} the Kronecker delta [159]. Eq. (5.2a) and (5.3) are then approximated by

$$\mathbb{E}[F(\mathbf{p})] \approx \sum_{i=1}^{N_{\mathrm{SC}}} w_i F(\mathbf{p}^{(i)}), \tag{5.24a}$$

Table 5.1: Different types of continuous distributions and their corresponding gPC basis polynomials where $a, b \in \mathbb{R}$ (adapted from [159]).

Distribution	gPC basis	Support
Gaussian	Hermite	$]-\infty, +\infty[$
Gamma	Laguerre	$]-\infty, +\infty[$
Beta	Jacobi	$[a, b]$
Uniform	Legendre	$[a, b]$

and

$$\mathbb{V}[F(\mathbf{p})] \approx \sum_{i=1}^{N_{\mathrm{SC}}} w_i \left(F(\mathbf{p}^{(i)}) - \mathbb{E}[F(\mathbf{P})]\right)^2, \tag{5.24b}$$

where N_{SC} depicts the total number of collocation points $\mathbf{p}^{(i)}$ and w_i are the corresponding weights. The collocation points are selected according to quadrature rules, typically, one relies on Gaussian quadrature. For the multivariate cases, i.e., $N_D > 1$ one relies on tensor product collocation. Let us define an interpolating operator Q_{n_i} such that

$$Q_{n_i}[F] = \Pi_{n_i} F(P_i), \tag{5.25}$$

is a polynomial of degree n_i for a function F in the i^{th} variable. It uses $n_i + 1$ nodes in the set $\Theta_{n_i} = \left\{p_i^{(1)}, \dots, p_i^{(n_i)}\right\}$. Then one constructs the interpolant for F on the entire space by

$$Q_{N_{\mathrm{SC}}} = Q_{n_1} \otimes \ldots \otimes Q_{n_{N_D}} \tag{5.26}$$

on the nodal sets

$$\Theta_{N_{\mathrm{SC}}} = \Theta_{n_1} \times \ldots \times \Theta_{n_{N_D}}, \tag{5.27}$$

where the total number of nodes is $N_{\mathrm{SC}} = n_1 n_2 \ldots n_{N_D}$ [159]. If it is assumed that $n_1 = \ldots = n_{N_D} = n$, then $N_{\mathrm{SC}} = n^{N_D}$. The convergence of the method is then given by [159]

$$\left(I - Q_{N_{\mathrm{SC}}}\right)[F] = \mathcal{O}(N_{\mathrm{SC}}^{-\alpha/N_D}), \tag{5.28}$$

where $\alpha > 0$ is a constant related to the smoothness of the problem. If $N_D \gg 1$, the convergence will be slow and moreover the number of collocation points will increase drastically. Thus, using stochastic collocation one does suffer from the *curse of dimensionality*, however, for small dimensional problems and smooth problems one has exponential convergence [5].

There exist other, possibly more efficient approaches for the choice of collocation points such as Smolyak sparse grids [138] and the nested Clenshaw-Curtis nodes [8]. They both still rely on the tensor product construction but they are only a subset of the full grids.

5.4 Global Sensitivities

In addition to the local sensitivities introduced in Section 4.2, one can also define *global sensitivities*. The following derivation is based on [140]. The QoI can be written in the form

$$F(\mathbf{P}) = F_0 + \sum_{s=1}^{N_D} \sum_{i_1 < \ldots < i_s}^{N_D} F_{i_1,\ldots,i_s}\left(P_{i_1}, \ldots, P_{i_s}\right),$$

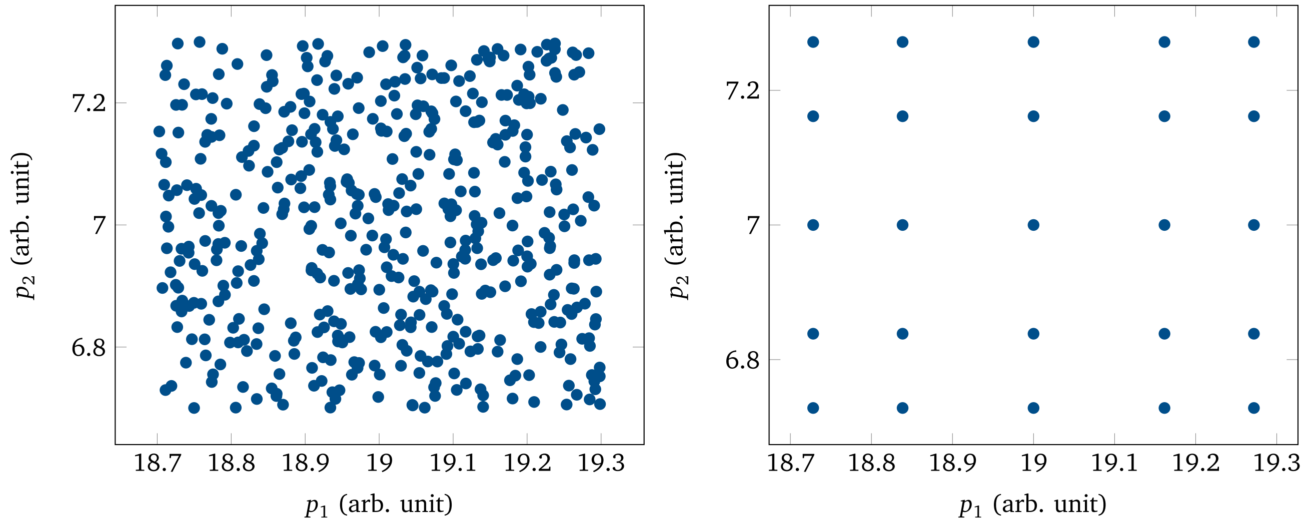

(a) Monte Carlo sampling with $N_{\mathrm{MC}} = 500$ random samples.
(b) Stochastic collocation with Gauss-Legendre quadrature.

Figure 5.2: Sampling methods for the $N_D = 2$ dimensional random parameter space.

with $1 \leq i_1 < \ldots < N_D$. It can be shown that $F_0 = \mathbb{E}[F(\mathbf{P})]$, for a detailed discussion see [140]. This representation is often addressed as the Analysis of Variances (ANOVA) [3]. Rearranging, squaring and integrating the left and the right hand side results in

$$\int_{\text{Ш}} F^2(\mathbf{P})\,\mathrm{d}\text{ш} - F_0^2(\mathbf{P}) = \sum_{s=1}^{N_D} \sum_{i_1<\ldots<i_s}^{N_D} \int_{\text{Ш}} \cdots \int_{\text{Ш}} F^2_{i_1,\ldots,i_s}\left(P_{i_1},\ldots,P_{i_s}\right)\,\mathrm{d}\text{ш}_{i_1}\ldots\,\mathrm{d}\text{ш}_{i_s} \tag{5.29}$$
$$= \mathbb{V}[F(\mathbf{P})],$$

which is the variance defined in (5.3). Let us define variances such that

$$\mathbb{V}_{i_1,\ldots,i_s}[F(\mathbf{P})] = \int_{\text{Ш}} \cdots \int_{\text{Ш}} F^2_{i_1,\ldots,i_s}\left(P_{i_1},\ldots,P_{i_s}\right)\,\mathrm{d}\text{ш}_{i_1}\ldots\,\mathrm{d}\text{ш}_{i_s}, \tag{5.30a}$$

and

$$\mathbb{V}[F(\mathbf{P})] = \sum_{s=1}^{N_D} \sum_{i_1<\ldots<i_s}^{N_D} \mathbb{V}_{i_1,\ldots,i_s}[F(\mathbf{P})]. \tag{5.30b}$$

One finally obtains the global sensitivity indices,

$$S_{i_1,\ldots,i_s} = \frac{\mathbb{V}_{i_1,\ldots,i_s}[F(\mathbf{P})]}{\mathbb{V}[F(\mathbf{P})]}, \tag{5.31}$$

for which it holds that

$$\sum_{s=1}^{N_D} \sum_{i_1<\ldots<i_s}^{N_D} S_{i_1,\ldots,i_s} = 1.$$

To estimate the sensitivities a standard MC procedure can be used [139] or more clever strategies as proposed by [133].

5.5 Résumé

In this chapter the reader has been introduced to the concepts of uncertainty quantification. The stochastic integrals, defining expectation value and higher order moments, have been approximated by Monte Carlo methods and stochastic collocation. Furthermore the notion of global sensitivities has been addressed. In the next chapter the methods will be applied to construct a robust optimization procedure.

6 Optimization

> "Well, now, my bumblebee, go on a spree..."
>
> Swan-Bird in *Flight of the Bumblebee*
> – N. Rimsky-Korsakov

In this chapter the mathematical formulations for the optimization problem are discussed. Let us assume that we want to optimize with respect to all parameters $\mathbf{P} \in \mathbb{R}^{N_p}$. The nominal optimization problem, often called a Non-linear Optimization Problem (NLP), can be written as,

$$\begin{aligned} \text{minimize} \quad & j_0(\mathbf{P}) && (6.1a)\\ \text{over} \quad & \mathbf{P} \in \mathbb{R}^{N_p} \\ \text{subject to} \quad & h_0(\mathbf{P}, F(\mathbf{P})) = 0 && (6.1b)\\ & g_0(\mathbf{P}, F(\mathbf{P})) \leq 0, && (6.1c) \end{aligned}$$

where $j_0 : \mathbb{R}^{N_p} \rightarrow \mathbb{R}$ is called the objective function, $F(\mathbf{P}) = F(A(\mathbf{P}))$ is the QoI, $h_0 : \mathbb{R}^{N_p} \times \mathbb{R} \rightarrow \mathbb{R}^{N_h}$ represent the equality constraints and $g_0 : \mathbb{R}^{N_p} \times \mathbb{R} \rightarrow \mathbb{R}^{N_g}$ are the inequality constraints. Introducing a set $\mathcal{P}_\mathrm{f}$, which contains all parameters $\mathbf{P}$ such that the solutions satisfy the constraints,

$$\mathcal{P}_\mathrm{f} = \left\{ \mathbf{P} \in \mathbb{R}^{N_p} \mid h_0(\mathbf{P}, F(\mathbf{P})) = 0 \wedge g_0(\mathbf{P}, F(\mathbf{P})) \leq 0 \right\}, \tag{6.2}$$

one can rewrite (6.1) as

$$\min_{\mathbf{P} \in \mathcal{P}_\mathrm{f}} j_0(\mathbf{P}). \tag{6.3}$$

Since F depends on the solution u of a PDE, the optimization has, what is called, a *PDE-constraint*. For a profound discussion of such optimization problems the interested reader is referred to [83]. Solving this nominal optimization problem leads to the optimal set of parameters $\mathbf{P}^*$.

Different algorithms can be found to solve (6.1) numerically, e.g. stochastic and deterministic methods. For electromagnetic problems there is a strong tendency in recent years to use *stochastic methods*. The most popular under these methods are Genetic Algorithm (GA) and nature inspired optimization algorithms. The former is based on natural selection and genetics, hence the name. In the latter, natural phenomena are mimicked. They include wind-driven optimization, where infinitesimally small air parcels are imitated [11], particle swarm optimization in which the behavior of swarms is simulated by incorporating self and swarm knowledge [130] and bat algorithms, where the hunt of bats for prey is imitated [160]. Their popularity is mainly caused by the fact that the finite element solver can be used as a black box and they easily allow for parallel computations. The drawback of these approaches is that a lot of configurations have to be calculated, which is costly since there are PDE constraints and thus a lot of finite element computations have to be performed.

In the class of *deterministic algorithms* one finds the gradient based optimization formulations to find local minima. The main advantage of the gradient algorithm with respect to the stochastic algorithms is that typically only a few steps are needed to find the minimum [54]. The found minimum, however, is in general a local minimum. The use of gradients requires the introduction of the concept of local sensitivities. When the optimization parameters describe changes in the geometry, the affine decomposition ensures an easy calculation of those sensitivities, see Section 4.1. Furthermore, combined with a model order reduction scheme, such as the Reduced Basis (RB) method, a numerical efficient optimization algorithm is constructed, e.g. [94, 114].

During production small deviations might occur on the optimization parameters and this might cause the slightly changed optimum to become suboptimal and even infeasible [15]. Optima that suffer from small deviations are often called sensitive optima. Instead of finding such solutions, one is more interested in finding a robust optimum, which is barely affected by those uncertainties. This robust optimum is actually a suboptimal solution of (6.1) but it is ensured that the solution stays feasible and nearly optimal under deviations.

Different approaches have been developed for robust optimization. For an overview the reader is referred to [18, 62]. The first idea for obtaining a robust design comes from Taguchi (e.g. [58]), where noise factors are introduced for mimicking the variations on the control parameters. In this dissertation the deterministic methods are favored. The robustification is firstly applied by considering a bounded uncertainty set. This allows for a reformulation of (6.1) by using a robust counterpart such that it yields the best worst-case value for the objective function. A profound mathematical discussion can be found in [16, 17]. The most common approach is to apply a linearization for the robust counterpart [50, 164].

This chapter is structured as followed: The first section is dedicated to different optimization algorithms. The second section deals with the two different formulations. One formulation is purely deterministic, the other one relies on stochastic measures as introduced in Chapter 5.

6.1 Optimization Algorithms

In this section two optimization algorithms are discussed, namely Particle Swarm Optimization (PSO) and Sequential Quadratic Programming (SQP). PSO [92] belongs to the class of stochastic optimization algorithms, whereas SQP is a gradient based deterministic optimization algorithm. The discussion on SQP is based on the Chapters 6, 16 and 18 in [111]. It is explained how both algorithm solve the NLP in (6.3) numerically.

6.1.1 Particle Swarm Optimization

The main idea is that one has a population of Q possible solutions, which are called particles. These particles move through the admissible set of the design space in search of an optimum. At every iteration step k the objective function for every particle position is evaluated. The obtained values are then compared to the best values in the history of each particle and to the best value of the entire swarm. The best set for the particles is denoted by $\hat{\mathbf{P}}_q$, with $q = 1, \dots, Q$ and for the swarm $\hat{\mathbf{P}}_{\text{sw}}$. The "velocity" and the position of the particles are updated according to [92] as

$$\mathbf{v}_q^{k+1} \leftarrow \lambda_0 \mathbf{v}_q^k + \lambda_1 \mathbf{N}_1 (\hat{\mathbf{P}}_q - \mathbf{P}_q^k) + \lambda_2 \mathbf{N}_2 (\hat{\mathbf{P}}_{\text{sw}} - \mathbf{P}_q^k), \tag{6.4a}$$

$$\mathbf{P}_q^{k+1} \leftarrow \mathbf{P}_q^k + \mathbf{v}_q^{k+1}. \tag{6.4b}$$

The constants λ_0, λ_1 and λ_2 are swarm characteristics. The matrices $\mathbf{N}_1$ and $\mathbf{N}_2$ are diagonal matrices where the elements are generated independently and uniformly for each particle at every step in $[0,1]$. This represents the *free will* of the swarm. The terms in the velocity update correspond, respectively, to

- maintaining a part of the current velocity,
- heading towards the particle's best found point ($\hat{\mathbf{P}}_q$), often addressed as the *cognitive component* of the particles,
- heading towards the swarm's best found point ($\hat{\mathbf{P}}_{\mathrm{sw}}$), often addressed as the *social component* of the particles.

Particles that leave the admissible set, are projected back to the boundary of this set. As initialization, i.e. $k = 0$, the particles are randomly and uniformly distributed over the admissible set and $\mathbf{v}_q = 0$. There are three possible stopping criteria for the algorithm

- a maximum number of iterations is reached,
- the majority of the particles is close enough to the best point $\hat{\mathbf{P}}_{\mathrm{sw}}$

  $$\frac{1}{Q}\sum_{q=1}^{Q} \|\hat{\mathbf{P}}_{\mathrm{sw}} - \mathbf{P}_{k,p}\|_2 < \epsilon, \tag{6.5}$$

  with a user-defined tolerance ϵ,
- no further change in the global best point $\hat{\mathbf{P}}_{\mathrm{sw}}$ over N_{stall} consecutive iterations occurs.

6.1.2 Sequential Quadratic Programming

To numerically determine a solution of (6.3) also SQP is used. For a given iterate $\mathbf{P}^k$, with $k \in \mathbb{N}_0$, SQP solves the NLP by solving Quadratic Programming (QP) subproblems [111]. The obtained solution $\mathbf{P}^{k+1}$ is then used in the next iteration step until the solution $\mathbf{P}^*$ of (6.3) is found. The SQP resembles the Newton and the quasi-Newton methods for the numerical solution of non-linear algebraic systems of equations [111].

Quadratic Programming

Let us introduce the gradient

$$\nabla_{\mathbf{P}} j_0(\mathbf{P}) := \left(\frac{\partial j_0(\mathbf{P})}{\partial P_1}, \dots, \frac{\partial j_0(\mathbf{P})}{\partial P_{N_p}}\right)^\top, \tag{6.6}$$

and the Hessian of j_0,

$$(Hj_0(\mathbf{P}))_{mn} := \left(\frac{\partial^2 j_0(\mathbf{P})}{\partial P_m \partial P_n}\right), \quad 1 \le m, n \le N_p. \tag{6.7}$$

For vector valued functions such as h_0, the Jacobian is introduced by a slight abuse of notation by,

$$\nabla h_0(\mathbf{P}, F(\mathbf{P})) := \left(\nabla_{\mathbf{P}} h_0^{(1)}(\mathbf{P}, F(\mathbf{P})), \dots, \nabla_{\mathbf{P}} h_0^{(N_h)}(\mathbf{P}, F(\mathbf{P}))\right)^\top. \tag{6.8}$$

One has to remark that the derivatives can actually be calculated using the sensitivities introduced in Section 4.2. Moreover, in the case of an affine decomposition they can be calculated in a closed form.

The QP subproblems must have the same local properties as the NLP with respect to $\mathbf{P}^k$. The objective function j_0 can then be replaced by a local quadratic approximation around $\mathbf{P}^k$,

$$j_0(\mathbf{P}) \approx j_0(\mathbf{P}^k) + \nabla j_0(\mathbf{P}^k)(\mathbf{P}-\mathbf{P}^k) + \frac{1}{2}(\mathbf{P}-\mathbf{P}^k)^\top H j_0(\mathbf{P}^k)(\mathbf{P}-\mathbf{P}^k). \tag{6.9}$$

Replacing the constraints by their local affine approximations yields

$$g_0(\mathbf{P}, F(\mathbf{P})) \approx g_0(\mathbf{P}^k, F(\mathbf{P}^k)) + \nabla g_0(\mathbf{P}^k, F(\mathbf{P}^k))(\mathbf{P}-\mathbf{P}^k), \tag{6.10}$$
$$h_0(\mathbf{P}, F(\mathbf{P})) \approx h_0(\mathbf{P}^k, F(\mathbf{P}^k)) + \nabla h_0(\mathbf{P}^k, F(\mathbf{P}^k))(\mathbf{P}-\mathbf{P}^k). \tag{6.11}$$

Defining $\mathbf{d}(\mathbf{P}) := (\mathbf{P}-\mathbf{P}^k)$ and $\mathbf{B}_k := H j_0(\mathbf{P}^k)$, the QP can be rewritten as

$$\begin{aligned}
\text{minimize}\quad & \nabla j_0^\top(\mathbf{P}^k)\mathbf{d}(\mathbf{P}) + \frac{1}{2}\mathbf{d}^\top(\mathbf{P})\mathbf{B}_k\mathbf{d}(\mathbf{P}), && (6.12a)\\
\text{over}\quad & \mathbf{d}(\mathbf{P}) \in \mathbb{R}^{N_p}, &&\\
\text{subject to}\quad & h_0(\mathbf{P}^k, F(\mathbf{P}^k)) + \nabla h_0(\mathbf{P}^k, F(\mathbf{P}^k))\mathbf{d}(\mathbf{P}) = 0, && (6.12b)\\
& g_0(\mathbf{P}^k) + \nabla g_0(\mathbf{P}^k, F(\mathbf{P}^k))\mathbf{d}(\mathbf{P}) \le 0. && (6.12c)
\end{aligned}$$

Define a Lagrangian functional $\mathcal{L} : \mathbb{R}^{N_p \times N_h \times N_g} \to \mathbb{R}$,

$$\mathcal{L}(\mathbf{P}, \boldsymbol{\kappa}, \boldsymbol{\lambda}) := j_0(\mathbf{P}) + \boldsymbol{\kappa}^\top h_0(\mathbf{P}, F(\mathbf{P})) + \boldsymbol{\lambda}^\top g_0(\mathbf{P}, F(\mathbf{P})), \tag{6.13}$$

where the vectors $\boldsymbol{\kappa} \in \mathbb{R}^m$ and $\boldsymbol{\lambda} \in \mathbb{R}^p_+$ depict the Lagrange multipliers. Then (6.12) can be transformed into the Lagrangian formulation, resulting in

$$\begin{aligned}
\text{minimize}\quad & \nabla\mathcal{L}^\top(\mathbf{P}^k, \boldsymbol{\kappa}^k, \boldsymbol{\lambda}^k)\mathbf{d}(\mathbf{P}) + \frac{1}{2}\mathbf{d}^\top(\mathbf{P})\mathbf{B}_k\mathbf{d}(\mathbf{P}), && (6.14a)\\
\text{over}\quad & \mathbf{d}(\mathbf{P}) \in \mathbb{R}^{N_p}, &&\\
\text{subject to}\quad & h_0(\mathbf{P}^k, F(\mathbf{P}^k)) + \nabla h_0(\mathbf{P}^k)\mathbf{d}(\mathbf{P}) = 0, && (6.14b)\\
& g_0(\mathbf{P}^k, F(\mathbf{P}^k)) + \nabla g_0(\mathbf{P}^k, F(\mathbf{P}^k))\mathbf{d}(\mathbf{P}) \le 0, && (6.14c)
\end{aligned}$$

where $\boldsymbol{\kappa}^k$ and $\boldsymbol{\lambda}^k$ are the multipliers of the QP under consideration and $\mathbf{B}_k$ is redefined as the Hessian of the Lagrangian, i.e. $H\mathcal{L}(\mathbf{P}^k, \boldsymbol{\kappa}^k, \boldsymbol{\lambda}^k)$. The above expression stems from the quadratic Taylor expansion

$$l_k = l(\mathbf{P}^k, \boldsymbol{\kappa}^k, \boldsymbol{\lambda}^k) := \mathcal{L}(\mathbf{P}^k, \boldsymbol{\kappa}^k, \boldsymbol{\lambda}^k)\mathbf{d}(\mathbf{P}) + \nabla\mathcal{L}^\top(\mathbf{P}^k, \boldsymbol{\kappa}^k, \boldsymbol{\lambda}^k)\mathbf{d}(\mathbf{P}) + \frac{1}{2}\mathbf{d}^\top(\mathbf{P})H\mathcal{L}(\mathbf{P}^k, \boldsymbol{\kappa}^k, \boldsymbol{\lambda}^k)\mathbf{d}(\mathbf{P}). \tag{6.15}$$

Introducing the set of active constraints $\mathcal{I}_{\mathbf{ac}}$, which is defined as

$$\mathcal{I}_{\mathbf{ac}}(\mathbf{P}) := \left\{ i \in \{1, \ldots, N_g\} \mid g_0^{(i)}(\mathbf{P}) = 0 \right\}, \tag{6.16}$$

and introducing its complement,

$$\mathcal{I}_{\mathbf{in}}(\mathbf{P}) := \left\{1, \ldots, N_g\right\} \setminus \mathcal{I}_{\mathbf{ac}}(\mathbf{P}), \tag{6.17}$$

it can be shown that (6.12) and (6.14) are equivalent when $\boldsymbol{\lambda}_i^k = 0, \forall i \in \mathcal{I}_{\mathbf{in}}(\mathbf{P}^k)$. It can be proven that solving (6.14) leads to finding a local minimum $\mathbf{P}^*$ of the original problem [111].

Instead of using the Hessian of the Lagrangian, i.e. $\mathbf{B}_k$, for every iteration, one can use a quasi-Newton approximation such as, e.g., the Broyden-Fletcher-Goldfarb-Shanno (BFGS) method [111].

Damped Broyden-Fletcher-Goldfarb-Shanno Method

The approximations of $\mathbf{B}_k$ of the Hessian of the Lagrangian are obtained by

$$\nabla\mathcal{L}\left(\mathbf{P}^{k+1},\boldsymbol{\kappa}^{k+1}\right)-\nabla\mathcal{L}(\mathbf{P}^{k},\boldsymbol{\kappa}^{k+1})\approx H\mathcal{L}\left(\mathbf{P}^{k+1},\boldsymbol{\kappa}^{k+1}\right)(\mathbf{P}^{k+1}-\mathbf{P}^{k}), \tag{6.18}$$

which leads to the secant equation,

$$\mathbf{B}_{k+1}\mathbf{s}_k=\mathbf{y}_k \tag{6.19}$$

with

$$\mathbf{s}_k=\mathbf{P}^{k+1}-\mathbf{P}^{k} \quad \text{and} \quad \mathbf{y}_k=\nabla\mathcal{L}\left(\mathbf{P}^{k+1},\boldsymbol{\kappa}^{k+1}\right)-\nabla\mathcal{L}\left(\mathbf{P}^{k},\boldsymbol{\kappa}^{k+1}\right). \tag{6.20}$$

The positive definite matrix $\mathbf{B}_{k+1}$ maps the displacement $\mathbf{s}_k$ to the change in gradient $\mathbf{y}_k$ if and only if the curvature condition

$$\mathbf{s}_k^{\top}\mathbf{y}_k>0 \tag{6.21}$$

holds. When this condition is fulfilled the secant equation always has a solution $\mathbf{B}_{k+1}$.

For the BFGS formula $\mathbf{B}_k^{-1}$ is considered. The secant condition, (6.19), must hold and thus

$$\mathbf{B}_{k+1}^{-1}\mathbf{y}_k=\mathbf{s}_k. \tag{6.22}$$

To determine $\mathbf{B}_{k+1}$ uniquely, it is imposed that for all symmetric matrices satisfying the secant equation, the closest to the current matrix $\mathbf{B}_k$ is the matrix $\mathbf{B}_{k+1}$. This means, one has to solve

$$\min_{\mathbf{B}^{-1}}\left\|\mathbf{B}^{-1}-\mathbf{B}_k^{-1}\right\| \tag{6.23a}$$

$$\text{subject to} \quad \mathbf{B}^{-1}=\left(\mathbf{B}^{-1}\right)^{\top}, \quad \mathbf{B}^{-1}\mathbf{y}_k=\mathbf{s}_k. \tag{6.23b}$$

It is known that the minimization problem can easily be solved using the weighted Frobenius norm,

$$\|\mathbf{A}\|_{\mathbf{W}}=\left\|\mathbf{W}^{1/2}\mathbf{A}\mathbf{W}^{1/2}\right\|_F, \tag{6.24}$$

with $\|\cdot\|_F$ defined as $\|\mathbf{A}\|_F^2=\sum_{i=1}^{n}\sum_{j=1}^{n}a_{ij}^2$ and where weighting matrices $\mathbf{W}$ satisfying $\mathbf{W}\mathbf{y}_k=\mathbf{s}_k$ are used.

The unique solution of (6.23) is given by

$$\mathbf{B}_{k+1}^{-1}=\left(I-\rho_k\mathbf{s}_k\mathbf{y}_k^{\top}\right)\mathbf{B}_k^{-1}\left(I-\rho_k\mathbf{y}_k\mathbf{s}_k^{\top}\right)+\rho_k\mathbf{s}_k\mathbf{s}_k^{\top}, \tag{6.25}$$

with

$$\rho_k=\frac{1}{\mathbf{y}_k^{\top}\mathbf{s}_k}. \tag{6.26}$$

Using the Sherman-Morrison-Woodbury formula (see Appendix A in [111]) the update can be expressed in function of $\mathbf{B}_k$,

$$\mathbf{B}_{k+1}=\mathbf{B}_k+\frac{\mathbf{y}_k\mathbf{y}_k^{\top}}{\mathbf{y}_k^{\top}\mathbf{s}_k}-\frac{\mathbf{B}_k\mathbf{s}_k\mathbf{s}_k^{\top}\mathbf{B}_k}{\mathbf{s}_k^{\top}\mathbf{B}_k\mathbf{s}_k}. \tag{6.27}$$

This is the main advantage of quasi-Newton methods. The approximations of the Hessians do not have to be recomputed at every iteration, instead they are slightly modified accounting for the information (e.g. curvature measured during the step k) on the objective function and the knowledge used for the current Hessian approximation.

If the Hessian of the Lagrangian contains negative eigenvalues, the BFGS method may become problematic since the approximation is done with a positive definite matrix. When $\mathbf{s}$ and $\mathbf{y}$ are defined as in (6.20) it might be that the curvature condition is violated, even when the iterates are close to the solution. To overcome this issue *damped BFGS updates* can be defined. Let $\mathbf{r}_k$ be defined as

$$\mathbf{r}_k := \theta_k \mathbf{y}_k + (1-\theta_k)\mathbf{B}_k \mathbf{s}_k, \tag{6.28}$$

where θ_k is defined as

$$\theta_k = \begin{cases} 1 & \text{if } \mathbf{s}_k^\top \mathbf{y}_k \geq 0.2 \mathbf{s}_k^\top \mathbf{B}_k \mathbf{s}_k, \\ \frac{0.8 \mathbf{s}_k^\top \mathbf{B}_k \mathbf{s}_k}{\mathbf{s}_k^\top \mathbf{B}_k \mathbf{s}_k - \mathbf{s}_k^\top \mathbf{y}_k} & \text{if } \mathbf{s}_k^\top \mathbf{y}_k < 0.2 \mathbf{s}_k^\top \mathbf{B}_k \mathbf{s}_k. \end{cases} \tag{6.29}$$

Updating $\mathbf{B}_k$ is done by

$$\mathbf{B}_{k+1} = \mathbf{B}_k + \frac{\mathbf{r}_k \mathbf{r}_k^\top}{\mathbf{r}_k^\top \mathbf{s}_k} - \frac{\mathbf{B}_k \mathbf{s}_k \mathbf{s}_k^\top \mathbf{B}_k}{\mathbf{s}_k^\top \mathbf{B}_k \mathbf{s}_k}, \tag{6.30}$$

Choosing $\theta_k = 0$ results in $\mathbf{B}_{k+1} = \mathbf{B}_k$ and choosing $\theta = 1$ gives the possible indefinite update as in (6.27). If $\theta_k \in \,]0,1[$, it is ensured that the new approximation stays close enough to the current approximation $\mathbf{B}_k$ so that the positive definiteness is ensured.

6.2 Formulations for the Objective Function and Constraints

In this section two formulations for the objective function and the constrains are discussed. The focus is first on the deterministic formulation and afterwards on the stochastic formulation. For both formulation, the nominal optimization problem and it robust counterparts are discussed.

6.2.1 Deterministic Formulation

The NLP in (6.1) is the deterministic formulation for the nominal optimization problem. The robust counterpart is introduced by a *worst-case* optimization procedure. In this case the deviations are not considered by relying on every Probability Density Function (PDF) of the uncertain parameters. Instead, they are restricted to bounded uncertainty sets [17]. The discussion on robust optimization in the deterministic formulation is mainly based on [50, 164].

Robust Optimization

The worst-case counterpart of (6.3) can be expressed as

$$\min_{\bar{\mathbf{P}} \in \bar{\mathcal{P}}_\infty} \max_{\boldsymbol{\delta} \in \mathcal{U}_\infty} j_0(\bar{\mathbf{P}} + \boldsymbol{\delta}), \tag{6.31a}$$

subject to

$$\max_{\boldsymbol{\delta} \in \mathcal{U}_\infty} h_0\left(\bar{\mathbf{P}} + \boldsymbol{\delta}, F(\bar{\mathbf{P}} + \boldsymbol{\delta})\right) = 0, \quad \text{and} \quad \max_{\boldsymbol{\delta} \in \mathcal{U}_\infty} g_0\left(\bar{\mathbf{P}} + \boldsymbol{\delta}, F(\bar{\mathbf{P}} + \boldsymbol{\delta})\right) \leq 0 \tag{6.31b}$$

where $\boldsymbol{\delta} = \left(\delta_1, \ldots, \delta_{N_p}\right)^\top$ and

$$\begin{aligned} \mathcal{U}_\infty &:= \left\{\boldsymbol{\delta} \in \mathbb{R}^{N_p} \mid \delta^{\mathrm{l}} \leq \delta_i \leq \delta^{\mathrm{u}}, i = 1 \ldots, N_p\right\} \\ &= \left\{\boldsymbol{\delta} \in \mathbb{R}^{N_p} \mid \left\|\mathbf{D}^{-1}\boldsymbol{\delta}\right\|_\infty \leq 1\right\}, \end{aligned} \tag{6.32}$$

with δ^{l} and δ^{u} the lower and upper bounds for δ_i and $\mathbf{D}$ an implicitly defined scaling matrix. The reduced parameter space is defined as

$$\bar{\mathcal{P}}_\infty := \left\{\bar{\mathbf{P}} \in \bar{\mathcal{P}} \mid \bar{\mathbf{P}} + \boldsymbol{\delta} \in \bar{\mathcal{P}} \wedge \boldsymbol{\delta} \in \mathcal{U}_\infty\right\} \tag{6.33}$$

in which $\bar{\mathcal{P}} \subset \mathbb{R}^{N_p}$ is a compact parameter space.

Linearized Robust Optimization (1-norm)

The nested optimization problem (6.31) is often hard to solve and therefore the max problem is approximated by a first order Taylor expansion, as proposed in [50]. This results in

$$j_0(\bar{\mathbf{P}}+\boldsymbol{\delta}) \approx j_0(\mathbf{P}) + \nabla_{\bar{\mathbf{P}}} j_0(\bar{\mathbf{P}})\boldsymbol{\delta}, \tag{6.34a}$$

$$h_0^{(m)}(\bar{\mathbf{P}}+\boldsymbol{\delta}) \approx h_0^{(m)}(\mathbf{P}) + \nabla_{\bar{\mathbf{P}}} h_0^{(m)}(\bar{\mathbf{P}})\boldsymbol{\delta}, \tag{6.34b}$$

$$g_0^{(n)}(\bar{\mathbf{P}}+\boldsymbol{\delta}) \approx g_0^{(n)}(\mathbf{P}) + \nabla_{\bar{\mathbf{P}}} g_0^{(n)}(\bar{\mathbf{P}})\boldsymbol{\delta}, \tag{6.34c}$$

where $m = 1,\dots,N_h$, $n = 1,\dots,N_g$. Combining (6.31) and (6.34) results in the linear approximation of the robust optimization setting:

$$\min_{\bar{\mathbf{P}}\in\bar{\mathcal{P}}_\infty} j_1 := j_0(\bar{\mathbf{P}}) + \left\| D\nabla_{\bar{\mathbf{P}}} j_0(\bar{\mathbf{P}}) \right\|_1, \tag{6.35a}$$

subject to

$$h_1(\bar{\mathbf{P}}) := h_0\left(\bar{\mathbf{P}}, F(\bar{\mathbf{P}})\right) + \left\| D\nabla_{\bar{\mathbf{P}}} h_0\left(\bar{\mathbf{P}}, F(\bar{\mathbf{P}})\right) \right\|_1 = 0, \tag{6.35b}$$

$$g_1(\bar{\mathbf{P}}) := g_0\left(\bar{\mathbf{P}}, F(\bar{\mathbf{P}})\right) + \left\| D\nabla_{\bar{\mathbf{P}}} g_0\left(\bar{\mathbf{P}}, F(\bar{\mathbf{P}})\right) \right\|_1 \leq 0. \tag{6.35c}$$

The dual norm $||\cdot||_*$is here defined as

$$\begin{array}{rccl} ||\cdot||_*: & \mathbb{R}_p^N & \rightarrow & \mathbb{R} \\ & \mathbf{g} & \mapsto & ||\mathbf{g}||_* := \max\limits_{\mathbf{g}\in\mathbb{R}_p^N, ||\boldsymbol{\delta}||\leq 1} \mathbf{g}^\top \boldsymbol{\delta}. \end{array}$$

In this particular case, one can use the property that the dual of $||D^{-1}\cdot||_\infty$ is given by $||D\cdot||_1$. A drawback of introducing the norms is that they are not differentiable. To circumvent this issue slack variables are introduced in order to obtain a differentiable problem. One can define a smooth counterpart for (6.35), namely,

$$\min_{\bar{\mathbf{P}}\in\bar{\mathcal{P}},\xi\in\mathbb{R}^{N_p}} j_0(\bar{\mathbf{P}}) + \mathbf{v}^\top \xi^{(0)}$$

together with the constraints

$$h_0^{(m)}(\bar{\mathbf{P}}) + \mathbf{v}^\top \xi^{(m)} = 0$$

$$g_0^{(n)}(\bar{\mathbf{P}}) + \mathbf{v}^\top \xi^{(n)} \leq 0$$

and

$$-\xi^{(0)} \leq D\nabla_{\bar{\mathbf{P}}} j_0(\bar{\mathbf{P}}) \leq \xi^{(0)},$$

$$-\xi^{(m)} \leq D\nabla_{\bar{\mathbf{P}}} h_0^{(m)}(\bar{\mathbf{P}}) \leq \xi^{(m)},$$

$$-\xi^{(n)} \leq D\nabla_{\bar{\mathbf{P}}} g_0^{(n)}(\bar{\mathbf{P}}) \leq \xi^{(n)},$$

where $m = 1,\dots,N_h$, $n = 1,\dots,N_g$, and $\boldsymbol{\xi} = \left(\xi^{(1)},\dots,\xi^{(N_p)}\right)$ and $\mathbf{v} = (1,\dots,1)^\top \in \mathbb{R}^{N_p}$. This optimization problem can again be solved using either the SQP method or the PSO algorithm discussed in the previous sections. However, for SQP additional second-order sensitivities s_i^2 as defined in (4.11) are required. Even though this approach is numerically very efficient, especially in combination with model order reduction schemes and/or an affine decomposition, the approximation might describe the influence of the uncertain parameters inaccurately, see e.g. [51]. Therefore some works, e.g. [94, 136], extended the worst-case optimization approach by considering second order approximations.

Linearized Robust Optimization (2-norm)

Even though the max-norm in the definition of (6.32) is more common, one could also pick the 2-norm instead. One can define a new uncertainty set

$$\mathcal{U}_2 := \left\{ \boldsymbol{\delta} \in \mathbb{R}^{N_p} \mid \left\| \mathbf{D}^{-1} \boldsymbol{\delta} \right\|_2 \leq 1 \right\}, \tag{6.37}$$

and redefine the reduced parameter space as

$$\overline{\mathcal{P}}_2 := \left\{ \bar{\mathbf{P}} \in \overline{\mathcal{P}} \mid \bar{\mathbf{P}} + \boldsymbol{\delta} \in \overline{\mathcal{P}} \wedge \boldsymbol{\delta} \in \mathcal{U}_2 \right\}. \tag{6.38}$$

This yields the following optimization problem,

$$\min_{\bar{\mathbf{P}} \in \overline{\mathcal{P}}_2} j_2 := j_0(\bar{\mathbf{P}}) + \left\| D \nabla_{\bar{\mathbf{P}}} j_0(\bar{\mathbf{P}}) \right\|_2, \tag{6.39a}$$

subject to

$$h_2(\bar{\mathbf{P}}) := h_0\left(\bar{\mathbf{P}}, F(\bar{\mathbf{P}})\right) + \left\| D \nabla_{\bar{\mathbf{P}}} h_0\left(\bar{\mathbf{P}}, F(\bar{\mathbf{P}})\right) \right\|_2 = 0, \tag{6.39b}$$

$$g_2(\bar{\mathbf{P}}) := g_0\left(\bar{\mathbf{P}}, F(\bar{\mathbf{P}})\right) + \left\| D \nabla_{\bar{\mathbf{P}}} g_0\left(\bar{\mathbf{P}}, F(\bar{\mathbf{P}})\right) \right\|_2 \leq 0. \tag{6.39c}$$

The formulation does not optimize the worst case relying on (6.32) but will still improve its robustness. It does optimize the worst case for (6.37). This norm has been used in for example [50].

6.2.2 Stochastic Formulation

In the stochastic formulation the uncertainties are taken into account by considering the stochastic quantities describing the distributions. As discussed in Chapter 5 those quantities are given by integration but can be approximated by applying quadrature. The quadrature becomes trivial if one uses a linear approximation of the problem [41].

In this section it is assumed that $\mathbf{P} = \mathbf{P}(\text{щ})$, such that $\mathbf{P}(\text{щ}) = \bar{\mathbf{P}} + \boldsymbol{\Delta}(\text{щ})$ with $\boldsymbol{\Delta} \sim \mathcal{U}\left(\boldsymbol{\delta}^{\mathrm{l}}, \boldsymbol{\delta}^{\mathrm{u}}\right)$, where $\boldsymbol{\delta}^{\mathrm{l}} = \left(\delta_1^{\mathrm{l}}, \ldots, \delta_{N_p}^{\mathrm{l}}\right)$, $\boldsymbol{\delta}^{\mathrm{u}} = \left(\delta_1^{\mathrm{u}}, \ldots, \delta_{N_p}^{\mathrm{u}}\right)$ and $\delta_i^{\mathrm{l}} = -\delta_i^{\mathrm{u}}$.

Nominal Optimization

The cost function and its constraints can now be defined in terms of expectation values, as in [144],

$$\min_{\bar{\mathbf{P}} \in \overline{\mathcal{P}}_2} j_3(\mathbf{P}) := \mathbb{E}\left[j_0(\mathbf{P}) \right], \tag{6.40a}$$

subject to

$$h_3(\mathbf{P}) := \mathbb{E}\left[h_0\left(\mathbf{P}, F(\mathbf{P})\right) \right] \tag{6.40b}$$

$$g_3(\mathbf{P}) := \mathbb{E}\left[g_0\left(\mathbf{P}, F(\mathbf{P})\right) \right]. \tag{6.40c}$$

This optimization problem is again deterministic and can be solved by using the same techniques as for the nominal deterministic optimization, however, with increased computational costs for approximating the probabilistic integrals.

Robust Optimization

In [41] the robustification is obtained by the *mean-variance approach*. In the objective function the expectation value and the variance are considered. The variance is weighted by a risk aversion parameter. This idea has been extended to the constraints in [86]. In this dissertation the risk aversion parameter is kept dimension free, i.e. free from physical units, by replacing the variance by the standard deviation. The robust counterpart for (6.31) in the stochastic formulation reads then as,

$$\min_{\bar{\mathbf{P}} \in \bar{\mathcal{P}}_2} j_4(\mathbf{P}) := \mathbb{E}\left[j_0(\mathbf{P})\right] + \beta \ \mathrm{std}\left[j_0(\mathbf{P})\right] \tag{6.41a}$$

subject to

$$h_4(\mathbf{P}) := \mathbb{E}\left[h_0\left(\mathbf{P}, F(\mathbf{P})\right)\right] + \beta \ \mathrm{std}\left[h_0(\mathbf{P}, F(\mathbf{P}))\right] = 0, \tag{6.41b}$$

$$g_4(\mathbf{P}) := \mathbb{E}\left[g_0\left(\mathbf{P}, F(\mathbf{P})\right)\right] + \beta \ \mathrm{std}\left[g_0(\mathbf{P}, F(\mathbf{P}))\right] \leq 0, \tag{6.41c}$$

where β is weighting parameter similar to $\mathbf{D}$ in (6.32). In [151] this approach has been extended by taking the higher moments into account.

Linearized Robust Optimization

Relying on the linearization introduced in (5.4) and (5.7), one can define a linearized complement of (6.41), with objective function

$$\begin{aligned} j_5(\bar{\mathbf{P}}) &= \mathbb{E}\left[j_0(\bar{\mathbf{P}} + \boldsymbol{\Delta}(\text{щ}))\right] + \beta \ \mathrm{std}\left[j_0(\bar{\mathbf{P}} + \boldsymbol{\Delta}(\text{щ}))\right] \\ &\approx j_0(\bar{\mathbf{P}}) + \beta \left\| \mathrm{std}\left[\boldsymbol{\Delta}(\text{щ})\right] \circ \nabla_{\bar{\mathbf{P}}} j_0(\bar{\mathbf{P}}) \right\|_2, \end{aligned}$$

and constraints

$$\begin{aligned} h_5^{(m)}(\bar{\mathbf{P}}, F(\bar{\mathbf{P}})) &= \mathbb{E}\left[h_0^{(m)}(\bar{\mathbf{P}} + \boldsymbol{\Delta}(\text{щ}), F(\bar{\mathbf{P}} + \boldsymbol{\Delta}(\text{щ})))\right] + \beta \ \mathrm{std}\left[h_0^{(m)}(\bar{\mathbf{P}} + \boldsymbol{\Delta}(\text{щ}), F(\bar{\mathbf{P}} + \boldsymbol{\Delta}(\text{щ}))\right] \\ &\approx h_0^{(m)}(\bar{\mathbf{P}}, F(\bar{\mathbf{P}})) + \beta \left\| \mathrm{std}\left[\boldsymbol{\Delta}(\text{щ})\right] \circ \nabla_{\bar{\mathbf{P}}} h_0^{(m)}(\bar{\mathbf{P}}, F(\bar{\mathbf{P}})) \right\|_2, \\ g_5^{(n)}(\bar{\mathbf{P}}, F(\bar{\mathbf{P}})) &= \mathbb{E}\left[g_0^{(n)}(\bar{\mathbf{P}} + \boldsymbol{\Delta}(\text{щ}), F(\bar{\mathbf{P}} + \boldsymbol{\Delta}(\text{щ})))\right] + \beta \ \mathrm{std}\left[g_0^{(n)}(\bar{\mathbf{P}} + \boldsymbol{\Delta}(\text{щ}), F(\bar{\mathbf{P}} + \boldsymbol{\Delta}(\text{щ}))\right] \\ &\approx g_0^{(n)}(\bar{\mathbf{P}}, F(\bar{\mathbf{P}})) + \beta \left\| \mathrm{std}\left[\boldsymbol{\Delta}(\text{щ})\right] \circ \nabla_{\bar{\mathbf{P}}} g_0^{(n)}(\bar{\mathbf{P}}, F(\bar{\mathbf{P}})) \right\|_2. \end{aligned}$$

The linearization applied in (6.42) has recently been extended by including quadratic approximations [2].

The introduction of the linearization leads to the theorem:

Theorem 2 *Assume that*

(i) the quantity of interest is linear in u, such that $\partial F / \partial u$ *=const,*

(ii) all perturbations are independently and identically distributed, and

(iii) the distributions of the perturbations are symmetric around 0, i.e. $\mathbb{E}\left[\boldsymbol{\Delta}(\text{щ})\right] = 0$*,*

all hold true, then by choosing $\beta = \frac{D_{ii}}{\mathrm{std}[\Delta_i(\text{щ})]}$ *it follows that, by construction, an equivalence between the optimization formulation with linearized stochastic quantities, i.e.* (6.39)*, and linearized worst-case optimization using the 2-norm, i.e.* (6.42)*, has been established.*

6.3 Résumé

In this chapter different optimization formulations have been introduced. In the stochastic formulation, one considers the expectation values of the parameters for the nominal optimization. To find a robust optimum the formulation includes the standard deviations. In the deterministic setting the robust optimization is done by considering the worst case scenario. In order to have a differentiable formulation, a linearization is applied, which introduces the 1-norm in the formulation. It is shown that when a linearization is applied to the robust optimization problem in the stochastic formulation and a 2-norm is used in the deterministic formulation, the two formulations are actually equivalent.

The Non-linear Optimization Problem has been identified to have a Partial Differential Equation (PDE) as constraint. The reader was introduced to two different types of optimization algorithms. Firstly, particle swarm optimization was discussed, as an example of a stochastic optimization algorithm. Secondly, the deterministic algorithm sequential quadratic programming, which relies on gradients, was addressed. The calculation of these gradients is very efficient, when relying on an affine decomposition (see Section 4.1) and when using the reduced basis method (see Section 4.3), which reduces the cost of solving the PDE. The next part of this dissertation focuses on the modeling of different applications. Optimization will be applied on two of the examples.

Movement III

Largo: Modeling and Discretization of Applications

7 Coaxial Cable

> "Waves from moving sources: Adagio. Andante. Allegro moderato"
>
> *Electromagnetic Theory*
> – O. Heaviside

For testing uncertainty approaches like the multilevel Monte Carlo (MLMC) method a simple device, namely a coaxial cable (Figure 7.1), is considered firstly. The main advantage is that there exists a Closed Form Solution (CFS) of Maxwell's eddy current equations which can be used to determine numerical errors. Secondly, since only a small number of random parameters will be included, stochastic collocation (SC) can be used as a cheap reference solution for the expectation value of the considered quantity of interest Quantity of Interest (QoI). Another advantage is that due to the simple geometry, a hierarchy of regular meshes can be constructed.

In the first section, a short explanation of the physical phenomena in a coaxial cable are introduced and discussed. The second section deals with the modeling and discretization. The final section introduces the uncertainties and the problem description for the uncertainty quantification is defined.

7.1 Background

Coaxial cables were firstly patented by Oliver Heaviside [107] and are used as transmission lines. They consists of an inner copper wire which is embedded in a dielectric medium. Concentric to the wire there is a metallic tube which acts as a shield. On the outside of the tube there is an insulator. The advantages of this construction is that for an ideal cable with a perfectly conducting wire, the electromagnetic field related to the signal in the wire only propagates in the region between the wire and the tube. Furthermore the shield also keeps interference of external fields low.

The current in the wire varies sinusoidally with an angular frequency ω and the magnitude of the current is depicted by $\hat{I}_\mathrm{s}$,

$$I_\mathrm{s} = \hat{I}_\mathrm{s} \sin(\omega t) . \tag{7.1}$$

The time-varying current induces a time varying magnetic field (see (2.1a)). This varying magnetic field will induce an electric field in the tube (see (2.1b)). As a consequence, currents in the tube will be

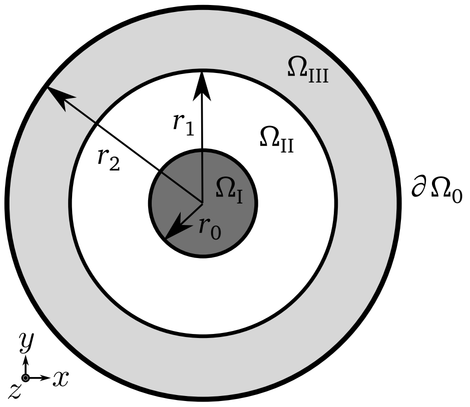

Figure 7.1: Cross-sectional view of a coaxial cable.

induced (see (2.2c)) which generate a magnetic field that will counteract the changing magnetic field from the wire. This helps the shielding of the signal. The currents induced in the tube are called *eddy currents*. The location where the main part of these currents are located is determined by the skin depth,

$$\delta_{\mathrm{sk}} = \sqrt{\frac{2}{\omega\sigma\mu}},$$

where σ and μ are the material properties of the region where the currents have been induced.

The magnetic energy per length ℓ_z, i.e. W, in a region is given by,

$$W_i = \int_{\Omega_i} \frac{\mu_i \vec{H}_i \cdot \vec{H}_i^*}{2}\,\mathrm{d}\Omega_i, \tag{7.2}$$

in which $\vec{H}^*$ depicts the complex conjugate of the magnetic field strength and i is an index referring to the regions so that the total magnetic energy of the system is given by $W = \sum_{i=1}^{3} W_i$. The CFS, written in polar coordinates, for the magnetic field strengths in the different regions are given by [142],

$$\vec{H}(r) = \begin{cases} \frac{J_{\mathrm{s}} r}{2}\vec{e}_\phi & 0 < r \leq r_0, \\ \frac{J_{\mathrm{s}}}{2}\frac{r_0^2}{r}\vec{e}_\phi & r_0 < r < r_1, \\ \frac{J_{\mathrm{s}}}{2}\frac{r_0^2}{r_1}\frac{\frac{\mathrm{I}_1(\xi r)}{\mathrm{I}_0(\xi r_2)} + \frac{\mathrm{K}_1(\xi r)}{\mathrm{K}_0(\xi r_2)}}{\frac{\mathrm{I}_1(\xi r_1)}{\mathrm{I}_0(\xi r_2)} + \frac{\mathrm{K}_1(\xi r_1)}{\mathrm{K}_0(\xi r_2)}}\vec{e}_\phi & r_1 \leq r \leq r_2, \end{cases} \tag{7.3}$$

where $\mathrm{I}_0(\cdot)$ and $\mathrm{I}_1(\cdot)$ are, respectively, the modified Bessel functions of zeroth and first order of the first kind and $\mathrm{K}_0(\cdot)$ and $\mathrm{K}_1(\cdot)$ are, respectively, the modified Bessel functions of zeroth and first order of the second kind. The Helmholtz constant ξ is given by

$$\xi = \frac{1+\imath}{\delta_{\mathrm{sk}}}.$$

7.2 Model and Discretization

To model the coaxial cable one identifies three different regions (see Figure 7.1), such that $\overline{\Omega} = \overline{\Omega}_{\mathrm{I}} \cup \overline{\Omega}_{\mathrm{II}} \cup \overline{\Omega}_{\mathrm{III}}$. The magnetoquasistatic approximation of Maxwell's equations is used to model coaxial cables. The only source term originates from the current in the central wire. It is assumed that the source current is homogeneously distributed over the wire's cross-sectional surface. The source current density is then

Table 7.1: Parameters of the coaxial cable.

μ_I	μ_0	r_0	2.54 mm
μ_II	μ_0	r_2	25.4 mm
μ_III	$\mu_0\mu_\mathrm{r}$	$\bar{r}_1$	12.7 mm
σ_I	0 MS/m	$\bar{I}_\mathrm{s}$	100 A
σ_II	0 MS/m	$\bar{\mu}_\mathrm{r}$	1000
σ_III	58 MS/m		

given by $\vec{J}_\mathrm{s} = I_\mathrm{s}/(\pi r_0^2)\vec{e}_z$, where r_0 is the radius of the wire. In 2D this reduces to (2.8) which is solved on Ω. The insulating layer is modeled by applying homogeneous Dirichlet conditions on $\partial\Omega$. Applying the Ritz-Galerkin method, one retrieves

$$\imath\omega\mathbf{M}\mathbf{a} + \mathbf{K}\mathbf{a} = \mathbf{j}, \tag{7.4}$$

where **a** represents the discretized version of A_z and **j** is the discretized source term. The wire inner region Ω_I is the copper wire. The dielectric region, Ω_II is assumed to be filled with air. The outer region Ω_III depicts the tube, which is considered to be constructed from steel. Region I and II are modeled with the permeability of vacuum μ_0 and with a vanishing conductivity. Region III has a permeability $\mu_\mathrm{III} = \mu_\mathrm{r}\mu_0$, with μ_r the relative permeability and a conductivity σ_III. The dimensions and material properties of every region are depicted in Table 7.1.

7.3 Uncertainties

The three parameters which are considered are all assumed to be uncertain, meaning that $\mathbf{P} : \text{Ш} \to \Gamma_{\text{Ш}} \subset \mathbb{R}^3$. These are the relative permeability μ_r of the third region, the inner radius of the third region r_1 and the magnitude of the applied current. The random parameters are considered independent random variables with a uniform distribution,

$$\begin{aligned} r_1(\text{ш}) &= \bar{r}_1 + \Delta_1(\text{ш}), \quad \text{with} \quad \Delta_1 \sim \mathfrak{U}(-2.54\,\mathrm{mm}, 2.54\,\mathrm{mm}), && (7.5a)\\ \hat{I}_\mathrm{s}(\text{ш}) &= \bar{I}_\mathrm{s} + \Delta_2(\text{ш}), \quad \text{with} \quad \Delta_2 \sim \mathfrak{U}(-10\,\mathrm{A}, 10\,\mathrm{A}), && (7.5b)\\ \mu_\mathrm{r}(\text{ш}) &= \bar{\mu}_\mathrm{r} + \Delta_3(\text{ш}), \quad \text{with} \quad \Delta_3 \sim \mathfrak{U}(-400, 400), && (7.5c) \end{aligned}$$

with nominal values

$$\begin{aligned} \bar{r}_1 &= \mathbb{E}[r_1] &= 12.7\,\mathrm{mm}, && (7.5d)\\ \bar{I}_\mathrm{s} &= \mathbb{E}[I_\mathrm{s}] &= 100\,\mathrm{A}, && (7.5e)\\ \bar{\mu}_\mathrm{r} &= \mathbb{E}[\mu_\mathrm{r}] &= 1000. && (7.5f) \end{aligned}$$

The uncertainty quantification one wants to conduct can be written as

Problem 1 *Find* $\mathbb{E}[W(\mathbf{a})]$ *and* $\operatorname{std}[W(\mathbf{a})]$, *where* **a** *are the Degrees of Freedom (DoF)s for* A_z *given by the discretization of*

$$\imath\omega\sigma A_z(x,y) - \nabla\cdot(\nu\nabla A_z(x,y)) = J_{\mathrm{tot},z}(x,y) \quad \textit{on} \quad \Omega.$$

with homogeneous boundary conditions on $\partial\Omega$ *and while considering the uncertainties described by* (7.5).

7.4 Résumé

The coaxial cable will be used as a benchmark problem for the multilevel Monte Carlo method. The advantage is that there is a closed form solution for the quantity of interest, so that it can be used to determine the spatial error. This means that it will be possible to test the use of a Richardson-extrapolation based error indicator as a control for the spatial error. Furthermore, due to the simple geometry the handling of the meshes will be easy, which will enable to study if different methods to determine the spatial discretization for the different levels will influence the results.

8 Stern–Gerlach Magnet

> “Anyone who is not shocked by quantum theory has not understood it.”
>
> *Niels Bohr*

The second device that is in focus of this work is the Stern-Gerlach magnet depicted in Figure 8.1. This application is used to show how the use of Iso-Geometric Analysis (IGA) facilitates shape optimization of electromagnetic devices. A Stern-Gerlach magnet enables scientists to study the intrinsic angular momentum of atoms, molecules and nanoclusters. The magnet is a Rabi-type magnet and already in use at the KU Leuven in Belgium. A first optimization has been conducted [101]. A key design requirement for such magnets is the presence of a strong and homogeneous gradient of the magnetic field in the region where the particle beam passes Ω_{beam}. The current design achieves a field gradient of 200 T/m in x-direction and an inhomogeneity of the field gradient of maximum 5 %.

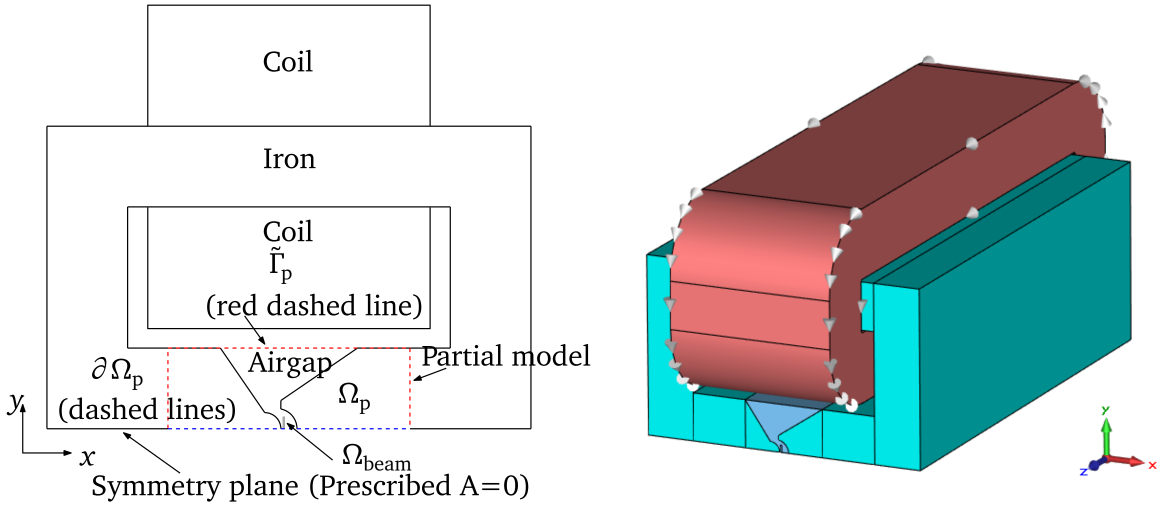

Figure 8.1: 2D model and 3D model of one half of the Stern-Gerlach magnet. The latter is constructed with CST EM STUDIO® [39].

This chapter is structured as follows. In its first section, the background of the experiment is briefly discussed so that the importance of the field gradient becomes clear. Afterwards, the model of the magnet is addressed and the Quantities of Interest (QoIs) are introduced. The last section deals with the optimization problem.

8.1 Background of the Stern–Gerlach Experiment

The setup of the experiment is to send a beam of atoms, molecules or clusters along the z-direction through (see Figure 8.1) a non-uniform magnetic field $\vec{B} = (B_x, B_y, B_z)$, which is aligned in the x-direction. The possible deflection of the beam due to the magnetic field gradient is measured by the impact of the atoms, molecules or clusters on a detection screen, positioned perpendicular to the initial direction of the beam.

When a magnetic moment $\vec{\mu} = (\mu_x, \mu_y, \mu_z)$ is placed in a magnetic field, a force

$$\vec{F} = \sum_{i \in x,y,z} \mu_i \nabla B_i \tag{8.1}$$

acts on the dipole. One might expect that the magnetic moment would align with the axis of the local magnetic field, however this is not the case and they will precess around this axis [9].

In the setup shown in Figure 8.1, it is assumed that $\partial B_y / \partial x$ and $\partial B_z / \partial x$ vanish along the trajectory of the beam. Furthermore the displacement of the magnetic moment during a precession period is small and thus the contributions of μ_y and μ_z to (8.1) can be disregarded [9]. As a consequence only the x-component of the force, i.e.

$$F_x = \mu_x \frac{\partial B_x}{\partial x}, \tag{8.2}$$

is relevant.

Since $\mu_x$is small, the acting forces are also small and there is the need for long magnets or strong field gradients to obtain a sufficient deflection. If one places a detection screen, to see the deflection of the particles of the beam in the x-direction, one would, based on classical mechanics, expect to detect a continuous spread. However, in the case of the original experiment where silver atoms were used [66], only two clearly distinguishable spots were detected. These spots correspond to particles with magnetic moments,

$$\mu_x = \pm \frac{1}{2} \gamma \mu_{\mathrm{B}},$$

where $\gamma = 2.00232$ is the gyromagnetic ratio and $\mu_{\mathrm{B}} = 9.27 \cdot 10^{-24}\,\mathrm{J/T}$ is the Bohr magneton. To understand the results of the measurement one has to have a closer look to the structure of a silver atom. The nucleus of the atom is surrounded by an electron cloud containing 47 electrons. 46 form a closed inner core, and that core has a total angular momentum equal to zero. Hence, there is no magnetic moment due to the core. The remaining electron has a zero orbital angular momentum. This implies that the only source for this detected angular moment is caused by the intrinsic *spin* of the electron. This experiment shows that the spin of an electron can only have two quantum states, namely a ’plus’-state and a ’minus’-state. For an in-depth quantum mechanical description of the experiment and the observed results, the interested reader is referred to [9].

In the case of clusters, the different rotational, vibrational, electronic quantum states possess different effective dipole moments. The presence of a magnetic field will then induce shifts of the energy states [101], i.e., the Zeeman effect.

8.2 Model and Discretization

To model the Stern–Gerlach magnet, one has to solve the magnetostatic approximation of Maxwell's equation, i.e. (2.8b), with homogeneous Dirichlet conditions on the boundary of Ω. Since the magnet is already in operation, it is desired to keep the current coils and the current outer yoke unchanged. Therefore, they will not be included in the optimization part. The domain under consideration is thus Ω_p, which is further addressed as "the partial domain". The remaining part of Ω_0 will be represented by a magnetic equivalent circuit, which can be interpreted as a reduced order model, and will be coupled to the field by field-circuit coupling [119]. An in-depth discussion of this procedure is beyond the scope of this thesis and the interested reader is referred to [118].

To simulate the partial domain, `GeoPDEs` [56] is used. The domain is split into three patches: one for the left pole, one for the airgap and one for the right pole. The control points and weights defining the shape of the poles will be used as optimization variables later on. The initial internal parametrization has been optimized using the Winslow functional [72]. Deformations of the boundary are automatically translated to the interior by the NURBS. As a consequence, remeshing or manual mesh transformation is unnecessary.

For comparison, the full reference model and the optimized model will also be calculated by using classical finite elements. This will be done in 2D using FEMM [103] and in 3D using CST EM STUDIO® [39]. From the solution of (2.8b), the magnetic field gradient in x-direction $\kappa = \kappa(x,y,z) = \mathrm{d}|\vec{B}(x,y,z)|/\mathrm{d}x$ can be determined. The average magnetic field gradient in Ω_beam,

$$\kappa_\mathrm{av} = \frac{1}{|\Omega_\mathrm{beam}|}\int_{\Omega_\mathrm{beam}} \kappa \,\mathrm{d}\Omega, \tag{8.3}$$

and the inhomogeneity of the field gradient is defined by

$$\epsilon_\mathrm{in} = \sqrt{\frac{1}{|\Omega_\mathrm{beam}|}\int_{\Omega_\mathrm{beam}} \left(\frac{\kappa}{\kappa_\mathrm{av}} - 1\right)^2 \mathrm{d}\Omega}. \tag{8.4}$$

8.3 Optimization

As seen in (8.2), a higher field gradient will lead to a stronger force and thus a larger deflection of the clusters. This implies that, in order to obtain a better resolution, a higher gradient of the magnetic field and a more homogeneous magnetic field gradient is desired. This is especially important since the different levels might be energetically close to each other.

The cost function has to contain two requirements, one for the gradient and one for the inhomogeneity thereof,

$$j(\mathbf{x},\mathbf{y},\mathbf{w}) = \frac{\kappa_\mathrm{w}}{|\kappa_\mathrm{av}(\mathbf{x},\mathbf{y},\mathbf{w})|} + \left(1 - \frac{\kappa_\mathrm{w}}{|\kappa_\mathrm{av}(\mathbf{x},\mathbf{y},\mathbf{w})|}\right)\epsilon_\mathrm{in}(\mathbf{x},\mathbf{y},\mathbf{w}), \tag{8.5}$$

where $\kappa_\mathrm{w} = 8\,\mathrm{T/m}$ is a weighting parameter, chosen in such a way that the gradient is as high as possible without compromising the homogeneity of the field [118]. The vectors $\mathbf{x} = \{x_i\}$, $\mathbf{y} = \{x_i\}$ and $\mathbf{w} = \{w_i\}$ are the geometrical DoFs of the control points (x-coordinate, y-coordinate and weight). Furthermore, the control points $1'$ and $3'$ are coupled in the x-direction to the point 1 and 3 so that an angle of 90° is obtained with the symmetry plane of the magnet (see Figure 8.2).

The optimization problem reads

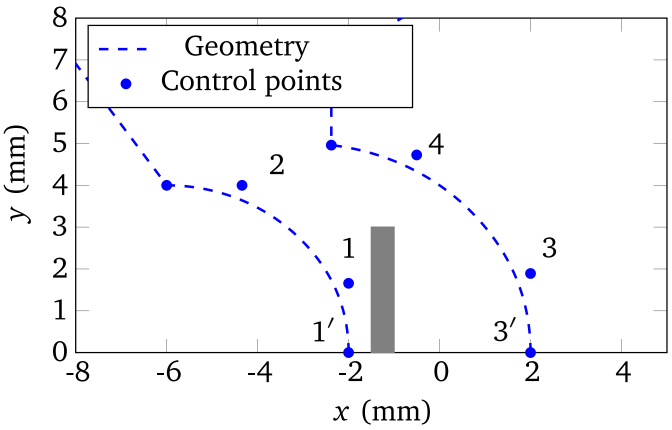

Figure 8.2: Initial geometry of the pole tips of the Stern–Gerlach magnet

Problem 2 *Find* $(\mathbf{x}, \mathbf{y}, \mathbf{w})$ *such that*

$$\min_{\mathbf{x},\mathbf{y},\mathbf{w}} j(\mathbf{x}, \mathbf{y}, \mathbf{w}),$$

while preserving the validity of the geometry, which leads to the following constraints,

$$\begin{aligned}
&x_1 \in [-3.0; -2.0]\,\text{mm}, && y_1 \in [1.66; 2.00]\,\text{mm}, && w_1 = 0.85,\\
&x_2 \in [-5.0; -2.0]\,\text{mm}, && y_2 \in [2.50; 4.50]\,\text{mm}, && w_2 \in [0.35; 2.85],\\
&x_3 \in [+1.5; +2.5]\,\text{mm}, && y_3 \in [1.89; 2.50]\,\text{mm}, && w_3 = 0.87,\\
&x_4 \in [-2.0; +2.0]\,\text{mm}, && y_4 \in [4.00; 5.50]\,\text{mm}, && w_4 \in [0.37; 2.87].
\end{aligned}$$

8.4 Résumé

The Stern-Gerlach will be subjected to an optimization procedure to increase the magnetic field gradient and the homogeneity of the field gradient. The device will be modeled using Iso-Geometric Analysis. The control points describing the shape of the device will be chosen as optimization parameters.

9 Permanent Magnet Synchronous Machine

> “If you want to find the secrets of the universe, think in terms of energy, frequency and vibration.”
>
> *Discussion with Ralph Bergstresser*
> – N. Tesla

The main application of this thesis is the interior Permanent Magnet Synchronous Machine (PMSM) depicted in Figure 9.1. The machine design is based on [115]. It is a three-phase $m = 3$ machine consisting of $N_{\mathrm{pp}} = 3$ pole pairs. It has a double layered distributed winding with two slots per pole per phase. The coils are constructed from copper. The length of the machine is $\ell_z = 10\,\mathrm{cm}$. The machine is constructed of laminated steel. Every pole has one buried NdFeB Permanent Magnet (PM). A detailed description of the geometry and the material properties is found in Appendix A.

The first electrical machines excited with permanent magnets date back to the first part of the 19th century [67]. However, since the quality of the hard magnetic materials was rather poor there was a stronger tendency to electrically excited systems. Further research and development in the late 19th focused on induction machines and led to the introduction of the three-phase alternating current systems and its application for a cage induction motor by Mikhail Dolivo-Dobrowolski. Previous steps to two-phase machines were done by Nikolai Tesla and Galileo Ferraris. Only after the development of AlNiCo magnets in 1932, the use of PMs in electrical machines revived [67]. Starting from the 1960s rare-earth magnets appear more and more in electric machines and since the mid-80s there is the tendency to use NdFeB-magnets. Their application has become more and more popular since they exhibit a high remanent magnetic field combined with a high coercive magnetic field strength [20]. Due to these properties, rare-earth PMSMs achieve a high power density and efficiency [163]. Therefore it is possible to construct more compact machines [125], hence the strong interest for their application in e-mobility. However the production costs of PMSMs are rather high in comparison with other types of electric machines [163] which originates from high material costs of the rare-earth elements. Not only the production costs are a reason to reduce the amount of PM material in PMSMs. There are also environmental arguments. The separation of rare earth elements is known to be very polluting [21]. A reduction in the magnet size, will thus result in a reduction of the ecological footprint. The application of the optimization to the PMSM is discussed in Section 9.6.

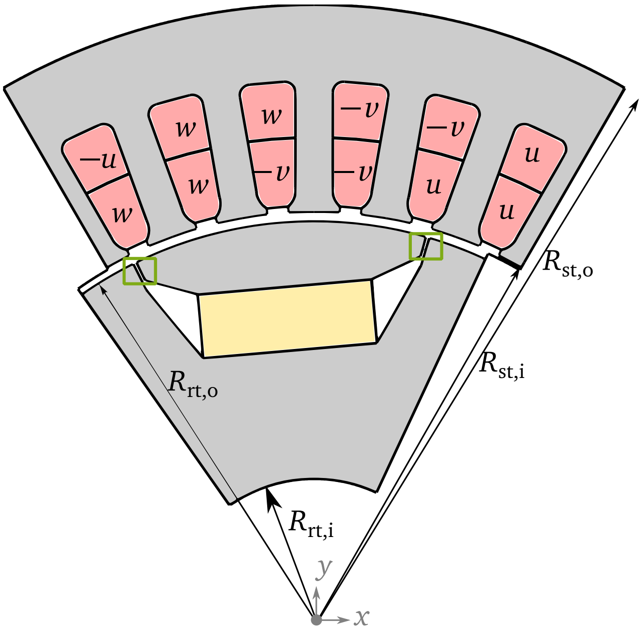

Figure 9.1: One pole of the PMSM. The red regions indicate the copper windings, in yellow the NdFeB-magnet is depicted, the gray regions are constructed from laminated steel and the regions filled with air are shown in white. The green squares depicts the air bridges that mimic the saturated iron bridges. The three phases are indicated by uvw.

Another way to reduce the ecological footprint of electric machine is by constructing more robust machine designs which may for example increase their life span. These robust designs are obtained by studying the impact of uncertainties on the machine properties, such as the generated mechanical torque. The uncertainties may originate from variations in the material properties, the geometry and the applied sources of the machine [35]. In Section 9.5 different types of uncertainties are addressed and their modeling is explained.

Before conducting optimization and uncertainty quantification it is explained which are the important quantities of a PMSM and how they are defined. Also the Park-tranformation is introduced (Section 9.1). To calculate these quantities, one relies on the fields in the machine. In Section 9.2 it is addressed how the fields are obtained. To consider rotation, it is not convenient to calculate the full machine in one piece. Therefore, domain decomposition methods are discussed in Section 9.3. In the section thereafter, the Quantities of Interests (QoIs) and their computation from the fields are discussed.

9.1 Theoretic Background of a Permanent Magnet Synchronous Machines

The three phases in the machine are addressed by u, v, w. All stator windings are connected in series. Let θ depict the electrical angle and $\Theta = \theta / N_{\mathrm{pp}}$ the mechanical angle. The currents are then given by

$$\begin{aligned} I_u &= \hat{I} \cos(\theta), \\ I_v &= \hat{I} \cos\left(\theta - \frac{2\pi}{3}\right), \\ I_w &= \hat{I} \cos\left(\theta + \frac{2\pi}{3}\right), \end{aligned}$$

with $\hat{I}$ the magnitude of the current. For $\theta = 0$ it is assumed that the phase u generates a flux which is aligned with the axis of the PMs. To determine the voltages induced in the coils by the magnetic flux in the machine, one can use the lumped flux-linkage model. The calculation of the Quantities of Interest

(QoIs) rely on the lumped parameters [67]. For an electric machine they can be determined form the magnetic vector potential which is often calculated using finite elements.

9.1.1 Flux-linkage Model

In the flux-linkage model the induced voltages are determined by the fluxes linked to the stator windings. The fluxes are expressed by

$$\begin{bmatrix}\Phi_u\\ \Phi_v\\ \Phi_w\end{bmatrix} = \begin{bmatrix}L_{uu} & L_{uv} & L_{uw}\\ L_{vu} & L_{uu} & L_{vw}\\ L_{wu} & L_{wv} & L_{ww}\end{bmatrix}\begin{bmatrix}I_u\\ I_v\\ I_w\end{bmatrix} + \begin{bmatrix}\cos(\theta)\\ \cos\left(\theta-\frac{2\pi}{3}\right)\\ \cos\left(\theta+\frac{2\pi}{3}\right)\end{bmatrix}\Phi_{\text{pm}}, \tag{9.1}$$

or shortly

$$\mathbf{\Phi}_{uvw} = \mathbf{L}_{uvw}\mathbf{I}_{uvw} + \mathbf{P}_{uvw}\Phi_{\text{pm}}, \tag{9.2}$$

where $\mathbf{\Phi}_{uvw}$ contains the magnetic fluxes, $\mathbf{I}_{uvw}$ depicts the currents, $\mathbf{P}_{uvw}$ corrects for the different phases, Φ_{pm} is the magnetic flux caused by the PMs and $\mathbf{L}_{uvw}$ is the symmetric stator inductance matrix. The entries of the matrix are given by

$$\begin{aligned}
L_{uu} &= L_{\text{self}} + L_{\text{sal}}\cos(2\theta),\\
L_{vv} &= L_{\text{self}} + L_{\text{sal}}\cos\left(2\theta-\frac{2\pi}{3}\right),\\
L_{ww} &= L_{\text{self}} + L_{\text{sal}}\cos\left(2\theta+\frac{2\pi}{3}\right),\\
L_{uv} &= L_{\text{mut}} + L_{\text{sal}}\cos\left(2\theta-\frac{\pi}{3}\right),\\
L_{vw} &= L_{\text{mut}} + L_{\text{sal}}\cos(2\theta),\\
L_{uw} &= L_{\text{mut}} + L_{\text{sal}}\cos\left(2\theta+\frac{2\pi}{3}\right),
\end{aligned}$$

where L_{self} is the average self-inductance of a stator phase, L_{mut} is the average mutual inductance between two phases. L_{sal} is an inductance introduced by the saliency of the rotor. Deriving the fluxes to the time results in the voltages of the stator

$$\begin{bmatrix}U_u\\ U_v\\ U_w\end{bmatrix} = \frac{\mathrm{d}}{\mathrm{d}t}\begin{bmatrix}\Phi_u\\ \Phi_v\\ \Phi_w\end{bmatrix}. \tag{9.3}$$

9.1.2 Park Transformation

Analyzing a PMSM is often based on a two-axis model with constant parameters. The quantities discussed above are transformed in d-q axis components. The *direct* axis (d-axis) is the axis aligned with the geometric center of the magnetic field caused by the magnet under no-load condition (Figure 9.2a). More precisely, there are $2N_{\text{pp}}$ axes that are aligned with the north and south poles of the magnets. The *quadrature* axis (q-axis) are the bisectors of these direct axes. Their components will be indicated by subscripts “d” and “q”. For completeness also the *zero-sequence* component is considered and its components will be depicted by “0”. This transformation is called the *Park* transformation after the person who introduced it [116] and is given by

$$\mathbf{U}_{\mathrm{dq0}} = \begin{bmatrix} U_{\mathrm{d}} \\ U_{\mathrm{q}} \\ U_0 \end{bmatrix} = \underbrace{\frac{2}{3}\begin{bmatrix} \cos(\theta) & \cos\left(\theta - \frac{2\pi}{3}\right) & \cos\left(\theta + \frac{2\pi}{3}\right) \\ -\sin(\theta) & -\sin\left(\theta - \frac{2\pi}{3}\right) & -\sin\left(\theta + \frac{2\pi}{3}\right) \\ \frac{1}{2} & \frac{1}{2} & \frac{1}{2} \end{bmatrix}}_{\mathbf{T}} \begin{bmatrix} U_u \\ U_v \\ U_w \end{bmatrix}, \tag{9.4}$$

and similarly for currents it holds

$$\mathbf{I}_{\mathrm{dq0}} = \mathbf{T}\mathbf{I}_{uvw}. \tag{9.5}$$

The transformation is a mapping of a balanced three-phase system of stator currents in the uvw-frame onto a set of constant currents in the dq0-frame. The electrical angle can be expressed as $\theta = \omega t - \zeta$, with ω the electrical angular frequency and ζ the current reference phase angle. This leads to

$$\left\{\begin{array}{lcl} I_u & = & \hat{I}\cos(\omega t) \\ I_v & = & \hat{I}\cos\left(\omega t - \frac{2\pi}{3}\right) \\ I_w & = & \hat{I}\cos\left(\omega t + \frac{2\pi}{3}\right) \end{array}\right. \quad \text{and} \quad \left\{\begin{array}{lcl} I_{\mathrm{d}} & = & \hat{I}\cos(\zeta) \\ I_{\mathrm{q}} & = & \hat{I}\sin(\zeta) \\ I_0 & = & 0 \end{array}\right. \tag{9.6}$$

This means that the time-dependent currents I_u, I_v, I_w are mapped onto direct currents $I_{\mathrm{d}}, I_{\mathrm{q}}, I_0$.

For the flux-linkage one can write

$$\begin{array}{rcl} \mathbf{\Phi}_{\mathrm{dq0}} & = & \mathbf{T}\mathbf{\Phi}_{uvw}, \\ & = & \mathbf{T}\mathbf{L}_{uvw}\mathbf{I}_{uvw} + \mathbf{T}\mathbf{P}_{uvw}\Phi_{\mathrm{pm}}, \\ & = & \mathbf{T}\mathbf{L}_{uvw}\mathbf{T}^{-1}\mathbf{I}_{\mathrm{dq0}} + \mathbf{T}\mathbf{P}_{uvw}\Phi_{\mathrm{pm}}, \\ & = & \mathbf{L}_{\mathrm{dq0}}\mathbf{I}_{\mathrm{dq0}} + \mathbf{P}_{\mathrm{dq0}}\Phi_{\mathrm{pm}}, \end{array}$$

with

$$\mathbf{L}_{\mathrm{dq0}} = \begin{bmatrix} L_{\mathrm{d}} & 0 & 0 \\ 0 & L_{\mathrm{q}} & 0 \\ 0 & 0 & L_0 \end{bmatrix} \quad \text{and} \quad \mathbf{P}_{\mathrm{dq0}} = \begin{bmatrix} 1 \\ 0 \\ 0 \end{bmatrix}. \tag{9.7}$$

The entries of the inductance matrix are given by

$$\begin{array}{rcl} L_{\mathrm{d}} & = & L_{\mathrm{self}} - L_{\mathrm{mut}} + \frac{3}{2}L_{\mathrm{sal}}, \\ L_{\mathrm{q}} & = & L_{\mathrm{self}} - L_{\mathrm{mut}} - \frac{3}{2}L_{\mathrm{sal}}, \\ L_0 & = & L_{\mathrm{self}} + 2L_{\mathrm{mut}}. \end{array}$$

The relation between the voltages and the flux-linkage can be reformulated to

$$\begin{array}{rcl} \mathbf{U}_{\mathrm{dq0}} & = & \mathbf{T}\mathbf{U}_{uvw}, \\ & = & \mathbf{T}\dfrac{\mathrm{d}\mathbf{\Phi}_{uvw}}{\mathrm{d}t}, \\ & = & \mathbf{T}\dfrac{\mathrm{d}\left(\mathbf{T}^{-1}\mathbf{\Phi}_{\mathrm{dq0}}\right)}{\mathrm{d}t}, \\ & = & \dfrac{\mathrm{d}\mathbf{\Phi}_{\mathrm{dq0}}}{\mathrm{d}t} + \left(\mathbf{T}\dfrac{\mathrm{d}\mathbf{T}^{-1}}{\mathrm{d}t}\right)\mathbf{\Phi}_{\mathrm{dq0}}. \end{array} \tag{9.8}$$

The second term accounts for the motional effects, and it holds that

$$\frac{\mathrm{d}\mathbf{T}^{-1}}{\mathrm{d}t} = \begin{bmatrix} 0 & -\omega & 0 \\ \omega & 0 & 0 \\ 0 & 0 & 0 \end{bmatrix}, \tag{9.9}$$

with $\omega = \mathrm{d}\theta/\mathrm{d}t$.

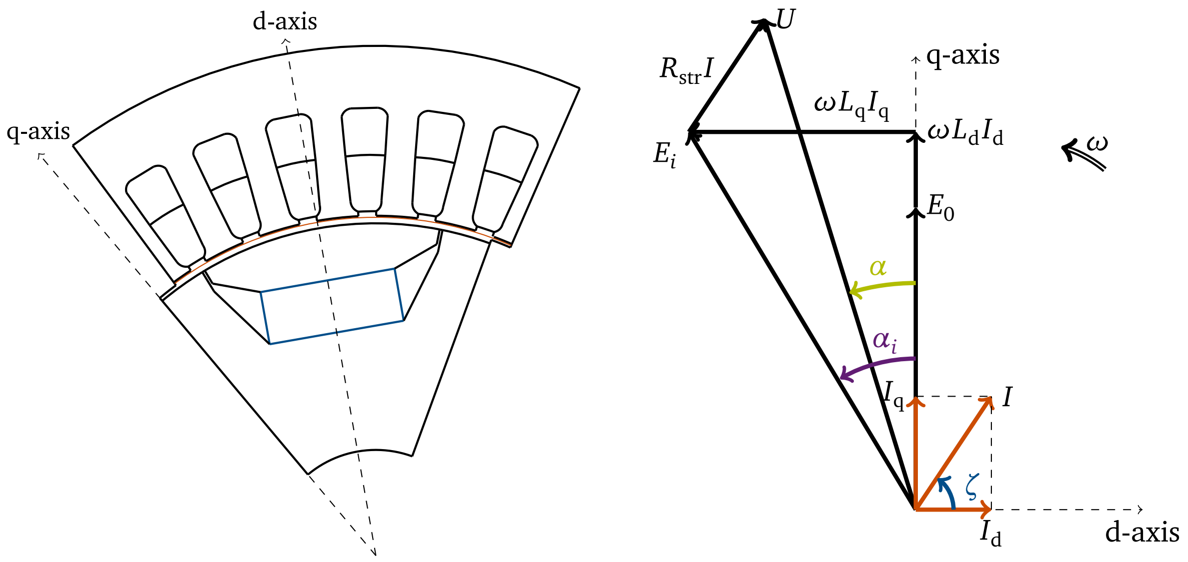

(a) Alignment of the direct and quadrature axis. The red arc depicts the extraction arc for the loading method.

(b) Phasor diagram of the two-axis model of the PMSM.

Figure 9.2: Visualization of the d- and q-axis and the resulting phasor diagram.

9.1.3 Determining Power and Torque in the dq0-Axis Model

Using the Park transformation one can now calculate the torque of the PMSM by relying on the dq0-quantities. The fluxes in the dq0-frame can be expressed as

$$\left\{\begin{array}{lcl} \Phi_\mathrm{d} & = & L_\mathrm{d} I_\mathrm{d} + \Phi_\mathrm{pm}, \\ \Phi_\mathrm{q} & = & L_\mathrm{q} I_\mathrm{q}, \\ \Phi_0 & = & L_0 I_0. \end{array}\right. \tag{9.10}$$

Using (9.8), one finds for the voltages,

$$\left\{\begin{array}{lcl} U_\mathrm{d} & = & R_\mathrm{str} I_\mathrm{d} + L_\mathrm{d}\frac{\mathrm{d}I_\mathrm{d}}{\mathrm{d}t} + \frac{\mathrm{d}\Phi_\mathrm{pm}}{\mathrm{d}t} - \omega L_\mathrm{q} I_\mathrm{q}, \\ U_\mathrm{q} & = & R_\mathrm{str} I_\mathrm{q} + L_\mathrm{q}\frac{\mathrm{d}I_\mathrm{q}}{\mathrm{d}t} + \omega L_\mathrm{d} I_\mathrm{d} + \omega \Phi_\mathrm{pm}, \\ U_0 & = & R_\mathrm{str} I_0 + L_0\frac{\mathrm{d}I_0}{\mathrm{d}t}, \end{array}\right. \tag{9.11}$$

where the first term represents the resistive drop in the stator windings and R_str is the resistance of a single winding. During stationary operation the equations reduce to

$$\left\{\begin{array}{lcl} U_\mathrm{d} & = & R_\mathrm{str} I_\mathrm{d} - \omega L_\mathrm{q} I_\mathrm{q}, \\ U_\mathrm{q} & = & R_\mathrm{str} I_\mathrm{q} + \omega L_\mathrm{d} I_\mathrm{d} + \omega \Phi_\mathrm{pm}, \\ U_0 & = & R_\mathrm{str} I_0. \end{array}\right. \tag{9.12}$$

Since the applied excitation is a symmetric three-phase excitation, it holds that $I_0 = 0\,\mathrm{A}$ and one can neglect the third equation. The third term in the second equation is the voltage induced in the coils by the magnets. This quantity is called the Electromotive Force (EMF), E_0. Using a phasor diagram (Figure 9.2b) the phase voltage is then given by

$$\underline{U} = U_\mathrm{d} + \jmath U_\mathrm{q} = R_\mathrm{str}\underbrace{\left(I_\mathrm{d} + \jmath I_\mathrm{q}\right)}_{\underline{I}} + \jmath\omega\left(L_\mathrm{d} I_\mathrm{d} + \jmath L_\mathrm{q} I_\mathrm{q}\right) + \jmath E_0. \tag{9.13}$$

The power put into the stator windings is given by

$$P = \frac{3}{2}U_\mathrm{d}I_\mathrm{d} + \frac{3}{2}U_\mathrm{q}I_\mathrm{q} + 3U_0I_0.$$

Using (9.11) one gets

$$P = \underbrace{\frac{3}{2}R_\mathrm{str}\left(I_\mathrm{d}^2 + I_\mathrm{q}^2 + 2I_0^2\right)}_{P_\mathrm{l}} + \underbrace{\frac{3}{2}\frac{\mathrm{d}}{\mathrm{d}t}\left(\frac{1}{2}L_\mathrm{d}I_\mathrm{d}^2 + \frac{1}{2}L_\mathrm{q}I_\mathrm{q}^2 + L_0I_0\right)}_{P_\mathrm{e}} + \frac{3}{2}I_\mathrm{d}\frac{\mathrm{d}\Phi_\mathrm{pm}}{\mathrm{d}t} + \underbrace{\frac{3}{2}\omega\left(\Phi_\mathrm{pm} + \left(L_\mathrm{d} - L_\mathrm{q}\right)I_\mathrm{d}\right)I_\mathrm{q}}_{P_\mathrm{m}}.$$

The first term depicts the Joule losses in the windings. The second term is the power causing an increase of magnetic energy in the PMSM. The third term depicts the change of magnetic flux from the magnets. This term will be put to zero, since it is assumed that the flux of the magnets remains the same. The last term is the amount of power transformed into mechanical power. From the mechanical power, the mechanical torque can be determined

$$\tau_\mathrm{m} = \frac{P_\mathrm{m}}{\omega_\mathrm{m}} = \frac{N_\mathrm{pp}P_\mathrm{m}}{\omega} = \frac{3}{2}N_\mathrm{pp}\Phi_\mathrm{pm}I_\mathrm{q} + \frac{3}{2}N_\mathrm{pp}\left(L_\mathrm{d} - L_\mathrm{q}\right)I_\mathrm{d}I_\mathrm{q}, \tag{9.14}$$

where the mechanical angular frequency is introduced and defined as $\omega_\mathrm{m} = \omega/N_\mathrm{pp}$. The mechanical torque consists of two contributions. The first term is the *synchronous* torque τ_syn and the second term is the *reluctance* torque τ_rel. The efficiency of a machine is given by

$$\epsilon = \frac{P_\mathrm{m}}{P_\mathrm{m} + P_\mathrm{l}}. \tag{9.15}$$

If one knows the lumped parameters and induced voltages, one is able to determine the torque of the machine. The lumped parameters and the voltages are determined by numerical simulation of the machine. In the Section 9.2 it is discussed how the Magnetic Vector Potential (MVP) over the computational domain is determined by finite element analysis.

9.2 Modeling and Discretization

The machine will be simulated by using the classical Finite Element method (FEM) and Iso-Geometric Analysis (IGA). On the outer radius of the stator $R_\mathrm{st,o}$ and on the inner radius of the rotor $R_\mathrm{rt,i}$ homogeneous Dirichlet conditions are imposed. To comply with the symmetry of the machine, anti-periodic boundary conditions are imposed on the left and right side of the machine. In the case where the full machine has to be simulated, e.g. when uncertainties break the symmetry of the machine, the central region is added to the simulation and modeled as air to mimic the stainless steel shaft that mounts the rotor. Obviously, no boundary conditions are then imposed on the inner radius of the rotor.

The small iron bridges in the rotor are replaced by air bridges, marked by the green square in Figure 9.1, to mimic the saturation of steel and to avoid the need for non-linear finite element solves.

The values to model the material properties are listed in Table 9.1. Note that the lamination of the steel sheets is accounted for by applying a zero conductivity and that the conductors are modeled with zero conductivity, since the strands have diameters below the skin depth.

The physics in the machine can be modeled by using the magnetostatic approximation of Maxwell's equations. For cylindrical machines with lengths comparable to or larger than their diameters, 2D field models are typically used to calculate the major machine parameters up to an accuracy that is sufficient in practice. Therefore, the Maxwell equations reduce to the Poisson's equation mentioned in (2.8b). In the case the simulation is performed using classical FEM, the construction of the geometry and the

Table 9.1: Parameters describing the material properties of the PMSM.

Material properties		
Conductivity of iron	σ_{Fe}	0 S/m
Conductivity of copper	σ_{Cu}	0 S/m
Conductivity of PM	σ_{PM}	6667 S/m
Relative permeability of iron	$\mu_{\mathrm{r,Fe}}$	500
Relative permeability of copper	$\mu_{\mathrm{r,Cu}}$	1
Relative permeability of PM	$\mu_{\mathrm{r,PM}}$	1.05
Remanent magnetic field of PM	B_{r}	0.94 T

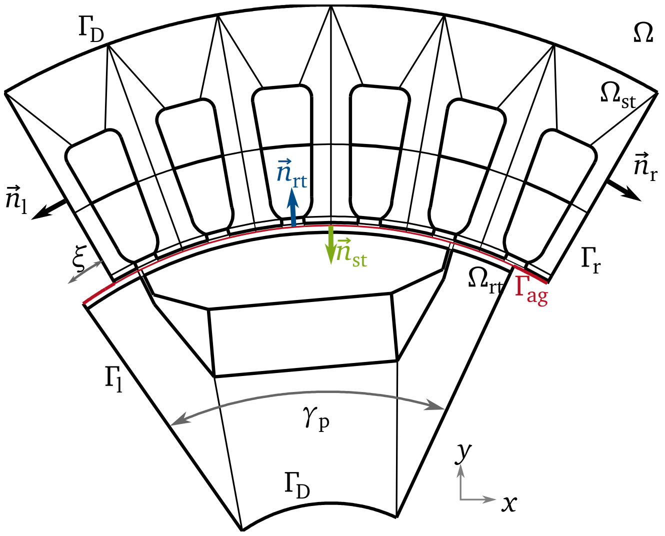

Figure 9.3: Cross-sectional view of one pole of the PMSM. The thick lines indicate the geometry, the thin lines indicate the boundaries of the different patches. The quantities important for solving the coupled problem are indicated.

generation of the mesh is done using `FEMM` [103] and `TRIANGLE` [135]. To simulate the machine with IGA the full computational domain is decomposed in two subdomains, Ω_{st} connected to the stator and Ω_{rt} connected to the rotor. Both subdomains are independently constructed with different patches as shown in Figure 9.3. In the airgap the patches from the stator and the rotor side are not conforming on Γ_{ag}. The coupling between the two domains is discussed in Section 9.3. The simulation of the machine with IGA is performed using `GeoPDEs` [56]. In both cases, the Ritz-Galerkin approach is applied and one finally solves the linear system of equations

$$\mathbf{K}\mathbf{a} = \mathbf{j},$$

where $\mathbf{a}$, the degrees of freedom, depicts the discretized MVP and the right-hand side $\mathbf{j}$ is the discretized counterpart of the sources, which in this application are the applied currents in the windings and the magnetization of the PMs.

9.3 Domain Decomposition Methods

Sometimes it is not convenient to simulate an electric machine in one piece with one mesh. This can be caused by the topology, the presence of different materials or the use of non-conforming meshes at a certain interface in the machine. As mentioned previously, in the simulation of IGA non-conforming patches are introduced. Therefore, the full computational domain is subdivided along a circular arc

$\Gamma_{\mathrm{ag}} = \overline{\Omega}_{\mathrm{rt}} \cap \overline{\Omega}_{\mathrm{st}}$ in the airgap which separates the domain associated with the rotor Ω_{rt} from the domain associated with the stator Ω_{st} (Figure 9.3).

Poison's equation, given in (2.8b), transforms into

$$\begin{cases} -\nabla\cdot\left(\nu\nabla A_{z,q}\right) &= J_{z,q} \qquad \text{in } \Omega_q,\\ A_{z,q}|_{\Gamma_{\mathrm{D}}} &= 0,\\ A_{z,q}|_{\Gamma_{\mathrm{l}}} &= -A_{z,q}|_{\Gamma_{\mathrm{r}}},\\ \nu\nabla A_{z,q}|_{\Gamma_{\mathrm{l}}}\cdot\vec{n}_{\mathrm{l}} &= \nu\nabla A_{z,q}|_{\Gamma_{\mathrm{r}}}\cdot\vec{n}_{\mathrm{r}},\\ A_{z,\mathrm{rt}}|_{\Gamma_{\mathrm{ag}}} &= A_{z,\mathrm{st}}|_{\Gamma_{\mathrm{ag}}},\\ \nu\nabla A_{z,\mathrm{rt}}|_{\Gamma_{\mathrm{ag}}}\cdot\vec{n}_{\mathrm{st}} &= \nu\nabla A_{z,\mathrm{st}}|_{\Gamma_{\mathrm{ag}}}\cdot\vec{n}_{\mathrm{st}}, \end{cases} \tag{9.16}$$

where $q \in \{\mathrm{rt}, \mathrm{st}\}$ and $\vec{n}_{\mathrm{st}}$ is a unit vector perpendicular to the airgap interface directed from stator to rotor. The continuity of the MVP and the continuity of the azimuthal component $H_\theta = \nu\nabla A_{z,\mathrm{rt}}|_{\Gamma_{\mathrm{ag}}}\cdot\vec{n}_{\mathrm{st}}$ of the magnetic field strength is imposed by the last two equations. In the following distinct ways to set up this stator-rotor coupling are discussed.

9.3.1 Iterative Substructuring

A first way to accomplish the coupling is an iterative substructuring coupling scheme. It invokes a Dirichlet-to-Neumann (D-N) map from the first domain, here Ω_{rt}, followed by a Neumann-to-Dirichlet (N-D) map for the second domain, here Ω_{st}. The explanation of the procedure is based on [123]. The decomposition in (9.16) is handled in an iterative manner. Let λ^0 be an initial value for the solution for the MVP at Γ_{ag} and let k be an indicator for the iteration steps. Then Poisson's problem is first solved for the rotor taking λ^k as a Dirichlet boundary condition at Γ_{ag},

$$\begin{cases} -\nabla\cdot\left(\nu\nabla A^{k+1}_{z,\mathrm{rt}}\right) &= J_z \qquad \text{in } \Omega_{\mathrm{rt}},\\ A^{k+1}_{z,\mathrm{rt}}|_{\Gamma_{\mathrm{D}}} &= 0,\\ A^{k+1}_{z,\mathrm{rt}}|_{\Gamma_{\mathrm{l}}} &= -A^{k+1}_{z,\mathrm{rt}}|_{\Gamma_{\mathrm{r}}},\\ \nu\nabla A^{k+1}_{z,\mathrm{rt}}|_{\Gamma_{\mathrm{l}}}\cdot\vec{n}_{\mathrm{l}} &= \nu\nabla A^{k+1}_{z,\mathrm{rt}}|_{\Gamma_{\mathrm{r}}}\cdot\vec{n}_{\mathrm{r}},\\ A^{k+1}_{z,\mathrm{rt}}|_{\Gamma_{\mathrm{ag}}} &= \lambda^k. \end{cases} \tag{9.17}$$

Solving this gives the Neumann data $\nu\nabla A^{k+1}_{z,\mathrm{rt}}|_{\Gamma_{\mathrm{ag}}}\cdot\vec{n}_{\mathrm{st}}$. Afterwards Poisson's problem is solved for the stator enforcing the newly retrieved Neumann data at Γ_{ag}, i.e.,

$$\begin{cases} -\nabla\cdot\left(\nu\nabla A^{k+1}_{z,\mathrm{st}}\right) &= J_z \qquad \text{in } \Omega_{\mathrm{st}},\\ A^{k+1}_{z,\mathrm{st}}|_{\Gamma_{\mathrm{D}}} &= 0,\\ A^{k+1}_{z,\mathrm{st}}|_{\Gamma_{\mathrm{l}}} &= -A^{k+1}_{z,\mathrm{st}}|_{\Gamma_{\mathrm{r}}},\\ \nu\nabla A^{k+1}_{z,\mathrm{st}}|_{\Gamma_{\mathrm{l}}}\cdot\vec{n}_{\mathrm{l}} &= \nu\nabla A^{k+1}_{z,\mathrm{st}}|_{\Gamma_{\mathrm{r}}}\cdot\vec{n}_{\mathrm{r}},\\ \nu\nabla A^{k+1}_{z,\mathrm{st}}|_{\Gamma_{\mathrm{ag}}}\cdot\vec{n}_{\mathrm{st}} &= \nu\nabla A^{k+1}_{z,\mathrm{rt}}|_{\Gamma_{\mathrm{ag}}}\cdot\vec{n}_{\mathrm{st}}, \end{cases} \tag{9.18}$$

from which the Dirichlet data is updated by

$$\lambda^{k+1} = \gamma A^{k+1}_{z,\mathrm{st}} + (1-\gamma)\lambda^k, \tag{9.19}$$

with $\gamma \in [0,1]$ a relaxation parameter. The relaxation factor is required to guarantee the convergence of the iterative substructuring approach [123]. The iterations continue until a stopping criterion is fulfilled. This criterion should be lower then a user-defined tolerance and is given by the relative L^2 errors of two successive iterations for the stator and rotor domain, i.e.,

$$\epsilon_{\mathrm{rt}} = \left\|A^{k+1}_{z,\mathrm{rt}} - A^{k}_{z,\mathrm{rt}}\right\|_{L^2(\Omega_{\mathrm{rt}})} \Big/ \left\|A^{k+1}_{z,\mathrm{rt}}\right\|_{L^2(\Omega_{\mathrm{rt}})} < \texttt{tol}, \quad \text{and} \tag{9.20}$$

$$\epsilon_{\mathrm{st}} = \left\|A^{k+1}_{z,\mathrm{st}} - A^{k}_{z,\mathrm{st}}\right\|_{L^2(\Omega_{\mathrm{st}})} \Big/ \left\|A^{k+1}_{z,\mathrm{st}}\right\|_{L^2(\Omega_{\mathrm{st}})} < \texttt{tol}. \tag{9.21}$$

In the following chapters the full iterative scheme will be addressed as D-N.

9.3.2 Harmonic Stator-Rotor Coupling

Another coupling method has been introduced in [42] and can be interpreted as a sliding surface method where mortaring is used to conduct the coupling [12]. Let us introduce two polar coordinates systems, one is connected to the stator (r, θ) and one connected to the rotor (r, θ'). Let ξ depict the angular displacement of the rotor domain with respect to the stator domain, such that $\theta' = \theta - \xi$. On the interface the following conditions must hold,

$$\begin{cases} A_{z,\mathrm{st}}|_{\Gamma_{\mathrm{ag}}}(\theta) & = A_{z,\mathrm{rt}}|_{\Gamma_{\mathrm{ag}}}(\theta - \xi), \\ H_{\theta,\mathrm{st}}(\theta) & = H_{\theta,\mathrm{rt}}(\theta - \xi), \end{cases} \tag{9.22}$$

such that the continuity still holds. Now the basis functions to express $H_{\theta,\mathrm{st}}(\theta)$ and $H_{\theta,\mathrm{rt}}(\theta')$ are chosen to be a superposition of harmonic functions [42],

$$H_{\theta,\mathrm{st}}(\theta) = \sum_{\ell \in L} \lambda_{\mathrm{st},\ell} e^{-\imath \ell \theta}, \tag{9.23}$$

$$H_{\theta,\mathrm{rt}}(\theta') = \sum_{\ell \in L} \lambda_{\mathrm{rt},\ell} e^{-\imath \ell \theta'}, \tag{9.24}$$

with as degrees of freedom on Γ_{ag} the Fourier coefficients $\lambda_{\mathrm{st},\ell}$ and $\lambda_{\mathrm{rt},\ell}$. The set of N_Γ harmonics is depicted by L. It contains all harmonic orders ℓ for which the harmonic functions $e^{-\imath\ell\theta}$ and $e^{-\imath\ell\theta'}$ fulfill the anti-periodic boundary conditions on Γ_{l} and Γ_{r}. Depicting the angular extend of the pole by γ_{p}, this property can be written as $e^{-\imath\ell\theta} = -e^{-\imath\ell(\theta+\gamma_{\mathrm{p}})}$. Thanks to the choice of harmonic trial functions, it is possible to construct a conforming discretization for $H_{\theta,\mathrm{st}}$ and $H_{\theta,\mathrm{rt}}$ at Γ_{ag}, which enables an easier handling of the tangential continuity of the field strength in a strong way. This leads to

$$\lambda_{\mathrm{st},\ell} = r_{\ell\ell}(\xi) \lambda_{\mathrm{rt},\ell}, \tag{9.25}$$

in which the phase shifts $r_{\ell\ell}(\xi) = e^{\imath\ell\xi}$ are gathered in the rotation matrix $\mathbf{R}(\xi)$ such that (9.25) can be shortly written as $\boldsymbol{\lambda}_{\mathrm{st}} = \mathbf{R}(\xi)\boldsymbol{\lambda}_{\mathrm{rt}}$.

Applying the discretization discussed in Section 3.3 on the Poisson equation for the rotor and stator domain leads to

$$\mathbf{K}_{\mathrm{st}}\mathbf{a}_{\mathrm{st}} + \mathbf{h}_{\mathrm{st}} = \mathbf{j}_{\mathrm{st}}, \tag{9.26}$$

$$\mathbf{K}_{\mathrm{rt}}\mathbf{a}_{\mathrm{rt}} + \mathbf{h}_{\mathrm{rt}} = \mathbf{j}_{\mathrm{rt}}, \tag{9.27}$$

where the extra terms $\mathbf{h}_{\mathrm{st}}$ and $\mathbf{h}_{\mathrm{rt}}$ are given by [42],

$$h_{\mathrm{st},i} = -\int_{\Gamma_{\mathrm{ag}}} H_{\theta,\mathrm{st}}(\theta) w_i(\theta)\, \mathrm{d}\theta, \tag{9.28}$$

$$h_{\mathrm{rt},i} = \int_{\Gamma_{\mathrm{ag}}} H_{\theta,\mathrm{rt}}(\theta') w_i(\theta')\, \mathrm{d}\theta'. \tag{9.29}$$

Discretizing $H_{\theta,\mathrm{st}}$ and $H_{\theta,\mathrm{rt}}$ by harmonic functions leads to

$$\mathbf{h}_{\mathrm{st}} = \mathbf{G}_{\mathrm{st}}\mathbf{R}(\xi)\boldsymbol{\lambda}_{\mathrm{rt}}, \tag{9.30}$$

$$\mathbf{h}_{\mathrm{rt}} = \mathbf{G}_{\mathrm{rt}}\boldsymbol{\lambda}_{\mathrm{rt}}, \tag{9.31}$$

where $\mathbf{G}_{\mathrm{st}}$ and $\mathbf{G}_{\mathrm{rt}} \in \mathbb{R}^{N_\Gamma \times N_{\mathrm{DoF}}}$ are coupling matrices containing the integrals

$$g_{\mathrm{st},i\ell} = -\int_{\Gamma_{\mathrm{ag}}} e^{-\imath\ell\theta} w_i(\theta)\,\mathrm{d}\theta, \tag{9.32}$$

$$g_{\mathrm{rt},i\ell} = \int_{\Gamma_{\mathrm{ag}}} e^{-\imath\ell\theta'} w_i(\theta')\,\mathrm{d}\theta'. \tag{9.33}$$

One has to note that these integrals combine IGA basis functions and harmonic functions, which is similar to the mortar method [12]. The Harmonic Stator-Rotor Coupling (HS-RC) method can thus be interpreted as a special kind of mortar method, in which the space of the Lagrange multipliers is exchanged by a space spanned by harmonic functions. A profound discussion of the mortar method is beyond the scope of this thesis, but interested readers are referred to [32] for an application with finite elements and to [30] for an application in the IGA setting.

The continuity of the magnetic vector potential at the airgap interface is imposed in a weak sense, meaning that the complex conjugate of the harmonic functions are used as test functions. This gives [42],

$$-\mathbf{R}(\xi)\mathbf{G}_{\mathrm{st}}^H\mathbf{a}_{\mathrm{st}} + \mathbf{G}_{\mathrm{rt}}^H\mathbf{a}_{\mathrm{rt}} = 0, \tag{9.34}$$

where the Hermitian transposes of the already calculated matrices have to included.

Finally, combining (9.26), (9.27) and (9.34) leads to the saddle-point problem

$$\begin{bmatrix} \mathbf{K} & \mathbf{G}^H(\xi) \\ \mathbf{G}(\xi) & 0 \end{bmatrix}\begin{bmatrix} \mathbf{A}(\xi) \\ \boldsymbol{\lambda}_{\mathrm{rt}} \end{bmatrix} = \begin{bmatrix} \mathbf{J} \\ 0 \end{bmatrix}, \tag{9.35}$$

with the blocks

$$\mathbf{K} = \begin{bmatrix} \mathbf{K}_{\mathrm{rt}} & 0 \\ 0 & \mathbf{K}_{\mathrm{st}} \end{bmatrix}, \quad \mathbf{G}(\xi) = \begin{bmatrix} -\mathbf{R}(\xi)\mathbf{G}_{\mathrm{st}}^H & \mathbf{G}_{\mathrm{rt}}^H \end{bmatrix}, \quad \mathbf{A}(\xi) = \begin{bmatrix} \mathbf{a}_{\mathrm{st}}(\xi) \\ \mathbf{a}_{\mathrm{rt}}(\xi) \end{bmatrix}, \quad \mathbf{J} = \begin{bmatrix} \mathbf{j}_{\mathrm{st}} \\ \mathbf{j}_{\mathrm{rt}} \end{bmatrix}.$$

The saddle point poblem in (9.35) might become instable when the number of harmonics N_Γ used to effectuate the coupling is too big with respect to N_{DoF} [29]. Stability of the system is assured if it satisfies the *inf–sup* condition [10]. One way to numerically verify this condition is determining the *inf–sup constant* ς following the method in [33]. Consider the eigenvalue problem

$$\mathbf{G}^H\mathbf{K}^{-1}\mathbf{G}\mathbf{x} = \eta^2\mathbf{M}\mathbf{x}, \tag{9.36}$$

with

$$m_{\ell k} = \int_{\Gamma_{\mathrm{ag}}} e^{-jk\theta} e^{j\ell\theta}\,\mathrm{d}\Gamma. \tag{9.37}$$

Given the sequence of eigenvalues η_i found by solving (9.36), the inf-sup constant is given

$$\varsigma = \min_i \eta_i. \tag{9.38}$$

The saddle-point problem is considered stable if ς is bounded away from zero. It has to be noted that for determining the eigenvalues the L^2-norm (see Section 3.1) is considered in this work. The appropriate norm however should stem from $H^{1/2}$ [33].

9.3.3 Locked Step Method

Alternatively, one can enforce a conforming mesh at the interface. One example is a pseudo time-stepping technique, sometimes addressed as a locked step method, [120]. It is a method for considering the rotation of the rotor in an electric machine. This method can be categorized as a sliding surface method, but with a conforming mesh at the interface. The nodes on Γ_{ag} have to be distributed equidistantly. The time-step has to be chosen so that the rotor domain is rotated by exactly $n \in \mathbb{N}$ nodes between successive time-steps. For every time-step or angle ($\xi = \xi(t)$) the connections between the nodes on Γ_{ag} have to be updated. This means that at every angle, the mesh remains conforming and thus the last equation in (9.16) is always automatically fulfilled.

The system of equations read as

$$\begin{bmatrix} \mathbf{K}_{\mathrm{st}} & 0 & \mathbf{P}_{\mathrm{st}} \\ 0 & \mathbf{K}_{\mathrm{rt}} & \mathbf{P}_{\mathrm{rt}}(\xi) \\ \mathbf{P}_{\mathrm{st}}^{\top} & \mathbf{P}_{\mathrm{rt}}^{\top}(\xi) & 0 \end{bmatrix} \begin{bmatrix} \mathbf{a}_{\mathrm{st}}(\xi) \\ \mathbf{a}_{\mathrm{rt}}(\xi) \\ \boldsymbol{\lambda} \end{bmatrix} = \begin{bmatrix} \mathbf{j}_{\mathrm{rt}}(\xi) \\ \mathbf{j}_{\mathrm{st}}(\xi) \\ 0 \end{bmatrix}, \tag{9.39}$$

where the last row and the last column ensures that $A_{z,\mathrm{rt}}|_{\Gamma_{\mathrm{ag}}} = A_{z,\mathrm{st}}|_{\Gamma_{\mathrm{ag}}}$ and in which the Lagrange multipliers $\boldsymbol{\lambda}$ and the matrices $\mathbf{P}_{\mathrm{st}}$ and $\mathbf{P}_{\mathrm{rt}} \in \{-1, 0, 1\}^{N_{\mathrm{DoF}}}$ are introduced.

9.4 Calculation of the Quantities of Interest

Previously, the quantities of interest, i.e. the EMF and the torque, have been introduced. It has been shown how the mechanical torque of the machine can be calculated from lumped parameters and how the system of equations are influenced by applying a domain decomposition. In this section it is explained how the lumped parameters and the induced voltages are calculated from the MVP obtained by the finite element method.

9.4.1 Loading Method

Applying the loading method [125] enables the calculation of the parameters under load conditions. Solving (an approximation of) Maxwell's equations (e.g. (2.8b)) gives the magnetic vector potential over the computational domain. The main idea of the loading method is to perform a Fourier analysis on the magnetic vector potentials $A_z(R_{\mathrm{ct}}, \theta)$ on an arc connected to the inner surface of the stator, i.e. $R_{\mathrm{ct}} \approx R_{\mathrm{st,i}}$. In Figure 9.2a this arc is depicted in red. On that arc the magnetic vector potential is decomposed in a Fourier series,

$$A_z(R_{\mathrm{ct}}, \theta) = \sum_{n=1}^{\infty} a_n(A_z)\cos(nN_{\mathrm{pp}}\theta) + b_n(A_z)\sin(nN_{\mathrm{pp}}\theta),$$

with a_n and b_n the Fourier coefficients. Introducing $A_n = A_n(A_z) = \sqrt{a_n^2(A_z) + b_n^2(A_z)}$ and writing

$$\Phi_n(A_z) = 2\ell_z A_n, \tag{9.40}$$

then the magnetic airgap flux is found for $n = 1$ where it holds that the coefficient a_1 corresponds to half the q-axis flux and the coefficient b_1 corresponds to half the d-axis flux [125]. The inner torque angle α_i is determined by

$$\alpha_i(A_z) = \arctan\left(\frac{b_1(A_z)}{a_1(A_z)}\right).$$

When the machine rotates at synchronous speed, the flux will induce a voltage in each stator winding, given by

$$E_{i,1}(A_z) = \frac{\omega}{\sqrt{2}} N_{\mathrm{wd}} k_{\mathrm{wd},1} \Phi_1(A_z),$$

where N_{wd} is the number of windings per phase and $k_{\mathrm{wd},1}$ are the winding factors for $n = 1$. Generally these factors are given by [67]

$$k_{\mathrm{wd},n} = \underbrace{\frac{\sin\left(q\frac{n\alpha_{\mathrm{el}}}{2}\right)}{q\sin\left(\frac{n\alpha_{\mathrm{el}}}{2}\right)}}_{1.} \underbrace{\sin\left(\frac{n\pi}{2}\frac{\gamma_{\mathrm{c}}}{\gamma_{\mathrm{p}}}\right)}_{2.} \underbrace{\frac{\sin\left(\frac{n\eta}{2}\right)}{\frac{n\eta}{2}}}_{3.}$$

where q denotes the coil sides per phase belt, α_{el} the electrical angle between two slots, γ_{c} and γ_{p} depict, respectively, the coil and pole pitch and η the skewing angle. The winding factors can be interpreted as correcting factors taking into account

1. the distribution of the windings in different slots,
2. the coil shortening,
3. the skewing of the stator slots.

Now that the induced voltage has been determined, one can rely on the phasor diagram in Figure 9.2b and determine the direct inductance L_{d} using

$$E_{i,1}(A_z)\sin(\alpha_i(A_z)) = \omega L_{\mathrm{d}} I_{\mathrm{d}}.$$

The quadrature inductance L_{q} is found by

$$E_{i,1}(A_z)\cos(\alpha_i(A_z)) = \omega L_{\mathrm{q}} I_{\mathrm{q}} + E_0(A_z).$$

The EMF is calculated under no-load condition. This implies that I_{d} and I_{q} are both zero and as a consequence $\alpha_i = 0$. This implies that $b_1(A_z) = 0$. The EMF is then calculated by

$$E_0(A_z) = E_{i,1}(A_z) = \sqrt{2}\omega N_{\mathrm{wd}} k_{\mathrm{wd},1} \ell_z a_1(A_z)$$

and thus linearly dependents on the coefficient a_1. All lumped parameters and induced voltages are now determined. From them the torque can be calculated, one writes $\tau(A_z)$.

To measure the occurrence of undesired higher harmonics on the EMF, the Total Harmonic Distortion (THD) is introduced

$$\mathrm{THD}_{E_0} = \frac{\sqrt{\sum_{n=2}^{\infty} E_{i,n}^2(A_z)}}{E_0(A_z)}.$$

9.4.2 Energy Balance Method

Another method to determine the torque is the energy balance method. The method relies on the principle of conservation of energy [110] and needs the explicit rotation of the rotor. Using finite elements, the implementation of the rotation is easily handled by the time stepping method of Section 9.3.3.

The change in magnetic energy at a time step t is given by

$$\frac{\mathrm{d}W(\mathbf{a}(t))}{\mathrm{d}t} = P_{\mathrm{e}}(\mathbf{a}(t)) - P_{\mathrm{l}}(t) - P_{\mathrm{m}}(\mathbf{a}(t)), \tag{9.41}$$

with P_e the electrical energy, P_l the losses and P_m the mechanical energy. The torque can be calculated by a time-averaging approach. Therefore the right hand side is integrated over one full period T, i.e. one full rotation of the rotor. Conservation of energy means that $W(\mathbf{a}(t)) = W(\mathbf{a}(t+T))$, and thus

$$\underbrace{\frac{1}{T}\int_0^T P_\mathrm{m}(\mathbf{a}(t))\,\mathrm{d}t}_{\bar{P}_\mathrm{m}} = \underbrace{\frac{1}{T}\int_0^T P_\mathrm{e}(\mathbf{a}(t))\,\mathrm{d}t}_{\bar{P}_\mathrm{e}} - \underbrace{\frac{1}{T}\int_0^T P_\mathrm{l}(t)\,\mathrm{d}t}_{\bar{P}_\mathrm{l}}.$$

The average electrical energy is calculated from the applied currents

$$\bar{P}_\mathrm{e} = \frac{1}{T}\int_0^T \mathbf{u}_\mathrm{str}^\top(\mathbf{a}(t))\mathbf{i}_\mathrm{str}(t)\,\mathrm{d}t,$$

$\mathbf{u}_\mathrm{str}$ and $\mathbf{i}_\mathrm{str}$ represent respectively, the voltages and currents in the coils. The currents are related to the source currents by $\mathbf{j}_\mathrm{scr}(t) = \mathbf{X}_\mathrm{str}\mathbf{i}_\mathrm{str}(t)$, where $\mathbf{X}_\mathrm{str}$ is a winding as introduced in [134]. The voltages are defined by

$$\mathbf{u}_\mathrm{str}(\mathbf{a}(t)) = \mathbf{R}_\mathrm{str}\mathbf{i}_\mathrm{str}(t) + \frac{\mathrm{d}\left(\mathbf{X}_\mathrm{str}^\top\mathbf{a}(t)\right)}{\mathrm{d}t},$$

where $\mathbf{R}_\mathrm{str}$ is the DC resistance of the coils. The time averaged losses read as

$$\bar{P}_\mathrm{l} = \frac{1}{T}\int_0^T \mathbf{i}_\mathrm{str}^\top(t)\mathbf{R}_\mathrm{str}\mathbf{i}_\mathrm{str}(t)\,\mathrm{d}t.$$

The time averaged mechanical energy is

$$\bar{P}_\mathrm{m} = \frac{1}{T}\int_0^T \left(P_\mathrm{e}(\mathbf{a}(t)) - P_\mathrm{l}(t)\right)\,\mathrm{d}t,$$

from which the time averaged torque can be calculated

$$\bar{\tau}_1 = \frac{1}{T}\int_0^T \tau_\mathrm{m}(\mathbf{a}(t))\,\mathrm{d}t := \frac{1}{T\omega_\mathrm{m}}\int_0^T P_\mathrm{m}(\mathbf{a}(t))\,\mathrm{d}t,$$

where ω_m is enforced to be constant. Calculation of the higher harmonics of the torque is based on (9.41), namely

$$\tau_\mathrm{m}(\mathbf{a}(t)) = \frac{1}{\omega_\mathrm{m}}\left(P_\mathrm{e}(\mathbf{a}(t)) - P_\mathrm{l}(t) - \frac{\mathrm{d}W(\mathbf{a}(t))}{\mathrm{d}t}\right),$$

where the magnetic energy is given by $W(t) = {}^1\!/_2\mathbf{a}^\top(t)\mathbf{K}(t)\mathbf{a}(t)$. Due to the symmetry of the machine the Fourier series of τ_m looks like

$$\tau_\mathrm{m} = \sum_{n=1}^{\infty}\tau_n\cos(\omega_n t + \phi_n).$$

From this spectrum of the torque the THD is calculated by

$$\mathrm{THD}_\tau = \frac{\sqrt{\sum_{i=2}^{\infty}2\tau_i^2}}{\tau_1},$$

where the factor 2 corrects for the single-sided spectrum and where τ_i are the higher harmonics of the torque.

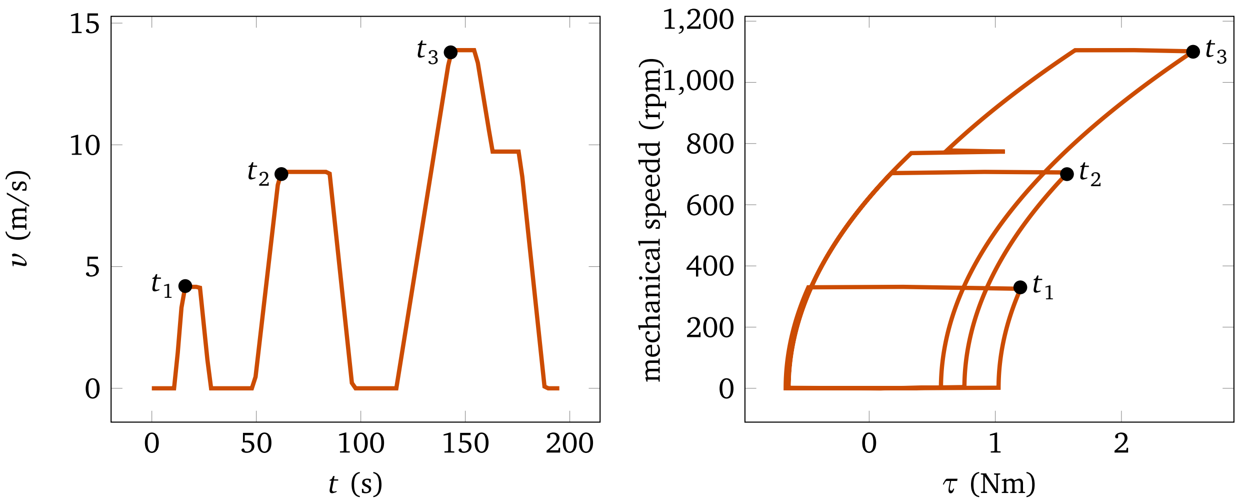

(a) Velocity–time plain **(b)** Mechanical speed–torque plain

Figure 9.4: Urban driving cycle taken from the new European driving cycle, see e.g. [95].

9.4.3 Determining the Efficiency over a Driving Cycle

A driving cycle is given by the velocity v of the vehicle as a function in time $t \in [0, t_{\text{end}}]$. From the change in velocity over time, the acceleration is determined $a(t) = {}^{\mathrm{d}v(t)}/_{\mathrm{d}t}$. The force F needed to accelerate the vehicle on a flat surface is given by

$$F(t) = ma(t) + F_{\text{rr}} + F_{\text{dr}}(t),$$

where m is the total mass of the vehicle, F_{rr} is the resistive rolling force and F_{dr} the drag force. Those forces are given by, respectively,

$$F_{\text{rr}} = C_r F_{\text{n}} \quad \text{and} \quad F_{\text{dr}}(t) = \frac{1}{2} C_d \rho_{\text{air}} A_{\text{front}} v(t)^2,$$

where C_r is the rolling resistance, C_d the drag coefficient, ρ the air density and A_{front} the frontal area of the vehicle. For the normal force F_{n} it holds that $F_{\text{n}} = F_{\text{g}} = mg$, with $g = 9.81\,\text{m/s}^2$ the gravitational acceleration of the Earth. Assuming that r_{wh} is the radius of the wheels, one can transform the velocity to an angular mechanical speed $\omega(t) = v(t)/r_{\text{wh}}$ and determine the needed torque for acceleration,

$$\tau(t) = r_{\text{wh}} \frac{F(t)}{N_{\text{dr}}},$$

with N_{dr} the number of drives mounted on the axes. The initial driving cycle has been transformed from a path in velocity–time plain to a path in the mechanical speed–torque plain (Figure 9.4). At every point of the mechanical speed–torque plain one can now determine the efficiency of the machine by (9.15).

Let the path in the mechanical speed–torque plain be parametrized by the physical time t, the efficiency over time is determined by

$$\mathcal{E} = \frac{\int_0^{t_{\text{end}}} P_{\text{m}}(t)\,\mathrm{d}t}{\int_0^{t_{\text{end}}} \left(P_{\text{m}}(t) + P_{\text{l}}(t)\right)\,\mathrm{d}t}. \tag{9.42}$$

9.5 Uncertainties

Due to the increased computational power and improved algorithms, electric machines can be simulated with high accuracy. As a consequence uncertainties, introduced during production have a bigger impact on the accurately determined QoIs. Therefore it is desirable to already incorporate these uncertainties in the modeling phase of electric machines, so that more robust machine designs are developed. The uncertainties considered in this dissertation are related to rotor eccentricity (Section 9.5.1), variations on PMs due to uncertainties in the geometry and material properties (Section 9.5.2) and variations of the material properties in the welding regions of the stator (Section 9.5.3). In this section the modeling of these uncertainties is discussed. The stochastic quantities are determined by Stochastic Collocation (SC) and the Monte Carlo (MC) method. When the number of uncertain parameters is high Multilevel Monte Carlo (MLMC) is used.

9.5.1 Rotor Eccentricity

Eccentricity occurs when the centers of the rotor and stator of a machine do not fully match. This eccentric position causes additional harmonics in the spectrum of the current [153], introduces an unbalanced magnetic pull [53] and gives rise to vibrations [14] and noise [152]. Especially for interior PMSMs rotor eccentricity can have major negative effects on the magnets. Due to the eccentricity the airgap in a part of the machine becomes bigger. As a consequence the magnets might get demagnetized [20].

Different types of eccentricity are identified in the literature. In the case of static eccentricity the rotor still rotates around its central axis. The width of the airgap remains constant over time. In the case of dynamic eccentricity the rotational axis of the rotor is in the central point of the stator and thus the width of the airgap varies over time. Considering the full 3D extent of the machine, this kind of eccentricity is also addressed as a cylindrical whirling motion [150].

In this work, also inclined rotor shafts are considered (Figure 9.6). In this case it is assumed that the rotor still rotates around its own central axis, but the bearings that mount the rotor have an independent eccentric position. The movement of the rotor can be interpreted as the static case of the combined whirling motion discussed in [150]. In what follows the different models to describe the eccentricities are discussed.

To model eccentricities the full geometry of the machine needs to be simulated, since an eccentric rotor destroys the symmetry of the machine. The region where the axis of the rotor is located, is modeled as an region filled with air in order to resemble the bearings that mounts the rotor.

Static Eccentricity

In the case of static eccentricity the two bearings that mount the rotor have the same displacement. When a coordinate system is assigned to the center of the stator, then the position of the center of the rotor can be expressed in polar coordinates $(R_0(\text{ш}), \theta_0(\text{ш}))$. The magnitude of the displacement is given by $R_0(\text{ш})$ and the direction is denoted by $\theta_0(\text{ш})$. These parameters are considered uncertain and independently distributed according to

$$R_0 \sim \mathcal{N}(0, \sigma_{R_0}^2), \quad \text{and} \quad \theta_0 \sim \mathcal{U}(0^\circ, 60^\circ), \tag{9.43a}$$

with

$$\sigma_{R_0} = \operatorname{std}\left[R_0(\text{ш})\right] = 0.2/3\,\text{mm}, \tag{9.43b}$$

so that the expected position of the rotor is in the center of the stator. Due to the symmetry of the machine every possible configuration can be obtained by restricting the outcomes of θ to $[0^\circ, 60^\circ]$ and by allowing negative values for the samples $R_0(\text{ш})$. The Uncertainty Quantification (UQ) one wants to conduct can be written as:

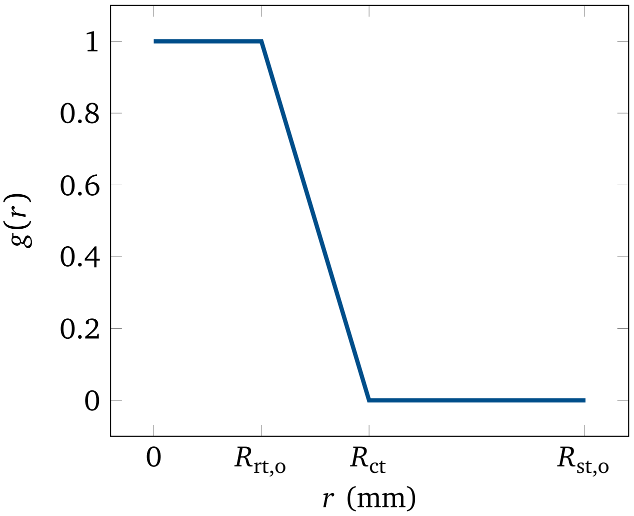

Figure 9.5: Visualization of the map to model rotor eccentricity.

Problem 3 *Find* $\mathbb{E}\left[E_0(\mathbf{a})\right]$*,* $\mathbb{E}\left[\text{THD}_{E_0}(\mathbf{a})\right]$*,* $\text{std}\left[E_0(\mathbf{a})\right]$ *and* $\text{std}\left[\text{THD}_{E_0}(\mathbf{a})\right]$ *where* $\mathbf{a}$ *are the Degrees of Freedom (DoFs) for* A_z *given by the discretization of*

$$-\nabla\cdot(\nu\nabla A_z(x,y)) = J_{\text{tot},z}(x,y) \quad \textit{on} \quad \Omega$$

with homogeneous boundary conditions on $\partial\Omega$ *and while considering the uncertainties in* (9.43) *describing static eccentricity.*

To avoid numerical noise caused by remeshing, the FE nodes of the triangulation (x_i, y_i) used to simulate a healthy machine are mapped to (x_i', y_i') according to

$$x_i'(\text{щ}) \quad = x_i'(R_0(\text{щ}), \theta_0(\text{щ})) \quad = x_i + R_0(\text{щ})\cos(\theta_0(\text{щ}))\, g(r), \tag{9.44}$$
$$y_i'(\text{щ}) \quad = y_i'(R_0(\text{щ}), \theta_0(\text{щ})) \quad = y_i + R_0(\text{щ})\sin(\theta_0(\text{щ}))\, g(r). \tag{9.45}$$

Let $r = \sqrt{x_i^2 + y_i^2}$ depict the radial position of every node, then $g(r)$ is defined as (see also Figure 9.5)

$$g(r) = \begin{cases} 1 & \text{if} \quad 0 \le r \le R_{\text{rt,o}}, \\ \dfrac{R_{\text{ct}} - r}{R_{\text{ct}} - R_{\text{rt,o}}} & \text{if} \quad R_{\text{rt,o}} < r < R_{\text{ct}}, \\ 0 & \text{if} \quad R_{\text{ct}} \le r \le R_{\text{st,o}}, \end{cases}$$

where R_{ct} is the radius of a chosen contour in the airgap, $R_{\text{rt,o}}$ is the rotor's outer radius and $R_{\text{st,o}}$ is the stator's outer radius.

The computational cost of the UQ procedure is rather high, especially when one uses the MC method, since the full machine has to be simulated for every sample. In order to reduce the computational cost a Response Surface Model (RSM) is constructed. An example is represented by the black dots in Figure 9.6b. For every node of the response surface a full machine calculation is performed and the EMF is calculated. For every generated sample $(R_0^{(k)}, \theta_0^{(k)})$ the corresponding EMF is determined by using cubic spline interpolation on the RSM. In this way, one is able to calculate many samples at relative low computational cost.

Inclined Rotor Shaft

To study the influence of an inclined rotor shaft the RSM introduced in the previous paragraph is exploited. In Figure 9.6b the procedure has been visualized for a random configuration. The positions of

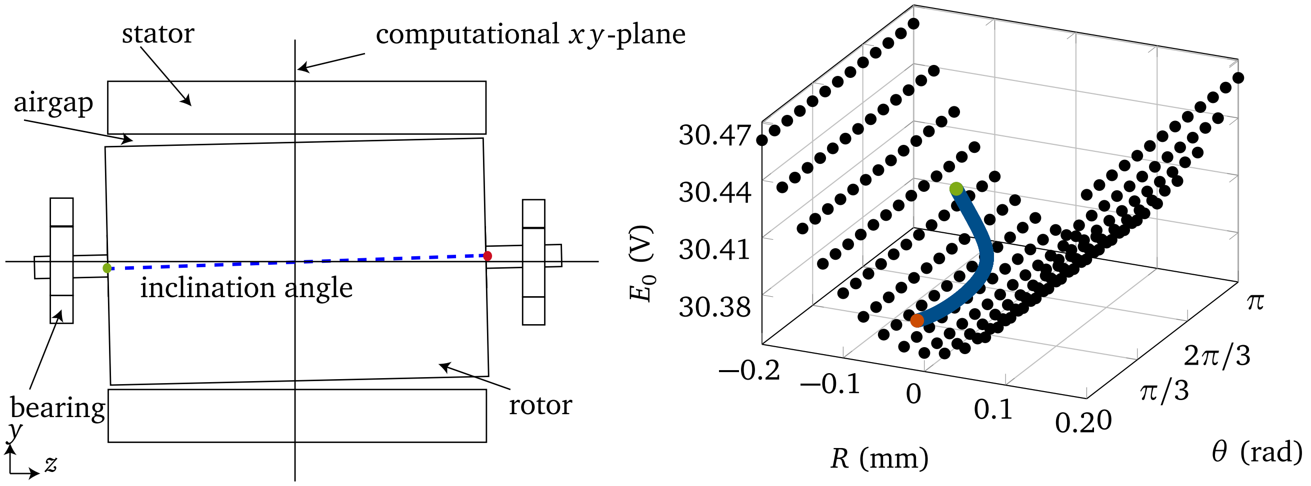

(a) Schematic view of an inclined rotor shaft.

(b) The black dots depict the nodes of the RSM (17×13) used for determining the EMF of a machine with an inclined rotor shaft.

Figure 9.6: The green and red dot depict, respectively the position of the front and back bearing. The blue line traces the central axis of the rotor and represents the different slices.

the front and back bearing are chosen randomly and are depicted, respectively, by the green and red dot. Once the positions of the front and back bearing have been determined, one can trace the position of the center of the rotor through the full machine, which is depicted by the blue curve. Every point of the blue curve can be interpreted as a 2D-slice of the machine, where the cross sections of the rotor are perpendicular to the stator shaft. The EMFs for the front and back bearings are determined by using cubic spline interpolation using the RSM. Integration from the green dot to the red dot along the blue curve results in the EMF of the machine with the inclined rotor shaft. This procedure can be interpreted as an extreme case of the multi-slice model presented in [27] and used to study eccentricities in [149]. However, in these works the slices are defined explicitly, where in this procedure the slices are defined implicitly by interpolation.

The parameters R_0 and R_1 define the displacement of the front and back bearing, whereas the parameters θ_0 and θ_1 depict the directions of their displacement, respectively . It is assumed that all parameters are independently distributed according to

$$R_i \sim \mathcal{N}(0, \sigma_{R_i}^2), \quad \text{and} \quad \theta_i \sim \mathcal{U}(0°, 180°), \tag{9.46a}$$

with

$$\sigma_{R_i} = \mathrm{std}\,[R_i(\text{щ})] = 0.2/3\,\mathrm{mm} \tag{9.46b}$$

where $i \in \{0, 1\}$. The UQ one wants to conduct can be written as

Problem 4 *Find* $\mathbb{E}\,[E_0(\mathbf{a})]$*, and* $\mathrm{std}\,[E_0(\mathbf{a})]$ *where* $\mathbf{a}$ *are the DoFs for* A_z *given by the discretization of*

$$-\nabla \cdot (\nu \nabla A_z(x, y)) = J_{\mathrm{tot},z}(x, y) \quad \textit{on} \quad \Omega$$

with homogeneous boundary conditions on $\partial\Omega$ *and while considering the uncertainties in* (9.46) *describing an inclined rotor shaft.*

As a final remark it has to be noted that possible 3D-effects are neglected by this procedure. For example, in 2D simulations it is assumed that the magnetic vector potential only has a z-component, which is obviously in real life not a valid assumption when the rotor is inclined.

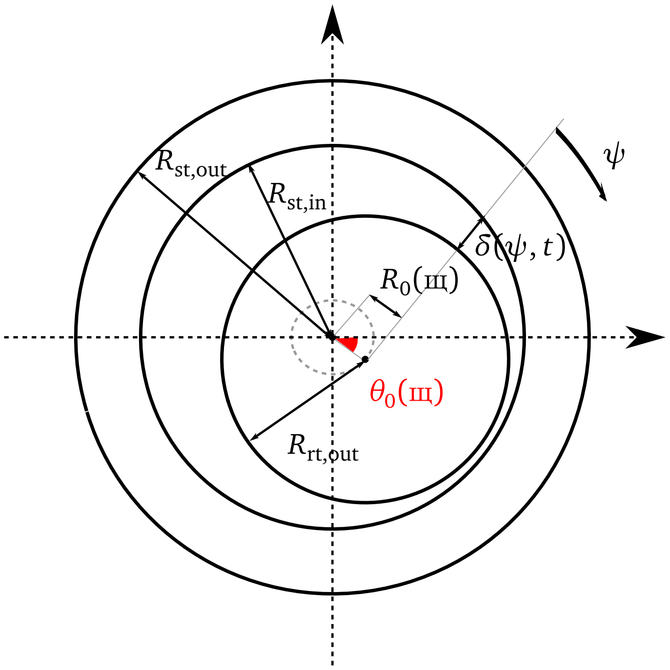

Figure 9.7: Schematic representation of the full machine with rotor eccentricity (figure adapted from [13]).

Dynamic Rotor Eccentricity

Combining the model constructed for static eccentricity with the notion of time-stepping, one is able to create a model that describes dynamic rotor eccentricity and which is equivalent to the model in [61].

The width of the airgap $\delta(\psi,\text{ш},t)$ (see Figure 9.7) can be expressed as a function of the arc ψ, such that

$$\delta(\psi,\text{ш},t)=\delta_{\mathrm{m}}\left[1-\varepsilon_{\mathrm{m}}(\text{ш})\cos(\alpha(\psi,t,\text{ш}))\right], \tag{9.47}$$

where the eccentricity $\varepsilon_{\mathrm{m}}(\text{ш})=R_0(\text{ш})/\delta_{\mathrm{m}}$ and $\delta_{\mathrm{m}}=(R_{\mathrm{st,in}}-R_{\mathrm{rt}})$ represents the mean mechanical airgap width. The angle α is given by

$$\alpha(\psi,\text{ш},t)=\psi-\omega_{\mathrm{m}}t-\theta_0(\text{ш}). \tag{9.48}$$

The parameters R_0 and θ_0 have the same distributions as in (9.43). The standard deviation corresponds to $\varepsilon_{\mathrm{m}}=7\%$. The impact of dynamic eccentricity on the torque and its total harmonic distortion is studied. To reduce the computational cost, RSMs are constructed. Only for the nodes the full time-stepping procedure is conducted in order to determine the torque and its THD. The values for the samples are, just as for static eccentricity, determined by cubic spline interpolation. The UQ one wants to conduct can be written as

Problem 5 *Find* $\mathbb{E}[\tau(\mathbf{a})]$, $\mathbb{E}[\mathrm{THD}_\tau(\mathbf{a})]$, $\mathrm{std}[\tau(\mathbf{a})]$ *and* $\mathrm{std}[\mathrm{THD}_\tau(\mathbf{a})]$ *where* $\mathbf{a}$ *are the DoFs for* A_z *given by the discretization of*

$$-\nabla\cdot(\nu\nabla A_z(x,y))=J_{\mathrm{tot},z}(x,y)\quad \text{on}\quad \Omega$$

with homogeneous boundary conditions on $\partial\Omega$ *and while considering the uncertainties in* (9.43) *describing dynamic eccentricity.*

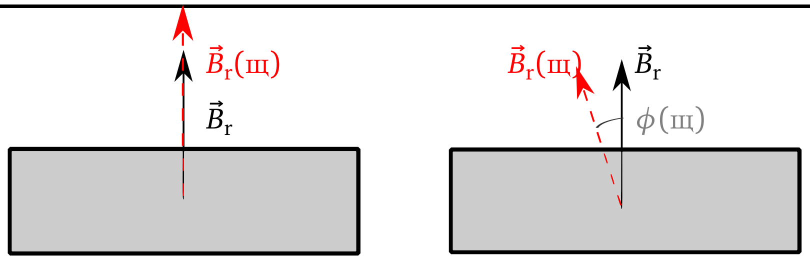

Figure 9.8: Representation of the model for the uncertainties in the material properties of the PMs. On the left the magnitude of the field is uncertain whereas on the right the orientation of the field.

9.5.2 Magnets

The construction of PMs introduces uncertainties in its material properties [90]. A model to represent these uncertainties has been proposed in [112] and has been adapted for this thesis. The magnitude of the remanent magnetic field $B_{\mathrm{r}} = \left|\vec{B}_{\mathrm{r}}\right|$ is assumed to be uniform for the full magnet and contrary to [112] the angular dependencies of the magnitude of the remanent magnetic field are neglected (see Figure 9.8).

The magnitude of the remanent magnetic field $B_{\mathrm{r}} = \left|\vec{B}_{\mathrm{r}}\right|$ and its full orientation ϕ are considered uncertain. They are assumed to be independently and uniformly distributed,

$$\begin{aligned} B_{\mathrm{r},j}(\omega) &= \bar{B}_{\mathrm{r},j} + \Delta_{1,j}(\omega), \quad \text{with} \quad \Delta_{1,j} \sim \mathfrak{U}(-0.05\,\mathrm{T}, 0.05\,\mathrm{T}), && (9.49a) \\ \phi_j(\omega) &= \bar{\phi}_j + \Delta_{2,j}(\omega), \quad \text{with} \quad \Delta_{2,j} \sim \mathfrak{U}(-3^\circ, 3^\circ), && (9.49b) \end{aligned}$$

with nominal values

$$\begin{aligned} \bar{B}_{\mathrm{r},j} &= \mathbb{E}\left[B_{\mathrm{r},j}\right] &= 0.94\,\mathrm{T}, && (9.49c) \\ \bar{\phi}_j &= \mathbb{E}\left[\phi_j\right] &= 0^\circ, && (9.49d) \end{aligned}$$

where $j \in \{1, \ldots, 6\}$.

There can also be uncertainties in the geometry of the magnets. Let us consider the parameters P_1, P_2, P_3 as shown in Figure 9.9 so that $\mathbf{P} = [P_1, P_2, P_3]$. P_1 and P_2 describe respectively the width and the height of the magnet. The third parameter depicts the maximal distance from the magnet to the surface of the rotor. The parameters are independently and uniformly distributed,

$$P_i(\omega) = \bar{P}_i + \Delta_i(\omega), \quad \text{with} \quad \Delta_i \sim \mathfrak{U}(-0.2\,\mathrm{mm}, 0.2\,\mathrm{mm}), \quad \text{and} \quad i = 1, \ldots, 3, \qquad (9.50a)$$

such that $\boldsymbol{\Delta}(\omega) = [\Delta_1(\omega), \Delta_2(\omega), \Delta_3(\omega)]$ and the nominal values are

$$\bar{P}_1 = 19\,\mathrm{mm}, \quad \bar{P}_2 = 7\,\mathrm{mm}, \quad \bar{P}_3 = 7\,\mathrm{mm}. \qquad (9.50b)$$

The UQ one wants to conduct can be written as

Problem 6 *Find* $\mathbb{E}\left[E_0(\mathbf{a})\right]$, *and* $\operatorname{std}\left[E_0(\mathbf{a})\right]$ *where* $\mathbf{a}$ *are the DoFs for* A_z *given by the discretization of*

$$-\nabla \cdot (\nu \nabla A_z(x,y)) = J_{\mathrm{tot},z}(x,y) \quad on \quad \Omega$$

with homogeneous boundary conditions on Γ_D *and anti-periodic boundary conditions on* Γ_l *and* Γ_r *and while considering the uncertainties in* (9.50) *describing the size and position of the magnets.*

The geometric uncertainties will be considered during the optimization of the size of the PMs of the machine.

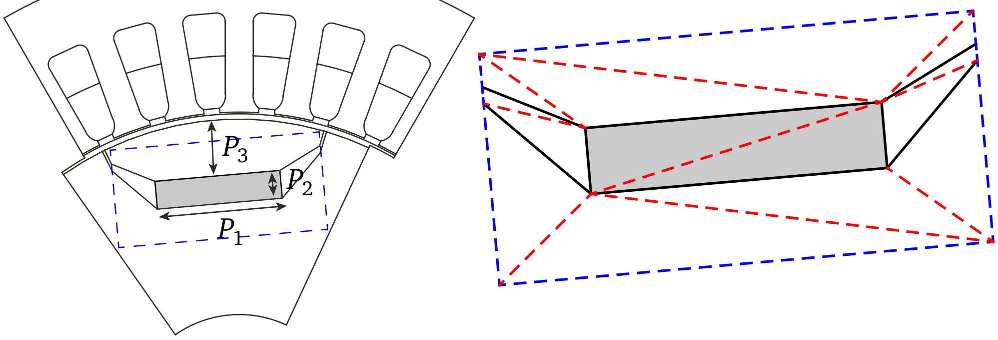

Figure 9.9: Parameters describing the size and the position of the magnet. The region of the affine decomposition is indicated by the blue dashed box. On the right the triangulation into N_L subdomains is shown by the red dashed lines. Figure adapted from [25].

9.5.3 Welding Influences

Recently there is a trend to use more and more segmentation for constructing the stator of a machine, e.g. [165]. In this method every tooth of the stator corresponds to one segment and these segments are then welded together to construct the full machine. This technique is especially beneficial if a concentrated winding, an example is shown in Figure 1.1, is used. The application of this winding scheme results in, for example, shorter end turns with respect to distributed winding schemes, a higher fill factor, especially when coupled with segmented stator structures, e.g. [128]. Furthermore, the introduction of segmentation eases the winding of the coils during production.

The heat produced during the welding process affects certain zones of the machine. These zones can extend to several millimeters into the material and the permeability of the steel in those regions is significantly decreased [36, 93].

Although the PMSM in this thesis does not have a concentrated winding scheme and segmentation would probably not be beneficial for its construction, it is assumed that the stator teeth are welded together. It is further assumed that welding introduces uncertainties on the reluctivity of the iron material used in those regions. Those regions are depicted in red in Figure 9.10. The distributions of the reluctivity in the welding regions are given by

$$\nu_j(\omega) = \bar{\nu}_j + \Delta_j(\omega), \text{with} \quad \Delta_j \sim \mathcal{U}(-330\,\mathrm{mH}^{-1}, 330\,\mathrm{mH}^{-1}), \tag{9.51a}$$

with nominal values

$$\bar{\nu}_j = \mathbb{E}\left[\nu_j\right] = 1100\,\mathrm{mH}^{-1}, \tag{9.51b}$$

where $j \in \{1, \ldots, 36\}$.

Together with the uncertain material properties of the magnets, given by (9.49), their impact on the magnetic energy W in the machine is studied. Due to the high number of uncertain parameters a MLMC procedure is applied. The UQ one wants to conduct can be written as

Problem 7 *Find* $\mathbb{E}[W(\mathbf{a})]$ *and* $\operatorname{std}[W(\mathbf{a})]$ *where* $\mathbf{a}$ *are the DoFs for* A_z *given by the discretization of*

$$-\nabla \cdot (\nu \nabla A_z(x,y)) = J_{\mathrm{tot},z}(x,y) \quad \text{on} \quad \Omega$$

with homogeneous boundary conditions on $\partial\Omega$ *and while considering the uncertainties described by* (9.49) *and* (9.51).

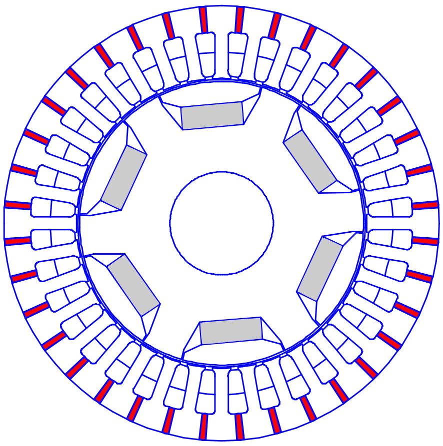

Figure 9.10: Full geometry of the machine, where the regions affected by the welding process are depicted in red.

9.6 Optimization of the Size of the Permanent Magnets

The PMSM is subjected to optimization. The goal is to reduce the size S_{pm} of the PMs. Since the calculations are performed in 2D, $S_{\mathrm{pm}} = P_1 P_2$ is a valid measure for the size of the PMs. The distance from the magnets to the rotor surface is chosen to be a free parameter which is allowed to change during the optimization process. This implies that $\mathbf{P} = [P_1, P_2, P_3]$. The changes induced by variations on the parameters P_1, P_2, P_3 can be described affinely, hence an affine decomposition is introduced in a region around the magnet (Figure 9.9). The domain is decomposed into $N_L = 14$ subdomains. This decomposition introduces some extra constraints to the optimization procedure [94]. Two different optimizations are performed. For the first optimization the QoI is the EMF, $E_0(\mathbf{P}) = E_0(\mathbf{a}(\mathbf{P}))$. The second optimization in this dissertation has as QoIs the effiency over a driving cycle, $\mathcal{E}(\mathbf{P}) = \mathcal{E}(\mathbf{a}(\mathbf{P}))$ and the maximal torque of the machine $\tau_{\max}(\mathbf{P}) = \tau_{\max}(\mathbf{a}(\mathbf{P}))$. All QoIs are calculated from the MVP and one thus deals with PDE-constrained optimization [83].

9.6.1 Considering the Electromotive Force

The optimized machine should still fulfill a desired electromotive force E_{d}. The nominal optimization problem reads as:

Problem 8 *Find* **P** *such that*

$$\min_{\mathbf{P}\in\mathbb{R}^{N_p}} J_1(\mathbf{P}) := P_1 P_2 \tag{9.52a}$$

subject to

$$G_1(\mathbf{P}, E_0(\mathbf{P})) := \begin{pmatrix} P_1^{\mathrm{l}} - P_1 \\ P_2^{\mathrm{l}} - P_2 \\ P_3^{\mathrm{l}} - P_3 \\ P_3 - P_3^{\mathrm{u}} \\ P_2 + P_3 - 15 \\ 3P_1 - 2P_3 - 50 \\ E_{\mathrm{d}} - E_0(\mathbf{a}(\mathbf{P})) \end{pmatrix} \leq 0, \tag{9.52b}$$

where $E_0(\mathbf{P})$ *contains the PDE* (2.8b) *implicitly.*

The first four constraints are related to the lower and upper bounds of $\mathbf{P}$: $(P_1^{\mathrm{l}}, P_2^{\mathrm{l}}, P_3^{\mathrm{l}}) = (1, 1, 5)$ and $(P_1^{\mathrm{u}}, P_2^{\mathrm{u}}, P_3^{\mathrm{u}}) = (\infty, \infty, 14)$. The validity of the affine decomposition is ensured by the fifth constraint. It enforces that the subdomains do not intersect. Since only a subdomain of the geometry is considered it is also required to stay in that region. The second-to-last constraint is a design constraint, which enforces that the PM remains burried in the rotor. As a consequence the depth of the magnet is linked to its width. The last constraint is the requirement to fulfill the prescribed EMF. Here the result of the PDE comes into play.

The stochastic and deterministic formulations (Section 6.2) are used to solve the optimization problem. The optimization is performed using the Sequential Quadratic Programming (SQP) algorithm (Section 6.1.2), particle swarm optimization [92] and genetic algorithm (e.g. [158]). For the stochastic formulations the notation will be shortened so that $J_1(\text{щ}) = J_1(\mathbf{P}(\text{щ}))$ and $G_1(\text{щ}) = G_1(\mathbf{P}(\text{щ}), E_0(\mathbf{P}(\text{щ})))$. It is assumed that the deviations on the parameter $\mathbf{P}$ follow the distributions mentioned in (9.50). An overview of the different methods and their corresponding cost function and constraints is given in Table 9.2.

9.6.2 Considering the Efficiency along a Driving Cycle and the Maximal Torque

In this case the nominal cost function is the same as in Problem 8 whereas the last constraint is now replaced by two other constraints, expressing the desire to maintain a prescribed mean efficiency $\mathcal{E}_{\mathrm{d}}$ along a driving cycle and to fulfill a prescribed maximal torque τ_{d}.

The optimization problem reads

Problem 9 *Find* $\mathbf{P}$ *such that*

$$\min_{\mathbf{P}\in\mathbb{R}^{N_p}} J_1(\mathbf{P}) := P_1 P_2 \tag{9.53a}$$

subject to

$$G_2(\mathbf{P}, \mathcal{E}(\mathbf{P}), \tau_{\max}(\mathbf{P})) := \begin{pmatrix} P_1^{\mathrm{l}} - P_1 \\ P_2^{\mathrm{l}} - P_2 \\ P_3^{\mathrm{l}} - P_3 \\ P_3 - P_3^{\mathrm{u}} \\ P_2 + P_3 - 15 \\ 3P_1 - 2P_3 - 50 \\ \mathcal{E}_{\mathrm{d}} - \mathcal{E}(\mathbf{a}(\mathbf{P})) \\ \tau_{\mathrm{d}} - \tau_{\max}(\mathbf{a}(\mathbf{P})) \end{pmatrix} \leq 0. \tag{9.53b}$$

where $\mathcal{E}(\mathbf{P})$ *and* $\tau_{\max}(\mathbf{P})$ *contain the PDE* (2.8b) *implicitly.*

This optimization is only performed using SQP and with the nominal deterministic formulation as depicted by (9.53a) and (9.53b) and by a robust optimization in the stochastic formulation described in Section 6.2.2.

Optimization considering a driving cycle has been applied in [44], where the aim was to minimize the torque ripple and the power losses. They robustified the machine design with respect to different driving cycles by enforcing an reduction in the differences of torque ripple and power losses between an urban driving cycle and an highway driving cycle. The optimization was performed by a genetic algorithm. In [95] a design optimization of a PMSM has been performed in order to increase the efficiency of the machine. However, the optimization was only conducted for a small set of selected points of the new European driving cycle.

Table 9.2: Overview of the numerical procedures used to optimize the PMSM, where $j = 1,\dots,N_G$, with N_G the number of constraints. A value equal to 1 in the column MOR indicates the use of Model Order Reduction (i.e. reduced basis method) to lower the computational cost.

Name	Method	UQ	MOR	Cost function	Constraints
Nominal (i)	SQP	-	0	$J_1(\mathbf{P})$	$G_1(\mathbf{P}, E_0(\mathbf{P}))$
Nominal (ii)	SQP	SC	0	$\mathbb{E}\left[J_1(\omega)\right]$	$\mathbb{E}\left[G_1^{(j)}(\omega)\right]$
Nominal (iii)	SQP	MC	0	$\mathbb{E}\left[J_1(\omega)\right]$	$\mathbb{E}\left[G_1^{(j)}(\omega)\right]$
Nominal (iv)	PSO	-	0	$J_1(\mathbf{P})$	$G_1(\mathbf{P}, E_0(\mathbf{P}))$
Nominal (v)	GA	-	0	$J_1(\mathbf{P})$	$G_1(\mathbf{P}, E_0(\mathbf{P}))$
Linearized (i)	SQP	-	0	$J_1(\bar{\mathbf{P}}) + \left\Vert \nabla_{\bar{\mathbf{P}}} J_1(\bar{\mathbf{P}}) \right\Vert_1$	$G_1^{(j)}(\bar{\mathbf{P}}, E_0(\bar{\mathbf{P}})) + \left\Vert D \nabla_{\bar{\mathbf{P}}} G_1^{(j)}(\bar{\mathbf{P}}, E_0(\bar{\mathbf{P}})) \right\Vert_1$
Linearized (ii)	SQP	-	0	$J_1(\bar{\mathbf{P}}) + \left\Vert \nabla_{\bar{\mathbf{P}}} J_1(\bar{\mathbf{P}}) \right\Vert_2$	$G_1^{(j)}(\bar{\mathbf{P}}, E_0(\bar{\mathbf{P}})) + \left\Vert D \nabla_{\bar{\mathbf{P}}} G_1^{(j)}(\bar{\mathbf{P}}, E_0(\bar{\mathbf{P}})) \right\Vert_2$
Linearized (iii)	SQP	SC	0	$J_1(\bar{\mathbf{P}}) + \beta \left\Vert \mathrm{std}\left[\boldsymbol{\Delta}(\omega)\right] \circ \nabla_{\bar{\mathbf{P}}} J_1(\bar{\mathbf{P}}) \right\Vert_2$	$G_1^{(j)}(\bar{\mathbf{P}}, E_0(\bar{\mathbf{P}})) + \beta \left\Vert \mathrm{std}\left[\boldsymbol{\Delta}(\omega)\right] \circ \nabla_{\bar{\mathbf{P}}} G_1^{(j)}(\bar{\mathbf{P}}, E_0(\bar{\mathbf{P}})) \right\Vert_2$
Linearized (iv)	SQP	SC	1	$J_1(\bar{\mathbf{P}}) + \beta \left\Vert \mathrm{std}\left[\boldsymbol{\Delta}(\omega)\right] \circ \nabla_{\bar{\mathbf{P}}} J_1(\bar{\mathbf{P}}) \right\Vert_2$	$G_1^{(j)}(\bar{\mathbf{P}}, E_0(\bar{\mathbf{P}})) + \beta \left\Vert \mathrm{std}\left[\boldsymbol{\Delta}(\omega)\right] \circ \nabla_{\bar{\mathbf{P}}} G_1^{(j)}(\bar{\mathbf{P}}, E_0(\bar{\mathbf{P}})) \right\Vert_2$
Robust (i)	SQP	SC	0	$\mathbb{E}\left[J_1(\omega)\right] + \beta\ \mathrm{std}\left[J_1(\omega)\right]$	$\mathbb{E}\left[G_1^{(j)}(\omega)\right] + \beta\ \mathrm{std}\left[G_1^{(j)}(\omega)\right]$
Robust (ii)	SQP	MC	0	$\mathbb{E}\left[J_1(\omega)\right] + \beta\ \mathrm{std}\left[J_1(\omega)\right]$	$\mathbb{E}\left[G_1^{(j)}(\omega)\right] + \beta\ \mathrm{std}\left[G_1^{(j)}(\omega)\right]$
Robust (iii)	PSO	SC	0	$\mathbb{E}\left[J_1(\omega)\right] + \beta\ \mathrm{std}\left[J_1(\omega)\right]$	$\mathbb{E}\left[G_1^{(j)}(\omega)\right] + \beta\ \mathrm{std}\left[G_1^{(j)}(\omega)\right]$
Robust (iv)	GA	SC	0	$\mathbb{E}\left[J_1(\omega)\right] + \beta\ \mathrm{std}\left[J_1(\omega)\right]$	$\mathbb{E}\left[G_1^{(j)}(\omega)\right] + \beta\ \mathrm{std}\left[G_1^{(j)}(\omega)\right]$
Robust (v)	SQP	SC	1	$\mathbb{E}\left[J_1(\omega)\right] + \beta\ \mathrm{std}\left[J_1(\omega)\right]$	$\mathbb{E}\left[G_1^{(j)}(\omega)\right] + \beta\ \mathrm{std}\left[G_1^{(j)}(\omega)\right]$
Robust (vi)	SQP	MC	1	$\mathbb{E}\left[J_1(\omega)\right] + \beta\ \mathrm{std}\left[J_1(\omega)\right]$	$\mathbb{E}\left[G_1^{(j)}(\omega)\right] + \beta\ \mathrm{std}\left[G_1^{(j)}(\omega)\right]$
Robust (vii)	PSO	SC	1	$\mathbb{E}\left[J_1(\omega)\right] + \beta\ \mathrm{std}\left[J_1(\omega)\right]$	$\mathbb{E}\left[G_1^{(j)}(\omega)\right] + \beta\ \mathrm{std}\left[G_1^{(j)}(\omega)\right]$
Robust (viii)	GA	SC	1	$\mathbb{E}\left[J_1(\omega)\right] + \beta\ \mathrm{std}\left[J_1(\omega)\right]$	$\mathbb{E}\left[G_1^{(j)}(\omega)\right] + \beta\ \mathrm{std}\left[G_1^{(j)}(\omega)\right]$

9.7 Résumé

This chapter introduced the Permanent Magnet Synchronous machine (PMSM). It was described how the quantities of interest are calculated and how the uncertainties are modeled.

To summarize, the numerical methods applied for the machine are listed:

- Numerical modeling: The spectrum of the electromotive force, calculated by the loading method, will be determined by the classical Finite Element Method (FEM) and Iso-Geometric Analysis (IGA). In the IGA setting two domain decomposition approaches will be applied, namely, an iterative substructuring and a harmonic stator-rotor coupling.
- Uncertainty quantification: Stochastic Collocation (SC) and Monte Carlo (MC) will be used to model different types of rotor eccentricity. The quantity of interest is the electromotive force. To study dynamic eccentricity the rotation will be accounted for by a time stepping technique. The influence of this uncertainty is examined on the spectrum of the torque, which is determined by the energy balance method.

  The multilevel MC method is used to study the influence of uncertainties in permanent magnets and uncertainties introduced by welding the different stator teeth to each other.
- Optimization: The optimization aims to reduce the size of the permanent magnets. Two different problems are formulated. The first one considers the electromotive force. In this problem description it is also assumed that the size of the magnet and its position in the rotor is uncertain. The optimization will be performed by different algorithms, namely sequential quadratic programming, particle swarm optimization and genetic algorithm. The problem will be written down in an affine sense, such that the parameter variation can be handled easily. The deterministic and stochastic formulations of Section 6.2 will be compared. In the case where the stochastic quantities will be needed, model order reduction will be applied.

  The second optimization problem considers the efficiency of the machine along a driving cycle and the maximal torque of the machine. Sequential quadratic programming is used as optimization algorithm.

Movement IV

Andante con moto: Validation and Results

10 Simulation of a Permanent Magnet Synchronous Machine with Iso-Geometric Analysis

This chapter addresses the results of the modeling of the Permanent Magnet Synchronous Machine (PMSM) introduced in Section 9 with Iso-Geometric Analysis (IGA). The geometry of the rotor and the stator are constructed independently by a multipatch approach. The Degrees of Freedom (DoFs) at the interfaces of the patches are glued together using static condensation so that a global C^0 continuity is achieved [156]. At an interface in the airgap where the rotor and stator domains meet, the patches are non-conforming. As a consequence a coupling method at that interface is required. Two coupling methods, namely a Dirichlet-to-Neumann (D-N)-mapping and a Harmonic Stator Rotor Coupling (HS-RC) which have been introduced in Section 9.3, will be tested on the machine. The validity and stability of HS-RC method will first be tested on two simplified examples. This will be discussed in the first section of this chapter. Afterwards, the application to the PMSM is discussed. In theory, it is possible to model the full machine as a whole using a conforming multipatch approach, but this would lead though to a major increase of the number of patches. Furthermore, the introduction of an angular displacement of the rotor with respect to the stator would become complicated, since it would require a mesh adaptation procedure or a complete re-parametrization. The following results are taken from [22].

10.1 Validation of the Harmonic Stator-Rotor Coupling

To verify IGA in combination with the harmonic stator-rotor coupling (IGA-HS-RC), two simplified examples are constructed (see Figure 10.1). On those domains a Poisson's equations with homogeneous Dirichlet boundary conditions is solved,

$$\begin{cases} -\nabla \cdot (\nabla A) & = j \qquad \text{in } \Omega, \\ \qquad\quad A & = 0 \qquad \text{on } \partial\Omega, \end{cases} \tag{10.1}$$

with

$$j = 2x\left(22x^2y^2 + 21y^4 - 45y^2 + x^4 - 5x^2 + 4\right),$$

so that, for this source term, a Closed Form Solution (CFS) exists [156].

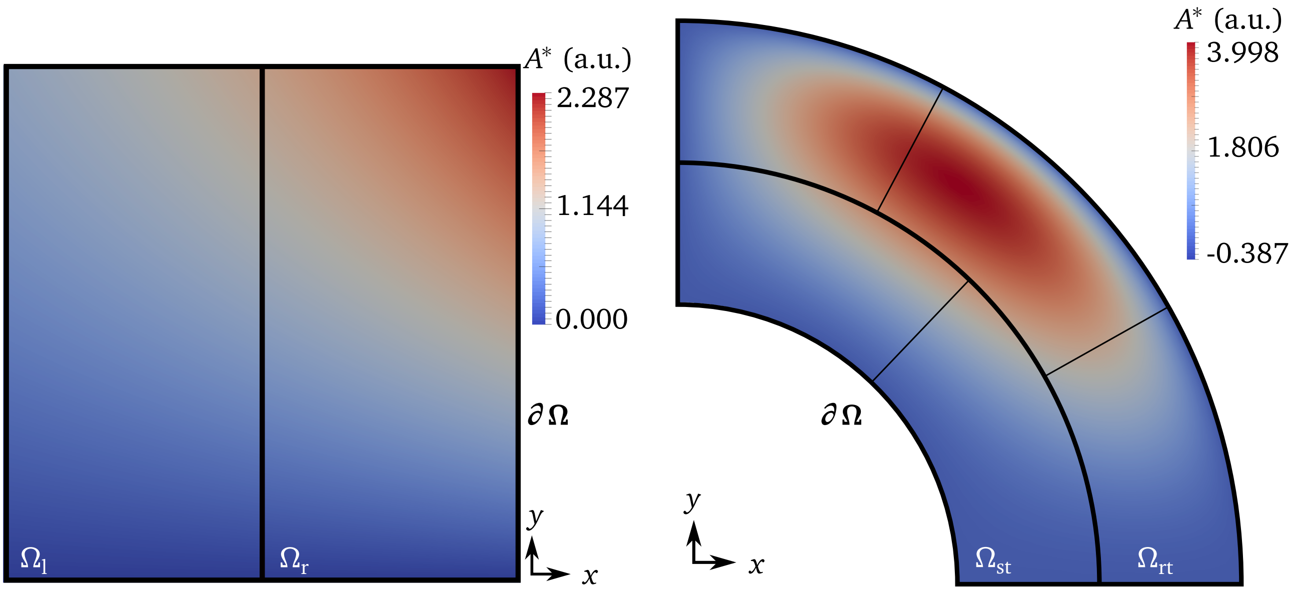

(a) Unit square for verifying the IGA-HS-RC. The black lines identify the two domains and the color map depicts the fabricated solution a^*.

(b) Simplified model for verifying the IGA-HS-RC. The thick black lines depict the two domains, the thin black lines identify the patches and the color map depicts the fabricated solution a^*.

Figure 10.1: Simplified models to test the IGA-HS-RC procedure.

The first test case is a unit square subdivided in two subdomains, so that $\overline{\Omega} = \overline{\Omega}_\mathrm{l} \cup \overline{\Omega}_\mathrm{r}$ and the interface $\overline{\Omega}_\mathrm{l} \cap \overline{\Omega}_\mathrm{r} = \Gamma_\mathrm{ag}$ is a straight line. The coupling method is tested for different discretization levels and different numbers of coupling harmonics N_Γ. This example allows us to study the stability of the problem without considering the full technicity of the geometry map. The value for the inf-sup constant ς indicating the stability of the problem is shown in Figure 10.2a as a function of the mesh size. When the function space spanned by the Lagrange multipliers is too rich with respect to the function space for the field variables, ς approaches zero and thus the saddle-point problem becomes singular.

It was mentioned in section 9.3.2 that the HS-RC could be interpreted in the context of mortar methods. This type of methods has already been applied in the framework of IGA [30] in which the B-spline discretization on the domains has been exploited to generate a stable Lagrange multiplier space. Moreover, the pairing is stable when, if one uses basis functions of degree p, basis functions of order $p-2$ are used on the interface. To compare the IGA-HS-RC method with these findings, Ω_l is chosen as the master side and the Lagrange multipliers are chosen according to [30]. Since for the two subdomains second order discretization is considered, constant basis functions are taken on Γ_ag. The stability is shown in Figure 10.2. It is seen that the mortar method remains stable. However the possible implementation of rotation is cumbersome.

The second test case is a quarter of an annulus with inner and outer radius equal to 1 m and 2 m respectively. The domain is subdivided in two subdomains, which are addressed as Ω_rt and Ω_st (such that $\overline{\Omega} = \overline{\Omega}_\mathrm{rt} \cup \overline{\Omega}_\mathrm{st}$) to keep the analogy with the electric machine. The subdomains are constructed with multiple patches in such a way that they do not match at the interface $\Gamma_\mathrm{ag} = \overline{\Omega}_\mathrm{rt} \cap \overline{\Omega}_\mathrm{st}$. The convergence of the proposed method is shown in Figure 10.3. The L^2-error with respect to the CFS is defined as

$$\varepsilon_{L^2} := \|A - A^*\|_{L^2} = \sqrt{\int_\Omega (A - A^*)^2 \,\mathrm{d}\Omega}. \tag{10.2}$$

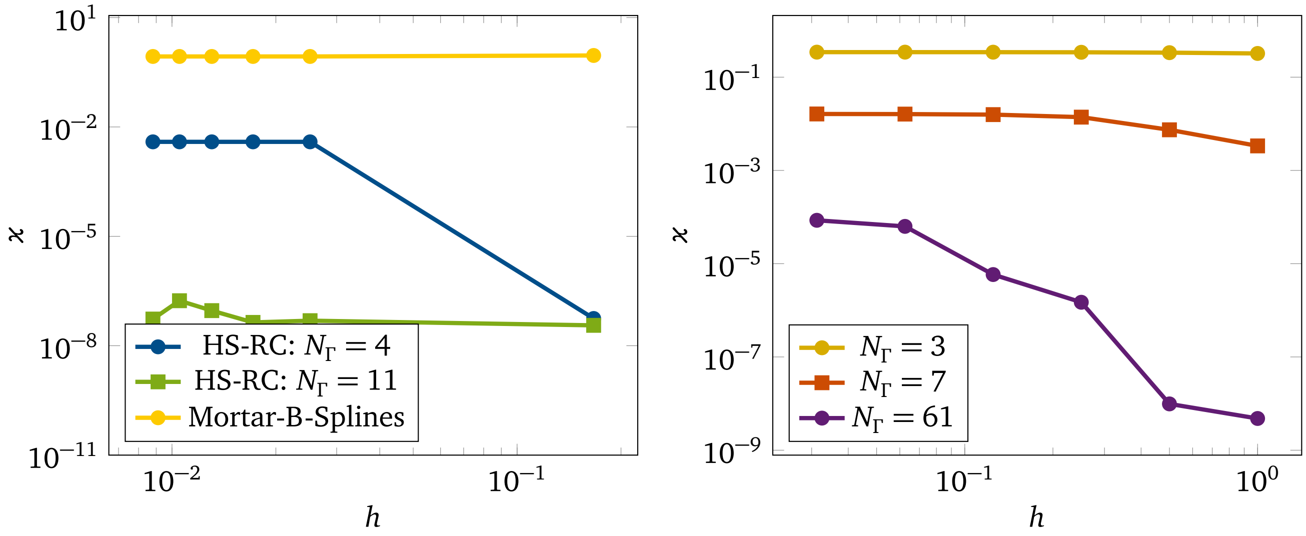

(a) Unit square **(b)** Annulus

Figure 10.2: Numerically evaluated inf-sup constant for the two test-cases using a discretization of order 2.

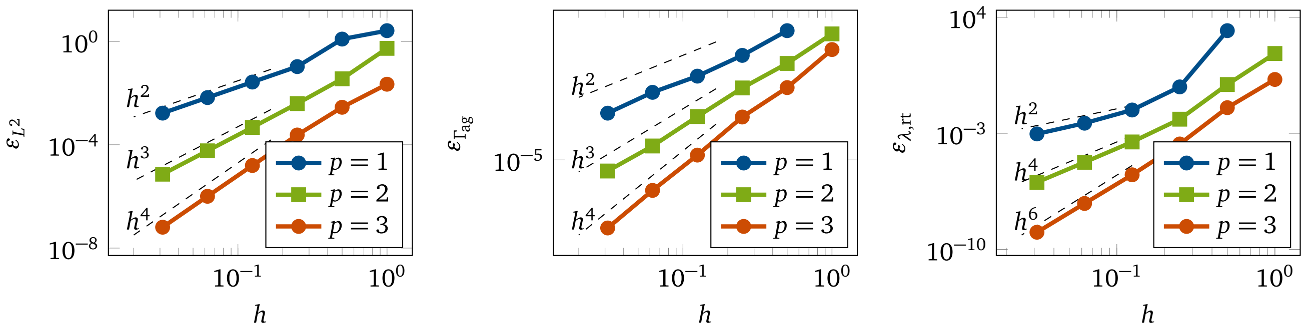

(a) Convergence of the IGA-HS-RC to the CFS solution. **(b)** Convergence of the jump at the interface Γ_{ag}. **(c)** Convergence of the Neumann data at the interface Γ_{ag}.

Figure 10.3: Convergence study for different choices of discretization degrees and increasing mesh refinement. The results are obtained with 7 harmonics used for the coupling $\ell = \{-3, \ldots, 3\}$. The dashed lines depict the expected convergence order.

The expected order of convergence, i.e. $\mathcal{O}(h^{p+1})$, is achieved (Figure 10.3a). Since the method only imposes weak continuity of A across Γ_{ag}, the jump of the solution across Γ_{ag} is studied (Figure 10.3b), with the norm

$$\varepsilon_{\Gamma_{ag}} := \left\| A_{rt|\Gamma_{ag}} - A_{st|\Gamma_{ag}} \right\|_{L^2}. \tag{10.3}$$

The convergence of the Lagrange multipliers themselves is depicted in Figure 10.3c. Here, the Neumann data are compared with the exact solution by the norm

$$\varepsilon_{\lambda,rt} := \left\| \nabla A^* \cdot \vec{n}_{rt} - \sum_{\ell \in L} \lambda_{rt,\ell} e^{-i\ell\theta} \right\|_{L^2}. \tag{10.4}$$

The Lagrange multipliers converge and the order of convergence is observed to be $\mathcal{O}(h^{2p})$.

The stability of this test case is shown in Figure 10.2b. If the volumetric discretization is not fine enough, increasing the number of harmonic N_Γ leads to an inf-sup constant ς that goes to zero. This

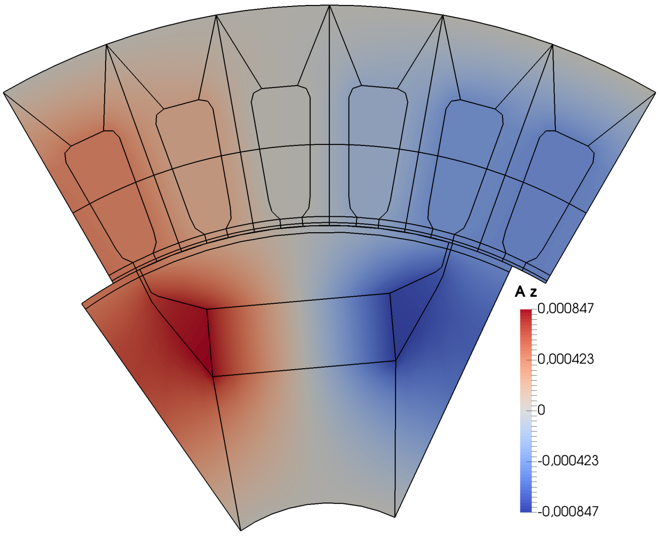

Figure 10.4: Magnetic vector potential A_z in a PMSM pole computed using IGA ($p = 2$), and harmonic stator-rotor coupling ($L_{\mathrm{ap}} = \pm 3, \pm 9, \pm 15$).

implies that the saddle-point problem becomes unstable. For the modeling of the PMSM, one has thus to make sure that the number of DoFs should not be too low compared to the number of coupling harmonics used.

10.2 Results for the Permanent Magnet Synchronous Machine

To compare the results obtained with IGA, the machine is also discretized with classical FEM. The geometry is constructed in `FEMM` [103] and the mesh is generated by `Triangle` [135]. Afterwards, the mesh is used by the in-house code `Niobe` to solve (2.8b) on the computational domain. The discretization with IGA is handled by `GeoPDEs` [56]. In post-processing the QoIs are calculated. In this application these are the Electromotive Force (EMF) and the Total Harmonic Distortion (THD) of its spectrum. Due to the symmetry of the machine one is able to only consider one pole of the machine, by applying anti-periodic boundary conditions on the left and right side of the pole, i.e. on Γ_{l} and Γ_{r}. On the inner and outer arc, homogeneous Dirichlet conditions are applied.

Using IGA, the rotor and stator domain are constructed from 12 and 78 patches respectively, see Figure 10.4. The implementation of the D-N map in IGA (IGA-D-N) is straightforward. However, on Γ_{ag} anti-periodic boundary conditions are needed. To comply with the boundary condition on Γ_{l} and Γ_{r} only a certain set L of harmonic orders are allowed in the HS-RC coupling, since they need to fulfill the anti-periodicity. Due to the six-pole symmetry, only multiples of 3 are allowed. In combination with the anti-periodicity, this further excludes all multiples of 6. The set one can choose is thus $L_{\mathrm{ap}} = \pm 3, \pm 9, \pm 15, \ldots$. Furthermore, since in this work, the interest is only in real-valued solutions, it is necessary to consider a double sided spectrum. This means that, if ℓ is chosen, then also $-\ell$ is added to the coupling modes. In Figure 10.4, the calculated magnetic vector potential is shown using the IGA-HS-RC procedure. The singular parametrization in the windings does not affect the smoothness of the solution [22].

10.2.1 Comparison of the Coupling Approaches

In [22] the results discussed in this subsection were published. The convergence of the solution as a function of the iteration step for the IGA-D-N algorithm is shown in Figure 10.5a. The results are obtained using splines with degree 2 with C^1 regularity. The number of DoFs is 3200 and the incremental errors, i.e. (9.20) and (9.21), fulfill the prescribed tolerance $\texttt{tol} = 10^{-7}$ after 29 iterations.

Table 10.1: Comparison of the computational efficiency between IGA with iterative substructuring and IGA with HS-RC and $L_{\text{ap}} = \pm 3, \pm 9, \pm 15$ as the set of harmonics. The times mentioned refer to the sum of assembly and solving time. Results adapted from [19].

		D-N (`tol`$= 10^{-3}$)				HS-RC	
Ref. Level	p	$N_{\text{DoF, rt}}$	$N_{\text{DoF, st}}$	N_{it}	Time (s)	N_{DoF}	Time (s)
1	1	32	193	9	67.021	241	3.335
2	1	137	746	9	123.462	908	6.610
4	1	563	2932	9	248.232	3538	13.675
8	1	2279	11624	9	528.551	13982	30.437
16	1	9167	46288	9	1200.739	55606	73.414
1	2	100	650	9	75.401	771	3.356
2	2	256	1515	10	161.381	1801	6.813
4	2	784	4325	10	330.292	5157	15.004
8	2	2704	14265	10	710.511	15053	33.953
16	2	10000	51425	9	1490.251	61581	85.595

The suitability of IGA for machine simulation is tested by a convergence analysis as depicted in Figure 10.5b, where the IGA-D-N coupling method is used. As a reference solution $A_{z,\text{DN}-\text{ref}}$ a highly refined simulation with cubic NURBS, with 2 matching derivatives at the elements' boundaries, are used, i.e. B-Spline basis functions with degree $p = 3$ and C^2 regularity. The convergence of the relative error defined by

$$\epsilon_{\text{DN}} = \left\|A_{z,\text{DN}} - A_{z,\text{DN-ref}}\right\|_{L^2} / \left\|A_{z,\text{DN-ref}}\right\|_{L^2}$$

is shown, where $A_{z,\text{DN}}$ is the obtained solution for different choices of the basis functions and regularity and increasing mesh refinement. In the case of the lowest regularity (C^0 basis functions of degree $p = 1$ and $p = 2$), the method is equivalent to a FEM simulation on quadrilateral elements, albeit the geometry remains exactly represented. From the figure one can also see the positive influence of the higher smoothness of IGA on the solution compared to FEM in the results for $p = 2$. For the same level of accuracy fewer DoFs are needed when the regularity of the basis functions is higher.

In Table 10.1 the computational times for all coupling methods are listed. The matrices that have to be solved by the iterative coupling are obviously smaller than in the fully coupled system. However, this, at first sight, computational gain is lost by the iterative procedure, which slows down the approach. The major bottleneck in the current implementation is the evaluation of the solution at given points in the physical domain, which is needed for the Dirichlet and Neumann data. This is in the IGA framework cumbersome due to the fact that it demands the computation of the inverses of the NURBS mappings in order to retrieve the corresponding points in the reference domain. Since these mappings are non-linear and this is step is repeatedly carried out, one has to rely on a Newton-Raphson scheme to conduct this step which slows down the algorithm.

Another convenience of the HS-RC is the uncomplicated implementation of the relative rotation. For a relative angular displacement ξ of the rotor with respect to the stator, only the rotation matrix, introduced in Section 9.3.2 has to be re-calculated, which is a negligible extra cost. This is in strong contrast to the iterative procedure, since here the right hand sides for both subproblems have to be re-assembled for every ξ.

10.2.2 Comparison with Finite Element Method

The IGA-HS-RC approach is compared to the first order FEM with a conforming discretization in the airgap so that for the FEM no coupling is needed. In Figure 10.6 the convergence of the classical first

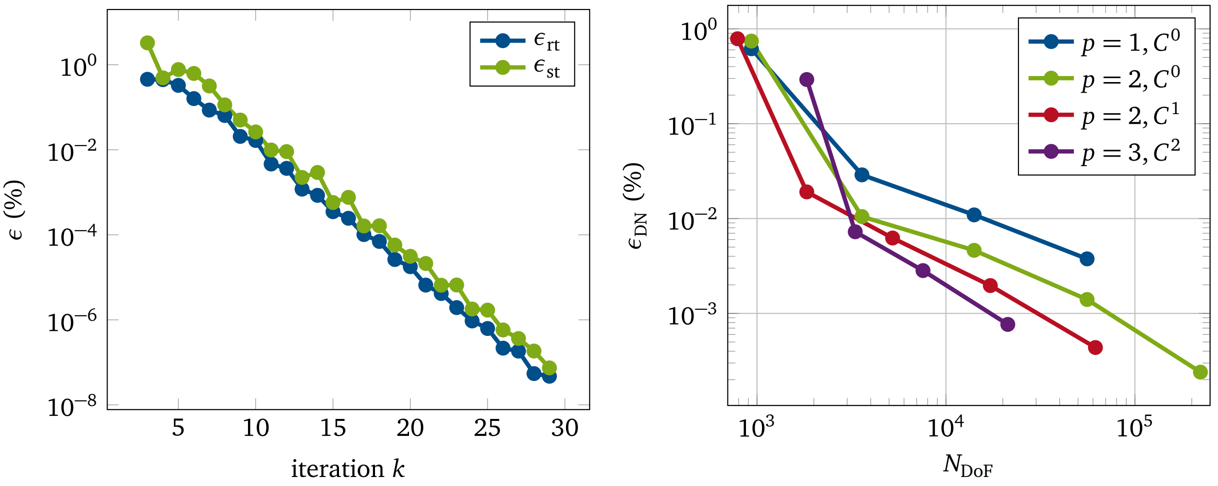

(a) Evolution of the errors (9.20) and (9.21) as a function of the interation step for the IGA-D-N procedure using splines with degree 2 and C^1 regularity.

(b) Convergence of the IGA-D-N for basis functions with different degrees and regularity.

Figure 10.5: Convergence for the results obtained for the PMSM using IGA-D-N.

Table 10.2: Comparison between FEM and IGA for the calculated EMF and THD.

	E_1	THD	N_{DoF}	Time (s)
FEM	29.8 V	$5.72 \cdot 10^{-2}$ %	225667	103.45
IGA-HS-RC	30.4 V	$5.87 \cdot 10^{-2}$ %	5157	15.00
IGA-D-N	30.6 V	$6.06 \cdot 10^{-2}$ %	5109	330.29

order FEM on triangles to the finest IGA with second degree B-spline basis functions is shown. The depicted relative error is defined as

$$\epsilon_{\mathrm{FEM}} = \left\| A_{z,\mathrm{FEM}} - A_{z,\mathrm{ref}} \right\| / \left\| A_{z,\mathrm{ref}} \right\| .$$

A part of the spectra of the EMF obtained by the different approaches are shown in Figure 10.7. The EMF and the THD calculated from the spectra are given in Table 10.2. The results are in good agreement with each other. The relative difference is only 3% and 6%, for the EMF and the THD respectively. The differences in the spectrum itself originate from the fact that IGA is by construction conserving the symmetry of the machine, since, for example for the slots, the same mapping, beside for a rotational shift, is used. As a consequence, the mesh of the IGA method is thus conforming to the geometry of the machine, which cannot be easily guaranteed by the finite element mesher. The preservation of the symmetry is even stronger imposed by using a HS-RC. The efficiency of the IGA-HS-RC method is once more stressed when looking to the computational times. The lower number of DoFs for IGA reduces the computational time with a factor close to 7 with respect to the classical FEM while obtaining the same accuracy.

10.3 Conclusion

Iso-Geometric Analysis has been successfully applied to model a Permanent Magnet Synchronous Machine. The advantages are the exact parametrization of circular arcs in the geometry and the higher regularity of the solution. The rotor and the stator are modeled with a multipatch approach for dealing

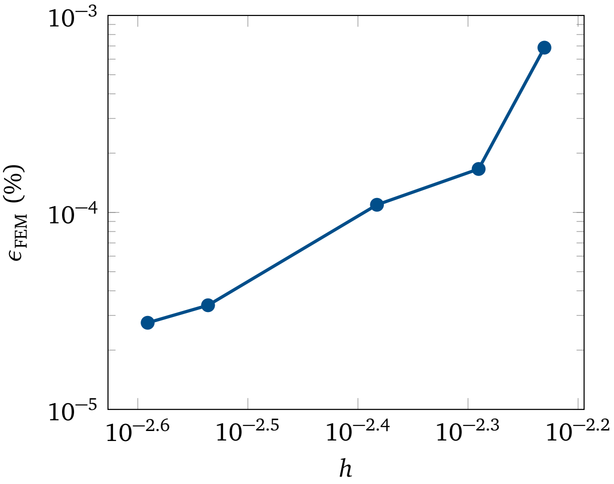

Figure 10.6: Convergence of a first order FEM simulation for increasing level of mesh refinement to a fine IGA-HS-RC solution with second degree basis functions and $L_{\text{ap}} = \pm 3, \pm 9, \pm 15$.

with regions with different material properties. On an arc in the airgap the patches are not matching and a coupling procedure has to be carried out. Two methods have been studied, namely, a Dirichlet-to-Neumann map and a harmonic stator-rotor coupling. The latter is verified on a test case for which the convergence of the spatial discretization has been shown. The harmonic stator-rotor coupling leads to a saddle-point problem for which stability has been numerically verified. The procedure has been applied to a permanent magnet synchronous machine. Iso-Geometric Analysis with a harmonic stator-rotor coupling is shown to be a new and promising alternative to classical finite element procedures for electric machine simulation.

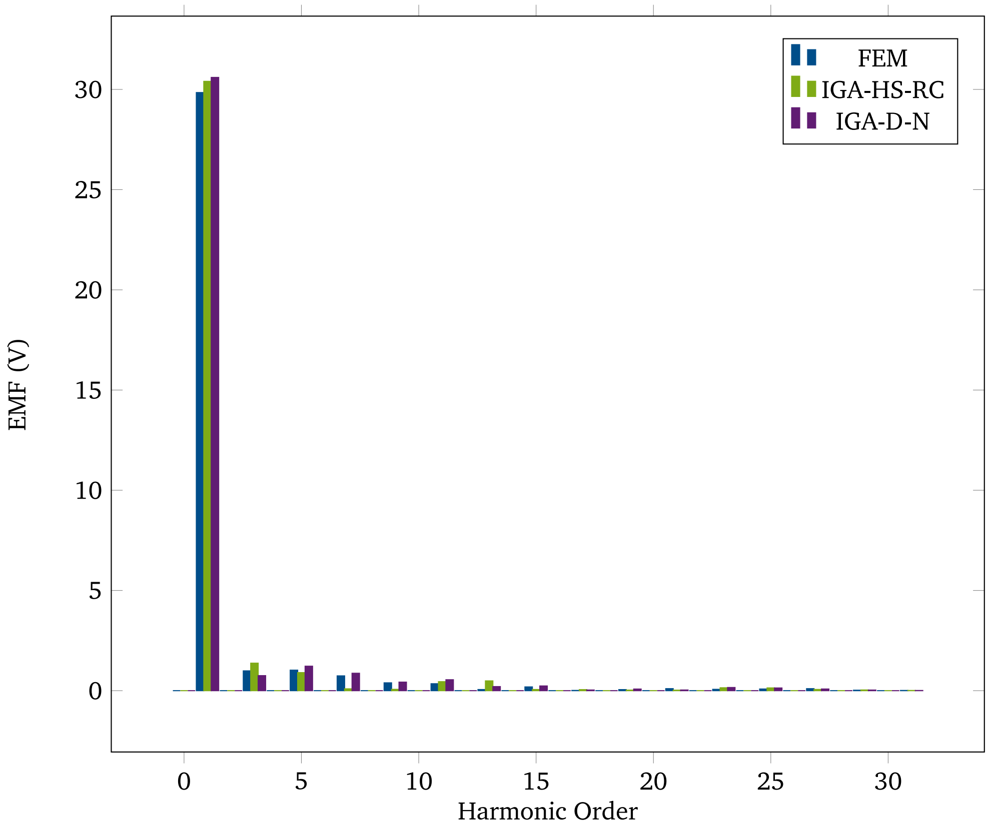

Figure 10.7: Spectrum of the EMF of the PMSM depicting the first 31 modes, figure adapted from [22].

11 Uncertainty Quantification

In this chapter the results of uncertainty quantification are discussed. In the first section the focus is on Multilevel Monte Carlo (MLMC) and its application on the coaxial cable (Chapter 7). The second section deals with the Uncertainty Quantification (UQ) of a Permanent Magnet Synchronous Machine (PMSM). The influences of different uncertainties introduced in Section 9.5 are studied and discussed.

11.1 Coaxial Cable with Uncertainties Modeled by Multilevel Monte Carlo

This triptych presents the results for MLMC applied to study the uncertainties of the performance parameters in the coaxial cable, introduced in Section 7.3. In the first panel the standard procedure is tested and the parameters of Theorem 1 on page 41 are determined. The second panel discusses the use of the Richardson extrapolator and the last panel discusses the results for the usage of nested or non-nested meshes. The uncertainty quantification that is conducted is found in Problem 1. The results presented in this section were published in [64].

11.1.1 Spatial Error Based on the Closed Form Solution

As mentioned previously the Quantity of Interest (QoI) is the total magnetic energy W in the system. To estimate the parameter α, which describes the decay of the weak error, one has to determine the expectation of the magnetic energy, i.e. $\mathbb{E}[W(\mathbf{P}_\ell)]$ and $\mathbb{E}[W(\mathbf{P})]$. To determine those quantities, Stochastic Collocation (SC) is used for calculating the expectation value and the variances and the sampling is done using the Closed Form Solution (CFS). The convergence of the procedure is shown in Figure 11.1. The polynomial degree of SC n_i is equal for all parameters, meaning that $N_{\mathrm{SC}} = (n_i + 1)^3$ and n_i is varied between 3 and 12. The error shown in Figure 11.1b is defined as

$$\varepsilon_{\mathrm{SC}} = \frac{\left|\mathbb{E}[W]_{n_i} - \mathbb{E}[W]_{12}\right|}{\mathbb{E}[W]_{12}}, \tag{11.1}$$

where the subscript indicates the polynomial order.

Calculating $|\mathbb{E}[W_\ell - W]|$ on different meshes, i.e. levels, and applying a least square regression results in $\alpha = 2$, (see Figure 11.2a [63]), which confirms the theoretical predictions in Section 5.2.1. A similar approach is applied to determine β (Theorem 1). A β amounting to 4 is attained (see Figure 11.2b),

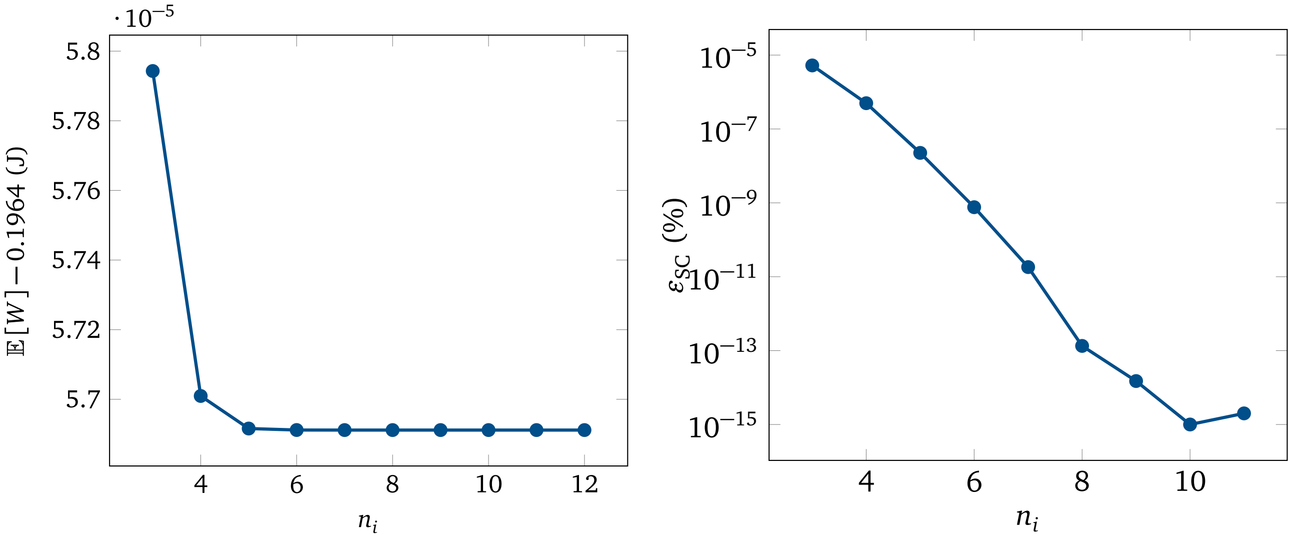

(a) Convergence of the expectation value of the magnetic energy with respect to polynomial degree.

(b) Convergence of the relative error of the expectation value of the magnetic energy with respect to polynomial degree.

Figure 11.1: Convergence of the SC method for the expectation value of the energy.

which is also in accordance to the theoretical predictions. Furthermore it can be noticed that $\mathbb{V}[W_\ell]$ is nearly constant over the different levels and is thus not influenced by the mesh size. This is a confirmation of the theorem that the Mean Square Error (MSE) can be divided in a contribution by the error due to the variance and a contribution by the error caused by the Finite Element Method (FEM) approximation.

In Figure 11.3 the influence of the user defined error bound ε for the MSE is depicted. Defining a sharper bound increases the computational costs (see Figure 11.3a). Adding a level will decrease the variance and will bring the expectation value closer to the one obtained by using the CFS and SC. The dominant costs are on the coarsest level, which is indicated by the verticality of the depicted lines. This is confirmed by the results in Figure 11.3b, which show that the major part of the samples are taken on the coarsest level. Applying a sharper bound also increases the number of levels, since the weak error has to decrease accordingly.

11.1.2 Richardson-Extrapolation-Based Error Indicator

The MLMC method is now applied using the extrapolation-based error indicator. Figure 11.4 summarizes the main results [64]. The extrapolator is a suitable alternative for the CFS, since there is only a negligible increase in the cost by using the extrapolator (Figure 11.4a). To obtain these results the MSE was bound to $\varepsilon = 2 \cdot 10^{-4}$. The error bars depict 3σ confidence intervals, where σ is the standard deviation (std). The std has been approximated with the MLMC sampling. Figure 11.4b compares the total costs of the MLMC methods (see (5.20)) to the standard MC method. The MSE for the MC method is given by

$$\mathrm{MSE}_{\mathrm{MC}} = N_{\mathrm{MC}}^{-1}\mathbb{V}[W_\ell] + (\mathbb{E}[W_\ell - \mathbb{E}[W]])^2 .$$

The required level ℓ and thus the required mesh size h_ℓ is determined by the second term, which is the finite element error. It is imposed that the weak error is below $\varepsilon^2/2$. Afterwards, the total number of samples is calculated by relying on (5.11), with the requirement that $\varepsilon_{\mathrm{MC}} \leq \varepsilon^2/2$. The total costs are then given by (5.12), where $N_{\mathrm{DoF}} = N_{\mathrm{DoF},\ell}$.

Since $\beta > \gamma$, Theorem 1 predicts $C_{\mathrm{MLMC}} \sim \mathcal{O}\left(\varepsilon^2\right)$. This confirms the results in Figure 11.4b. Also the cost of the standard MC increases as expected, namely $\mathcal{O}(\varepsilon^3)$, which can be seen by combining (5.11) and (5.12).

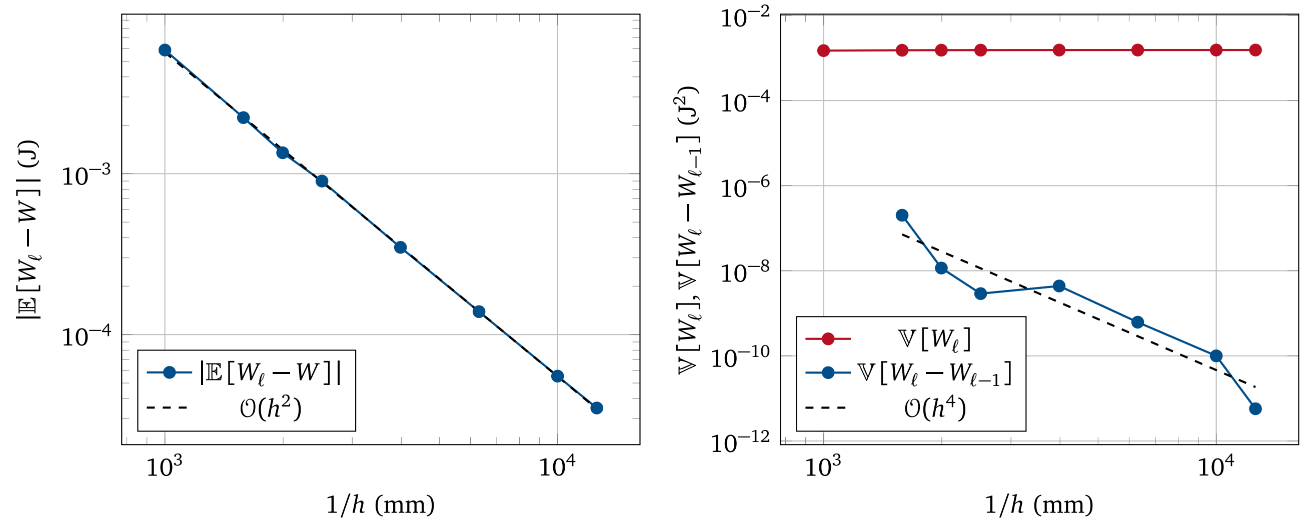

(a) In blue the decay of the weak error as a function of the meshsize is depicted.

(b) In red and in blue the decay of $\mathbb{V}[W_\ell]$ and $\mathbb{V}[W_\ell - W_{\ell-1}]$, respectively as a function of the mesh size.

Figure 11.2: Numerical results for determining α and β, which respectively measure the decay of the weak error and the variance. The dots indicate the different levels used during the procedure. The least square regressions are depicted in black.

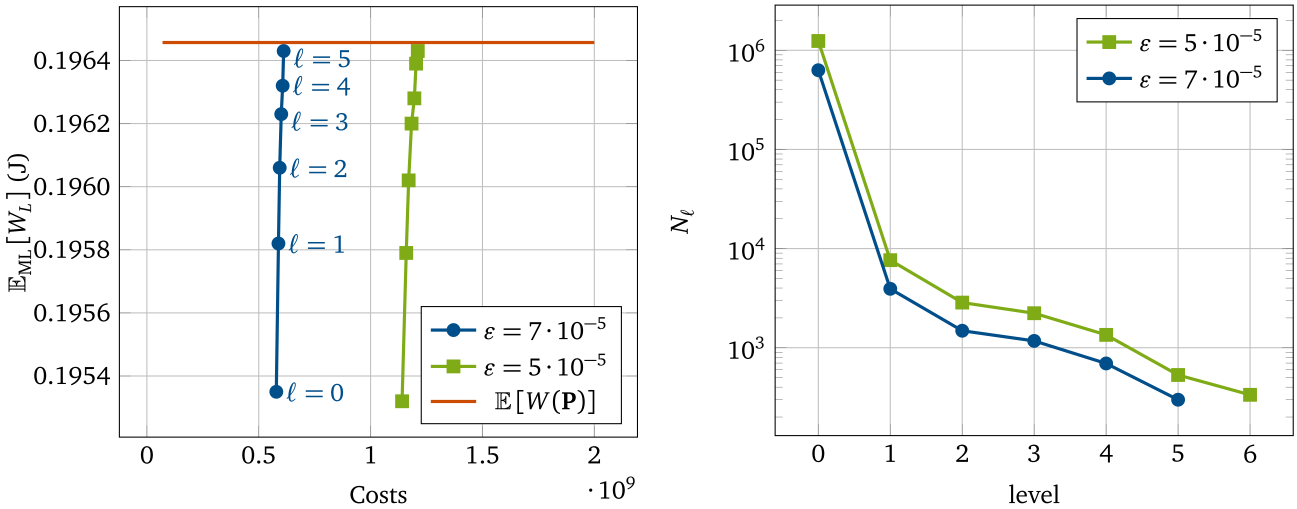

(a) Evolution of the expectation value as a function of the cost for two different bounds. The horizontal red line depicts the expectation value obtained by SC on the CFS .

(b) Evolution of the number of samples per level for two different bounds.

Figure 11.3: Influence of the use of different error bounds ε on the costs, the number of samples per level and the number of levels. The total number of levels N_L is determined by using the CFS.

11.1.3 Study of the Influence of the Mesh

For the different levels, different meshes are needed. One way to construct the levels is by using nested meshes, meaning that the coarsest level is refined by adding nodes at the center of the existing edges. The newly constructed mesh, thus, inherits the coarser levels and makes the same approximation for the geometry. A drawback is that the refinement factor λ in $h_\ell = h_0 \lambda^\ell$ is not freely tunable. For a 2D mesh,

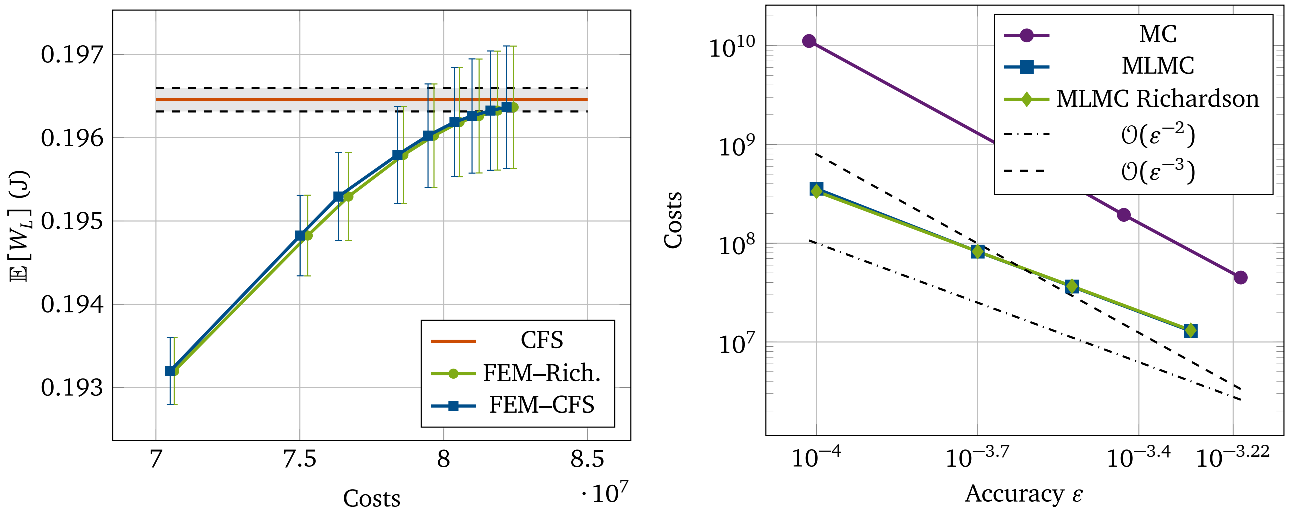

(a) Evolution of the expectation value as a function of the cost for $\varepsilon = 2 \bullet 10^{-4}$. The gray zone indicates the 99% confidence interval around the mean value obtained with SC on the CFS (in red).

(b) Total costs for the classical MC approach and the two MLMC procedures as a function of the bound for the MSE.

Figure 11.4: Comparison of MLMC procedure where the CFS or the Richardson extrapolator is used to determine the weak error.

Table 11.1: MSE for nested and remeshed levels

mesh	MSE
nested	$1.3101 \cdot 10^{-9}\,\mathrm{J}^2$
remeshed	$5.1589 \cdot 10^{-9}\,\mathrm{J}^2$

this implies a minimal increase of N_{DoF} by a factor two. Generating a totally new and finer mesh for every level not only improves the approximation of the solution (see Section 3.3) but also improves the approximation of the geometry with increasing level. Using nested meshes, one could project the nodes, that are added on the old edges constructing the geometry, to the actual geometry, however this strategy is not considered in this thesis. The material properties of an element in Ω, e.g. $\nu(\vec{x}, \mathbb{m})$, might vary for each level ℓ. This implies that a remeshing strategy violates the theoretical framework of MLMC. The results in Figure 11.5, however, show only a minor influence. The expectation value also converges to the one obtained using the CFS a bit faster, which is caused by the fact that the higher levels approximate the geometry in a better way.

To check if the MSE is below the user defined bound $\varepsilon = 10^{-4}$, the MLMC simulation is repeated 10 times and for the MSE,

$$\mathrm{MSE} = \mathbb{E}\left[(\mathbb{E}_{\mathrm{ML}}[W_L] - \mathbb{E}[W])^2\right] \leq \varepsilon^{-2},$$

the outer expectation value is estimated using MC. As one can read from Table 11.1, the MSE for both methods is below $\varepsilon^2/2$.

11.2 Permanent Magnet Synchronous Machine

The influence of different source of uncertainty on the behavior of a PMSM is studied in this section. The MLMC method tested in the previous section is now applied to model welding and magnet uncertainties

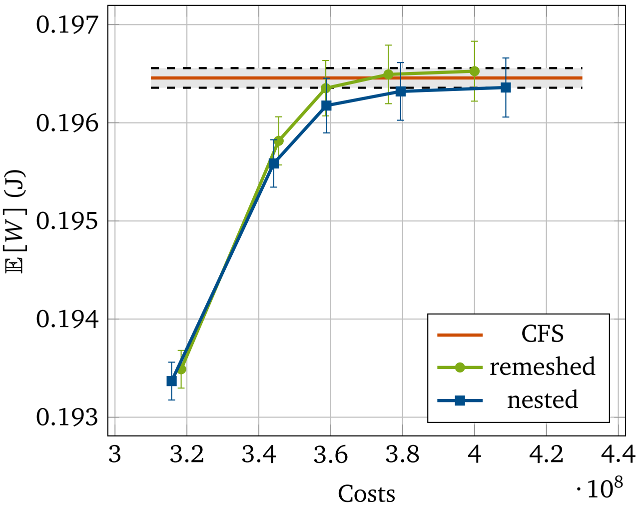

Figure 11.5: Evolution of the expectation value as a function of the cost for $\varepsilon = 10^{-4}$ using nested and remeshed levels. The gray zone indicates the 99% confidence interval around the mean value obtained with SC on the CFS (in red). Figure adapted from [64].

as addressed in Section 9.5.2 and Section 9.5.3 respectively. The second subsection focuses on the result for rotor eccentricity, which were obtained by SC and the standard MC method. Response Surface Models (RSMs) are used to accelerate the evaluations for determining the expectation values and standard deviations of the QoIs.

11.2.1 Welding and Magnet Material Uncertainties Modeled by Multilevel Monte Carlo

From the results of MLMC applied to the coaxial cable, it is clear that the spatial error calculated using the CFS can be replaced by a Richardson-extrapolation-based error indicator. Furthermore, it was also shown that remeshing can be used. These two findings allow to apply MLMC on the PMSM for Problem 7, since it facilitates the control of the mesh growth for every level.

To apply Theorem 1, the parameters α and β have to be determined first. To estimate α only the nominal values $\bar{\mathbf{P}} \in \mathbb{R}^{48}$ for the uncertain parameters, as given in (9.49) and (9.51), are considered. Different meshes, with different h_ℓ are used to model the machine. The total magnetic energy W is considered. The energy W_ℓ obtained at every level is compared with the result obtained on the finest level L by

$$\epsilon = \frac{\left|W_\ell(\bar{\mathbf{P}}) - W_L(\bar{\mathbf{P}})\right|}{\left|W_L(\bar{\mathbf{P}})\right|} = \mathcal{O}(h_\ell^k). \tag{11.2}$$

Additionally the convergence order of the Richardson indicator ϵ_{Rich} is computed. The parameter β is estimated by performing the MLMC simulation with additional samples on the levels, $N_{\mathrm{MC},0} = 33641$, $N_{\mathrm{MC},1} = N_{\mathrm{MC},2} = 1000$, $N_{\mathrm{MC},3} = 500$, $N_{\mathrm{MC},4} = 250$, $N_{\mathrm{MC},5} = 125$. To estimate both parameters a linear least square regression is performed on the obtained data. It is found that $\alpha \approx 1.66$ using the solution based on the FEM error and $\alpha \approx 1.7$ when the Richardson estimator is used (see Figure 11.6a). This suboptimal convergence rates were to be expected due to the singular right-hand-side, recall the remark in Section 3.2. The least square fitting for the variances results in $\beta \approx 2.2$ (see Figure 11.6b) [64].

The costs on the coarsest level are dominating (see Figure 11.7a), since those samples are needed to reduce the variance. Figure 11.7b depicts the overall costs as a function of the desired accuracy. It is clear that MLMC outperforms MC. The results of MC (blue line) are based on estimations, because the full machine simulations become intractable for such accuracies since they correspond to very fine meshes. The number of samples needed can be estimated by (5.11).

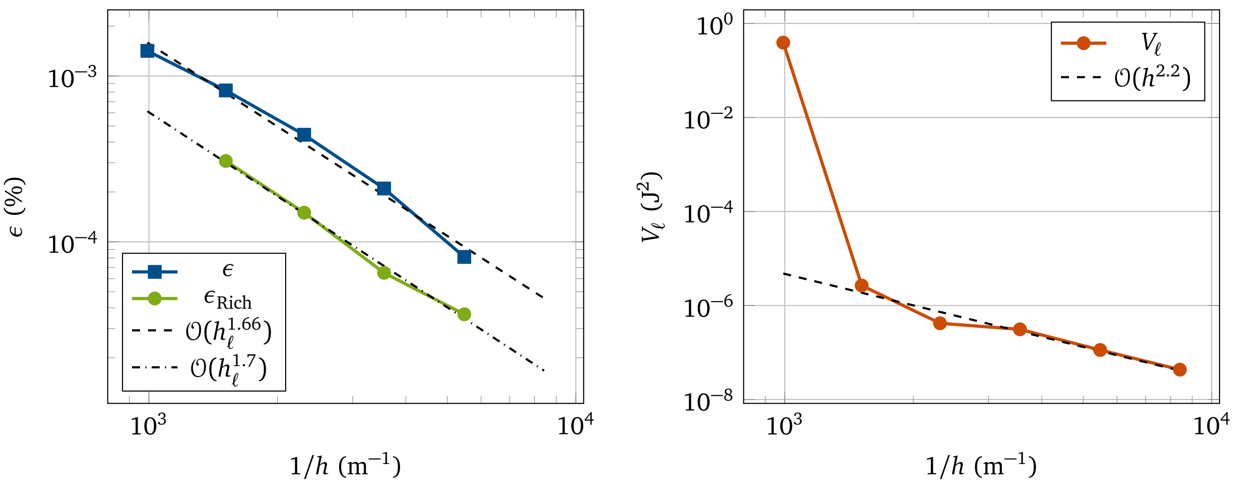

(a) Determinating α relying on the convergence of the W.

(b) Determinating β based on the calculations for the variance per level for $\varepsilon = 10^{-2}$.

Figure 11.6: Estimating the MLMC parameters α and β for modeling uncertainties in a PMSM. The dashed lines and the dashed-dotted line depict the linear least square regressions.

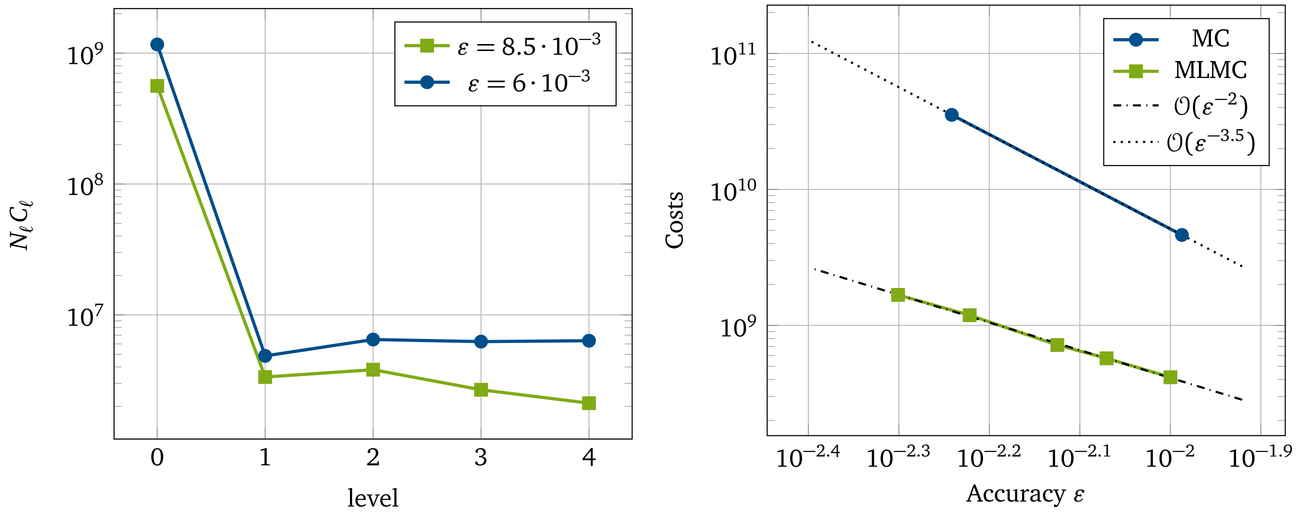

(a) Costs per level for two different user-specified error bounds ε.

(b) Evolution of the costs depending on the desired accuracy ε. The dotted and the dashed-dotted lines depict the linear least square regressions.

Figure 11.7: Study of the costs for the MLMC simulation for the PMSM.

The expected magnetic energy for machines with welding uncertainties and with uncertainties in the magnets is $\mathbb{E}_{\mathrm{ML}}[W] = 24.70\,\mathrm{J}$ with a $\mathrm{std}[W] = 0.61\,\mathrm{J}$, whereas the nominal energy was $W = 25.08\,\mathrm{J}$.

11.2.2 Rotor Eccentricity

Following [23, 24], three types of eccentricity were studied, i.e. static eccentricity (Problem 3), inclined rotor shaft (Problem 4) and dynamic eccentricity (Problem 5). The computations are performed on a computer with 128 Gb RAM Intel® Core™ and i7-3820K processors (3.60 GHz). The Electromotive Force (EMF) of the nominal, i.e. healthy, machine is 30.36 V and its Total Harmonic Distortion (THD) is $5.72 \cdot 10^{-2}\,\%$. The nominal torque and its THD are respectively $\tau = 4.060\,\mathrm{Nm}$ and $\mathrm{THD}_\tau = 0.063\,\%$. The

Table 11.2: Numerical results for the expectation values and standard deviations of the EMF and its THD for static eccentricity.

	Method	#FE-evals	$\mathbb{E}[E_0]$(V)	std$[E_0]$(10^{-2} V)	$\mathbb{E}\left[\mathrm{THD}_{E_0}\right]$($10^{-2}$ %)	std$\left[\mathrm{THD}_{E_0}\right]$($10^{-5}$ %)
(i)	MC	10000	30.3750	1.59167	5.73008	1.30366
(ii)	SC	20x20	30.3746	1.52322	5.73005	1.24649
(iii)	RSM-SC	17x13	30.3746	1.52321	5.73005	1.24636
(iv)	RSM-MC	17x13	30.3746	1.52345	5.73005	1.24651

mesh has been chosen so that the relative error of the FEM solution is below 10^{-4} where a mesh with $h_\ell = 0.01$ is used as a reference.

Static Eccentricity

Four different approaches are applied to study the influence of static eccentricity on the EMF and its spectrum. The first approach, denoted by (i) in Table 11.2 is a standard MC method for which 10000 samples are generated. The total computational cost is 47914 s. The second approach, (ii), relies on SC where a 20×20 tensor product grid is used, resulting in $N_{\mathrm{SC}} = 400$ and corresponding to a computational cost of 1061 s and an approximation error below 10^{-12} is obtained. The last two approaches make use of RSMs in order to reduce the computational cost. For the parameter R the number of knots N_R is 17 and for the parameter θ the number of knots is 13. From the knots a 17×13 tensor product grid is constructed. This implies that 221 FE simulations are needed which correspond to a computational time of 540 s. On the RSMs, a sampling with the SC method using a 20×20 grid (iii) and a MC sampling with $N_{\mathrm{MC}} = 10^7$ is performed (iv). The values of the E_0 for every sample are calculated by cubic spline interpolation [23].

The obtained expectation values are in good agreement (Table 11.2). The eccentricity increases the EMF but also the THD which implies that more undesirable effects, such as vibrations and noise, are introduced. The deviation in the results for (i) is due to the fact that the MC method has not yet fully converged. The estimated error on the expectation value is $1.3 \cdot 10^{-5}$ V. The convergence of the expectation value and the standard deviation using (iv) is shown in Figure 11.8. As a reference the result using method (iii) are plotted. The interpolation error is determined by comparing the results of the real FE calculations obtained for (i) and their interpolated counterparts on the RSM. For the used grid the error for the EMF is given by $\epsilon_{E_0} = 3.1 \cdot 10^{-7}$ V. For the THD an interpolation error $\epsilon_{\mathrm{THD}_{E_0}} = 9.8 \cdot 10^{-10}$ % is obtained. The influence of the number of grid points on the interpolation error is shown in Figure 11.9. The quantity l is the distance between two knots and defined as $0.6/(\mathrm{N_R} - 1)$ mm, where N_R is the number of knots for parameter R. The interpolation error increases with $\mathcal{O}(l^4)$ as expected from theory [122].

The global sensitivities are respectively $S_R \approx 1$ and $S_\theta < 10^{-4}$. This is linked to the symmetry in the stator of the machine. Obviously it does not matter in which direction the rotor is shifted. However the change in airgap width, related to R, does play an influential role.

Inclined Rotor Shaft

The RSM constructed for (iii) and (iv) is re-used to model uncertainties connected to an inclined rotor shaft configuration [23]. The results are depicted in Table 11.3. For (v), $N_{\mathrm{MC}} = 10^5$ and the procedure depicted in Figure 9.6b is applied to determine the EMF of the machine. For (vi), the same procedure is applied, but now the sample points are determined by using SC. The number of used collocation points

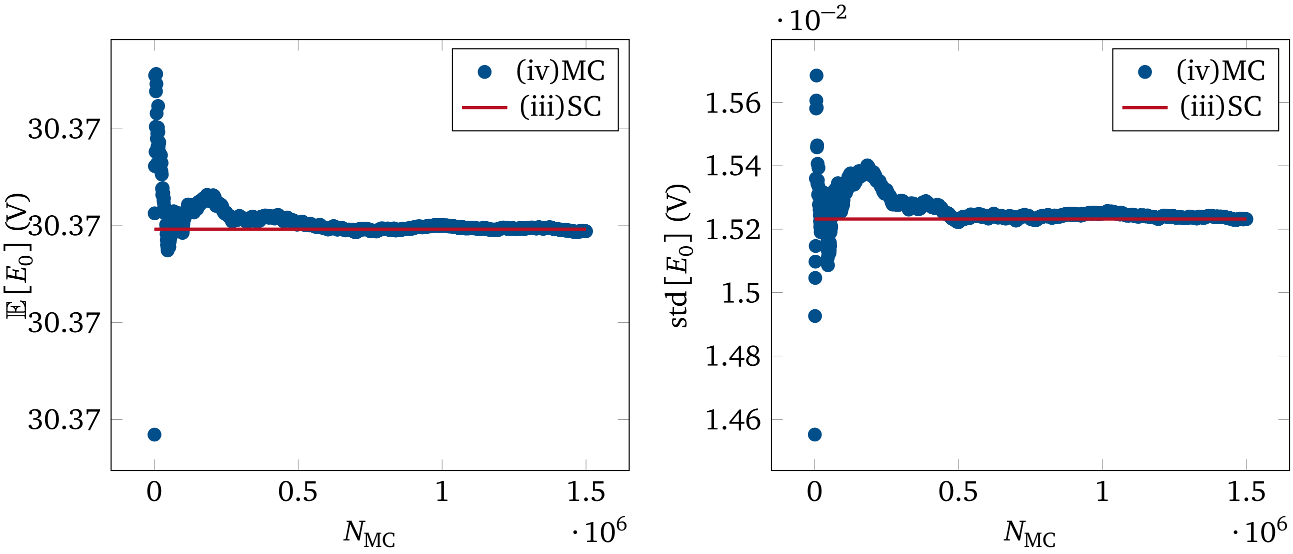

(a) Convergence of te expectation value to the reference solution. **(b)** Convergence of the std to the reference solution.

Figure 11.8: Convergence of the expectation value and the std of the EMF using MC to study static eccentricity. The sampling is done on the RSM introduced in Section 9.5.1. As a reference the results using SC with $N_{\mathrm{SC}} = 20^2$ are used.

Table 11.3: Numerical results for the expectation values and standard deviations of the EMF for machines with an inclined rotor shaft.

	Method	#FE-evals	$\mathbb{E}[E_0]$(V)	std $[E_0]$(10^{-3} V)
(v)	RSM-MC	17x13	30.3711	7.71216
(vi)	RSM-SC	17x13	30.3710	7.60380

is $N_{\mathrm{SC}} = 15^4$. The standard deviations are two times smaller than the results of static eccentricity. This affirms that static eccentricity being the more pessimistic scenario, since it can only be reproduced with an inclined rotor shaft where both bearings have per coincidence the same displacement.

Dynamic Eccentricity

The influence of dynamic eccentricity on the spectrum of the machine is depicted in Figure 11.10. The harmonic related to the cogging torque, i.e. the 36th harmonic, is increased by 16 % when $\varepsilon_{\mathrm{m}} = 50\,\%$. The increase in cogging torque due to eccentricity is conforming with the observations in previous works such as [85]. The influence of the higher frequencies also increases as the eccentricity raises [24].

For (viii) and (ix) (see Table 11.4) a RSM consisting of a 17 × 13 tensor grid is constructed. Again, cubic splines are used for interpolation. The construction of the RSM has a computational cost of approximately 3 h. This high cost is caused by the pseudo time stepping method, since for one node, 300 different machine positions have to be calculated. Due to this high computational cost, the procedures without RSMs are omitted. For (viii), 10^7 MC samples are calculated on the RSM. It is found that the shift is even more of a dominating parameter than for the static case. For the directional variation it is found that $S_\theta < 10^{-6}$. This is easily understood, since in the dynamic setting, the rotor is doing a full revolution and thus the directional change is less important.

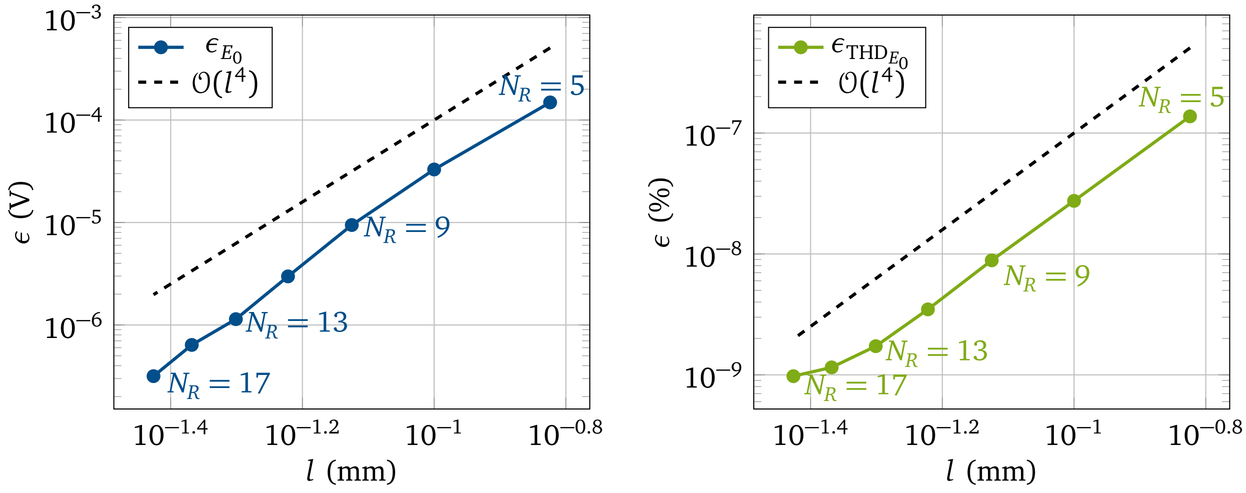

(a) EMF **(b)** THD

Figure 11.9: Increasing the number of knots for R with the number of knots for θ fixed to 13.

Table 11.4: Numerical results for the expectation values and standard deviations of the torque and its THD for dynamic eccentricity adapted from [24].

	Method	#FE-evals	$\mathbb{E}[\tau]$(Nm)	std $[\tau]$(10^{-3} Nm)	$\mathbb{E}[\mathrm{THD}_\tau]$(%)	std $[\mathrm{THD}_\tau]$(10^{-4} %)
(vii)	SC	5x5	4.06553	8.06614	0.0636837	7.72347
(viii)	RSM-MC	17x13	4.06553	8.06430	0.0636839	7.71464
(ix)	RSM-SC	17x13	4.06553	8.06307	0.0636836	7.72662

11.2.3 Preliminary Study of Geometric Uncertainties on the Magnets

During the optimization of the size of the Permanent Magnets (PMs) geometric uncertainties on the PMs are introduced. This preliminary study deals with the influence of these uncertainties on the EMF. The description is postulated in Problem 6. Only one pole of the machine is considered which corresponds to the case of a systematic error where six magnets have the same uncertain magnet size and the same uncertain position in the rotor. The expectation value and the standard deviation of the EMF is determined using SC and MC. For SC the polynomial degree for every parameter is set to four, implying $N_{\mathrm{SC}} = 5^3$ collocation points, so that an error of $\varepsilon_{\mathrm{SC}} < 10^{-6}$, see (11.1), can be obtained. For the MC 5000 samples are generated so that the estimated error is $\varepsilon_{\mathrm{MC}} = 0.003\,\mathrm{V}$. The results are listed in Table 11.5. From the standard deviations it is clear that the uncertainties on the magnets have a bigger impact on the EMF, than the uncertainties dealing with static eccentricity or an inclined rotor shaft.

11.3 Résumé

The Multilevel Monte Carlo (MLMC) method has been applied on an academic example. It is shown that the spatial error can be controlled by a Richardson-extrapolation-based error indicator. Furthermore it is shown that the different levels do not have to be constructed with nested meshes, but that one can remesh for every level. This two findings were essential to apply the method on a real world problem, i.e. a permanent magnet synchronous machine with uncertainties in the magnets and material uncertainties in the welding regions of the stator. It enabled the control of the mesh size parameters so that the finite element matrices related to the different levels are still manageable with reasonable costs. It is shown

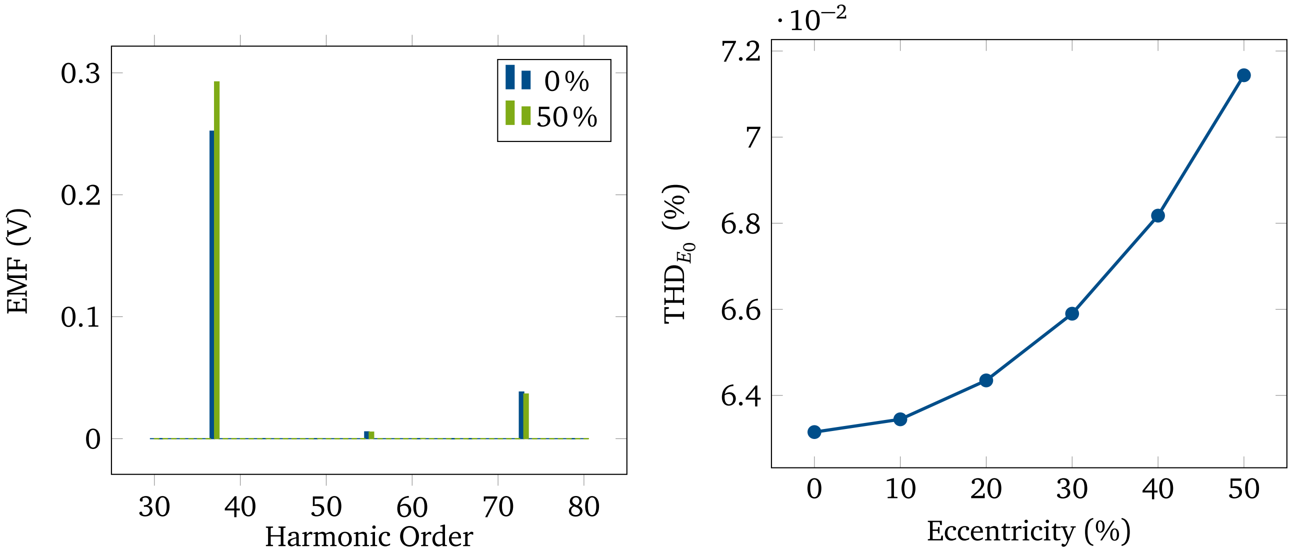

(a) A part of the spectrum for a nominal machine and a machine with $\varepsilon_m = 50\,\%$.

(b) The THD as a function of rotor eccentricity.

Figure 11.10: Study of the influence of eccentricity on the spectrum of the torque.

Table 11.5: Numerical results for Problem 6.

Method	#FE-evals	$\mathbb{E}[E_0]$(V)	std $[E_0]$(V)
SC	125	30.3688	0.2046
MC	5000	30.3730	0.2095

that the overall computational cost for determining the expectation value and the standard deviation is one order of magnitude lower for MLMC than for standard MC.

The influence of rotor eccentricity has been quantified for three different types of eccentricity, namely, static eccentricity, inclined rotor shaft and dynamic eccentricity. For the first two settings the electromotive force (EMF) and its total harmonic distortion have been studied. It is found that for eccentric machines both quantities increase due to the eccentricity and that static eccentricity is the most pessimistic scenario. In the case of dynamic eccentricity the focus was on the torque and its spectrum. It was found that the cogging torque increases and that higher frequencies become more and more dominant. Finally the influence of the uncertainties on the geometric parameters describing the permanent magnets were studied. The obtained standard deviation indicates that the electromotive force is more influenced by these uncertainties than by eccentricity.

12 Optimization

In this chapter the results of the optimization problems previously introduced in Section 8.3 and Section 9.6 are discussed. First the focus is on the Stern–Gerlach magnet for which a shape optimization with an underlying Iso-Geometric Analysis (IGA) model is performed. The second application is the reduction of the size of the Permanent Magnets (PMs) in the machine. The focus is here on the comparison between two different robust optimization formulations and their equivalences. The third and final optimization is dealing with the driving cycle of PMSM.

12.1 Shape optimization of a Stern–Gerlach magnet using Iso-Geometric Analysis

The optimization under consideration is described in Problem 2 and is conducted in two parts. Firstly, a global optimization with a pattern search algorithm from MATLAB's Optimization Toolbox, `GPSPositiveBasis2N`, is performed. As initial geometry Ω_{ref} is chosen. Third order B-splines are employed and the `GeoPDEs`' mesh is refined such that the relative error of the solution is smaller than 10^{-2}. Afterwards, a gradient-based optimization is conducted by using Matlab's `fmincon` function. To have a smooth solution for the gradients, the order of the basis functions is increased to 5. To reduce the computational costs, the optimization is carried out using a linearized model, meaning that the non-linear saturation is frozen such that a constant but inhomogeneous reluctivity is used [118].

For the reflection of the particles a high field gradient was desired. The gradients of the initial geometry are shown in Figure 12.1 and the ones produced by the optimized geometry are depicted in Figure 12.2. The discrepancies are attributed to the 2D approximation, the exact representation of the geometry and the frozen saturation used in the IGA simulation. Both simulations show that the optimized geometry provides a higher and more homogeneous gradient. The smoothness of the field gradient is even more pronounced in the IGA simulation, due to the use of higher order B-Splines. The optimized geometry is depicted in Figure 12.3. The resulting values for the optimization parameters are

$$\begin{aligned}
x_1 &\in 2.00\,\mathrm{mm}, & y_1 &\in 1.66\,\mathrm{mm}, & w_1 &= 0.85,\\
x_2 &\in 4.11\,\mathrm{mm}, & y_2 &\in 4.50\,\mathrm{mm}, & w_2 &= 1.25,\\
x_3 &\in 2.50\,\mathrm{mm}, & y_3 &\in 1.90\,\mathrm{mm}, & w_3 &= 0.87,\\
x_4 &\in 2.00\,\mathrm{mm}, & y_4 &\in 4.00\,\mathrm{mm}, & w_4 &= 0.37.
\end{aligned}$$

Table 12.1 contains the numerical results. The average magnetic field gradient has been improved with at least 12.5 % and the homogeneity of the field with at least 60 %.

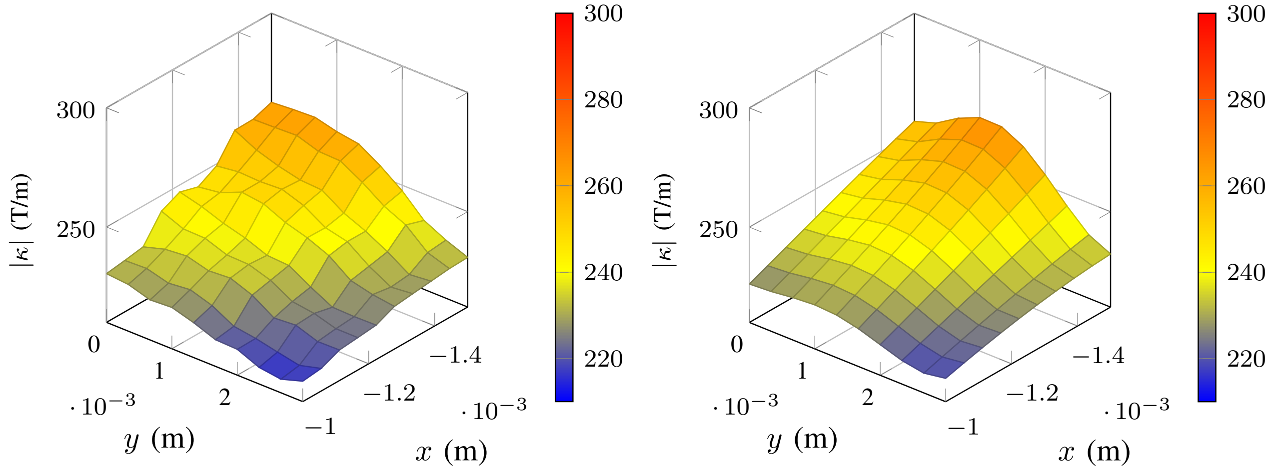

(a) 3D simulation using CST EM STUDIO®.

(b) 2D simulation using GeoPDEs.

Figure 12.1: Comparison of the magnetic field gradient κ for the initial geometry of the Stern–Gerlach magnet. Figures adapted from [118].

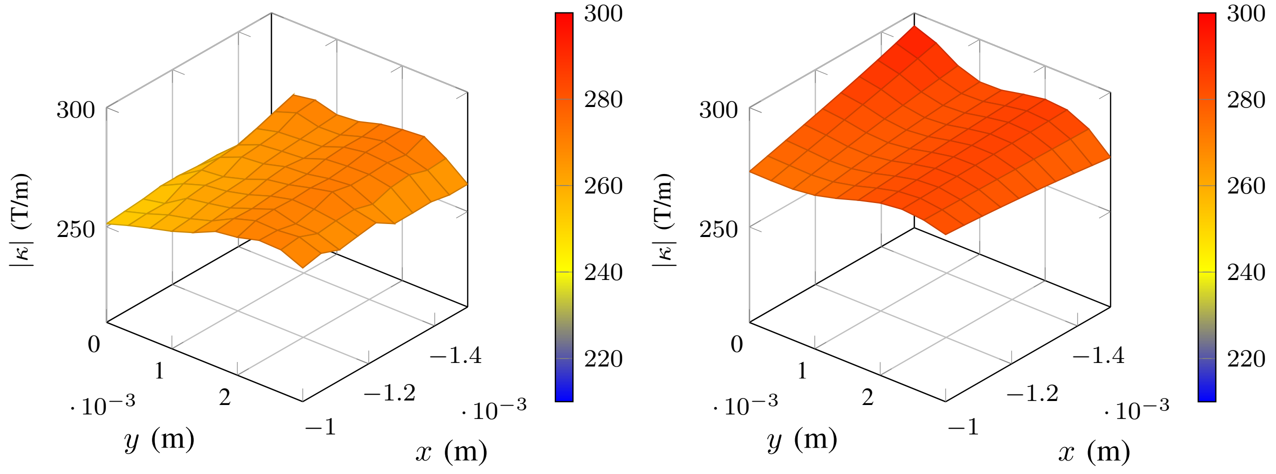

(a) 3D simulation using CST EM STUDIO®.

(b) 2D simulation using GeoPDEs

Figure 12.2: Comparison of the magnetic field gradient κ for the optimized geometry of the Stern–Gerlach magnet. Figures adapted from [118].

Table 12.1: Improvement in the average magnetic field gradient and inhomogeneity of the magnetic field in a Stern–Gerlach magnet after optimization.

	Ω_{ref}		$\Omega^{\star}$		Improvement (%)	
	κ_{av} (T/m)	ϵ_{in}	κ_{av} (T/m)	ϵ_{in}	κ_{av}	ϵ_{in}
FEMM (2D)	−238	0.0523	-	-	-	-
CST (3D)	−237	0.0503	−266	0.0201	12.2	60.0
GeoPDEs (2D)	−240	0.0477	−282	0.0122	17.5	74.4

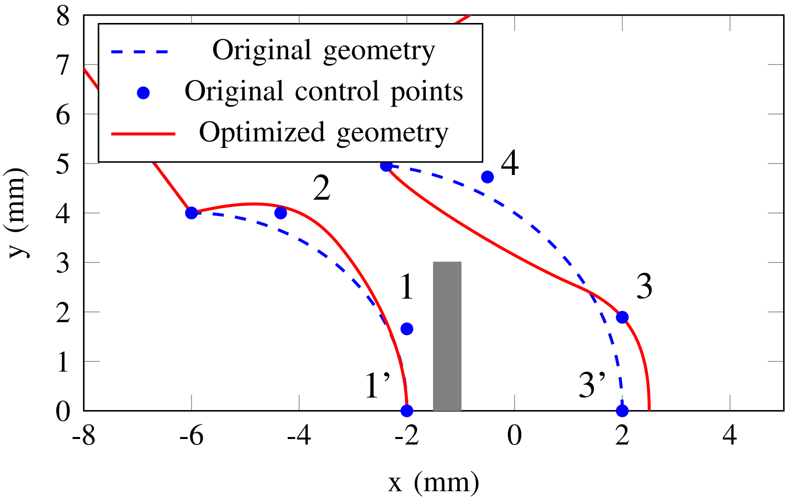

Figure 12.3: Comparison of the initial and optimized poles of the Stern–Gerlach magnet (adapted from [118]).

12.2 On the Equivalence Between Robust Optimization Formulations

Now the results for the optimization of the PMSM discussed in Section 9.6 are addressed. First the focus is on the nominal optimization (see Problem 8) with the deterministic and stochastic formulation. Secondly, the results for the different robust optimization formulations are discussed and the quality of the robustness of the optimum with respect to deviations is studied. To study the robustness of each optimum, the same Monte Carlo (MC) sampling with $N_{\text{MC}} = 10000$ is performed around each optimal configuration. The distributions are according to the ones mentioned in Section 9.5.2. For every sample the EMF, E_0 is determined and compared with the desired EMF, E_{d}. The failure rate is defined as $N_{\text{fail}}/N_{\text{MC}}$, where N_{fail} is the number of machines with $E_0 < E_{\text{d}}$. The results were published in [24]. The mesh has been chosen so that the relative error of the FEM solution is below 10^{-4} where a mesh with $h_{\ell} = 0.01$ is used as a reference.

The optimization algorithms under consideration are Sequential Quadratic Programming (SQP) with damped Broyden-Fletcher-Goldfarb-Shanno updates for the Hessians, Particle Swarm Optimization (PSO) and genetic algorithm (GA). The stochastic quantities for the stochastic formulations are determined by Stochastic Collocation (SC) and MC. For the former a 5 × 5 × 5 tensor grid is constructed and a Gauß-Legendre quadrature is applied, so that $\varepsilon_{\text{SC}} < 10^{-5}$, see (11.1). For the latter $N_{\text{MC}} = 5000$ random samples are generated such that $\varepsilon_{\text{MC}} < 1\%$ for all optimizations. All computations are performed on a 16 GB RAM Intel® Core™ with i7-3820K processors (3.60 GHz).

As a reminder, the reader is referred to Table 9.2 for an overview of the different formulations and optimization algorithms under consideration.

Table 12.2: Numerical results for the different nominal optimization formulations [25]. The corresponding cost functions and constraints are listed in Table 9.2.

Name	RB	Method	UQ	**P**(mm)	$S_{\mathrm{pm}}(\mathrm{mm}^2)$	E_0 (V)	Failure (%)	Time (s)
Initial	-	-	-	(19.00, 7.00, 7.00)	133	30.370	50.17	-
Nominal (i)	-	SQP	-	(21.07, 2.98, 6.61)	62.80	30.37	51.14	3.3
Nominal (ii)	-	SQP	SC	(21.07, 2.98, 6.61)	62.80	30.37	50.19	224
Nominal (iii)	-	SQP	MC	(21.07, 2.98, 6.61)	62.83	30.37	50.19	10774
Nominal (iv)	-	PSO	-	(21.06, 2.98, 6.60)	62.80	30.37	51.34	818
Nominal (v)	-	GA	-	(21.44, 2.98, 7.16)	63.39	30.37	51.33	2385

12.2.1 Nominal Optimization

In the PSO, the swarm consists of 50 particles and a maximum of 100 iterations is allowed. N_{stall} is chosen to be 15. For both methods the swarm characteristics are set to $\lambda_0 = 0.5$ and $\lambda_1 = \lambda_2 = 1.49$ and the change tolerance is set to 10^{-6}. The own SQP is stopped when an accuracy of 10^{-3} is reached or when a maximum of 10 iterations is reached. The `MATLAB` implementation of the GA is used as a standard comparison.

Table 12.2 summarizes the results for the nominal optimization problem [25]. All methods result in comparable PM sizes and the new designs maintain the desired electromotive force. The size of the magnets has been reduced ny more than 50 %, which implies that the initial configuration resembled a poor design. The SQP with the deterministic formulation, i.e. Nominal (i), outperforms PSO and GA by, respectively, two and three orders of magnitude. In the field of optimization there is a strong tendency to use nature inspired optimization algorithms, such PSO and GA, since the discretizing can be used as a black-box. However, for this example it is shown, that manipulating the discretization by relying on an affine parametrization, the deterministic optimization algorithm outperforms PSO and GA.

12.2.2 Robust Optimization

The Reduced Basis (RB) used in the simulations is based on *dictionaries* (cf. Figure 4.2). In this application the parameter space is split into $N_{\mathrm{Par}} = 40$ partitions. Every partition represents a cube Q_{ijk} in the parameter space, which is defined as

$$\begin{aligned} Q_{ijk} =& [t_i^{(1)}, t_{i+1}^{(1)}] \times [t_j^{(2)}, t_{j+1}^{(2)}] \times [t_k^{(3)}, t_{k+1}^{(3)}] \\ \text{with} \quad t_i^{(l)} \in& p^{(l)}; \\ p^{(1)} =& [0.5, 3, 6, 8, 11, 13, 16, 18, 21, 23, 26.5]; \\ p^{(2)} =& [0.5, 7.5, 10.5]; \\ p^{(3)} =& [4.5, 7.5, 14.5]. \end{aligned}$$

For each partition a separate reduced order model is generated. In the online phase for a given parameter P the associated partition is determined and the corresponding reduced model is utilized. This results in low dimensional models that can be evaluated rapidly. In this application the construction of the dictionary, i.e. the offline phase, took 234 s and the initial number of unknowns (8128) has been reduced to 40 bases of size 27.

Table 12.3 summarizes the results for the robust optimization procedures. The maximal deviation considered was $\Delta^{\mathrm{b}} = 0.2\,\mathrm{mm}$. The resulting geometries are depicted in Figure 12.4. One sees that the size of the PM has decreased substantially while maintaining the desired EMF. When a lot of PDE evaluations

Table 12.3: Robust optimization results obtained by for $\Delta^{\mathrm{b}} = 0.2\,\mathrm{mm}$ [25]. The column RB list the number of basis function used and 'Time' distinguishes between online and offline costs if RB was used. The corresponding cost functions and constraints are listed in Table 9.2.

Name	RB	Method	UQ	$\mathbf{P}$(mm)	$S_{\mathrm{pm}}(\mathrm{mm}^2)$	E_0 (V)	Failure (%)	Time (s)
Initial	-	-	-	(19.00, 7.00, 7.00)	133	30.370	50.17	-
Linearized (i)	-	SQP	-	(20.88, 3.73, 6.82)	77.66	31.09	0	6.7
Linearized (ii)	-	SQP	-	(20.95, 3.44, 6.78)	72.01	30.82	4.28	15
Linearized (iii)	-	SQP	SC	(20.95, 3.44, 6.82)	72.10	30.82	4.03	585
Linearized (iv)	27	SQP	SC	(20.95, 3.44, 6.82)	72.10	30.82	4.03	234+301
Robust (i)	-	SQP	SC	(20.86, 3.53, 6.78)	73.66	30.82	4.36	239
Robust (ii)	-	SQP	MC	(20.86, 3.53, 6.78)	73.71	30.81	4.28	14400
Robust (iii)	-	PSO	SC	(21.16, 3.22, 6.68)	68.04	30.86	3.91	2670
Robust (iv)	-	GA	SC	(21.37, 3.23, 7.06)	69.02	30.85	4.02	3660
Robust (v)	27	SQP	SC	(20.86, 3.53, 6.78)	73.66	30.82	4.44	234+39
Robust (vi)	27	SQP	MC	(20.86, 3.53, 6.78)	73.71	30.82	4.04	234+1550
Robust (vii)	27	PSO	SC	(20.99, 3.27, 6.48)	68.52	30.84	4.21	234+265
Robust (viii)	27	GA	SC	(21.60, 3.23, 7.39)	69.86	30.85	4.27	234+1700

are needed, the use of the RB method accelerates the optimization procedures substantially. Applying SQP as optimization algorithm and using MC for determining the expectation values and standard deviations, one can observe an acceleration by a factor of almost 10. However, since the number of random variables under consideration is low, the use of SC is more beneficial and the gain of the reduced models is obsolete.

A previous work [99] considers the same optimization parameters and the authors used a deterministic and stochastic formulation for the nominal optimization. The robustification is only performed by a worst-case analysis and only evolutionary algorithms are used. However, the robust algorithm in that paper comes with an extensive computation time [99] and there is a need to apply a prediction to estimate the worst-case to avoid additional sampling. The results of Linearized (i) in Table 12.3 show that it is possible to apply a worst-case optimization with a minor increase in computational cost with respect to the nominal optimization when a gradient based method is used.

For PSO and GA the combination of SC and RB does pay off, since at every iteration many more PDE-solves have to be conducted. The difference in the permanent magnet sizes for applying RB or not is less then 0.1 % when using the SQP algorithm whereas for PSO and GA the difference is around 1 %. It seems that these procedures are slightly more influenced by the use of model order reduction.

Let us now focus on the failure rates. The robust optimization procedures give failure rates around 4 %, whereas for the worst case approach, Linearized (i), all machines fulfill the prerequisite. The gain in reduction of the size for the robust procedures, comes with the drawback that the resulting optima are less robust with respect to rare deviations under consideration.

The equivalence between the different approaches is shown in Figure 12.5. The maximal deviation Δ^{b} is decreased from 0.2 mm to 0 mm. The stochastic quantities in the UQ setting are determined by SC. As expected, all robust optimization methods converge to the optimized magnet size of Nominal (i) as Δ^{b} becomes smaller. The equivalence between Linearized (ii) and Linearized (iii) is also observed numerically, which is a numerical confirmation of Theorem 2 in Section 6.2.1. The results between Linearized (i) and Robust (i) do differ. This is caused by the fact that the former is a more pessimistic scenario since it mitigates the worst case. By incorporating the second moment, more stochastic information during optimization is considered. This eventually translates into more optimistic results, because rare events are less punished or even totally disregarded. Hence, a stronger reduction of the size of the PM is obtained (Table 12.3).

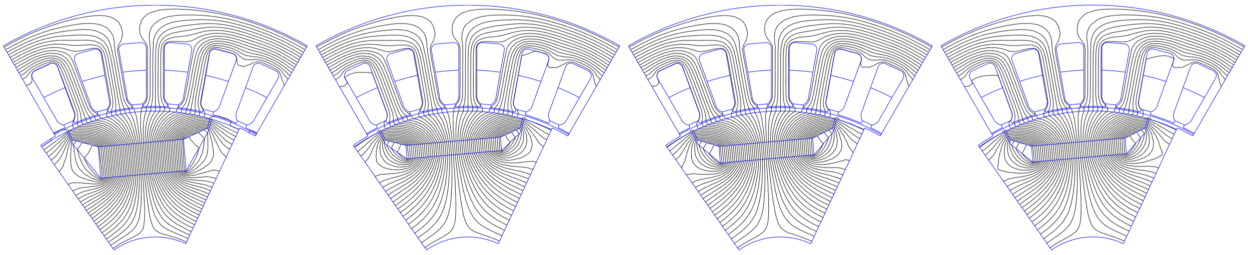

(a) Initial **(b)** Nominal (i) **(c)** Linearized (i) **(d)** Robust (v)

Figure 12.4: Optimized PMSM design

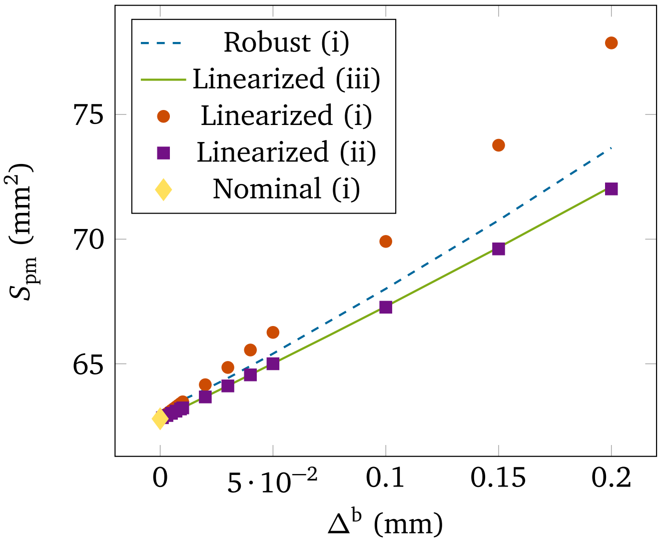

Figure 12.5: Optimization results for different values of Δ^{b}. The yellow diamond is the size of the PMs obtained by using Nominal (i). The red dots and the purple squares are the results using Linearized (i) and Linearized (ii) respectively. The green line depicts Linearized (iii). The blue line represents Robust (i).

12.3 Considering a Driving Cycle and the Maximal Torque

The driving cycle under consideration is the urban driving cycle shown in Figure 9.4a which is part of the new European driving cycle. The European driving cycle represents the usage of light-duty vehicles in Europe and is used in other works as a benchmark for optimization, e.g. [95]. The vehicle is assumed to be a e-Go-Cart and the values used to determine the torques are found in Appendix B. The optimization description is found in Problem 9.

For the robust optimization the stochastic quantities are determined by SC. The polynomial degree has been set to 4, so that $\varepsilon_{\mathrm{SC}} < 10^{-5}$, defined in (11.1). The optimization results are listed in Table 12.4. The nominal optimization and the robust optimization both reduce the size of the magnet, by 50 % and approximately 46 %, respectively. There is for both a slight increase in mean efficiency. However, the robust optimization results in a higher maximal torque. With respect to the optimization considering the EMF, the nominal optimization results in slightly larger permanent magnet sizes (approximately 5 %). This is contrast to the results obtained with robust optimization. The resulting magnets are 2.4 % smaller than the results of the optimization with respect to the EMF. The origin of these differences needs further investigation.

As in the previous section, the failure rates were determined again (Figure 12.7). Therefore a MC sampling was performed, with $N_{\mathrm{MC}} = 5000$. The distributions are according to the ones mentioned in Section 9.5.2. For every sample the efficiency and the maximal torque are determined and compared

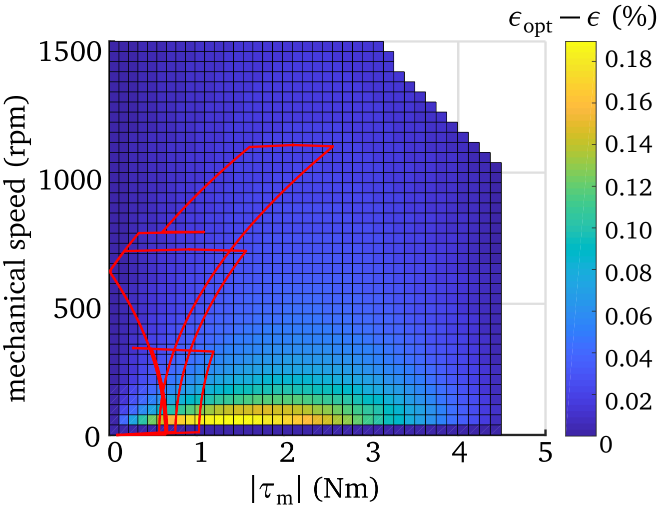

Figure 12.6: Difference in point-wise efficiency between the robust optimized and initial configuration.

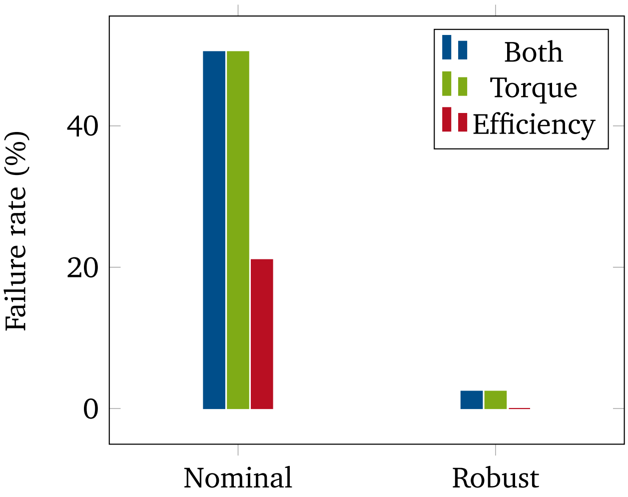

Figure 12.7: Failure rates around each found optimum. The blue bar considers both constraints. The green bars only considers the constraint on the maximal torque and the red bar only considers the constraint on the efficiency.

with their desired values. The failure rate is defined as $N_{\mathrm{fail}}/N_{\mathrm{MC}}$, where N_{fail} is the number of machines with $\mathcal{E} < \mathcal{E}_{\mathrm{d}}$ and $\tau_{\max} < \tau_{\mathrm{d}}$. The sampling around the nominal optimum results in a fail rate of 50.5 %. The robust optimum results in a failure rate of only 2.44 %. It is the restriction on the maximal torque that determines the overall failure rate. For the robust optimum all configurations fulfill the requirement on the efficiency.

12.4 Résumé

Iso-Geometric Analysis (IGA) has been used to model a Stern–Gerlach magnet. The geometry of the device has been optimized successfully by considering the weights and the positions of the nodes as optimization parameters. It has been shown that IGA can be useful tool for shape optimization of electromagnetic devices.

The size of the permanent magnets in a synchronous machine has been optimized while maintaining a desired electromotive force. The implementation of an affine decomposition enabled the parametrization of the geometry in the finite element method such that exact derivatives with respect to geometric

Table 12.4: Optimization results considering the efficiency and maximal torque

Name	$\mathbf{P}$(mm)	S_{pm}(mm^2)	$\mathcal{E}$ (%)	$\tau_{\max}$ (Nm)
Initial	(19.00, 7.00, 7.00)	133	96.37	4.49
Nominal	(20.89, 3.17, 6.34)	66.32	96.52	4.49
Robust	(21.08, 3.41, 6.53)	71.92	96.52	4.56

parameters were available. This alleviated one of the major drawbacks of gradient-type deterministic optimization methods. It was found that the gradient based optimization algorithm outperformed particle swarm optimization with a factor of 100. The equivalence between robust worst-case optimization and variance-based optimization has been numerically supported, if a linearization was applied and the norms were chosen adequately. The approaches were used to reduce the size of the permanent magnets in a permanent magnet synchronous machine while maintaining the electromotive force. Robust optimization in which standard deviations were considered resulted in less pessimistic optima. Whereas the worst-case optimization also considered scenarios which are possible but unlikely to happen. However, the computational time for variance based optimization was significantly increased whereas the implementation effort was reduced since no (further) derivatives were needed.

A final results in this section were related to the optimization of the size of the permanent magnets considering a urban driving cycle. It is found that the restriction on the maximal torque of the machine is more important than the restriction on the efficiency of the machine for determining the failure rates.

Movement V
Allegro vivace: Epilogue

13 Summary and Outlook

> "I am not young enough to know everything."
>
> Attributed to O. Wilde

In this dissertation different aspects for the development and simulation of electric devices have been addressed. The first aspect is the construction of reliable numerical models of the devices, which can serve as virtual prototypes. The application of Iso-Geometric Analysis (IGA) to the simulation of a Permanent Magnet Synchronous Machine (PMSM) has been proposed in this work. The advantages with respect to the classical finite element method are that the computational domain is represented exactly and a higher regularity of the solutions fields is guaranteed. A numerical efficient procedure was developed with the implementation of a particular domain decomposition method, namely harmonic stator-rotor coupling. The stability of this procedure has been studied and shown. The comparison with a monolithic finite element method (FEM) has demonstrated that the proposed procedure yields comparable values for the quantities of interest, however at a lower computational cost.

Another important step in the development of devices is the optimization of the machine. IGA has also been applied for the shape optimization of a Stern-Gerlach magnet. Exploiting the ingredients for constructing the geometry using B-Splines and Non Uniform Rational B-Splines NURBS, i.e. the notion of control points and weights, and exploiting the higher smoothness, a bigger improvement in the quantities of interest with respect to a 3D FEM procedure has been achieved.

Furthermore the influences of deviations on parameters describing the reference model have been studied. In the case of optimization, different robust optimization formulations and optimization algorithms were discussed and compared with each other. The formulations under consideration were deterministic and stochastic. The former considered the worst case scenario, whereas the latter took stochastic quantities into account. It was shown mathematically and confirmed numerically that both formulations are equivalent when a linearization was applied. Moreover, an affine decomposition has been introduced into the FEM-code to efficiently solve the Partial Differential Equations (PDEs). Therefore, a particularly efficient optimization procedure could be established by using sequential quadratic programming. For both formulations this deterministic algorithm outperformed all stochastic algorithms under consideration, i.e. particle swarm optimization and genetic algorithms. The implementation of a reduced order model showed beneficial when a lot of PDEs solves were required.

Finally, uncertainty quantification has been conducted on the PMSM. It was studied how different types of rotor eccentricity influence the electromotive force and the torque of the machine. Their expectation values and standard deviations were calculated. The eccentricities under consideration were static eccentricity, dynamic eccentricity and an inclined rotor shaft. The methods applied for uncertainty quantification were stochastic collocation and standard Monte Carlo (MC) method. A numerically cheap methodology was constructed using response surface models. A first model to mimic welding uncertainties in the stator region of the PMSM has been constructed. To reduce the computational cost to handle the high number of uncertain parameters a Multilevel Monte Carlo (MLMC) method has been proposed. MLMC has first been benchmarked on a coaxial cable. It was found that a Richardson-extrapolation-based error indicator is a reliable way to estimate the weak error caused by the discretization. It was also found that the meshes used for the different levels do not have to be nested. A reduction in computational costs of one order of magnitude has been achieved.

The easy handling of geometric changes in the optimization of the Stern-Gerlach Magnet and the successful simulation of an electric machine with IGA showed, that IGA appears to be a promising tool for considering geometric uncertainties in a PMSM. The computational benefits of using MLMC for uncertainty quantification with many uncertain parameters, might enable a detailed study of welding influences on an electric machine. The current model only considered uncertainties in the material properties due to the welding. However, the combination of IGA with MLMC might enable the consideration of geometric uncertainties due to the welding process, such as minor displacements of every stator tooth.

The current IGA model constructs the airgap of the machine with different patches. As mentioned along the patches only C^0-continuity is guaranteed. From different works, e.g. [84], it is known that the discretization of the airgap influences the results on the torque and its higher harmonics. The feasibility of constructing the airgap with one patch and applying a domain decomposition method for the stator-airgap-coupling and the rotor-airgapcoupling could be the study of future work.

The harmonic stator-rotor coupling proved very useful for incorporating the rotation of the machine. However, still some questions remain open. There is the question if there is a link between the harmonics one choses for the coupling and the harmonics of the electromotive force evaluated on the intersection of the two subdomains. Another open question is the observed convergence order of the Lagrange multipliers, i.e. $\mathcal{O}(h^{2p})$. In the current literature there is no theory found that proves the convergence rate of these Lagrange multipliers in the Iso-Geometric setting. Further studies could also focus on the stability of the saddle-point problem. In this work the stability has been guaranteed by a numerical study. From the work in [79] it is known that the saddle-point problem can be stabilized using regularization. The applicability of this regularization could be investigated for this coupling scheme.

The uncertainties addressed in this thesis only focused on parameters describing the machine. However, electric machines are driven with electronic controls. Further research could study how uncertainties in the control influence the behavior or the machine.

For the optimization with respect to the driving cycle, one could include uncertainties on the driving cycle to mimic changes in traffic. One could also include changes of the road pavement by varying the restive rolling force or change the relief of the trajectory by adding an extra variable force term.

Bibliography

[1] M. N. Albunni, V. Rischmuller, T. Fritzsche, and B. Lohmann, “Multiobjective optimization of the design of nonlinear electromagnetic systems using parametric reduced order models”, *IEEE Transactions on magnetics*, vol. 45, no. 3, pp. 1474–1477, 2009.

[2] A. Alexanderian, P. Noemi, G. Stadl, and O. Ghattas, “Mean–variance risk–averse optimal control of systems governed by PDEs with random parameter fields using quadratic approximations”, *SIAM/ASA Journal on Uncertainty Quantification*, vol. 5, no. 1, pp. 1166–1192, 2017.

[3] G. Archer, A. Saltelli, and I. Sobol, “Sensitivity measures, ANOVA-like techniques and the use of bootstrap”, *Journal of Statistical Computation and Simulation*, vol. 58, no. 2, pp. 99–120, 1997.

[4] I. Babuška and P. Chatzipantelidis, “On solving elliptic stochastic partial differential equations”, *Computer Methods in Applied Mechanics and Engineering*, vol. 191, no. 37-38, pp. 4093–4122, 2002.

[5] I. Babuška, F. Nobile, and R. Tempone, “A stochastic collocation method for elliptic partial differential equations with random input data”, *SIAM Journal on Numerical Analysis*, vol. 45, no. 3, pp. 1005–1034, 2007.

[6] I. Babuška, R. Tempone, and G. E. Zouraris, “Solving elliptic boundary value problems with uncertain coefficients by the finite element method: the stochastic formulation”, *Computer methods in applied mechanics and engineering*, vol. 194, no. 12-16, pp. 1251–1294, 2005.

[7] A. Barth, C. Schwab, and N. Zollinger, “Multi-level Monte Carlo finite element method for elliptic PDEs with stochastic coefficients”, *Numerische Mathematik*, vol. 119, no. 1, pp. 123–161, 2011.

[8] V. Barthelmann, E. Novak, and K. Ritter, “High dimensional polynomial interpolation on sparse grids”, *Advances in Computational Mathematics*, vol. 12, no. 4, pp. 273–288, 2000.

[9] J.-L. Basdevant and J. Dalibard, “The stern-gerlach experiment”, in *Quantum Mechanics*, Springer Verlag Berlin, 2002, ch. 7, pp. 157–176.

[10] K.-J. Bathe, “The inf–sup condition and its evaluation for mixed finite element methods”, *Computers & structures*, vol. 79, no. 2, pp. 243–252, 2001.

[11] Z. Bayraktar, M. Komurcu, J. Bossard, and D. Werner, “The wind driven optimization technique and its application in electromagnetics”, *IEEE Transactions on Antennas and Propagation*, vol. 61, no. 5, pp. 2745–2757, 2013.

[12] F. B. Belgacem, “The Mortar finite element method with Lagrange multipliers”, *Journal of Numerical Mathematics*, vol. 84, pp. 173–197, 1999.

[13] R. Belmans, A. Vandenput, and W. Geysen, “Calculation of the flux density and the unbalanced pull in two pole induction machines”, *Electrical Engineering (Archiv fur Elektrotechnik)*, vol. 70, no. 3, pp. 151–161, 1987.

[14] R. Belmans, A. Vandenput, and W. Geysen, “Influence of unbalanced magnetic pull on the radial stability of flexible-shaft induction machines”, *IEE Proceedings B - Electric Power Applications*, vol. 134, no. 2, pp. 101–109, 1987.

[15] A. Ben-Tal and A. Nemirovski, “Robust solutions of linear programming problems contaminated with uncertain data”, *Mathematical programming*, vol. 88, no. 3, pp. 411–424, 2000.

[16] A. Ben-Tal and A. Nemirovski, “Robust optimization–methodology and applications”, *Mathematical Programming*, vol. 92, no. 3, pp. 453–480, 2002.

[17] D. Bertsimas, D. B. Brown, and C. Caramanis, “Theory and applications of robust optimization”, *SIAM Review*, vol. 53, no. 3, pp. 464–501, 2011.

[18] H. G. Beyer and B. Sendhoff, “Robust optimization–a comprehensive survey”, *Computer methods in applied mechanics and engineering*, vol. 196, no. 33, pp. 3190–3218, 2007.

[19] P. Bhat, Z. Bontinck, S. Schöps, and H. De Gersem, “Modelling of electric machines using isogeometric analysis and non-overlapping schwarz domain decomposition”, *COMPEL: The international journal for computation and mathematics in electrical and electronic engineering*, vol. 37, no. 5, pp. 1805–1814, 2018.

[20] A. Binder, “Permanentmagneterregte synchronmaschinen”, in *Elektrische Maschinen und Antriebe: Grundlagen, Betriebsverhalten*. Springer-Verlag, 2012, ch. 9, pp. 603–732.

[21] K. Binnemans, P. T. Jones, B. Blanpain, T. Van Gerven, Y. Yang, A. Walton, and M. Buchert, “Recycling of rare earths: a critical review”, *Journal of cleaner production*, vol. 51, pp. 1–22, 2013.

[22] Z. Bontinck, J. Corno, S. Schöps, and H. De Gersem, “Isogeometric analysis and harmonic stator–rotor coupling for simulating electric machines”, *Computer Methods in Applied Mechanics and Engineering*, vol. 334, pp. 40–55, 2018.

[23] Z. Bontinck, H. De Gersem, and S. Schöps, “Response surface models for the uncertainty quantification of eccentric permanent magnet synchronous machines”, *IEEE Transactions on Magnetics*, vol. 52, no. 3, pp. 1–4, 2016.

[24] Z. Bontinck, O. Lass, H. De Gersem, and S. Schöps, “Uncertainty quantification for a permanent magnet synchronous machine with dynamic rotor”, in *Progress in Industrial Mathematics at ECMI 2016*, P. Quintela, P. Barral, D. Gomez, F. Pena, J. Rodriguez, P. Salgado, and M. Vazquez-Mendez, Eds., Springer Verlag, 2018, pp. 493–499.

[25] Z. Bontinck, O. Lass, H. De Gersem, S. Schöps, S. Ulbrich, and O. Rain, “Robust optimization formulations for the design of an electric machine”, *IET Science, Measurement & Technology*, vol. 12, no. 8, pp. 939–948, 2018.

[26] C. de Boor, *A Practical Guide to Splines*, rev., ser. Applied Mathematical Sciences. New York: Springer, 2001, vol. 27.

[27] B. Boualem and F. Piriou, “Numerical models for rotor cage induction machines using finite element method”, *IEEE transactions on magnetics*, vol. 34, no. 5, pp. 3202–3205, 1998.

[28] S. Brenner and R. Scott, *The mathematical theory of finite element methods*. Springer Science & Business Media, 2007, vol. 15.

[29] F. Brezzi, “On the existence, uniqueness and approximation of saddle-point problems arising from lagrangian multipliers”, *Revue française d’automatique, informatique, recherche opérationnelle. Analyse numérique*, vol. 8, no. R2, pp. 129–151, 1974.

[30] E. Brivadis, A. Buffa, B. Wohlmuth, and L. Wunderlich, “Isogeometric mortar methods”, *Computer Methods in Applied Mechanics and Engineering*, vol. 284, pp. 292–319, 2015.

[31] A. Buffa and C. Giannelli, “Adaptive isogeometric methods with hierarchical splines: error estimator and convergence”, *Mathematical Models and Methods in Applied Sciences*, vol. 26, no. 01, pp. 1–25, 2016.

[32] A. Buffa, Y. Maday, and F. Rapetti, “A sliding mesh-mortar method for a two dimensional currents model of electric enginges”, *ESAIM: Mathematical Modelling and Numerical Analysis*, vol. 35, no. 2, pp. 191–228, 2001.

[33] D. Chapelle and K.-J. Bathe, “The inf–sup test”, *Computers & structures*, vol. 47, no. 4-5, pp. 537–545, 1993.

[34] A. Chatterjee, “An introduction to the proper orthogonal decomposition”, *Current science*, vol. 78, no. 7, pp. 808–817, 2000.

[35] S. Clénet, “Uncertainty quantification in computational electromagnetics: the stochastic approach”, *International Compumag society Newsletters*, vol. 20, no. 1, pp. 2–12, 2013.

[36] A. J. Clerc and A. Muetze, “Measurement of stator core magnetic degradation during the manufacturing process”, *IEEE transactions on industry applications*, vol. 48, no. 4, pp. 1344–1352, 2012.

[37] K. A. Cliffe, M. B. Giles, R. Scheichl, and A. L. Teckentrup, “Multilevel Monte Carlo methods and applications to elliptic pdes with random coefficients”, *Computing and Visualization in Science*, vol. 14, no. 1, p. 3, 2011.

[38] A. Cohen, R. DeVore, and C. Schwab, “Analytic regularity and polynomial approximation of parametric and stochastic elliptic PDEs”, *Analysis and Applications*, vol. 09, no. 01, pp. 11–47, 2011.

[39] Computer Simulation Technology AG, *CST EM STUDIO®*, `www.cst.com`.

[40] J. A. Cottrell, T. J. R. Hughes, and Y. Bazilevs, *Isogeometric Analysis: Toward Integration of CAD and FEA*. Wiley, 2009.

[41] J. Darlington, C. Pantelides, B. Rustem, and B. A. Tanyi, “Decreasing the sensitivity of open-loop optimal solutions in decision making under uncertainty”, *European Journal of Operational Research*, vol. 121, no. 2, pp. 343–362, 2000.

[42] H. De Gersem and T. Weiland, “Harmonic weighting functions at the sliding interface of a finite-element machine model incorporating angular displacement”, *IEEE Transactions on Magnetics*, vol. 40, no. 2, pp. 545–548, 2004.

[43] L. Dedè, “Reduced basis method and a posteriori error estimation for parametrized linear-quadratic optimal control problems”, *SIAM Journal on Scientific Computing*, vol. 32, no. 2, pp. 997–1019, 2010.

[44] M. Degano, E. Carraro, and N. Bianchi, “Selection criteria and robust optimization of a traction PM-assisted synchronous reluctance motor”, *IEEE Transactions on Industry Applications*, vol. 51, no. 6, pp. 4383–4391, 2015.

[45] A. Demenko, “Movement simulation in finite element analysis of electric machine dynamics”, *IEEE Transactions on Magnetics*, vol. 32, no. 3, pp. 1553–1556, 1996.

[46] A. Der Kiureghian and O. Ditlevsen, “Aleatory or epistemic? does it matter?”, *Structural Safety*, vol. 31, no. 2, pp. 105–112, 2009.

[47] P. Di Barba, M. Bonislawski, R. Palka, P. Paplicki, and M. Wardach, “Design of hybrid excited synchronous machine for electrical vehicles”, *IEEE Transactions on Magnetics*, vol. 51, no. 8, pp. 1–6, 2015.

[48] P. Di Barba, M. E. Mognaschi, S. Wiak, M. Przybylski, and B. Slusarek, “Wind-driven optimization for the design of switched reluctance motors”, in *Electromagnetic Fields in Mechatronics, Electrical and Electronic Engineering (ISEF) Book of Abstracts, 2017 18th International Symposium on*, IEEE, 2017, pp. 1–2.

[49] J. Dick, F. Y. Kuo, and I. H. Sloan, “High-dimensional integration: the quasi-Monte Carlo way”, *Acta Numerica*, vol. 22, pp. 133–288, 2013.

[50] M. Diehl, H. G. Bock, and E. Kostina, “An approximation technique for robust nonlinear optimization”, *Mathematical Programming*, vol. 107, no. 1, pp. 213–230, 2006.

[51] M. Diehl, J. Gerhard, W. Marquardt, and M. Mönnigmann, “Numerical solution approaches for robust nonlinear optimal control problems”, *Computers & Chemical Engineering*, vol. 32, no. 6, pp. 1279–1292, 2008.

[52] M. A. Dihlmann and B. Haasdonk, “Certified PDE-constrained parameter optimization using reduced basis surrogate models for evolution problems”, *Computational Optimization and Applications*, vol. 60, no. 3, pp. 753–787, 2015.

[53] D. G. Dorrell, M. Popescu, and D. M. Ionel, “Unbalanced magnetic pull due to asymmetry and low-level static rotor eccentricity in fractional-slot brushless permanent-magnet motors with surface-magnet and consequent-pole rotors”, *IEEE Transactions on Magnetics*, vol. 46, no. 7, pp. 2675–2685, 2010.

[54] Y. Duan and D. M. Ionel, “A review of recent developments in electrical machine design optimization methods with a permanent magnet synchronous motor benchmark study”, *IEEE Transactions on Industry Applications*, vol. 49, no. 3, pp. 1268–1275, 2013.

[55] J. L. Eftang, A. T. Patera, and E. M. Rønquist, “An “hp” certified reduced basis method for parametrized elliptic partial differential equations”, *SIAM Journal on Scientific Computing*, vol. 32, no. 6, pp. 3170–3200, 2010.

[56] C. de Falco, A. Reali, and R. Vázquez, “GeoPDEs: a research tool for isogeometric analysis of PDEs”, *Advances in Engineering Software*, vol. 42, pp. 1020–1034, 2011.

[57] T. Finken, M. Hombitzer, and K. Hameyer, “Study and comparison of several permanent-magnet excited rotor types regarding their applicability in electric vehicles”, in *Emobility-Electrical Power Train, 2010*, IEEE, 2010, pp. 1–7.

[58] W. Y. Fowlkes and C. M. Creveling, *Engineering methods for robust product design: using Taguchi methods in technology and product development*. Addison-Wesley, 1995.

[59] J. Frochte, “Finite elemente in 1D”, in *Finite-Elemente-Methode: eine praxisbezogene Einführung mit GNU Octave/MATLAB*. Carl Hanser Verlag GmbH Co KG, 2016, pp. 59–111.

[60] J. Frochte, “Finite elemente in 2D”, in *Finite-Elemente-Methode: eine praxisbezogene Einführung mit GNU Octave/MATLAB*. Carl Hanser Verlag GmbH Co KG, 2016, pp. 112–168.

[61] H. Frohne, “Über den einseitigen magnetischen Zug in Drehfeldmaschinen”, *Archiv für Elektrotechnik*, vol. 51, no. 5, pp. 300–308, 1968.

[62] V. Gabrel, C. Murat, and A. Thiele, “Recent advances in robust optimization: an overview”, *European journal of operational research*, vol. 235, no. 3, pp. 471–483, 2014.

[63] A. Galetzka, Z. Bontinck, U. Römer, and S. Schöps, “Multilevel Monte Carlo simulation of the eddy current problem with random parameters”, in *2017 International Applied Computational Electromagnetics Society Symposium - Italy (ACES)*, 2017, pp. 1–2.

[64] A. Galetzka, Z. Bontinck, U. Römer, and S. Schöps, “A multilevel Monte Carlo method based on Richardson extrapolation error estimators for high-dimensional uncertainty quantification of low-frequency electromagnetic devices”, *IEEE transactions on magnetics*, submitted.

[65] P. Gangl, S. Amstutz, and U. Langer, “Topology optimization of electric motor using topological derivative for nonlinear magnetostatics”, *IEEE Transactions on Magnetics*, vol. 52, no. 3, pp. 1–4, 2016.

[66] W. Gerlach and O. Stern, “Das magnetische Moment des Silberatoms”, *Zeitschrift für Physik*, vol. 9, no. 1, pp. 353–355, 1922.

[67] J. F. Gieras, *Permanent magnet motor technology: design and applications*, 3rd ed. CRC press, 2009.

[68] M. B. Giles, “Multilevel Monte Carlo path simulation”, *Operations Research*, vol. 56, no. 3, pp. 607–617, 2008.

[69] M. B. Giles, “Multilevel Monte Carlo methods”, *Acta numerica*, vol. 24, pp. 259–328, 2015.

[70] M. B. Giles and B. J. Waterhouse, “Multilevel quasi-Monte Carlo path simulation”, in *Advanced Financial Modelling*, vol. 8, Walter de Gruyter, 2009, pp. 165–181.

[71] H. Gomez, T. J. Hughes, X. Nogueira, and V. M. Calo, “Isogeometric analysis of the isothermal Navier–Stokes–Korteweg equations”, *Computer Methods in Applied Mechanics and Engineering*, vol. 199, no. 25-28, pp. 1828–1840, 2010.

[72] J. Gravesen, A. Evgrafov, D.-M. Nguyen, and P. Nørtoft, “Planar parametrization in isogeometric analysis”, in *Mathematical Methods for Curves and Surfaces*, ser. Lecture Notes in Computer Science, M. Floater, T. Lyche, M.-L. Mazure, K. Mørken, and L. L. Schumaker, Eds., vol. 8177, Springer Berlin Heidelberg, 2014, pp. 189–212.

[73] M. Gubisch and S. Volkwein, “Proper orthogonal decomposition for linear-quadratic optimal control”, in *Model Reduction and Approximation: Theory and Algorithms*, P. Benner, A. Cohen, M. Ohlberger, and K. Willcox, Eds., SIAM, 2017, ch. 1, pp. 65–136.

[74] M. Gunzburger and C. Webster, “Uncertainty quantification for partial differential equations with stochastic coefficients”, in *The Beijing Intelligencer*, Springer, 2015, pp. 50–61.

[75] B. Haasdonk, M. Dihlmann, and M. Ohlberger, “A training set and multiple bases generation approach for parameterized model reduction based on adaptive grids in parameter space”, *Mathematical and Computer Modelling of Dynamical Systems*, vol. 17, no. 4, pp. 423–442, 2011.

[76] B. Haasdonk and M. Ohlberger, “Reduced basis method for finite volume approximations of parametrized linear evolution equations”, *ESAIM: Mathematical Modelling and Numerical Analysis*, vol. 42, no. 2, pp. 277–302, 2008.

[77] B. Haasdonk, “Tutorial on reduced basis”, in *Model Reduction and Approximation: Theory and Algorithms*, P. Benner, A. Cohen, M. Ohlberger, and K. Willcox, Eds., SIAM, 2017, ch. 2, pp. 65–136.

[78] A.-L. Haji-Ali, F. Nobile, E. von Schwerin, and R. Tempone, “Optimization of mesh hierarchies in multilevel monte carlo samplers”, *Stochastics and Partial Differential Equations Analysis and Computations*, vol. 4, no. 1, pp. 76–112, 2016.

[79] P. Hansbo, C. Lovadina, I. Perugia, and G. Sangalli, “A Lagrange multiplier method for the finite element solution of elliptic interface problems using non-matching meshes”, *Numerische Mathematik*, vol. 100, no. 1, pp. 91–115, 2005.

[80] O. Heaviside, “XLV. on the electromagnetic wave-surface”, *The London, Edinburgh, and Dublin Philosophical Magazine and Journal of Science*, vol. 19, no. 121, pp. 397–419, 1885.

[81] T. Henneron, H. Mac, and S. Clénet, “Error estimation of a proper orthogonal decomposition reduced model of a permanent magnet synchronous machine”, *IET Science, Measurement & Technology*, vol. 9, no. 2, pp. 172–177, 2015.

[82] M. W. Hess and P. Benner, “Fast evaluation of time–harmonic maxwell’s equations using the reduced basis method”, *IEEE Transactions on Microwave Theory and Techniques*, vol. 61, no. 6, pp. 2265–2274, 2013.

[83] M. Hinze, R. Pinnau, M. Ulbrich, and S. Ulbrich, *Optimization with PDE Constraints*, ser. Mathematical Modelling: Theory and Applications. Springer, 2008.

[84] D. Howe and Z. Zhu, “The influence of finite element discretisation on the prediction of cogging torque in permanent magnet excited motors”, *IEEE Transactions on magnetics*, vol. 28, no. 2, pp. 1080–1083, 1992.

[85] M.-F. Hsieh and Y.-H. Yeh, “Rotor eccentricity effect on cogging torque of pm generators for small wind turbines”, *IEEE Transactions on Magnetics*, vol. 49, no. 5, pp. 1897–1900, 2013.

[86] B. Huang and X. Du, “A robust design method using variable transformation and Gauss–Hermite integration”, *International Journal for Numerical Methods in Engineering*, vol. 66, no. 12, pp. 1841–1858, 2006.

[87] T. J. R. Hughes, J. A. Cottrell, and Y. Bazilevs, “Isogeometric analysis: CAD, finite elements, NURBS, exact geometry and mesh refinement”, *Computer methods in applied mechanics and engineering*, vol. 194, pp. 4135–4195, 2005.

[88] T. J. Hughes, J. A. Evans, and A. Reali, “Finite element and NURBS approximations of eigenvalue, boundary-value, and initial-value problems”, *Computer Methods in Applied Mechanics and Engineering*, vol. 272, pp. 290–320, 2014.

[89] R. Jankoski, U. Römer, and S. Schöps, “Modeling of spatial uncertainties in the magnetic reluctivity”, *COMPEL: The international journal for computation and mathematics in electrical and electronic engineering*, vol. 36, no. 4, pp. 1151–1167, 2017.

[90] F. Jurisch, “Production process based deviations in the orientation of anisotropic permanent magnets and their effects onto the operation performance of electrical machines and magnetic sensors–german”, in *International ETG-Kontress Tagungsband, (ETG-FB–107)*, vol. 1, VDE Verlag Berlin, 2007, pp. 255–261.

[91] J. F. Keithley, *The story of electrical and magnetic measurements: from 500 BC to the 1940s*. John Wiley & Sons, 1999.

[92] J. Kennedy and R. Eberhart, “Particle swarm optimization”, in *Neural Networks, 1995. Proceedings., IEEE International Conference on*, vol. 4, 1995, pp. 1942–1948.

[93] A. Krings, S. Nategh, O. Wallmark, and J. Soulard, “Influence of the welding process on the performance of slotless PM motors with sife and nife stator laminations”, *IEEE Transactions on Industry Applications*, vol. 50, no. 1, pp. 296–306, 2014.

[94] O. Lass and S. Ulbrich, “Model order reduction techniques with a posteriori error control for nonlinear robust optimization governed by partial differential equations”, *SIAM Journal on Scientific Computing*, vol. 39, no. 5, S112–S139, 2017.

[95] P. Lazari, J. Wang, and L. Chen, “A computationally efficient design technique for electric-vehicle traction machines”, *IEEE Transactions on Industry Applications*, vol. 50, no. 5, pp. 3203–3213, 2014.

[96] L. Lebensztajn, C. A. R. Marretto, M. C. Costa, and J.-L. Coulomb, “Kriging: a useful tool for electromagnetic device optimization”, *IEEE Transactions on Magnetics*, vol. 40, no. 2, pp. 1196–1199, 2004.

[97] S.-W. Lee, J. Lee, and S. Cho, “Isogeometric shape optimization of ferromagnetic materials in magnetic actuators”, *IEEE Transactions on Magnetics*, vol. 52, no. 2, pp. 1–8, 2016.

[98] R. M. Lewis, A. T. Patera, and J. Peraire, “A posteriori finite element bounds for sensitivity derivatives of partial-differential-equation outputs”, *Finite elements in analysis and design*, vol. 34, no. 3-4, pp. 271–290, 2000.

[99] M. Li, M. H. Mohammadi, T. Rahman, and D. Lowther, “Analysis and design of electrical machines with material uncertainties in iron and permanent magnet”, *COMPEL: The international journal for computation and mathematics in electrical and electronic engineering*, vol. 36, no. 5, pp. 1326–1337, 2017.

[100] M. Lukaniszyn, M. Jagiela, and R. Wrobel, “Optimization of permanent magnet shape for minimum cogging torque using a genetic algorithm”, *IEEE Transactions on Magnetics*, vol. 40, no. 2, pp. 1228–1231, 2004.

[101] B. Masschaele, T. Roggen, H. De Gersem, E. Jannsens, and T. Nguyen, “Design of a strong gradient magnet for the deflection of nanoclusters”, *IEEE Transactions on Applied Superconductivity*, vol. 22, no. 3, 2012.

[102] J. C. Maxwell, “A dynamical theory of the electromagnetic field”, *Philosophical transactions of the Royal Society of London*, vol. 155, pp. 459–512, 1865.

[103] D. Meeker, *Finite element method magnetics user’s manual*, Version 4.2 (09Nov2010 Build), 2010.

[104] X. Meng, S. Wang, J. Qiu, Q. Zhang, J. G. Zhu, Y. Guo, and D. Liu, “Robust multilevel optimization of PMSM using design for six sigma”, *IEEE Transactions on Magnetics*, vol. 47, no. 10, pp. 3248–3251, 2011.

[105] J. Mizia, K. Adamiak, A. Eastham, and G. Dawson, “Finite element force calculation: comparison of methods for electric machines”, *IEEE Transactions on Magnetics*, vol. 24, no. 1, pp. 447–450, 1988.

[106] P. Monk, *Finite Element Methods for Maxwell’s Equations*. Oxford University Press, 2003.

[107] P. J. Nahin, “Preface to the Johns Hopkins edition”, in *Oliver Heaviside: the life, work, and times of an electrical genius of the Victorian age*. The Johns Hopkins University Press Baltimore and London, 2002, pp. xix–xxiii.

[108] S. A. Nasar, L. Unnewehr, and I. Boldea, *Permanent magnet, reluctance, and self-synchronous motors*. CRC press, 1993.

[109] F. Negri, G. Rozza, A. Manzoni, and A. Quarteroni, “Reduced basis method for parametrized elliptic optimal control problems”, *SIAM Journal on Scientific Computing*, vol. 35, no. 5, A2316–A2340, 2013.

[110] S. Niu, S. Ho, and W. Fu, “Power balanced electromagnetic torque computation in electric machines based on energy conservation in finite-element method”, *IEEE transactions on magnetics*, vol. 49, no. 5, pp. 2385–2388, 2013.

[111] J. Nocedal and S. J. Wright, *Numerical optimization*, 2nd ed., ser. Springer Series in Operations Research and Financial Engineering. Springer, 2006.

[112] P. Offermann and K. Hameyer, “Stochastic models for the evaluation of magnetisation faults”, *COMPEL: The International Journal for Computation and Mathematics in Electrical and Electronic Engineering*, vol. 33, no. 1/2, pp. 245–253, 2013.

[113] P. Offermann, H. Mac, T. T. Nguyen, S. Clénet, H. De Gersem, and K. Hameyer, “Uncertainty quantification and sensitivity analysis in electrical machines with stochastically varying machine parameters”, *IEEE Transactions on Magnetics*, vol. 51, no. 3, pp. 1–4, 2015.

[114] I. Oliveira and A. Patera, “Reduced-basis techniques for rapid reliable optimization of systems described by affinely parametrized coercive elliptic partial differential equations”, *Optimization and Engineering*, vol. 8, no. 1, pp. 43–65, 2007.

[115] U. Pahner, R. Mertens, H. De Gersem, R. Belmans, and K. Hameyer, “A parametric finite element environment tuned for numerical optimization”, *IEEE Transactions on Magnetics*, vol. 34, no. 5, pp. 2936–2939, 1998.

[116] R. H. Park, “Two-reaction theory of synchronous machines generalized method of analysis - part I”, *Transactions of the American Institute of Electrical Engineers*, vol. 48, no. 3, pp. 716–727, 1929.

[117] A. T. Patera and G. Rozza, *Reduced Basis Approximation and a Posteriori Error Estimation for Parametrized Partial Differential Equations*. MIT, 2007.

[118] A. Pels, Z. Bontinck, J. Corno, H. De Gersem, and S. Schöps, “Optimization of a Stern-gerlach Magnet by magnetic field-circuit coupling and isogeometric analysis”, *IEEE Transactions on Magnetics*, vol. 51, no. 12, 2015.

[119] D. A. Philips, “Coupling finite elements and magnetic networks in magnetostatics”, *International Journal for Numerical Methods in Engineerin*, vol. 35, no. 10, pp. 1991–2002, 1992.

[120] T. Preston, A. Reece, and P. Sangha, “Induction motor analysis by time-stepping techniques”, *IEEE Transactions on Magnetics*, vol. 24, no. 1, pp. 471–474, 1988.

[121] C. Prud′Homme, D. V. Rovas, K. Veroy, L. Machiels, Y. Maday, A. T. Patera, and G. Turinici, “Reliable real-time solution of parametrized partial differential equations: reduced-basis output bound methods”, *Journal of Fluids Engineering*, vol. 124, no. 1, pp. 70–80, 2002.

[122] A. Quarteroni, R. Sacco, and F. Saleri, “Polynomial interpolation”, in *Numerical Mathematics*, ser. Texts in Applied Mathematics. Springer, 2000, vol. 37, ch. 8, pp. 327–370.

[123] A. Quarteroni and A. Valli, *Domain Decomposition Methods for Partial Differential Equations*, ser. Numerical Mathematics and Scientific Computation. Oxford University Press, 1999, pp. 103–144.

[124] A. Quarteroni and A. Valli, *Numerical Approximation of Partial Differential Equations*, ser. Springer Series in Computational Mathematics. Berlin: Springer, 2008, vol. 23.

[125] M. A. Rahman and P. Zhou, “Determination of saturated parameters of PM motors using loading magnetic fields”, *IEEE transactions on magnetics*, vol. 27, no. 5, pp. 3947–3950, 1991.

[126] R. Ramarotafika, A. Benabou, and S. Clénet, “Stochastic modeling of soft magnetic properties of electrical steels: application to stators of electrical machines”, *IEEE Transactions on Magnetics*, vol. 48, no. 10, pp. 2573–2584, 2012.

[127] D. A. Reed, “Computational science: ensuring america’s comeptitiveness”, President’s Information Technology Advisory Committee, Tech. Rep., 2005.

[128] A. M. El–Refaie, “Fractional–slot concentrated-windings synchronous permanent magnet machines: opportunities and challenges”, *IEEE Transactions on industrial Electronics*, vol. 57, no. 1, pp. 107–121, 2010.

[129] L. F. Richardson, “IX. the approximate arithmetical solution by finite differences of physical problems involving differential equations, with an application to the stresses in a masonry dam”, *Philosophical Transactions of the Royal Society A*, vol. 210, no. 459-470, pp. 307–357, 1911.

[130] J. Robinson and Y. Rahmat-Samii, “Particle swarm optimization in electromagnetics”, *IEEE Transactions on Antennas and Propagation*, vol. 52, no. 2, pp. 397–407, 2004.

[131] G. Rozza, D. B. P. Huynh, and A. T. Patera, “Reduced basis approximation and a posteriori error estimation for affinely parametrized elliptic coercive partial differential equations”, *Archives of Computational Methods in Engineering*, vol. 15, no. 3, 2007.

[132] S. J. Salon, *Finite Element Analysis of Electrical Machines*. Kluwer, 1995.

[133] A. Saltelli, “Making best use of model evaluations to compute sensitivity indices”, *Computer physics communications*, vol. 145, no. 2, pp. 280–297, 2002.

[134] S. Schöps, H. De Gersem, and T. Weiland, “Winding functions in transient magnetoquasistatic field-circuit coupled simulations”, *COMPEL: The international journal for computation and mathematics in electrical and electronic engineering*, vol. 32, no. 6, pp. 2063–2083, 2013.

[135] J. R. Shewchuk, “Triangle: engineering a 2D quality mesh generator and Delaunay triangulator”, in *Applied Computational Geometry: Towards Geometric Engineering*, ser. Lecture Notes in Computer Science, M. C. Lin and D. Manocha, Eds., vol. 1148, Springer-Verlag, 1996, pp. 203–222.

[136] A. Sichau and S. Ulbrich, “A second order approximation technique for robust shape optimization”, *Applied Mechanics and Materials*, vol. 104, p. 13, 2011.

[137] G. Y. Sizov, P. Zhang, D. M. Ionel, N. A. Demerdash, and M. Rosu, “Automated multi-objective design optimization of PM AC machines using computationally efficient FEA and differential evolution”, *IEEE Transactions on Industry Applications*, vol. 49, no. 5, pp. 2086–2096, 2013.

[138] S. Smolyak, “Quadrature and interpolation formulas for tensor products of certain classes of functions”, in *Soviet Mathematics Doklady*, vol. 4, 1963, pp. 240–243.

[139] I. M. Sobol, “Sensitivity estimates for nonlinear mathematical models”, *Mathematical modelling and computational experiments*, vol. 1, no. 4, pp. 407–414, 1993.

[140] I. M. Sobol, “Global sensitivity indices for nonlinear mathematical models and their Monte Carlo estimates”, *Mathematics and computers in simulation*, vol. 55, no. 1-3, pp. 271–280, 2001.

[141] T. Steinmetz, S. Kurz, and M. Clemens, “Domains of validity of quasistatic and quasistationary field approximations”, *COMPEL: The international journal for computation and mathematics in electrical and electronic engineering*, vol. 30, no. 4, pp. 1237–1247, 2011.

[142] R. L. Stoll, “One-dimensional eddy-current flow”, in *The analysis of eddy currents*, Oxford University Press, 1974, ch. 2, pp. 10–27.

[143] S. Stringari and R. R. Wilson, “Romagnosi and the discovery of electromagnetism”, *Rendiconti Lincei*, vol. 11, no. 2, pp. 115–136, 2000.

[144] S. Sundaresan, K. Ishii, and D. R. Houser, “A robust optimization procedure with variations on design variables and constraints”, *Engineering Optimization*, vol. 24, no. 2, pp. 101–117, 1995.

[145] T. Tärnhuvud and K. Reichert, “Accuracy problems of force and torque calculation in FE-systems”, *IEEE Transactions on Magnetics*, vol. 24, no. 1, pp. 443–446, 1988.

[146] A. L. Teckentrup, R. Scheichl, M. B. Giles, and E. Ullmann, “Further analysis of multilevel Monte Carlo methods for elliptic PDEs with random coefficients”, *Numerische Mathematik*, vol. 125, no. 3, pp. 569–600, 2013.

[147] I. Temizer, P. Wriggers, and T. Hughes, “Contact treatment in isogeometric analysis with NURBS”, *Computer Methods in Applied Mechanics and Engineering*, vol. 200, no. 9-12, pp. 1100–1112, 2011.

[148] V. N. Temlyakov, “Greedy approximation”, *Acta Numerica*, vol. 17, pp. 235–409, 2008.

[149] A. Tenhunen, “Finite-element calculation of unbalanced magnetic pull and circulating current between parallel windings in induction motor with non-uniform eccentric rotor”, *Proceedings of Electromotion*, vol. 1, pp. 19–24, 2001.

[150] A. Tenhunen, T. Benedetti, T. Holopainen, and A. Arkkio, “Electromagnetic forces of the cage rotor in conical whirling motion”, *IEE Proceedings B - Electric Power Applications*, vol. 150, no. 5, pp. 563–568, 2003.

[151] H. Tiesler, R. M. Kirby, D. Xiu, and T. Preusser, “Stochastic collocation for optimal control problems with stochastic PDE constraints”, *SIAM Journal on Control and Optimization*, vol. 50, no. 5, pp. 2659–2682, 2012.

[152] H. A. Toliyat, M. S. Arefeen, and A. G. Parlos, “A method for dynamic simulation of air-gap eccentricity in induction machines”, *IEEE transactions on industry applications*, vol. 32, no. 4, pp. 910–918, 1996.

[153] H. A. Toliyat and N. A. Al-Nuaim, “Simulation and detection of dynamic air-gap eccentricity in salient-pole synchronous machines”, *IEEE transactions on industry applications*, vol. 35, no. 1, pp. 86–93, 1999.

[154] I. Tsukerman, “Accurate computation of “ripple solutions” on moving finite element meshes”, *IEEE Transactions on magnetics*, vol. 31, no. 3, pp. 1472–1475, 1995.

[155] S. Ullmann and J. Lang, “POD-Galerkin modeling and sparse-grid collocation for a natural convection problem with stochastic boundary conditions”, in *Sparse Grids and Applications - Munich 2012*, ser. Lecture Notes in Computational Science and Engineering, J. Garcke and D. Pflüger, Eds., Springer, 2014, pp. 295–315.

[156] R. Vázquez, “A new design for the implementation of isogeometric analysis in Octave and Matlab: GeoPDEs 3.0”, *Computers & Mathematics with Applications*, vol. 72, no. 3, pp. 523–554, 2016.

[157] A.-V. Vuong, C. Giannelli, B. Jüttler, and B. Simeon, “A hierarchical approach to adaptive local refinement in isogeometric analysis”, *Computer Methods in Applied Mechanics and Engineering*, vol. 200, no. 49-52, pp. 3554–3567, 2011.

[158] A. Wang and J. Guo, “A novel hybrid genetic algorithm for optimal design of interior permanent magnet machine”, in *Electromagnetic Fields in Mechatronics, Electrical and Electronic Engineering (ISEF) Book of Abstracts, 2017 18th International Symposium on*, IEEE, 2017, pp. 1–2.

[159] D. Xiu, *Numerical Methods for Stochastic Computations: A Spectral Method Approach*. Princeton University Press, 2010.

[160] X.-S. Yang, “A new metaheuristic bat-inspired algorithm”, *Nature inspired cooperative strategies for optimization (NICSO 2010)*, pp. 65–74, 2010.

[161] S. Zaglmayr, “High order finite elements for electromagnetic field computation”, PhD thesis, Kepler University, Linz Austria, 2006.

[162] M. J. Zahr and C. Farhat, “Progressive construction of a parametric reduced-order model for PDE-constrained optimization”, *International Journal for Numerical Methods in Engineering*, vol. 102, no. 5, pp. 1111–1135, 2015.

[163] M. Zeraoulia, M. E. H. Benbouzid, and D. Diallo, “Electric motor drive selection issues for HEV propulsion systems: a comparative study”, *IEEE Transactions on Vehicular Technology*, vol. 55, no. 6, pp. 1756–1764, 2006.

[164] Y. Zhang, “General robust-optimization formulation for nonlinear programming”, *Journal of optimization theory and applications*, vol. 132, no. 1, pp. 111–124, 2007.

[165] Z. Zhu and Y. Li, “Modularity techniques in high performance permanent magnet machines and applications”, *CES Transactions on Electrical Machines and Systems*, vol. 2, no. 1, pp. 93–103, 2018.

Publications

Full Journal

Z. Bontinck, H. De Gersem and S. Schöps, “Response surface models for the uncertainty quantification of eccentric permanet magnet synchronous machines”, *IEEE transactions on magnetics*, vol. 52, no. 3, 2016.

Z. Bontinck, J. Corno, S. Schöps and H. De Gersem, “Isogeometric analysis and harmonic stator–rotor coupling for simulating electric machines”, *Computer methods in applied mechanics and engineering*, vol. 334, pp. 40–55, 2018.

Z. Bontinck, O. Lass, S. Schöps, H. De Gersem, S. Ulbrich and O. Rain, “Robust optimization formulations for the design of an electric machine”, *IET Science, Measurement & Technology*, vol. 12, no. 8, pp. 939–948, 2018.

A. Pels, Z. Bontinck, J. Corno, H. De Gersem and S. Schöps, “Optimization of a Stern–Gerlach magnet by magnetic field-circuit coupling and isogeometric analysis”, *IEEE transactions on magnetics,* vol. 51, no. 12, 2015.

P. Bhat, Z. Bontinck, J. Corno, S. Schöps and H. De Gersem, “Modelling of Electric Machines Using Isogeometric Analysis and Non-Overlapping Schwarz Domain Decomposition”, *COMPEL*, vol. 37, no. 5, pp. 1805-1814, 2018.

I. Ion, Z. Bontinck, D. Loukrezis, U. Römer, O. Lass, S. Ulbrich, S. Schöps and H. De Gersem, “Robust Shape Optimization of Electric Devices Based on Deterministic Optimization Methods and Finite Element Analysis With Affine Decomposition and Design Elements”, *Electrical Engineering*, vol. 100, no. 4, pp. 2635–2647, 2018.

A. Galetzka, Z. Bontinck, U. Römer and S. Schöps, “A multilevel Monte Carlo method based on Richardson extrapolation error estimators for high-dimensional uncertainty quantification of low-frequency electromagnetic devices”, *IEEE transactions on magnetics*, submitted.

Conference Proceedings

A. Galetzka, Z. Bontinck, U. Römer and S. Schöps, “Multilevel Monte Carlo simulation of the eddy current problem with random parameters”, In *2017 International Applied Computational Electromagnetics Society Symposium (ACES)*, Florence, Italy, 2017.

Z. Bontinck, O. Lass, H. De Gersem and S. Schöps, “Uncertainty quantification for a permanent magnet synchronous machine with dynamic rotor eccentricity”, in *Industrial Mathematics at ECMI 2016: Theory and Algorithms*, P. Quintela, P. Barral, D. Gomez, F.J. Pena, J. Rodriguez, P. Salgado, M.E. Vazquez-Mendez, Eds., Springer Verlag, 2018, pp. 493–499.

Chapters

Z. Bontinck, O. Lass, O. Rain and S. Schöps, “Model Order Reduction for Rotating Electrical Machines”, in *Reduced-Order Modeling (ROM) for Simulation and Optimization*, W. Keiper, A. Milde, S. Volkwein, Eds., Springer Verlag, 2018, Ch 6., pp. 121–140.

A Description of the Geometry and the Material Properties of the Permanent Magnet Synchronous Machine

The parameters of the machine are listed in Table A.1 and in Table A.2. The geometrical parameters are depicted in Figure A.1.

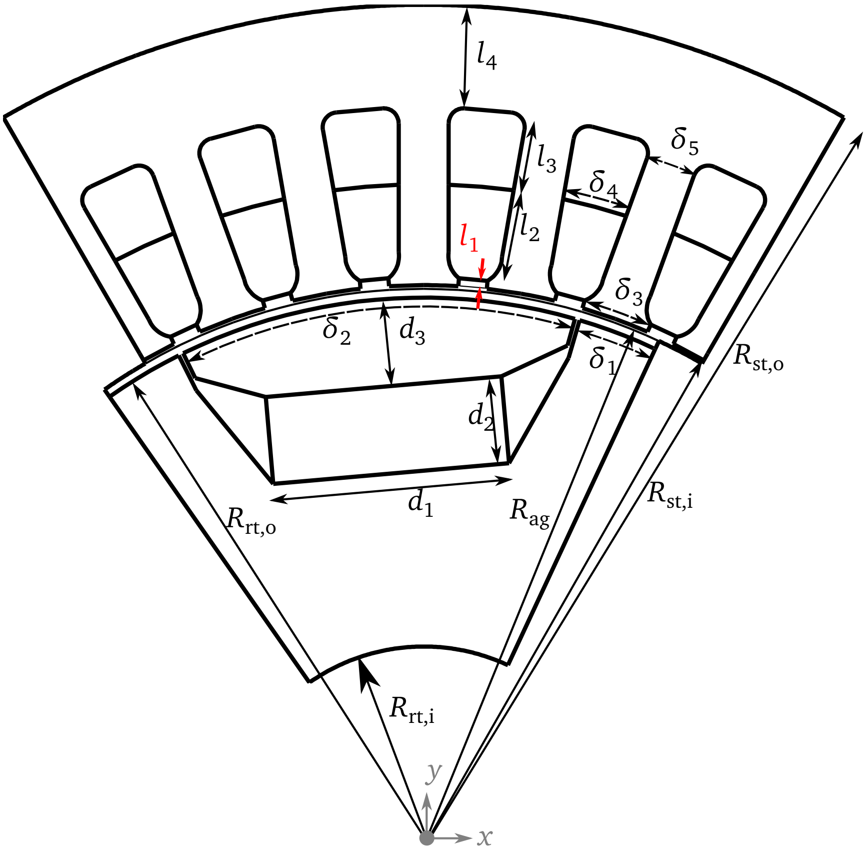

Figure A.1: Geometry of the permanent magnet synchronous machine

Table A.1: Parameters describing the material properties.

Material properties		
Conductivity of iron	σ_{Fe}	0 S/m
Conductivity of copper	σ_{Cu}	0 S/m
Conductivity of PM	σ_{PM}	0 S/m
Relative permeability of iron	$\mu_{\mathrm{r,Fe}}$	500
Relative permeability of copper	$\mu_{\mathrm{r,Cu}}$	1
Relative permeability of PM	$\mu_{\mathrm{r,PM}}$	1.05
Remanent magnetic field of PM	B_{r}	0.94 T

Table A.2: Parameters describing the geometry of the machine.

Rotor		
Inner radius rotor	$R_{\mathrm{rt,i}}$	16 mm
Outer radius rotor	$R_{\mathrm{rt,o}}$	44 mm
Magnet width	d_1	19 mm
Magnet height	d_2	7 mm
Depth of the magnet in rotor	d_3	7 mm
	δ_1	8.5°
	δ_2	42°
Stator		
Inner radius stator	$R_{\mathrm{st,i}}$	45 mm
Outer radius stator	$R_{\mathrm{st,o}}$	67.5 mm
Number of turns	N_w	12
	δ_3	7°
	δ_4	5.7°
	δ_5	4°
	l_1	0.6 mm
	l_2	5.4 mm
	l_3	5 mm
	l_4	8.2 mm
Skew angle	η	0.52°
Airgap		
Radius of Γ_{ag}	R_{ag}	44.7 mm

B Values for Determining the Driving Cycle of a e-Go-Cart

Table B.1: Values for determining the driving cycle of a ego-cart.

Properties of the go-cart		
Mass	m	15 kg
Radius wheel	r_{wh}	12 cm
Frontal area	A_{front}	$1\,\text{m}^2$
Number of drives per axis	N_{dr}	2
Constants and material properties		
Rolling resistance	C_{rr}	0.01
Drag coefficient	C_{dr}	0.29
Air density	ρ_{air}	1.20

Curriculum Vitae

Okt. 2013 – Sep. 2018	Scientific Collaborator Technische Universität Darmstadt (Darmstadt – Germany) Graduate School of Computational Engineering Institut für Theorie Elektromagnetischer Felder
Sep. 2012 – Aug. 2013	Lecturing Assistant KU Leuven Kulak (Kortrijk – Belgium) Science and Technology
Sep. 2011 – Jul. 2012	Specific Teacher Training in Natural Sciences KU Leuven (Leuven – Belgium)
Jul. 2009 – Jul. 2011	Master of Science in Astronomy and Astrophysics Katholieke Universiteit Leuven (Leuven – Belgium)
Jul. 2011	Master thesis Unravelling the Chemical and Physical Structure of the Stellar Winds in AGB Stars: On the Detection of High Excitation Water Lines in the Carbon Rich Star CIT 6
Sep. 2006 – Sep. 2010	Bachelor of Physics Katholieke Universiteit Leuven (Leuven – Belgium)
Jul. 2009	Bachelor thesis Production of Si_n, V_n and $\mathrm{Si}_x\mathrm{V}_y$ ($4 < x < 10$ and $1 < y < 3$) Clusters and the Determination of the Ionization Potential of V_n Clusters ($2 < n < 33$)
Sep. 1999 – Jun. 2005	ASO: Mathematics (8h) – Sciences Sint Andreaslyceum Sint Kruis (Bruges - Belgium)

Acknowledgement

> “Ode, an die Freunde.”
>
> Zeger Bontinck after Friedrich von Schiller

With this part, I am writing the final staves and notes to my sheet music. It has been a four-and-a-half-years-lasting journey in which I gathered and discovered different tones, sounds and motifs. These sounds all together allowed me to finish this composition and many of them I could discover by the discussion with my two musical tutors. Therefore, I would like to thank professor Sebastian Schöps and professor Herbert De Gersem for transforming me from an astrophysicist to an electrical and computational engineer.

Lieber Sebastian, du hast mich, wie es für einen guten Doktorvater gehört, nicht nur gefordert sondern auch gefördert. Deine Forderungen haben mich z.B. angespornt, mich tiefer mit Sobolevräumen zu beschäftigen und haben dafür gesorgt, dass dieses Endergebnis, worauf ich sehr stolz bin, zustande gekommen ist. Auch persönlich weiß ich dich sehr zu schätzen. Nicht nur beruflich haben wir schöne Zeiten erlebt (z.B. die ECMI-2014-Busfahrt oder den Hund im Catania-Flughafen) sondern auch in der Freizeit haben wir uns oft getroffen (Spiele- und Kinoabenden,...). Mein Wohlfühlen in Darmstadt habe ich auch an dir zu verdanken. Ein ganz herzliches Dankeschön.

Beste Herbert, je kent me sinds mijn studententijd in België en mijn periode als praktijkassistent aan de Kulak. Ik weet nog hoe ik op het einde van mijn contract aan de Kulak je gevraagd heb of het mogelijk was te doctoreren en toen heb je me over Darmstadt geïnformeerd. Zonder deze tip, was ik nooit in Darmstadt geland en zonder onze verdere samenwerking had ik nooit dit werk geschreven. Niet enkel de wetenschappelijke input die ik van je kreeg wist ik te appreciëren, maar ook de persoonlijk interactie, ik denk bijvoorbeeld aan de biertjes in Brugge of Helsinki, weet ik hoog te achten. Het is dan ook oprecht dat ik deze maten aan mijn werk toevoeg en aan jou opdraag.

Furthermore, I want to show my gratitude to my fellow-composers with whom I was able to publish some sonatas. In alphabetical order these are Dr. Jacopo Corno, Laura D’Angelo, Armin Galetzka, Ion Gabriel Ion, Dr. Oliver Lass, Dimitris Loukrezis, Andreas Pels and professor Dr. Ulrich Römer. Thank you all for your scientific input and the fruitful collaboration.

Compositions can only be written, when the composer is supported by a maecenas. My work was supported by the "Excellence Initiative" of the German Federal and State Governments and the Graduate School of Computational Engineering (GSC) at Technische Universität Darmstadt and by the German BMBF in the context of the SIMUROM project (grant nr. 05M2013).

Since distraction is needed to stay focussed, I also want to thank the Temflepuffers of the GSC. You were not only willing to answer my stupid questions, but you also were responsible for the enjoyable atmosphere in our offices, the entertainment during the lunches and the after-work distractions (SVD 98, Kneipentours, Orschel, hunting for facehuggers, Stacy-Chelsea ...).

Für eine andere Quelle der Entspannung, möchte ich mich gerne bei den Nassoven bedanken. Ihr wart immer bereit mit mir ein Bierchen zu trinken und mein Gemecker über die Doktorarbeit an zu hören. Es gibt dank sei euch immer ein Ort in Darmstadt wo ich heimkommen kann.

Tot slot heeft een muziekstuk enkel waarde als het door de muziekliefhebber geapprecieërd wordt. Daarom wil ik mijn Belgische fanbasis graag bedanken. Kjellemans en Michiel bedankt om de weg naar Darmstadt niet te lang te vinden en me af en toe te bezoeken. Anderzijds was ik in Leuven/Tienen ook nog altijd welkom voor een bezoekje. De trouwste fans, echter, volgen mij reeds 31 jaar. Mama, papa, Mieke, Elke en co een groot deel van dit werk heb ik aan jullie te danken. Door jullie niet aflatende steun is 4,5 jaar werk in dit muzikaal werk geresulteerd. Jullie bezoeken aan het Odenwald waren een aangename afwisseling gedurende mijn jaren in Darmstadt.

And alas, everything has an end, also this symphonic work, but let me use the last line for thanking for the music accompanying me during the writing,